COMPRESSIBLE TURBULENCE IN A HIGH-SPEED HIGH REYNOLDS NUMBER MIXING LAYER

by

Rodney Dale Welch Bowersox

Dissertation Submitted to the Faculty of the

Virginia Polytechnic Institute and State University

in partial fulfillment of the requirements for the degree of

DOCTOR OF PHILOSOPHY

in

Aerospace Engineering

APPROVED:

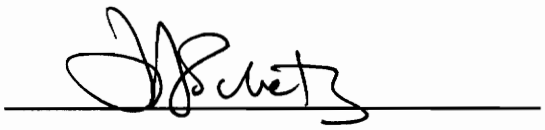

Dr. J. A. Schetz, Chairman

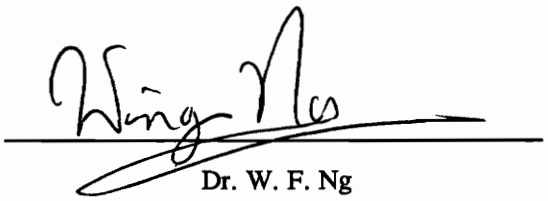

Dr. W. F. Ng

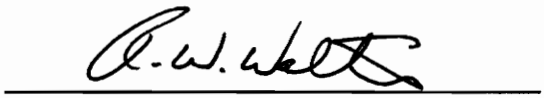

Dr. R. W. Walters

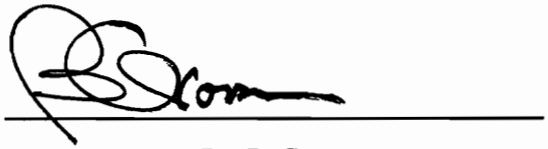

Dr. B. Grossman

Dr. A. K. Jakubowski

September, 1992

Blacksburg, Virginia

COMPRESSIBLE TURBULENCE IN A HIGH-SPEED HIGH REYNOLDS NUMBER MIXING LAYER

by

Rodney D. W. Bowersox

Joseph A. Schetz, Chairman

Aerospace Engineering

(ABSTRACT)

Compressible turbulence in a high-speed, high Reynolds number, supersonic free shear layer was studied. A two-dimensional free mixing layer was chosen to study turbulence rather than a wall bounded flow due to the experimental fact that the effects of compressibility become significant at lower Mach numbers. The mixing layer was generated by supersonic injection of air (M_s = 1.8, P_{ts} = 0.5 atm, T_{ts} = 295K, and Re/m = $7x10^6$) through a rearward facing tangential slot, into a supersonic free stream (M_∞ = 4.0, $P_{t\infty}$ = 12.5 atm, $T_{t\infty}$ = 290K, and Re/m = $70x10^6$). Flow visualization was accomplished by nanosecond Shadowgraph photography. The overall flow structure was documented with the Shadowgraph and conventional mean flow probes (Pitot pressure, cone-static pressure, and thermocouple probes). The turbulent structure of the flow field was also clearly depicted in the Shadowgraphs. Image processing techniques were developed in order to determine root-mean-square index of refraction (density) fluctuation levels from the Shadowgraph plates. Multiple overheat normal and cross-wire techniques were developed and/or improved for this study. The present research concentrated on the Reynolds averaged form of the Navier-Stokes equations, where the effects of compressibility are manifested through "apparent mass" terms (i.e. $\rho' u_i'$). These terms appear in all of the Reynolds averaged Navier-Stokes equations (continuity, momentum, and energy). A new turbulence transformation, coupled with innovative experimental methods, allowed the full compressible Reynolds shear stress (the typical incompressible term, $\rho u_i' u_j'$, as well as the apparent mass terms) to be directly measured. The full compressible heat flux and apparent mass terms were also estimated from the cross-wire results. Profiles were obtained at four downstream stations which were strategically located to map different levels of development of the shear flow. The first station was very close to the injector, about one free stream boundary layer thickness downstream ($x/\delta_\infty \approx 1$), hence, it is in the initial region. The second station was located at $x/\delta_\infty \approx 28$, which was near the beginning of the fully developed zone. The third station, $x/\delta_\infty = 83$, was just prior the shear layer and floor boundary layer merging. The last station was positioned just aft of the layer merging, $x/\delta_\infty = 106$. Reynolds averaging of the compressible Navier-Stokes equations implies that the compressible turbulence affects all of the governing equations. It was found, experimentally, that the effects of compressibility on turbulence were more than significant

accounting for about 75% of the total level of the Reynolds shear stress formulation for the present study (i.e. the apparent mass term multiplied by the axial velocity was about 3-4 times the typical incompressible shear term). For the present mean adiabatic flow, the compressible turbulence accounted for 100% of the turbulent heat flux. The apparent mass in the continuity equation was, by definition, only due to compressibility. These results led to the development of a new Compressible Apparent Mass Mixing Length Extension (CAMMLE) model that accounts for compressible turbulence in all of the governing equations (i.e. the turbulence terms in the continuity, momentum, and energy were all consistently formulated). The CAMMLE formulation is a generalization of the Situ-Schetz compressible mixing length formulation, which was developed to account for the apparent mass terms in the momentum equation. A total of seven turbulence models were experimentally evaluated, the CAMMLE model, the Prandtl incompressible and the Situ-Schetz compressible mixing length models, the Prandtl and Bradshaw turbulent kinetic energy (TKE) formulations, and two compressible TKE extensions that are based upon a newly defined compressible TKE formulation. The measured turbulence data was used to assess the various models, where the measured mean flow profiles were used in the model formulations. The incompressible formulations were generally successful in representing the measured incompressible part of the Reynolds shear stress. However, this term only accounted for about 25% of the total shear stress level. All of the compressible extensions provided accurate estimates of the full compressible Reynolds shear stress. In addition, the newly developed CAMMLE model was also successful in representing the apparent mass terms in the continuity equation. The CAMMLE model was also the only formulation to accurately predict the measured compressible turbulent heat flux in the energy equation. The CAMMLE, Situ-Schetz, and Prandtl incompressible mixing length models were all incorporated in to a 3-D finite volume Navier-Stokes code (GASP 2.0). The numerical simulations indicated that the new compressible apparent mass mixing length extension performed very well. The CFD results also enlightened a misuse with all of the current compressible turbulence models. With the exception of the new apparent mass formulation, all existing turbulence models neglect the compressible turbulence effects on the continuity equation and treat the energy equation in an ad hoc effective eddy viscosity and thermal conductivity fashion. The numerical and theoretical studies indicated that this led to poor prediction of the mixing layer width for cases where the free stream Mach number was significantly higher than the injection Mach number.

ACKNOWLEDGEMENTS

First, I would like to thank my advisor and mentor, Dr. Joseph Schetz, for the encouragement, guidance and confidence he has continuously administered, not only concerning this research project but with many of the other trials a graduate student must endure. Dr. Schetz has not only guided me through my graduate studies, he has been a role model, and the close friendship that has evolved will always be treasured.

I am also grateful to Dr. Wing Ng for continued experimental advise and for serving as a committee member. I would like to thank Dr. Robert Walters for sharing his numerical expertise and for serving as a committee member. Thanks are also due to Dr. A. K. Jakubowski and Dr. B. Grossman for serving as committee members and graciously providing valuable advise. Dr. A. Wicks is also owed thanks for being a substitute committee member during the Ph.D. defence and for his signal processing advice.

I would also like to thank Dr. R. Conners for his assistance in the Virginia Tech Electrical Engineering Spatial Data Analysis Lab. I am indebted to Ken Chadwick and Eric Fuller for providing "hands on" wind tunnel assistance. Dr. Dave Slack, Dr. Bill McGrory, Mike Applebaum, Curtis Mitchell and Andrew Godfrey are owed thanks for their help with the numerical portion of this study. I would like to thank Major Chuck Wood, Doug Lewis, Tibor Kiss and Jon Fleming, as well as many other graduate students, for their help and advise.

Gary Stafford is also owed thanks for his advise in designing the needed electronic instrumentation. Without the efforts of the Aeroshop this study could not have been completed. I would like to thank Frank Shelor, Jake Frazier, and Kent Morris for their skilled abilities, and for putting up with me randomly changing the prints.

My deepest gratitude goes to my wife, Selina, for her unselfish, seemingly unending, love and support. Finally, I am eternally grateful to my parents and little brother for their love and support and for providing the opportunity to go to college.

CONTENTS

English

A	Effective Reynolds number functions
	Van Driest Law of the Wall Damping constant
a	Bradshaw TKE model constant
	Hot-wire calibration constant
	QLS -Method coefficients
B	Cross-wire function
	Shear Layer Width
b	Cross-wire calibration slope
C_d	Prandtl TKE model constant
C_f	Skin friction
c	Cross-wire temperature calibration constant
D	Cross-wire function
d	Hot-wire diameter
E	Film exposure
e	Error
	Internal energy
F	x conservative flux vector
f	Frequency
	Hot-wire effective Reynolds number sensitivity
f_o	QLS - Method new loading factor constant
G	Gray Scale
	Single sided spectra function
	y conservative flux vector
GLS	General Least Squares
g	Hot-wire total temperature sensitivity
g_o	QLS - Method new loading factor slope
H	Linearization error analysis function
	Slot injector exit height

h	Enthalpy
	Film contrast
I	Linearization error analysis function
K	Gladstone-Dale constant
k	Champagne tangential cooling factor
	Kinetic energy
	Thermal conductivity
L	Distance from center of test section to photographic plate
	Length of hot-wire sensor
L_m	Mixing Length
L_{Ho}	Stagnation enthalpy mixing length
M	Local Mach number
m_f	QLS - Method Reynolds number sensitivity slope
m_g	QLS - Method total temperature sensitivity slope
N	Number of overheat ratios
Nu	Nusselt number
n	Index of refraction
	Thermal property power law powers
P_t	Local stagnation pressure
p	local static pressure
Pr	Prandtl number
Q	conservative variable vector
QLS	Quadratic Least Squares
q	Heat flux
	Heat transfer
R	Correlation function
	Resistance
Re	Reynolds number
Reo	Reynolds number evaluated with a reference viscosity
R_o	Mean mass flux ratio
rms	Root-Mean-Square

S	Single sided spectra function
	Situ-Schetz compressibility constant
	Single overheat matrix coefficients
T	Temperature
t	time
TKE	Turbulent kinetic energy
U	Mass averaged velocity component
	Total velocity
u	Cartesian velocity component
V	Voltage
v	Voltage
v	Cartesian velocity component
v_T	Characteristic turbulence velocity
w	Cartesian velocity component
x,y,z	Cartesian coordinates

Greek

α	Compressibility model function of Mach number
	Hot-wire function of Mach number
	Shadowgraph sensitivity function
β	High frequency Pitot pressure function of Mach number
	Hot-wire function of Mach number
γ	Hot-wire temperature coefficient of resistance
	Ratio of specific heats
δ	Boundary layer thickness
ε	Dissipation
ζ	Correlation space coordinate
	High frequency Pitot pressure function of Mach number
η	Correlation space coordinate
θ	Mass flux flow angle
	Turbulence structure angle
	Velocity-Temperature correlation

κ	Law of the Wall constant
	Single overheat total temperature correction factor
Λ	Integral length scale
λ	Micro length scale
μ	Dynamic viscosity
ρ	Local density
σ	Shadowgraph density fluctuation sensitivity
	Variance (or standard deviation)
τ	Shear
	Hot-wire temperature loading factor
ϕ	Cross-wire angle

Subscripts

C	Total temperature-Effective Reynolds number correlation linearization error
c	Compressible
	Cone-static
	Convective
e	Edge
	Effective
	Equilibrium
G	Spectra error
i,j	indices (x,y,z or 1,2 ...)
Lin	Total Linearization error
n	normal component
o	Reference condition
	Stagnation condition
R	Reynolds number linearization error
s	Slot injection
T	Total temperature linearization error
	Turbulent quantity
t	tangential
	total

TI	Turbulence intensity error
V	Voltage linearization error
v	Viscous
w	Wind axes
	wire
1	Local property prior to a shock
2	Local property aft of a shock
∞	Free stream
()'()'	Correlation error

Superscripts

S	Situ-Schetz
T	Turbulent quantity
$()'$	Time averaged fluctuating component
$()''$	Mass averaged fluctuating component
$\overline{()}$	Time averaged mean component

TABLES

FIGURES

CHAPTER 1
INTRODUCTION

Compressible turbulence modeling remains the controlling factor in the accuracy of all high speed, high Reynolds number, viscous computational boundary layer and Navier-Stokes predictions. Turbulence models are necessary since current (or near future) computational facilities do not have the speed or memory required to resolve the small turbulent scales directly [1,2,3]. Even large-eddy simulation (LES) computations are impractical, since the solutions are necessarily unsteady, hence, requiring large computing times [3]. In additional LES solutions still require turbulence modeling of the small scale turbulence.

The current emphasis on hypersonic flight and the supersonic combustion ram jet engine concept (SCRAM jet), coupled with the fact that most of the prior fundamental work on turbulence has concentrated on incompressible flows, requires that compressible turbulence modeling be addressed. The most common, or practical, approach to viscous computational fluid dynamic (CFD) predictions is based on either the classical Reynolds (time) averaged, or Favre (mass-weighted) averaged Navier-Stokes equations [4,5]. Closure formulations are needed for both averaging methods.

Historically, the analysis of incompressible turbulent flows had been systematic. The first step was the theoretical determination of the terms that needed to be modeled (i.e. for incompressible flows the Reynolds shear stress). Secondly, experiments were performed where both the mean flow and turbulence terms were measured. The third, and most important step, was to use the experimental data to arrive at a closure formulation. In other words, the acquired mean flow data was used to semi-empirically develop models that accurately represented the measured Reynolds shear stress. Finally, these formulations were numerically tested. References [1] and [6] presents detailed accounts of the development of incompressible turbulence models (algebraic, one, and two equation methods).

This systematic approach has not been applied to compressible flows for two possible reasons. First, the compressible turbulence terms are more complicated, and more expensive to measure, than their incompressible counterparts. For example the compressible Reynolds shear stress formulation contains four terms including the single incompressible term. The prevalent multi-disciplinary fluid dynamic philosophy could be the second contributor to the current state of compressible turbulence closure formulations. Since, high speed computers became a powerful research tool, fluid dynamics has separated into two disciplines,

computational and experimental. This has rendered the systematic analysis of turbulence modeling ineffective. For example, Ref. [5] presents detailed derivations of second order Reynolds and Favre averaged compressible Navier-Stokes equations. However, the equations were manipulated into forms that yielded terms that are currently experimentally impossible to measure (for example, fluctuating velocity and pressure correlations). Experimentalist, on the other hand, manipulate the governing equations such that current CFD routines are not directly applicable. For example, Ref. [6] presents the compressible turbulent boundary layer equations. However, the equations were formulated in a "mixed" Reynolds/Favre averaged form.

The complicated physics and the multi-disciplinary philosophy have compounded to yield the most common approach to compressible turbulence modeling. Since the compressible turbulence terms are prohibitively difficult and expensive to measure, experimentalist mainly acquire mean flow data. With this deficiency, it is impossible to perform the important semi-empirical closure formula analysis. Therefore, hindered by the lack of data, theoreticians either develop models based on intuition, or relinquish to incorporating ad hoc extensions of existing incompressible models. The models are then numerically "tuned" or "calibrated" to match the mean flow data.

The present study addresses compressible turbulence with the historically effective multi-disciplinary philosophy. First, the Reynolds averaged equations are formulated into form that is both experimentally and numerically convenient. Secondly, new experimental techniques are developed to yield turbulence data that allows the all important semi-empirical step to be performed. And, finally, the formulations are numerically tested. This introductory chapter presents the study objective, some review material, and the research methodology.

1.1 Objective

Situ and Schetz [4], motivated by SCRAMjet applications geared for the National Aerospace Plane (NASP), embarked upon a program to rigorously extend Prandtl mixing length theory to include variable density. Through an intuitive gradient transport analysis, a compressible mixing length eddy viscosity was proposed. As was alluded to earlier, compressible turbulence data of any kind is scarce, however, compressible turbulent shear or density-velocity correlations are nonexistent. Thus, the model could not be directly tested against turbulence data. The model was successful in predicting mean flow results for supersonic free shear layers and hypersonic wall boundary layers.

The goal of the present study was to gain a better understanding of the complicated physics accompanied with high speed turbulent flow fields using the systematic approach. Experimental information is crucial in the development of turbulence models that are to incorporate the significant flow physics (i.e. experimental data allows a semi-empirical analyses). Therefore, an experiment was designed and performed, where the compressible turbulent shear stress and heat flux components were measured. A free shear (mixing layer) was chosen over a boundary layer because the effects of compressibility appear at much lower Mach numbers [7].

Reference [5] suggested that the Reynolds averaged approach performs better for free shear layers than the mass (or Favre) averaged equations, hence, the present study addressed the effects of compressibility on the Reynolds averaged form of the Navier-Stokes equations. In order to measure the turbulence quantities, new experimental techniques, or novel interpretations of existing methods, had to be developed. Finally, closure formulations were evaluated and/or developed, both experimentally and numerically.

1.2 Slot Injection

Before any data could be taken, the flow field to be studied had to be defined. First, to model the compressible turbulent shear and heat flux in the facilities at Virginia Tech (see Chapter 3), a flow field had to be designed where the effects of compressibility would be significant. In boundary layers, the effects of compressibility are generally accepted to be negligible up to free stream Mach numbers on the order of 5.0. However, the maximum Mach number in the present facilities is 4.0. Based on the following comment by Bradshaw [7]

> "The mixing layer data are probably the most suitable for testing models of compressibility effects on turbulent flow, because those effects are likely to depend more on the fluctuating Mach number than on the mean Mach number. Taking a typical velocity fluctuation as (max kinematic shear stress)$^{1/2}$, $(\tau_m/\rho)^{1/2}$, for simplicity we find that the Mach number fluctuation is $M_e[|\tau_m/\rho_e U_e^2|]^{1/2}$. In the mixing layer, the quantity under the square root is of order 0.01 at low Mach number, while in a boundary layer it is of order $(C_f/2)$, say 0.001 to 0.002 at low Mach number. Thus compressibility effects appear at much lower M_e in mixing layers than in boundary layers ..."

A free shear layer was chosen for this study (see Fig. 1.1). Relying on the "Langley Curve" [7] (see Fig. 1.2(a)), which is an experimentally determined correlation between the shear layer spreading rate (dB/dx)

and the free stream Mach number, the effects of compressibility are expected to become significant for free stream Mach numbers greater than about 2.5, or, supported by the analysis of Ref. [8], for convective Mach numbers greater than about 0.3 (Fig. 1.2(b)). As a second benefit, tangential slot injection flows can contain features of both wall bounded layers and free shear layers [4]. For example, when the flow develops in the stream wise direction, the wall boundary layer can merge with the free shear layer. Also, large density gradients can occur across the layer. All of these details made slot injection attractive as a turbulence model study.

However, the flow also has interest for practical applications. Possible areas of interests include surface film cooling, SCRAMjet fuel injection, skin friction reduction, and/or energy addition to the layer in order to prevent boundary layer separation [13]. For the present study, air was injected into air. The wind tunnel set-up can be interpreted as an idealized near full-scale model SCRAMjet combustor. It consisted of Mach 1.8 air injected into a Mach 4.0 free stream, separated by a turbulent shear layer. The choices of these Mach numbers will be explained in Chapter 3. The free stream Mach number is typical for flight Mach numbers of 8-16. Figure 1.1 presents a sketch of the flow field. The free stream and slot injection Re/m were 67×10^6 and 7×10^6, respectively.

Over the years, starting in the 1940's, free shear layers have received a great deal of attention, both experimentally and numerically. The early theoretical treatment of Prandtl and Schlichting [9] concentrated on approximate analytical solutions, based on similar solutions and a kinematic eddy viscosity that was proportional to the stream velocity difference multiplied by the shear layer width [9].

A great wealth of supersonic experimental mean flow data has also been archived. Birch and Eggers [10] compiled surveys of the literature in the first Symposium on Turbulent Shear Flow. They identified the change in spreading rate as measure of the compressibility. The "Langley Curve" was developed. It is a correlation between the shear layer spreading rate and the free stream Mach number. For these studies, the second flow velocity was zero. Papamoschou and Roshko [8], 1986, furthered these correlations to include shear layers where the secondary flow velocity was not zero, by introducing the "convective" Mach number. They found that the convective Mach number is a useful compressibility-effect parameter, see Fig. 1.2(b).

Gilreath and Schetz [11], 1967, motivated by Supersonic combustion, investigated the mixing of two tangential supersonic streams. In 1988, Schetz, Walker and Cambell [12] performed experiments where turbulence data were acquired. This study was continued by Hyde, Smith, Schetz and Walker [13] (1989),

where again mean and turbulence data were acquired. The turbulence data of Refs. [12] and [13] consisted of mass flux and total temperature turbulence intensities, as well as Favre averaged data, which was important in determining the structure of the turbulent mixing. For turbulence modeling, however, the Reynolds averaged shear terms are needed to develop closure formulations, hence, the existing turbulence data offers limited use.

1.3 Turbulence Modeling

The following brief background information is intended to review the current state of compressible turbulence modeling, and to present a sound rationale for the present study. A more complete discussion can be found in ref. [6].

The prevailing trend in compressible turbulence modeling, at any level (i.e. zero, one or two equation), is based on ad hoc extensions of existing incompressible formulations. Typically, the local density and laminar viscosity are allowed to vary in the incompressible model relations. The Baldwin-Lomax [14] algebraic formulation is the popular choice for incompressible and compressible flows. Simply allowing the density to vary or adjusting the model constants does not rigorously incorporate the flow field physics. This deficiency can be inferred from Ref. [3]. A reason that this issue has not previously been addressed may be this misuse of the Favre averaged form of the Navier-Stokes equations, where the form of the boundary layer equations are similar to the incompressible equations. As suggested in Ref. [5], the mass averaged equations performed satisfactorily in wall bounded flows. However, in high speed free shear layers, even when Morkovin's hypothesis is satisfied [15] (i.e. the fluctuation Mach number is much less than one), the models were unsuccessful [5]. It is also important to note that the Favre averaging methods failed in the presence of shock and expansion waves [5]. With this, the logical procedure would be to concentrate on the Reynolds averaged form of the equations, even though the compressible forms are more complicated than the incompressible forms. Situ and Schetz rigorously extended the Prandtl shear stress mixing length model to compressible flows by including the density-transverse velocity correlation, which is multiplied by the stream wise velocity [4]. The Situ-Schetz formulation is similar to the wall shear formulation of Li and Nagamatsu [16], which was incorporated to develop a compressible skin friction law for wall boundary layers.

The situation for one and two equation models is even more dismal. Reference [3] reported that the compressible extension of a k-ε model entailed modifying one of the model constants from an existing incompressible model. These extensions performed satisfactorily for wall bounded flows. However, they

were inadequate for free shear layer flow fields. Reference [17] attempted to use a "compressible" k-ε model in a chemically reacting flow. The relatively poor results were attributed to the turbulence model. Thus, rigorous compressible TKE and k-ε derivations are necessary if these models are to be truly compressible.

All of the previous compressible turbulence efforts, both experimental and modeling, have concentrated on the momentum equations, i.e. the Reynolds shear stress. However, compressible turbulence affects all of the conservation equations. Compressible turbulence generates apparent mass flux terms in the continuity equation. In addition to the incompressible terms, the apparent mass fluxes also appear in the momentum equations (Situ and Schetz accounted for the apparent mass term that was multiplied by the axial velocity). Similarly, the apparent mass flux terms are multiplied by the mean stagnation enthalpy in the energy equation. The present study rigorously derives the effects of the compressible turbulence on all of the conservation equations. The poor heat transfer results recorded in Ref. [18] present an example of the inadequacy of turbulence modeling (this issue will be discussed at length in Chapters 2 and 7) for compressible flows. The gradient transport modeling methods of Situ and Schetz are employed to estimate the apparent mass terms.

1.4 Methodology

The study objective and the current status of compressible turbulence models dictated many of the specific details of the present study. Since the crucial information is the compressible turbulent shear stress, heat flux and apparent mass, and the velocity-density correlations prohibit any direct measurements, a new measurement technique was conceived. It stems from a turbulence transformation, of the Reynolds averaged shear and heat flux formulations, that yields forms that could be directly measured via some unconventional methods (see Chapter 2). Multiple overheat cross-wire anemometry and digital image processing of Shadowgraph photographs were employed.

Normal-wire anemometry has been well established in supersonic flows (see Chapter 4). However, cross-wire anemometry has received very little attention. This is probably due to the complicated experimental set-up (one needs at least three wire temperature for each wire), and the intricate data reduction routines (one must simultaneously solve for three turbulence intensities and three correlations). However, for the present study, the cross-wire and normal-wire techniques are rigorously developed/improved (Chapter 4), and new anemometry instrumentation was produced to aid in the data acquisition (Chapter 3). With the new

turbulence transformation (Chapter 2), multiple overheat cross-wire anemometry, with an innovative interpretation, becomes a powerful experimental tool.

To obtain accurate turbulence result with multiple overheat hot-wire anemometry (the term hot-wire has a general connotation, i.e. it includes normal-wire and cross-wire), more than the minimum of three wire temperatures should be used. This allows a least squares analysis to be applied [13]. Two possible methods obtaining the multiple overheat data can be envisioned. The simplest method would be to manually change the wire temperature between runs. This method has two obvious flaws. First, this technique requires a large number of tunnel runs, and the fragile wires (the starting and stopping shocks routinely breaks the wires) make this method unattractive. Secondly, in order to achieve accurate results, the tunnel conditions must be very closely matched from run to run (the total conditions are repeatable to about ±2% in the present facility). The second technique would be to step the probe across the flow pausing briefly at each step. During the pause, solid state circuitry could be employed to rapidly change the wire temperature (on the order of 5/100's of second per overheat). Hence, only one tunnel run would be required to obtain a profile. In addition, the flow properties should not change significantly during the short pause at each step. The circuitry described in Chapter 3 was developed to rapidly change the wire temperature, as well as being compatible with commercial hot-wire anemometers. Experimental scatter is inevitable, even with the rapid scanning multiple overheat methods. Therefore, new data reduction methods are conceived, in Chapter 4, to minimize error amplification.

The second piece of needed information is the root-mean-square density fluctuation levels. Therefore, a technique to digitally extract this information from image processing of nanosecond Shadowgraphs is derived (again see Chapter 4).

The new data acquisition methods are found to yield accurate, consistent, and repeatable results. These data, in conjunction with the more conventional data, provide the crucial turbulence information. With the acquisition of the compressible turbulence information, the evaluation of the compressible turbulence models is the next step.

Many existing turbulence models are experimentally evaluated, both compressible and incompressible (zero and one equation). The experimental data are used to develop logical compressible extensions. Finally, the algebraic models are numerically tested.

Figure 1.1 presents a sketch of the present flow field. As can be seen in the figure, the injector was operated at an overexpanded condition. This insured that the free mixing layer and the floor boundary layer merged by the end of the test section. Shadowgraph photographs and detailed mean flow and turbulence profiles, at four stations downstream of the injector model, were acquired. In order to document the initial conditions of the shear layer, the first station was located very close to the injector ($x/\delta_\infty \approx 1$, where δ_∞ ($\approx$4.5 mm) is the free stream boundary layer thickness at the lip of the injector (see Fig. 1.1)). The second station was at $x/\delta_\infty = 28$ which is near the beginning of the fully developed region (the region where the mean profiles are smoothly varying and monotonic). The third station was located just prior to the merging of the mixing and lower wall boundary layers ($x/\delta_\infty = 83$). The fourth station was located just aft of the layer merging ($x/\delta_\infty = 106$).

CHAPTER 2
FUNDAMENTALS OF TURBULENCE

This chapter begins with a review of the fundamental aspects of compressible turbulent flow analysis, starting with the "Reynolds" averaged Navier-Stokes (RANS) equations. Secondly, the turbulent shear stress (τ^T) and specific rate of heat flux (q^T) will be transformed into a form that can be directly measured. Finally, various turbulence closure formulations will be reviewed, including a rigorously developed compressible mixing length formulation.

2.1 Governing Equations

The derivation of the RANS can be found in Refs. [1] or [6]. This section presents the results of Reynolds averaging applied to the conservative form of the governing equations.

Reynolds averaging consists of replacing the turbulent, random, 3-D, unsteady flow variables by the mean plus the fluctuating component (e.g. $u(x,y,z,t) = \overline{u}(x,y,z) + u'(x,y,z,t)$) and time averaging. The turbulent random content is assumed to be contained by the fluctuating component [6]. Therefore, the 3-D Reynolds averaged Navier-Stokes equations are given by (continuity, momentum and energy)

$$
\begin{aligned}
c:\quad & \frac{\partial \overline{\rho}}{\partial t}+\frac{\partial}{\partial x_j}(\overline{\rho}\,\overline{u_j}+\overline{\rho' u_j'}) = 0 \\
m:\quad & \frac{\partial}{\partial t}(\overline{\rho}\,\overline{u_i}+\overline{\rho' u_i'})+\frac{\partial}{\partial x_j}(\overline{\rho}\,\overline{u_i}\,\overline{u_j}) = -\frac{\partial \overline{p}}{\partial x_i}+\frac{\partial}{\partial x_j}(\tau_{ij}+\tau_{ij}^T) \\
e:\quad & \frac{\partial}{\partial t}(\overline{\rho}\,\overline{e_o}+\overline{\rho' h_o'})+\frac{\partial}{\partial x_j}(\overline{\rho}\,\overline{h_o}\,\overline{u_j}) = \frac{\partial}{\partial x_j}(\overline{u_i}\,\overline{\tau_{ij}}+\overline{u_i'\tau_{ij}'}-q_j-q_j^T)
\end{aligned}
\qquad (2.1)
$$

where the subscript "o" denotes stagnation (or total) condition (e.g. $e_o = e + \frac{1}{2}u_i u_i$), and i,j = x,y or z. The energy equation given in Ref. [6] is in nonconservative form, hence the heat flux, and rate of work, have different formulations than here (this will be discussed more in Section 2.3). The laminar shear and heat flux terms are given by

$$\tau_{ij} = \mu\left(\frac{\partial u_i}{\partial x_j} + \frac{\partial u_j}{\partial x_i}\right)$$
$$\tau_{ii} = 2\mu\frac{\partial u_i}{\partial x_i} - \frac{2}{3}\mu\nabla\cdot\overline{V} \qquad (2.2)$$
$$q_i = -k\frac{\partial T}{\partial x_i}$$

The turbulent shear and heat flux terms are given by

$$\tau_{ij}^T = -\overline{\rho}\overline{u_i'u_j'} - \overline{u_i}\overline{\rho'u_j'} - \overline{u_j}\overline{\rho'u_i'} - \overline{\rho'u_i'u_j'}$$
$$q_i^T = +\overline{\rho}\overline{h_o'u_i'} + \overline{h_o}\overline{\rho'u_i'} + \overline{u_i}\overline{\rho'h_o'} + \overline{\rho'h_o'u_i'} \qquad (2.3)$$

For incompressible flows, the last three terms in the turbulent shear and heat flux are zero.

A second type of averaging, which was first suggested by Van Driest [21], is the mass (or Favre) averaging of the conservative form of the Navier-Stokes equations (FANS). References [1] and [5] present detailed derivations of the FANS. Favre averaging may be viewed as a compressible turbulence transformation such that the resulting equations have the same appearance as the incompressible RANS. Thus, Eqn. (2.3) reduces to having only one shear and heat flux term to model. Favre averaging methods have obtained success in boundary layer flows at moderate Mach numbers, however, they have not performed well in free shear layers, or in the presence of compression and expansion waves [5].

The present study concentrates on measurements and modeling of the "complete" compressible turbulence in Reynolds averaged form. However, the four terms in Eqn. (2.3) are prohibitively expensive and difficult to measure. Therefore, a new turbulence transformation is developed, such that the compressible shear and heat transfer can be measured.

2.2 Turbulence Transformation

This section presents a method of transforming Eqn. (2.3), into an equivalent expression which can be measured via multiple overheat cross-wire anemometry and Shadowgraph processing techniques (see Chapter 4 for data reduction methods).

The transformation uses the following identity

$$\begin{aligned} \rho\phi &= \overline{\rho\phi} + (\rho\phi)' \\ &= (\overline{\rho} + \rho')(\overline{\phi} + \phi') \end{aligned} \tag{2.4}$$

The procedure to transform the turbulence equation is as follows. First, averaging Eqn. (2.4)

$$\overline{\rho\phi} = \overline{\rho}\,\overline{\phi} + \overline{\rho'\phi'}$$

This equation leads to the Favre averaged Navier-Stokes equations. The second step was to subtract the mean equation from both right-hand sides of Eqn. (2.4), yielding the following fluctuation relation

$$(\rho\phi)' = \overline{\rho}\phi' + \overline{\phi}\rho' + (\rho'\phi' - \overline{\rho'\phi'}) \tag{2.4a}$$

First, substitute $\phi = u_i$ and $\phi = u_j$ in Eqn. (2.4a), secondly form the products of $(\rho u_i)'$ with $(\rho u_j)'$, then collect the Reynolds shear terms (Eqn. 2.3) on one side of the equation, hence, it can be shown that

$$\begin{aligned} \tau_{ij}^{T} = &-\frac{\overline{(\rho u_i)'(\rho u_j)'}}{\overline{\rho}} + \overline{\rho}\,\overline{u_i}\,\overline{u_j}\overline{\left(\frac{\rho'}{\overline{\rho}}\right)^2} + \overline{\rho' u_i' u_j'} \\ &- \frac{1}{\overline{\rho}}\left[\overline{\rho'^2 u'v'} + 3\overline{\rho' u_i'}\,\overline{\rho' u_j'}\right] \end{aligned} \tag{2.5a}$$

where the terms in the brackets can be neglected as fourth order. Multiplying $(\rho u_i)'$, in Eqn. (2.4a), by h_o', then collecting the Reynolds heat flux terms (Eqn. 2.3), it can be shown

$$q_i^{T} = +\overline{(\rho u_i)' h_o'} + \overline{h_o}\,\overline{\rho' u_i'} \tag{2.5b}$$

All of the 2nd order terms in Eqn. (2.5) can be measured directly, except the second heat flux term, via multiple overheat cross-wire anemometry and image processing of the Shadowgraphs (Chapter 4). However, the density-velocity correlation term can be estimated, by separating the cross-wire variables (Section 4.2.4). With Eqn. (2.5), the compressible turbulent shear stress can be directly measured. Thus, experimental data can be used to aid in the development and assessment of compressible turbulence models. This method differs from that of Owen [22] because Owen transformed the governing equations into a "mixed" averaged form (Reynolds and Favre), thus the techniques were limited to boundary layer flows. However, the "mixed" shear stress formulation could be measured via LDV and single overheat normal-wire anemometry. Conversely, the present method preserves the Reynolds averaged form of the governing equations, and the shear and heat flux formulations are transformed as an experimental convenience (i.e. modeling efforts will concentrate on Eqn. (2.3)). The apparent mass terms can be estimated from the cross-wire results making some assumptions about the pressure fluctuation levels (see Chapter 4).

2.3 Turbulence Models

Since practically all turbulence analyses have been applied to the 2-D thin layer momentum equation, where u is the axial velocity and v is the vertical or transverse velocity, the first part of this section presents a summary of mixing length and turbulent kinetic energy models. Secondly, compressible extensions are presented/developed. The second section also presents a detailed derivation of a compressible mixing length apparent mass formulation.

2.3.1 Shear Stress Formulations

This section presents a summary of mixing length and TKE models applied to thin layer type flows. The Prandtl mixing length model (PML) [6], which was developed and tested for incompressible flows (i.e. the first shear term in Eqn. (2.3) was modeled), and both the Prandtl (PEM) [6] and the Bradshaw (BEM) incompressible turbulent kinetic energy formulations were experimentally evaluated [6]. The incompressible formulations can be summarized by

$$\begin{aligned} PML:\ \tau_{xy}^{T} &= \mu_T \frac{\partial \overline{u}}{\partial y} \\ PEM:\ \tau_{xy}^{T} &= \overline{\rho}\sqrt{TKE}\, C_d^{1/4} L_m \frac{\partial \overline{u}}{\partial y} \\ BEM:\ \tau_{xy}^{T} &= a_1 \overline{\rho}(TKE) \end{aligned} \tag{2.6}$$

where μ_T, the eddy viscosity, can be related to the mixing length as

$$\mu_T = \overline{\rho}\left|\frac{\partial \overline{u}}{\partial y}\right| L_m^2 \tag{2.7}$$

The incompressible mixing length (L_m/B) was found to be 0.07 for planar mixing layers [23], and the typical TKE constants were $C_d = 0.08$ and $a_1 = C_d^{1/2} \approx 0.3$ [6].

Situ and Schetz extended the mixing length formulation to include compressible flows by developing a gradient transport model to include the compressible term multiplied by the stream wise velocity in the x-y component of the shear stress formulation [4]. The definition of a compressible turbulent kinetic energy (TKE_c) allows logical extensions of the Prandtl and Bradshaw TKE models. The compressible TKE is defined here as

$$TKE_c = \frac{\overline{(\rho u)'^2} + \overline{(\rho v)'^2} + \overline{(\rho w)'^2}}{2\overline{\rho}^2} \tag{2.8}$$

Therefore, the compressible extension for the Prandtl energy model is to define the eddy viscosity in terms of TKE_c instead of TKE (i.e. $\mu_T = \rho(TKE_c)^{1/2}L$, where $(TKE_c)^{1/2}$ is the new characteristic turbulence velocity). Similarly, the BEM can be could also be expressed in terms of TKE_c, in Eqn. (2.6). The compressible turbulence models can be summarized as

$$\begin{aligned} SSML:\ \tau_{xy}^T &= (\mu_T^S)\frac{\partial \overline{u}}{\partial y} \\ CPEM:\ \tau_{xy}^T &= \overline{\rho}\sqrt{TKE_c}\, L\frac{\partial \overline{u}}{\partial y} \\ CBEM:\ \tau_{xy}^T &= a_2\overline{\rho}TKE_c \end{aligned} \tag{2.9}$$

where μ_T is given by Eqn. (2.7) and $\mu^S{}_T$ is given by

$$\mu_T^S = |\overline{\rho}\frac{\partial \overline{u}}{\partial y} + \frac{\overline{u}}{S}\frac{\partial \overline{\rho}}{\partial y}|L_m^2 \tag{2.10}$$

Situ and Schetz (SSML) set the compressible mixing length constant, S, equal to the turbulent Schmidt number ($\in$ [0.5,0.9]), via the diffusion analogy [4]. As was mentioned in Chapter 1, the Situ-Schetz formulation is similar to the wall shear stress formulation of Li and Nagamatsu [16]. Li and Nagamatsu defined a compressible mixing length constant α, where $\alpha = 1/S$. Unlike the Situ-Schetz constant (S), Li and Nagamatsu suggested that $\alpha = f(M)$, where as $M \to 0$, $\alpha \to 0$, and as $M \to \infty$, $\alpha \to 1$. As can be seen, there is a contradiction here. The Situ-Schetz value of $S = Sc$ violates the upper limit of on alpha. The present analysis addresses this issue by deriving the Situ-Schetz formulation from the compressible extension of the Prandtl energy model.

The SSML can be obtained by defining the characteristic velocity of the turbulence as $v_T = |\partial(\overline{\rho}\,\overline{u})/\partial y|L_m/\overline{\rho}$, which can be justified by considering the compressible Prandtl energy model extension. The TKE_c can be written as

$$TKE_c \approx \frac{(1+r_{\rho v}+r_{\rho w})}{2\overline{\rho}^2}(\rho u)'^2 \tag{2.11}$$

where, experimentally, the correlations $r_{\rho v}$ and $r_{\rho w} \in [0.4,0.6]$, thus, $(1+r_{\rho v}+r_{\rho w})^{1/2}/2 \approx 1$. Therefore, expressing $(\rho u)'$ via the typical gradient transport (i.e. $(\rho u)' = |\partial(\overline{\rho u})/\partial y| L_m$), hence the characteristic turbulence velocity can be expressed as

$$\begin{aligned} \nu_T &= \sqrt{TKE_c} \\ &= \frac{1}{\overline{\rho}} \left|\frac{\partial \overline{\rho u}}{\partial y}\right| L_m \end{aligned} \tag{2.12}$$

Therefore, the characteristic length for the Prandtl TKE_c eddy viscosity can be defined as $L = L_m$, hence $S = 1$, by definition.

2.3.2 Compressible Apparent Mass Mixing Length Extension

Since, compressibility manifests itself in all of the governing equations through the apparent masses, the Situ-Schetz compressible extension is generalized here to include all of the conservation equations, for thin layer type flow fields. Therefore, the y-component of apparent mass (see Eqn. (2.3)) is expressed as

$$\overline{\rho' v'} = -\left|\frac{\partial \overline{\rho}}{\partial y}\right| \frac{\partial \overline{u}}{\partial y} \frac{L_m^2}{S} \tag{2.13}$$

Hence, the compressible turbulence contributions to the continuity are accounted for via Eqn. (2.13). The x-y shear component is expressed as the summation of the Prandtl mixing length model and the apparent mass multiplied by the axial velocity component, i.e.

$$\tau_{xy}^T = \left(\mu_T + \overline{u}\left|\frac{\partial \overline{\rho}}{\partial y}\right| \frac{L_m^2}{S}\right) \frac{\partial \overline{u}}{\partial y} \tag{2.14}$$

The compressible turbulent heat flux is also more complicated than the incompressible expression. As previously mentioned, current heat flux formulations are based on early work that was applied to the nonconservative form of the energy equation. The first term in the y-component of the heat flux, Eqn. (2.3), recall this analysis for thin layer flows, can be expanded into static enthalpy and velocities, assuming that $(\rho v)' \approx \overline{\rho} v'$ (i.e. $\overline{v}\rho' \approx 0$) and expressing $h_o' = h' + \overline{u} u'$ (i.e. replacing h_o, h, u, and v by their mean and

fluctuating components in the definition of the stagnation enthalpy, $h_o = h + \frac{1}{2}V^2$, and subtracting the mean), thus

$$\overline{\rho h_o' v'} = \overline{\rho} \overline{h' v'} + \overline{\rho} \overline{u} \overline{u' v'} \tag{2.15}$$

In the past, the first term has been considered the turbulent heat flux, and the second term has been associated with the rate of work done by the turbulence. The typical closure formulation for Eqn. (2.15) can be written, for a calorically perfect gas, as [6]

$$q_y^T = -k_T \frac{\partial \overline{T}}{\partial y} - \overline{u} \mu_T \frac{\partial \overline{u}}{\partial y} \tag{2.15a}$$

where $k_T = \mu_T C_p / Pr_T$. Situ and Schetz [4] replaced μ_T by $\mu^S{}_T$ in Eqn. (2.15a). However, this approach will not be followed here. Instead the gradient transport models will be applied directly to the heat flux formulation in conservative variables (Eqn. 2.3).

For compressible thin layer type flows, the y-component of the heat flux is written as

$$q_y^T \approx \overline{\rho} \overline{h_o' v'} + \overline{h_o} \overline{\rho' v'} \tag{2.16}$$

where the term multiplied by the transverse mean velocity ($\overline{v}$) and the third order term are neglected (this is the identical approximation in Ref.[4]). The first term in Eqn. (2.16) can be expressed as in Eqn. (2.15) implementing the typical incompressible modeling methods, or a gradient transport formulation can be applied directly, hence

$$\overline{h_o' v'} = -\frac{L_m^2}{Pr_T} \frac{\partial \overline{h_o}}{\partial y} \left| \frac{\partial \overline{u}}{\partial y} \right| \tag{2.17}$$

where $Pr_T = L_m / L_{ho}$. This formulation can be expanded to a form which is nearly identical to the typical incompressible methods in Eqn. (2.15a).

Applying Eqns. (2.13) and (2.17), Eqn. (2.16) can be modeled as

$$q_y^T = -L_m^2 \left[\frac{\overline{\rho}}{Pr_T} \left| \frac{\partial \overline{u}}{\partial y} \right| \frac{\partial \overline{h_o}}{\partial y} + \frac{\overline{h_o}}{S} \left| \frac{\partial \overline{\rho}}{\partial y} \right| \frac{\partial \overline{u}}{\partial y} \right] \tag{2.18}$$

For calorically perfect gases, Eqn. (2.18) can be rewritten in a slightly more convenient form

$$q_y^T = -k_T \frac{\partial \overline{T_t}}{\partial y} - \frac{C_p \overline{T_t}}{S} \left| \frac{\overline{T_t}}{\overline{u}} \right| \frac{\partial \overline{u}}{\partial y} L_m^2 \tag{2.19}$$

where again $k_T = \mu_T C_p / Pr_T$ and for incompressible planar mixing flows, the turbulent Prandtl number has been found to be about 0.8 [6].

In summary, the compressible effects on turbulence for thin layer type flows are accounted for via Eqn. (2.13). This term appears in the continuity, momentum (multiplied by the mean axial velocity component), and the energy equation (multiplied by the mean stagnation enthalpy). Equations (2.13), (2.14), and (2.18) collectively represent the Compressible Apparent Mass Mixing Length Extension (CAMMLE). Unfortunately, the CAMMLE model cannot be incorporated into existing codes as easily as previous models, i.e. the effective thermal conductivity and rate of work are not complete; the apparent mass terms should also be included. Most modern compressible formulations only include compressibility through the eddy viscosity [3,4,18]. Unfortunately, this does not yield a consistent turbulent heat flux formulation (see Chapter 7). Perhaps this explains the over prediction of heat transfer reported in Ref. [18]. Chapter 6 presents the experimental evaluation of the apparent mass mixing length model, as well as the incompressible Prandtl and the Situ-Schetz compressible eddy viscosity. Chapter 7 presents the results of the numerical study.

CHAPTER 3
FACILITIES AND INSTRUMENTATION

This chapter describes the experimental/computational facilities and the instrumentation used and/or developed in the present study. First, the Virginia Tech 23 x 23 cm Supersonic/Transonic Wind Tunnel will be described. Secondly, the Supersonic Tangential Injection Model (STIM), that was designed for this experiment, will be discussed. Also, presented is a description of the experimental instrumentation and procedures necessary to perform the present study including, the Virginia Tech Electrical Engineering department's image processing equipment. Various digital signal processing techniques will be reviewed. The last section briefly describes the computational facilities.

3.1 Experimental Facility

The present experimental work was performed in the Virginia Tech Supersonic/Transonic Wind Tunnel, see Fig. 3.1 for a schematic of the Virginia Tech Supersonic Facilities. This section describes the facility and the flow visualization optical set-up.

3.1.1 Supersonic Wind Tunnel

The tunnel is a blow down facility. The tunnel is presently fitted with Mach 2.4, 3.0, and 4.0 nozzle sections, as well as a variable downstream throat transonic section. The present work was performed at the highest possible Mach number. The air pumping system consists of an Ingersoll-Rand Type 4-HHE four-stage reciprocating air compressor, which is driven by a 500 hp, 480 volt Marathon Electric Motor. The compressor can pump the storage system up to 51 atmospheres. A drying and filtering system is provided, which includes drying by cooling and absorption. The latter is accomplished by a fully automated Lectodryer, Type BY-R, which uses activated alumina as the desiccant. The air storage consists of two tanks with a total volume of 23 cubic meters (see Fig. 3.1 for a schematic).

The settling chamber contains a perforated transition cone, several damping screens, a pressure transducer, and a thermocouple. A computer-controlled feedback circuit maintains a constant stagnation ($P_{t\infty}$) during each run. For the present study $P_{t\infty}$ was maintained at an absolute pressure of 12.5 ± 0.25 atm. The Mach number is controlled by interchangeable two-dimensional nozzle blocks. Table 3.1 summarizes the flow conditions for the present experiments. The test section was equipped with large, 3.81 cm thick, optical

grade plexiglass windows so that the facility's Shadowgraph and Schlieren optical set-up could be utilized. The flow visualization system will be discussed in the next section.

3.1.2 Shadowgraph Optics

The facility is equipped to take both nanosecond Shadowgraphs and microsecond spark Schlierens. For the present experiments, only Shadowgraphs were taken, thus this apparatus will be discussed. The light source was a Xenon Corporation Novatron 289B Nanopulse lamp, which was powered by a Model-437A Nanopulser. The light from the source was reflected into the test section by collimating mirror (see Fig. 3.2). A photographic plate was placed about 0.4 m from the center of the test section.

3.2 Supersonic Tangential Injector Model

As discussed in Chapter 1, the goal of the experimental work was to obtain turbulence data in a flow field where the effects of compressibility are significant. In order to achieve this end, a supersonic free shear layer was chosen. This section presents a discussion of the design considerations, methods and the final two-dimensional supersonic tangential injection model that spanned the 23 cm test section.

3.2.1 Design Considerations

To test all facets of the flow (i.e. the initial boundary layer region, the fully developed free shear layer [7], and the wall boundary layer-free shear layer interaction) the test section length had to be maximized, as well as designing the flow such that the free shear layer merged with the wall boundary layer by the last measurement station. The fully developed free shear layer region usually starts around x/δ_∞ of near 25 (for mean flow quantities, it has been suggested that the turbulence does not become fully developed until about x/δ_∞ = 70-100), where δ_∞ is the boundary layer thickness at the lip of the injector. Preliminary tests indicated that $\delta_\infty \approx 0.5$ cm for the present conditions (see Table 3.1 for free stream flow conditions). The shear layer in Ref. [24], had a spread angle of about 2-3°. Therefore, the exit height had to be about 2.5 cm and the test section had to be about 0.5 meters long. Figure 3.3 presents a sketch of the model concept incorporated in the Mach 4 nozzle block.

Four issues were involved in the determination of the slot exit Mach number. First, Ref. [8] indicated that the compressibility effects become significant for convective Mach numbers of about 0.3. Secondly, cross-wire anemometry requires that the Mach number be greater than about 1.4 (see Chapter 4). Thirdly, the air supply for the STIM was chosen to be the ambient air in the lab. Therefore, the maximum value for $P_{ts} \approx 0.93$ atm (i.e. Blacksburg, Virginia is at an elevation of about 300 m). Finally, the length of the model

had to be considered in order to have a long enough test section to obtain measurements about $100\delta_\infty$ down stream.

Based on the above considerations, the slot exit Mach number (M_s) was chosen to be 1.8. An exit height (H_e) of 2.54 cm met both the minimum height and maximum P_{ts} (based on the mass flow). The value for P_{ts} for the "proper" isentropic design exit Mach number was about 0.58 atm, which left a nice buffer range to control the exit flow conditions. Since, the distance from the limiting characteristic and the end of the test section was only about 0.64 m, the STIM had to be compact. The total length of the model was chosen to be 0.127 m long. See Fig. 3.3.

3.2.2 Model Design

Having chosen the slot exit Mach number, height, length, and width (= span of wind tunnel) of the model, the next step was designing the STIM. A Method of Characteristics [25] supersonic nozzle design program (NOZCHAR.FOR) was written, in FORTRAN, to design the supersonic portion of the STIM. The program designs a minimum length nozzle with a finite radius expansion given by the following parabolic equation

$$y = H_t + kx^2$$

where H_t is the throat height and k is a constant used to determine the length, or curvature, of the initial expansion. Seventy characteristics were used, and k was set equal to 0.3. The characteristic solution is given in Figs. 3.3(a) and 3.3(b). The length of the supersonic portion of the nozzle was determined to be 3.56 cm. The results of NOZCHAR were validated by running the finite volume code GASP [26], to obtain an inviscid solution on a 70x70 grid of the characteristic nozzle. These results are presented in Figs. 3.3(c) and 3.3(d). Comparing Figs. 3.3(b) and 3.3(d), it can be seen that results from NOZCHAR agree with those from GASP. The exit Mach Number profile produced by GASP was 1.8 ± 0.01.

The remaining 9.12 cm of the STIM length was fully utilized by the subsonic portion of the nozzle. Since, the ambient lab air was the supply for the slot, the flow had to make a 90° turn prior to the supersonic portion of the nozzle (i.e. the air entered the slot from under the wind tunnel). However, to insure a uniform exit profile, the subsonic portion had to have the straight section, prior to the throat, as long as possible. Figure 3.5 presents a sketch of the final design.

As can be seen in Fig. 3.5, the flow enters the STIM on the bottom, through a flow regulator plate. The flow regulator plate is simply a cover plate with drilled and tapped holes. The number of holes to be left open determined the total pressure of the injected air. Once the air has entered the STIM, it was drawn up and around the corner into the subsonic straight section. Turning vanes were incorporated to prevent separation around the turn. The Mach number in the subsonic straight section was about 0.6. The subsonic section was converged down to the throat, via a "blending" cubic polynomial. The air was then expanded through the diverging Method of Characteristics nozzle. Table 3.1 presents a summary of the free stream and STIM flow field characteristics.

As can be seen in Fig. 3.5, the upper plate of the STIM was designed to be quite thin (the lip thickness was machined to about 0.9 mm), and required complicated machining. Therefore, high grade aircraft aluminum (7075-T651) was chosen as the material for this piece, due to its high strength and machinability (steel suffered a chatter problem on the milling machine). However, testing of the model indicated that the top plate bowed by about 1 mm during the run. Thus, steel struts were constructed. The struts were about 0.1 mm thick; they were sharpened, and extended, parallel to the flow direction, from the subsonic portion to the about 6 mm from the lip of the top plate in order to minimize flow field disturbances. Two struts were located about 3.3 cm inward from each of the two side walls, leaving the center 16.4 cm of the span undisturbed.

The remaining parts were machined from standard aluminum. Since the supersonic portion of the nozzle required precise machining, parts 1 and 2 were machined on a computer controlled milling machine [27]. Therefore, the coordinates for the parts had to be entered into the milling machine software. This could be accomplished in two ways. One, enter the coordinates by hand using the current milling machine software, or two, write a program to write a milling program. The latter was chosen since each piece hand about 300 coordinates. Figure 3.6 presents a plot of the two parts to be milled on the computer controlled milling machine.

3.3 Mean Flow Instrumentation

The supersonic wind tunnel operation was controlled by an IBM PC. The "master" computer, the IBM PC, was equipped with a Metrabyte DAS-16F multifunction, high-speed A/D Interface board [28]. See Fig. 3.7 for a diagram of the tunnel control set-up. As shown in Fig. 3.7, the master computer controlled the operation of all the necessary subsystems; this was accomplished with the basic program MEAN.BAS. All of the subsystems presented in Fig. 3.7 will be discussed in the following subsections.

3.3.1 Settling Chamber

The master computer first opened the tunnel on/off valve, then the hydraulically-actuated control valve was opened to a preset initial opening. The total pressure in the settling chamber ($P_{t\infty}$) was measured with a 0-300 psia National Instruments pressure transducer. The output of the transducer was recorded and used in a feedback circuit. The feedback circuit controlled the position of the tunnel hydraulic control valve in order to follow the target pressure signal, which was output by the master computer. It usually took the control process about 5 seconds to stabilize at the target pressure, after which the master computer would send the traverse commands and trigger the data acquisition computers (see Section 3.1.3). The Mach 4.0 nozzle could run for about nine additional seconds before the air supply was depleted.

The total temperature in the settling chamber ($T_{t\infty}$) was monitored with a fine wire, butt-welded Chromel-Alumel (Type K), thermocouple, made by Omega Engineering Incorporated [29]. The 0.0127 cm diameter probe had a time constant on the order of 0.1 seconds [24]. The signal was recorded with the Zenith AT used for data acquisition.

3.3.2 Traverse, LVDT and Coordinate System

The traverse consisted of a Computer Devices Corporation Model 34D-9209A stepper motor which drove a gear system that moved the probe up and down. The speed and distance of the traverse were controlled by the master computer. The computer output the traverse control commands to the stepper motor through the RS-232 port on the PC.

The position of the probe was monitored with a Trans-Tek series 240 Linear Voltage Displacement Transducer (LVDT), which provided a voltage linear with displacement. The maximum traverse speed for the mean flow data was governed by the frequency response of the cone-static probe. Reference [30] found that a traverse speed of 0.5 cm/s would yield accurate results at similar conditions. Therefore, the traverse speed was set to 0.5 cm/s for all mean flow data runs.

The coordinate system is defined in Fig. 1.1: x was defined as positive downstream; y was positive up, and z completed the right hand system. All data positions were nondimensionalized by the STIM exit height. Detailed data profiles were obtained at four locations downstream of the injector (along the center line of the tunnel). The data locations were located at x/H = 0.2, 5, 15, and 19. The rationale for the station locations is discussed in Chapter 1.

3.3.3 Data Acquisition Computer

The mean flow data were recorded by a Zenith Data Systems AT. The Zenith was equipped with a Metrabyte DAS-20 high performance, high speed, multifunction A/D interface board [28]. The data acquisition was performed with the LABTECH NOTEBOOK integrated data acquisition, control, and analysis software package [28]. The data acquisition package allowed external triggering, which was utilized by the master PC. The sampling rate was set to 80 Hz for all mean flow data. Four channels of data were converted to engineering results and recorded, the probe position, the settling chambers conditions ($P_{t\infty}$ and $T_{t\infty}$), and either P_{t2} or p_c. However, before the signals reached the Zenith, they were passed through a low pass filter, which will be described in the next section.

3.3.4 Four-Pole Low Pass Bessel Filters

A bank of six 4-pole, 330 Hz cut-off low pass, Bessel filters were constructed to filter high frequency instrumentation noise. Bessel filters were chosen due to their uniform time delay which is independent of frequency [31]. Therefore, before any mean flow signal was recorded or calibrated, it was passed through a filter.

3.3.5 Downstream Pressure Probes

A conventional Pitot pressure probe, a high frequency response Pitot probe, and a cone-static probe were utilized in the present study. The ratio of the Pitot pressure, from the conventional probe, to the cone-static pressure can be used to compute the Mach number (see Chapter 4). It is important to note here, that in order to evaluate the velocity or density, the temperature must be measured. Total temperature profiles were measured with a hot-wire (again, see Chapter 4). The high frequency response Pitot probe was used to obtain rms Pitot pressure fluctuation profiles. Chapter 4 presents techniques to extract density and Mach number rms fluctuation levels.

The conventional Pitot probe was constructed from 1.59 mm outer diameter stainless steel tubing. The wall thickness of the tubing was about 0.25 mm. The opening of the tubing was "crimped" to a 1 x 2 mm rectangle, see Fig. 3.8(a). The frequency response was to found to be to fast to accurately measure [30]. The Pitot tube was inserted to a 6.35 mm stainless steel tube for reinforcement. The Pitot pressure was measured with a Stantham 0-100 psig transducer. An Ectron amplifier provided the transducer excitation voltage as well as amplifying the transducer output to the range required by the DAS-20 in the Zenith AT. The signal was, however, filtered by the Bessel filters before being recorded by the Zenith.

The high frequency response Pitot pressure probe was constructed by mounting a high frequency response Kulite 0-50 psia transducer on the end of a 6.35 mm stainless steel tube, which was aligned such that the transducer was perpendicular to the flow direction (see Fig. 3.8(b)). A 100 kHz anti-aliasing filter was employed with the Kulite. The signal was then recorded with a LeCroy 6810 waveform recorder [32].

The cone-static probe was a miniature 10° semivertex angle axisymmetric cone, see Fig. 3.8(c). The cone tip was machined from brass, and has four 0.34 mm pressure taps located 2.92 mm from the tip at 90° intervals around the circumference. The four taps lead to a common chamber, in order to "average" out errors due to misalignment, up to ±7° [33]. The cone tip was soldiered to a 1.59 mm stainless steel tubing (wall thickness was about 0.25 mm). The cone probe was inserted into a 6.35 mm stainless steel tube for reinforcement. The frequency response of the cone-static probe has been documented as about 0.1 seconds [30]. The pressure was measured with an Alinco 0-15 psia transducer. Like with the Pitot probe, an Ectron amplifier and a Bessel filter were used before the data were recorded by the Zenith AT.

3.3.6 LeCroy Waveform Recorder

The LeCroy 6810 Waveform Recorder is four channel, 12 bit, A/D converter which can sample from 20 Hz to 5 MHz. The system consisted of a LeCroy Model 8901A GPIB controller, Lecroy Model 8013A Instrument Housing, one LeCroy Model 6810 Waveform recorder, a National Instruments GPIB-PC Interface, and was controlled with an IBM-AT using the LeCroy Catalyst software [32]. See Fig. 3.7 for the wind tunnel set-up.

3.4 Hot-Wire Instrumentation

The data acquisition procedure for the hot-wire measurements was similar to that of the mean flow, however, the multiple overheat anemometry and the required high sampling rates did complicate the issue. A rapid overheat scanning scheme was chosen for the present work. Since the scanning hardware and software is not commercially available, it had to be developed. The scanning system was designed to be compatible with commercial anemometers (for the present study Dantec 55M CTA's were used).

The master computer controlled the tunnel and traverse as described in Section 3.3. The settling chamber conditions were recorded on the Zenith AT as described in Section 3.3. However, because of the high sampling rates required for hot-wire data, a second IBM AT was included in the set-up (see Fig. 3.9). Due to the added complexities of the hot-wire set-up, a new basic program, HWSTEP.BAS, was developed to

control all the necessary tasks. Since, many of the subsystems for the hot-wire set-up overlap those for the mean flow, only the ones that differ will be discussed.

3.4.1 HWSTEP.BAS

HWSTEP.BAS controlled the tunnel operation and data acquisition in the same fashion as MEAN.BAS. However, in order to perform the multiple overheat anemometry, the hot-wire probe had to stepped across the flow, pausing briefly at each step (0.276 seconds per step). During the pause at each step, the program also controlled the overheat scanning circuit (Section 3.4.5), which was designed to scan eight resistors. The amount of time at each resistance was controlled by HWSTEP (0.0345 seconds per overheat resistance).

3.4.2 Data Acquisition Computers

The upstream conditions were recorded on the Zenith AT as discussed in section 3.3.1. However, the hot-wire signals were recorded on an IBM AT equipped with a Metrabyte DAS-16f multifunction, high speed A/D interface board. The data were acquired with the STREAMER package [28]. STREAMER allows A/D conversions to be directly stored on a hard disk at sampling rates up to 90 kHz. The amount of data is limited by the available space on the hard disk. For the present study, the sampling rate was set to 20 kHz per channel. For the cross-wire three channels were recorded, the two hot-wire signals and the probe position.

3.4.3 Normal/Cross/Dual-Wire Probes

The normal-wire probe used for the present was the Dantec Model 55P11 miniature wire probe [35] (see Fig. 3.10(a)). The sensor was a platinum-coated tungsten wire. The length of the wire was 1.25 mm; the diameter of the wire was 5 μm, and the temperature coefficient of resistance was 0.36%/C° at 20° C, and was assumed constant over the temperature range encountered in the present study. The frequency response was found to be 100 kHz at an overheat ratio of about 2.1. At the lowest overheat ratio used in the present study (about 1.3), the frequency response was about 40 kHz, at the same anemometer tuning as for the overheat ratio of 2.1.

The cross-wire probe used for the present study was the Dantec Model 55P61 miniature wire probe (see Fig. 3.10(b)). The probe had two wires; one was at a 45° incidence to the axis of the probe, and the other was parallel to the first, but at -45° incidence. The wire sensors were identical to those found on the normal-wire 55P11 probes.

The dual-wire probe used for the present study was the Dantec Model 55P71 miniature wire probe (similar to the cross-wire probe). The probe had two parallel wires separated by 1.5 mm. The wire sensors were identical to those found on the normal-wire 55P11 probes, see Fig. 3.10(c).

3.4.4 Anemometers

The Dantec 55M CTA (Constant Temperature Anemometers) system anemometers were used [34]. The constant temperature method of operation was chosen because it permitted the measurements of rapid fluctuations, up to 1.2 MHz. However, the hot-wire sensors had a much slower response (maximum 100 kHz).

The 55M CTA system consisted of three major subsystems, the 55M01 Main Unit, 55M05 Power Pack, and the 55M12 Symmetrical Bridge. The 55M01 and 55M05 contained all the circuitry required to operate the anemometer. The 55M12 symmetrical bridge had a top resistance of 50 ohms (R_s), and required an external bridge arm to select the wire temperature (overheat ratio). Therefore, the overheat resistor could be externally supplied. The overheat scanning circuit described in the next section was the source for the external bridge arm.

3.4.5 Overheat Scanning Circuit

In order to obtain accurate results from hot-wire anemometry in a supersonic flow, a minimum of three wire temperature results are needed in the same flow. The scanning method was chosen to accomplish that end, i.e. the probe would pause briefly at location in the flow, while the overheat resistance was rapidly changed. However, the resistor scanner hardware and software had to be developed. Since the 55M12 required an external bridge arm, it was desirable to have the scanned resistance be able to be plugged directly into the bridge.

In order to achieve very rapid scanning of the resistance levels, solid state circuitry was chosen. Since commercial multiplexing chips are designed for low current (<20 ma), and the current through the anemometer was about 0.25-1.0 amps, a high amp multiplexing circuit was constructed from TTL IC's (Transistor-Transistor-Logic Integrated Circuits) and solid state high carry current relays. Figure 3.11 presents a schematic of the overheat scanning circuit.

The circuit had two inputs, the scan signal (V_{scan}) and the clear signal (CLR). The scan signal consisted of a pulse train of logic level low or high (0 or 5 volts). The time between pulses determined the time at

a particular overheat ratio. The CLR signal enabled the circuit at logic low level. The circuit was reset each time a logic level high was encountered on the CLR input.

The scan signal first encountered a LM310 voltage follower, this served as a buffer between the scanning circuit and the scan control circuit. The signal was then carried through the LM310 to a Schmitt trigger (SK7414N). The CLR signal was input directly to the SK7414. The output from the SK7414N was a "clean", inverted square wave (from logic level low to logic level high) corresponding to the scan pulse train. The scan signal then controlled the synchronous divide-by-8 counter circuit constructed from the next four chips (two SN74107's, a DM7400, and a DM7404) [36]. Figure 3.11(a) presents a schematic of the buffer and counter circuitry.

The three outputs from the counter circuit were now binary coded (0-7), via logic levels. The binary value depended on the how many pulses had passed through the circuit. The three outputs controlled an addressable peripheral driver chip (the NE590), which set one of the eight outputs, depending on the value of the binary code, to logic level low (0 volts) [37]. The low end of a Dunco solid state relay was attached to each of the eight lines from the NE590. Figure 3.11(b) presents the peripheral driver and 8-relay circuitry schematic.

When a particular relay closed, the resistor in line with that relay was put in parallel with a resistor set to a value equal to the highest overheat resistance. Thus, each time one of the relays closed, a different "pull-down" resistor was placed in parallel with the highest overheat resistor. Hence, with the current circuit, up to eight different overheat ratios could have been scanned. RCD RSF3A complex-oxide resistors were employed due to the required high power and low inductance. Figure 3.11(c) presents the resistor array schematic.

As can be seen in Fig. 3.11, many capacitors were been included in the circuit. The purpose of the capacitors was to filter very high frequency power supply and chip leakage noise. This noise caused "glitches" (i.e. caused the circuit to have random spurts of high frequency scanning).

The circuit was tested over a scanning range of one pulse per minute to about 50,000 pulses per second, allowing the circuit to free run for about 2 hours. At all frequencies tested, there was no evidence of glitching. However, the CLR signal was used as a safety precaution to minimize the effects of possible

glitches. After each scan of the eight resistors, the circuit was reset. Thus, in the case of a glitch, only one probe position would be contaminated.

HWSTEP was written specifically for operation with the scanner circuitry. A D/A analog output was used for the scanner signal, and a digital output for the reset signal. A digital channel had to be used since there was only one free analog channel. Two digital channels were not used because the cross talk between the digital output caused severe glitches in the circuit.

3.5 Image Processing Instrumentation

Since image processing of Shadowgraph (or Schlieren) photographs has not been previously performed at Virginia Tech, the Virginia Tech Aerospace Department does not possess the necessary processing equipment. Therefore, the Shadowgraph plates were digitized into gray scales in the Virginia Tech Bradley Department of Electrical Engineering Spatial Data Analysis (SDA) lab. The system to create the digital images was composed of three basic components. First, the Sierra Scientific solid state black and white camera had a 512x480 resolution. The second component was a Bogen Super Repro copy stand. The copy stand provided an adjustable height camera mount and four tungsten halogen light sources that could be easily positioned. The final component was the Perceptics display [38] that could digitize the RS-170 video signal produced by the Sierra camera, as well as display the image on a video monitor. Figure 3.12 presents a sketch of the image digitizing set-up. The images were stored as ASCII characters, thus the system could resolve 256 levels of grayscale.

3.6 Signal Processing Methods

Since, the "raw" signals, from all measurement techniques, were digitized and stored on a computer disk, digital signal processing techniques had to be employed to obtain useful information. The one-dimensional analyses were based upon Ref. [39], and the two-dimensional signal processing techniques came from Ref. [40]. The one-dimensional methods will be discussed first.

Defining $f = f(t)$ and $g = g(t)$ as one-dimensional digital data sets, where t is the independent variable. The average of f, and the zero mean cross-correlation of f and g are given by

$$\overline{f} = \frac{1}{N}\sum_{k=1}^{N} f_k$$
$$R_{fg}(r) = \frac{1}{N-(r+1)}\sum_{k=1}^{N-r} f_k g_{k+r} \qquad (3.1)$$

where N is the record length [39]. If r is set to zero, and g is replaced by f, then the autocorrelation function (R_{ff}) reduces to the variance, and the standard deviation is equal to the square root of the variance (where one of the statistical degrees of freedom has been used to compute the mean).

The one-dimensional data sets were transformed to the frequency domain via DFT's (Digital Fourier Transforms). The 1-D DFT is given by

$$F(i\omega_m) = \frac{2}{N}\sum_{k=0}^{N-1} f(k\Delta t)e^{\frac{-2\pi mki}{N}} \qquad (3.2)$$

where F is a complex number, ω_m is the frequency, and m is the frequency index (m = 1,2 ... N/2-1). The DC value (ω_0) is simply the mean value given in Eqn. (3.1). The cross-spectra can be computed by

$$G_{fg} = \frac{1}{2}F^*(i\omega_m)G(i\omega_m) \qquad (3.3)$$

where G_{fg} is the single sided cross spectra, F^* denotes the complex conjugate of F. The autospectra of F can be computed by replacing G by F [39] in Eqn (3.3).

If f = f(x,y), then the two-dimensional DFT is given by

$$F(i\omega_m, i\omega_n) = \frac{2}{MN}\sum_{k=1}^{M-1}\sum_{l=1}^{N-1} f(k,l)e^{\left[-2\pi i\left(\frac{mk}{M}+\frac{nl}{N}\right)\right]} \qquad (3.4)$$

where k and l are data array indices, and m and n are frequency indices [40]. The auto and cross-correlation were computed via Eqn. (3.3).

Equation 3.4 completes the summary of basic signal processing techniques used. Most of the data reduction was performed on the results of the above methods and not the raw signals. Thus, the above review was deemed necessary for completeness.

3.7 Computational Facilities

Experimental data reduction was performed on the Zenith AT, an Epson XT, or the Virginia Tech Aerospace Engineering Department Sun 3/280 Microsystems computing facility. All line plots were created with PLOTXY [41], and printed on a Sun Microsystems Laser Writer.

The GASP [26] solutions were computed on the NASA Langley CRAY-2S (Voyager) [42]. The General Dynamics Corporation GRIDGEN2D [43] software package was employed to generate the grids. GRIDGEN2D was run on the Virginia Tech Aerospace Engineering Department Silicon Graphics Computer Services IRIS 4D work station. Color contours of the solution were computed with the PLOT3D [44], which was also run on the IRIS. The color contours were plotted on a Tektronix 4693DX color printer.

CHAPTER 4
DATA REDUCTION TECHNIQUES

This chapter presents the data reduction techniques used and/or developed for this study. First, the mean flow techniques are discussed. These consisted of conventional pressure probes and thermocouples. Secondly, the hot-wire methods are described. The *effective Reynolds number* concept is introduced to generalize the hot-wire response to include cross-wires as well as normal-wire probes. Thirdly, modern two-dimensional autospectra methods are incorporated to process Shadowgraph photographs for density fluctuation levels. Unlike previous methods applied to Schlieren photographs, the methods developed here do not assume isotropic turbulence. High frequency parallel-wire and Pitot pressure data reduction techniques are discussed in the fourth section. Turbulence structure angles were estimated via the dual parallel-wire probe spectra and correlation data. Finally, techniques to extract density and Mach number fluctuation levels from Pitot pressure fluctuation levels are derived.

4.1 Mean Flow

Two types of mean flow data were acquired. One was the upstream total conditions, $P_{t\infty}$ and $T_{t\infty}$. The second type of data consisted of downstream profiles of Pitot pressure (P_{t2}), and cone-static pressure (p_c). Typically, $p_c/P_{t2} = f(M)$, where M is the Mach number [32]. The function involves the solution of axisymmetric flow over a cone. A Least Squares curve fit for the results is given by

$$\frac{1}{M} = -0.052976 + 4.6840x - 18.6786x^2 + 50.7006x^3 - 54.1577x^4 \qquad (4.1)$$

where $x = p_c/P_{t2}$ and $M \in [1.5,4.4]$. The standard deviation for the curve fit is 0.0006 (see Fig. 4.1). In a small region of the flow (close to the trailing edge of the top plate of the slot), the cone-static probe was ineffective due to the lip and overexpansion shocks striking the cone probe. In this region the Mach number was computed assuming a constant static pressure (p) and the Rayleigh-Pitot formula [45]. The remaining local mean quantities were computed using the usual perfect gas relations for compressible flow [25].

4.2 Hot-Wire

The hot-wire reduction techniques developed in this section include both cross-wire and normal-wire probes (typically hot-wire and normal-wire are synonymous, however, here, the term hot-wire denotes the general use of hot-wire anemometry). Normal-wire anemometry has been well established for supersonic

applications. However, the cross-wire has received very little attention. The purpose of this section is to develop new as well as to improve existing cross/normal-wire algorithms. The procedure is to develop the general hot-wire response equations, independent of wire orientation, then specialize to the normal-wire and cross-wire probes.

4.2.1 General Theory

For turbulent compressible flow, the dimensionless heat transfer, the Nusselt number, of a cylinder has the following functional form [46]

$$Nu = f(L/d, M, Pr, Re_e, \tau) \tag{4.2}$$

L/d is the wire aspect ratio; M is the Mach number; Pr is the Prandtl number; Re_e is the effective cooling Reynolds number (based on wire diameter); and τ is the temperature loading factor, which can be expressed as $\tau = (T_w - T_e)/Tt$, where T_w is the wire temperature. T_e is the temperature the unheated wire would attain if placed in the flow, called the equilibrium temperature. For Reynolds numbers greater than about 20, T_e is about 97% of T_t. For flows where the Mach number normal to the wire is greater than about 1.2, or $M \sin\phi \geq 1$ [47, Fig. 26(c)]; Pr is constant; and the aspect ratio $\gg 1$, then Eqn. (4.2) reduces to [46]

$$Nu = f(Re_e, \tau) \tag{4.3}$$

Experimentally, the data has been found to collapse onto the following curve (for wires normal to the flow)

$$Nu = (a\sqrt{Re} + b)(1 - c\tau) \tag{4.4}$$

Typically, the $c\tau$ term is neglected, which means that the hot-wire must be calibrated at each wire temperature.

The Nusselt number is defined here as

$$Nu = \frac{q_w}{\pi k_t L (T_w - T_e)} \tag{4.5}$$

where $q_w = i_w^2 R_w$ (the wire heat transfer = to the wire power). From anemometer circuit analysis [35], $i_w = V_w/(R_w + R_s + R_L)$. Therefore, assuming the equilibrium temperature to be the same as the total temperature, which results in no error if done in both the calibration and the data reduction, the Nusselt number can be expressed as

$$Nu = \frac{V_w^2 R_w}{(R_w+R_s+R_L)^2} \frac{1}{\pi k_t L (T_w - T_t)} \tag{4.6}$$

The thermal conductivity and viscosity are based on T_t in calculating Nu and Re. This is reasonable, since a bow shock proceeds the wire ($T_2/T_t \approx 1$), and most of the heat transfer takes place in the stagnation region. The correct temperature would be a bulk (or average) temperature based on T_t and T_2 [47], however, this temperature would be heavily weighted to T_t, which leads to simply evaluating the thermal properties at Tt.

The viscosity was computed using the Sutherland formula, and the thermal conductivity was computed from a curve fit of tabulated data [48]. However, to evaluate the turbulence equations, the functional forms for μ_t and k_t were needed. The typical power laws were incorporated, and are given by

$$k_t = k_o \left(\frac{T_t}{T_o}\right)^{n_k} \quad and \quad \mu_t = \mu_o \left(\frac{T_t}{T_o}\right)^{n_\mu} \tag{4.7}$$

$n_\mu = 0.77$ and $n_k = 0.89$ were found to match the data satisfactory. Combining Eqns. (4.4)-(4.7), the *hot-wire response equation* can be obtained, and is given by

$$\frac{V_w^2}{C_o} = \left(\frac{T_t}{T_o}\right)^{n_k} \left[a\sqrt{Reo_e} \left(\frac{T_t}{T_o}\right)^{-n_\mu/2} + b \right] (T_w - T_t) \tag{4.8}$$

where Reo_e is the effective Reynolds number with $\mu = \mu_o$, and

$$C_o = \frac{(R_w+R_s+R_L)^2}{R_w} \pi L k_o \tag{4.9}$$

Replacing V_w, Reo_e, and T_t by the mean plus the fluctuating component, and using the Binomial Theorem [49]; retaining only the first order terms and noting

$$\frac{\overline{V_w}^2}{C_o} = \left(\frac{\overline{T_t}}{T_o}\right)^{n_k}\left[a\sqrt{\overline{Re_e}} + b\right]\left(T_w - \overline{T_t}\right) \tag{4.10}$$

then solving for $v_w'/\overline{V}_w$, the resulting *hot-wire fluctuation equation* can be derived

$$\frac{v_w'}{\overline{V_w}} = f\left(\frac{Reo_e'}{\overline{Reo_e}}\right) + g\left(\frac{T_t'}{\overline{T_t}}\right) \tag{4.11}$$

where the *hot-wire sensitivities* are given by

$$f = \frac{1}{4}\left(1 + \frac{b}{a\sqrt{\overline{Re_e}}}\right)^{-1} \quad and \quad g = \frac{-\overline{T_t}}{2(T_w - \overline{T_t})} + \frac{n_k}{2} - f n_\mu \tag{4.12}$$

In order to evaluate the f and g, the mean quantities $\sqrt{\overline{Re}}_e$ and $\overline{T}_t$ must be evaluated. Therefore, it is convenient to rewrite Eqn. (4.10) as

$$\sqrt{\overline{Re_e}} + x_i\overline{T_t}\sqrt{\overline{Re_e}} + y_i\overline{T_t} = z_i \tag{4.13}$$

where $x_i = -1/T_{wi}$, $y_i = -b_i/(a_iT_{wi})$, and $z_i = \overline{V}^2_{wi}/(C_ia_iT_{wi}) - b_i/a_i$, where C is C_o with k_o replaced by k_t. The subscript i indexes the overheat ratio. At a minimum, two wire temperatures are required to resolve the unknowns $\sqrt{\overline{Re}}_e$ and $\overline{T}_t$. If more than two overheat ratios are used, then a least squares analysis yields

$$N\sqrt{\overline{Re_e}}+\overline{T_t}\left(\sum y_i-\sum x_i z_i\right)+2\overline{T_t}\sqrt{\overline{Re_e}}\sum x_i+\overline{T_t}^2\sum x_i y_i+\overline{T_t}^2\sqrt{\overline{Re_e}}\sum x_i^2=\sum z_i \tag{4.14}$$

$$\sqrt{\overline{Re_e}}\left(\sum y_i-\sum x_i z_i\right)+\overline{T_t}\sum y_i^2+2\sqrt{\overline{Re_e}}\,\overline{T_t}\sum x_i y_i+\sqrt{\overline{Re_e}}^2\sum x_i+\sqrt{\overline{Re_e}}^2\overline{T_t}\sum x_i^2=\sum y_i z_i \tag{4.15}$$

where N is the number of overheat ratios, and the summations are over the i overheat ratios. The solution of the above two nonlinear equations was iterative, where the Secant method was incorporated to drive the residual to zero.

To obtain the turbulence results, Eqn. (4.11) was squared and averaged, yielding

$$f_i^2\overline{\left(\frac{Reo_e'}{Reo_e}\right)^2}+2f_i g_i\overline{\left(\frac{Reo_e'}{Reo_e}\frac{T_t'}{T_t}\right)}+g_i^2\overline{\left(\frac{T_t'}{T_t}\right)^2}=\overline{\left(\frac{v_w'}{V_w}\right)^2}_i \tag{4.16}$$

Three overheat ratios are required to resolve the three turbulence terms. If more than three wire temperatures are used then a least squares analysis can be applied. The *General Least Squares Method* (GLS-Method) can be derived if a least squares analysis is applied directly to Eqn. (4.16), yielding the following 3x3 system

$$\begin{bmatrix} \sum f_i^4 & 2\sum f_i^3 g_i & \sum f_i^2 g_i^2 \\ \sum f_i^3 g_i & 2\sum f_i^2 g_i^2 & \sum f_i g_i^3 \\ \sum f_i^2 g_i^2 & 2\sum f_i g_i^3 & \sum g_i^4 \end{bmatrix} \begin{pmatrix} \overline{\left(\frac{Reo_e'}{Reo_e}\right)^2} \\ \overline{\left(\frac{Reo_e'}{Reo_e}\frac{T_t'}{T_t}\right)} \\ \overline{\left(\frac{T_t'}{T_t}\right)^2} \end{pmatrix} = \begin{pmatrix} \sum f_i^2 \overline{\left(\frac{v_w'}{V_w}\right)^2}_i \\ \sum f_i g_i \overline{\left(\frac{v_w'}{V_w}\right)^2}_i \\ \sum g_i^2 \overline{\left(\frac{v_w'}{V_w}\right)^2}_i \end{pmatrix} \tag{4.17}$$

where, the summations are over the N overheat ratios. This least squares method is general in the sense that the forms of f and g are not required. However, Eqn. (4.17) has one deficiency; each term in the sensitivity matrix, as well as the right hand side vector, has a combined power of four. All of the these terms are experimental, and thus contain inherent scatter. Therefore, small experimental errors in the sensitivities are amplified by a factor of about four, which intensify the problems of the already ill-conditioned 3x3 system. This complexity lead to the development of a new method which was designed to reduce the effects of experimental scatter, thus reducing the errors in the turbulence results.

The new method assumes that the errors in the measured hot-wire voltages are purely random and all bias errors arise in the sensitivities f and g. Realizing that at a given location in the flow, the only variable in Eqn. (4.16), that is not constant, is the wire temperature. Thus, defining a new wire temperature loading factor as

$$\tau^* = \frac{(T_w - \overline{T_t})}{\overline{T_t}} \tag{4.18}$$

Experimentally, it can be verified that sensitivities can be expressed as

$$\begin{aligned} f &= f_0 + m_f \frac{1}{\tau^*} \\ g &= g_0 + m_g \frac{1}{\tau^*} \end{aligned} \tag{4.19}$$

where f_0 and m_f are determined from the wire calibration, and $g_0=n_k/2-f_0 n_\mu$ and $m_g=-(1/2+n_\mu m_f)$, see Fig. 4.2. With Eqn. (4.19), Eqn. (4.16) can be rewritten as

$$\overline{\left(\frac{V_w'}{V_w}\right)^2} = a_0 + a_1\left(\frac{1}{\tau^*}\right) + a_2\left(\frac{1}{\tau^*}\right)^2 \tag{4.20}$$

where

$$\begin{bmatrix} f_0^2 & 2f_0g_0 & g_0^2 \\ 2f_0m_f & 2(f_0m_g+g_0m_f) & 2g_0m_g \\ m_f^2 & 2m_fm_g & m_g^2 \end{bmatrix} \begin{pmatrix} \overline{\left(\frac{Reo_e'}{Reo_e}\right)^2} \\ \overline{\frac{Reo_e'}{Reo_e}\frac{T_t'}{T_t}} \\ \overline{\left(\frac{T_t'}{T_t}\right)^2} \end{pmatrix} = \begin{pmatrix} a_0 \\ a_1 \\ a_2 \end{pmatrix} \tag{4.21}$$

A minimum of three overheat ratios are required to solve Eqn. (4.21). If more than three wire temperatures are used, then the constants, a_j, can be evaluated via a *Quadratic Least Squares* analysis of Eqn. (4.20). Once the a_j's are calculated, then the turbulence results can be computed by the inversion of Eqn. (4.21).

The Quadratic Least Squares Method (QLS-Method) assumes that the errors in the hot-wire voltages are random, and that the sensitivity f can be expressed as in Eqn. (4.19). If these assumptions are valid, then the errors in the turbulence results, due to the experimental scatter in the sensitivities, should be reduced by a factor of two, since the highest combined power in the coefficient matrix, Eqn. (4.21), is two. It is important to note, that the General Least Squares Method (GLS) and the QLS-Method will yield identical results if Eqn. (4.19) is valid and the scatter in f and g is purely random. Thus, the QLS-Method only reduces the effects of bias errors in f and g.

The remaining issue is the evaluation of the wire temperature. T_w can be computed, in Kelvin, using the following linear relation [35]

$$T_w = T_{ref} + \frac{100}{\gamma_{ref} R_{ref}} (R_w - R_{ref}) + 273.15 \qquad (4.22)$$

where the reference temperature was nominally 20°C, and γ_{ref}, the temperature coefficient of resistance was 0.36%/°C, for the wire types used in the present study.

The hot-wire equations derived in this section are general, since the form of Re_e has not been prescribed. The two forms of Re_e to be discussed correspond to the normal-wire probe and the cross-wire probe. The normal-wire in supersonic flow has been well established [46,50-62]. However, the solution methods developed here (Section 4.2.2), improved the results over the existing methods used at Virginia Tech [57]. The cross-wire in supersonic flow has received little attention in the literature [47,65-67], however, it has not been used previously at Virginia Tech. In Section 4.2.3, a detailed analysis of the cross-wire response equations is presented. The derivation parallels the similar incompressible analysis of Champagne [63]. Typically, however, velocity and density fluctuation information is desired. Section 4.2.4 presents the separation of the normal-wire and cross-wire mass flux and total temperature turbulence results into velocity and density turbulence information, in "Reynolds averaged" and "Favre averaged" forms. The separation of variables stems on the assumption that the p' effects on the hot-wire can be neglected. Finally, the last section presents an approximate single overheat technique based on the relaxed Crocco Analysis of Ref. [55].

The results of the following sections were coded in the fortran program MSHeAR (Multiple overheat Supersonic Hot-wire Anemometry Reduction). MSHeAR is a 3000 line modular code that performs both the calibration and reduction for both the normal-wire and the cross-wire probes, as well as post processing into Reynolds, Favre, and turbulent kinetic energy (TKE) results. All of the reduction techniques discussed, as-well-as the separation of the turbulence terms are included in MSHeAR.

4.2.2 Normal-Wire

As mentioned in the previous section, normal-wire anemometry has received a great deal of previous attention. For a normal-wire probe, Re_e is simply the x-component of the Reynolds number in the wind axes, i.e. Re_{wx}. Hence, the ***normal-wire response equation*** was obtained by substituting Re_{wx} into Eqn. (4.8). The GLS-Method for the normal-wire is similar to that described in Ref. [57], with the exception of the method for determining the $\overline{Re}_{wx}$ and $\overline{T}_t$.

Reference [57], assumed that product of $\overline{Re}_{wx}$ and $\overline{T}_t$ could be treated as a third unknown in Eqn. (4.13), thus the least squares analysis yielded a linear 3x3 system, instead of the two nonlinear results in Eqns. (4.14) and (4.15). The present study found the linear 3x3 system to be extremely stiff, and the method yielded inconsistent results, i.e. the product term did not equal the product of the separate terms, as assumed. Thus, the solution of the two nonlinear equations is preferred here.

4.2.3 Cross-Wire

As mentioned earlier, the cross-wire (or the swept-wire), in supersonic flow, has not received a great deal of attention. Early work has been published by NACA in the 1950's concerning the response of a swept wire at supersonic speeds [47]. Reference [47] found that if $M \sin\phi \geq 1$, then the cross-wire response was independent of Mach number. Therefore, Eqn. (4.3) should be valid. However, Ref. [65] attempted, without success, to account for tangential cooling for compressible subsonic Mach numbers. In 1966, Champagne [63] introduced the effective velocity to account for tangential cooling of the wire for incompressible flows. A cooling law such as that of Champagne has not been developed for inclined wires in supersonic flows. The more recent methods of Refs. [66,67] neglected the effects of transverse velocities, or make the p' assumption. Neither assumption is made here.

The cross-wire analysis developed in this section parallels the incompressible method of Champagne, with the addition of oblique shock theory and an introduction of an effective Reynolds number (used in Eqn. (4.4)) instead of the effective velocity. The method of Champagne has the advantage that if the tangential cooling constant is set to zero, then the methods are consistent with results in Ref. [47], where the response was found to be dependent on the normal Reynolds number component.

The following equations are derived in tunnel coordinates, where the angle, ϕ, is defined as the angle between the x-axis and the normal to the wire (positive counter-clockwise), see Fig. 4.3. The relationship between the normal and tangential Reynolds number components to the x and y components are given by the following matrix transformation

$$\begin{pmatrix} Re_n \\ Re_t \end{pmatrix} = \begin{bmatrix} cos(\phi) & sin(\phi) \\ -sin(\phi) & cos(\phi) \end{bmatrix} \begin{pmatrix} Re_x \\ Re_y \end{pmatrix} \tag{4.23}$$

the functional form of Re_e to be used in Eqn. (4.4) is given by

$$Re_e^2 = Re_n^2 + k_c^2 Re_t^2 = A_1 Re_x^2 + 2A_2 Re_x Re_y + A_3 Re_y^2 \tag{4.24}$$

where A_i are given by

$$\begin{aligned} A_1 &= cos^2(\phi) + k_c^2 sin^2(\phi) \\ A_2 &= (1 - k_c^2) cos(\phi) sin(\phi) \\ A_3 &= k_c^2 cos^2(\phi) + sin^2(\phi) \end{aligned} \tag{4.25}$$

The determination of k_c stems from analysis of Champagne [63] and the oblique shock theory [25]. The normal component of mass flux is conserved across the oblique shock just upstream of the wire. However, the tangential velocity is conserved, as opposed to the mass flux. Therefore, the tangential Reynolds number behind the shock can be written as

$$Re_{t2} = \frac{\rho_2}{\rho_1} Re_{t1} \tag{4.26}$$

where "1" refers to the conditions just prior to the shock, "2" represents the conditions between the shock and the wire. After making first order approximations

$$k_c = \frac{\overline{\rho_1}}{\overline{\rho_2}} k \tag{4.27}$$

where k = f(L/d), and must be determined experimentally. Notice, that if $\rho_2 = \rho_1$ (i.e. incompressible), then this method reduces to that in Ref. [63], where k = f(L/d).

Replacing Reo_e, Reo_x, and Reo_y by their mean plus the fluctuating component; applying the Binomial Theorem [49], and using the following definitions

$$
\begin{aligned}
R_o &= \frac{\overline{Reo_y}}{\overline{Reo_x}} \\
B_1 &= \frac{A_1}{B_3} \\
B_2 &= \frac{A_2}{B_3} \\
B_3 &= A_1 + 2A_2R_o
\end{aligned}
\tag{4.28}
$$

it can be shown that

$$
\begin{aligned}
\overline{Reo_{ej}} &= \overline{Reo_x}\sqrt{B_{3j}} \\
\left(\frac{\overline{Reo_e'}}{\overline{Reo_e}}\right)_j &= B_{1j}\left(\frac{\overline{Reo_x'}}{\overline{Reo_x}}\right) + B_{2j}\left(\frac{\overline{Reo_y'}}{\overline{Reo_x}}\right)
\end{aligned}
\tag{4.29}
$$

where j indexes one of the two wires on the cross-wire probe. In the derivation of Eqn. (4.29), it was assumed that $R_o^2 \ll 1$. Substituting Eqn. (4.29) into Eqn. (4.8), then the *cross-wire response equation* can be obtained. The methods discussed in Section 4.2.1 can now be applied to each of the two wires on the cross-wire probe.

The mean results can be further resolved into x and y components of Re, using the mean equation in Eqn. (4.29) and the results from both wires. Solving Eqn. (4.29), it can be shown

$$
\begin{aligned}
\overline{Reo_x}^2 &= \frac{\overline{Reo_{e1}}^2/A_{21} - \overline{Reo_{e2}}^2/A_{22}}{A_{11}/A_{21} - A_{12}/A_{22}} \\
\overline{Reo_y} &= \frac{1}{2\overline{Reo_x}} \frac{\overline{Reo_{e1}}^2/A_{11} - \overline{Reo_{e2}}^2/A_{12}}{A_{21}/A_{11} - A_{22}/A_{12}}
\end{aligned}
\tag{4.30}
$$

The turbulence results can be decomposed into x and y components via the fluctuation equation in Eqn. (4.29). Thus,

$$\overline{\left(\frac{Reo_x'}{Reo_x}\right)^2} = \frac{1}{D_2^2}\left[\frac{1}{B_{21}^2}\overline{\left(\frac{Reo_e'}{Reo_e}\right)_1^2} - \frac{2}{B_{21}B_{22}}\overline{\left(\frac{Reo_e'}{Reo_e}\right)_1\left(\frac{Reo_e'}{Reo_e}\right)_2} + \frac{1}{B_{22}^2}\overline{\left(\frac{Reo_e'}{Reo_e}\right)_2^2}\right]$$

$$\overline{\left(\frac{Reo_y'}{Reo_x}\right)^2} = \frac{1}{D_1^2}\left[\frac{1}{B_{11}^2}\overline{\left(\frac{Reo_e'}{Reo_e}\right)_1^2} - \frac{2}{B_{11}B_{12}}\overline{\left(\frac{Reo_e'}{Reo_e}\right)_1\left(\frac{Reo_e'}{Reo_e}\right)_2} + \frac{1}{B_{12}^2}\overline{\left(\frac{Reo_e'}{Reo_e}\right)_2^2}\right]$$

$$\overline{\frac{Reo_x'}{Reo_x}\frac{Reo_y'}{Reo_x}} = \frac{1}{2B_{11}B_{21}}\left[\overline{\left(\frac{Reo_e'}{Reo_e}\right)_1^2} - B_{11}^2\overline{\left(\frac{Reo_x'}{Reo_x}\right)^2} - B_{21}^2\overline{\left(\frac{Reo_y'}{Reo_x}\right)^2}\right] \tag{4.31}$$

where $D_1 = (B_{21}/B_{11}\text{-}B_{22}/B_{12})$ and $D_2 = (B_{11}/B_{21}\text{-}B_{12}/B_{22})$. The GLS-Method or the QLS-Method can be used to solve for all the terms on the right hand side of Eqn. (4.31) except the middle correlation between wire 1 and wire 2. The correlation term can be found from the covariance between the two wires on the cross-wire probe. The relationship for the covariance can be expressed as

$$\begin{aligned}\overline{\left(\frac{v_w'}{V_w}\right)_1\left(\frac{v_w'}{V_w}\right)_2} = {} & f_1f_2\overline{\left(\frac{Reo_e'}{Reo_e}\right)_1\left(\frac{Reo_e'}{Reo_e}\right)_2} + g_1g_2\overline{\left(\frac{T_t'}{T_t}\right)} \\ & + f_1g_2\overline{\left(\frac{Reo_e'}{Reo_e}\frac{T_t'}{T_t}\right)_1} + f_2g_1\overline{\left(\frac{Reo_e'}{Reo_e}\frac{T_t'}{T_t}\right)_2}\end{aligned} \tag{4.32}$$

With Eqn. (4.32), the fluctuation x and y components of the Reynolds number can now be computed.

The remaining turbulence variables to decompose into x and y components are the Reynolds number total temperature correlations. Therefore, it can be shown

$$\frac{\overline{Reo_x' T_t'}}{\overline{Reo_x}\,\overline{T_t}} = \frac{1}{D_2}\left[\frac{1}{B_{21}}\overline{\left(\frac{Reo_e' T_t'}{\overline{Reo_e}\,\overline{T_t}}\right)_1} - \frac{1}{B_{22}}\overline{\left(\frac{Reo_e' T_t'}{\overline{Reo_e}\,\overline{T_t}}\right)_2}\right]$$

$$\frac{\overline{Reo_y' T_t'}}{\overline{Reo_x}\,\overline{T_t}} = \frac{1}{D_1}\left[\frac{1}{B_{11}}\overline{\left(\frac{Reo_e' T_t'}{\overline{Reo_e}\,\overline{T_t}}\right)_1} - \frac{1}{B_{12}}\overline{\left(\frac{Reo_e' T_t'}{\overline{Reo_e}\,\overline{T_t}}\right)_2}\right] \qquad (4.33)$$

To measure the turbulence results in the x-z plane, the cross-wire probe was rotated by 90°, v was replaced by w, and y was replaced by z.

4.2.4 Separation of Turbulence Variables

The usual procedure for the separation of the mass flux and total temperature terms into velocity and density fluctuation results, for the normal-wire probe, has been well established [54]. The underlining assumption, in the uncoupling of the turbulence data, is that, for a thermally perfect gas ($p = \rho RT$), the effects of the pressure fluctuations, on the hot-wire response equations, are small compared to the density and temperature fluctuations. Making first order assumptions, the following results, where the p' terms will be included for completeness, can be obtained

$$\frac{u'}{\overline{u}} = \frac{(\rho u)'}{\overline{\rho u}} - \frac{\rho'}{\overline{\rho}}$$

$$\frac{v'}{\overline{u}} = \frac{(\rho v)'}{\overline{\rho u}} - R_o\frac{\rho'}{\overline{\rho}} \qquad (4.34)$$

$$\frac{\rho'}{\overline{\rho}} = \frac{1}{\alpha+\beta}\left[\beta\left(\frac{(\rho u)'}{\overline{\rho u}} + R_o\frac{(\rho v)'}{\overline{\rho u}}\right) - \frac{T_t'}{\overline{T_t}} + \alpha\frac{p'}{\overline{p}}\right]$$

where, $\alpha = [1 + \tfrac{1}{2}(\gamma-1)M^2]^{-1}$ and $\beta = (\gamma-1)\alpha M^2$. With Eqn. (4.34) and assuming $p' = 0$, one can arrive at all the turbulent shear terms in the "Reynolds Averaged" Navier-Stokes equations. Therefore, performing all the possible products with the above equation, the following 6x6 matrix can be obtained

$$
\begin{bmatrix}
1 & 0 & 1 & 2 & 0 & 0 \\
0 & 1 & R_o^2 & 0 & 2R_o & 0 \\
\beta^2 & \beta^2 R_o^2 & \alpha^2 & -2\alpha\beta & -2\alpha\beta R_o & 2\beta^2 R_o \\
0 & 0 & R_o & R_o & 1 & 1 \\
\beta & 0 & -\alpha & \beta-\alpha & \beta R_o & \beta R_o \\
0 & \beta R_o & -\alpha R_o & \beta R_o & \beta R_o^2-\alpha & \beta
\end{bmatrix}
\begin{pmatrix}
\overline{\left(\frac{u'}{\overline{u}}\right)^2} \\
\overline{\left(\frac{v'}{\overline{u}}\right)^2} \\
\overline{\left(\frac{\rho'}{\overline{\rho}}\right)^2} \\
\frac{\overline{\rho' u'}}{\overline{\rho}\,\overline{u}} \\
\frac{\overline{\rho' v'}}{\overline{\rho}\,\overline{u}} \\
\frac{\overline{u' v'}}{\overline{u}\,\overline{u}}
\end{pmatrix}
=
\begin{pmatrix}
\overline{\left(\frac{(\rho u)'}{\overline{\rho u}}\right)^2} \\
\overline{\left(\frac{(\rho v)'}{\overline{\rho u}}\right)^2} \\
\overline{\left(\frac{T_t'}{\overline{T_t}}\right)^2} \\
\frac{\overline{(\rho u)'(\rho v)'}}{\overline{\rho u}\,\overline{\rho u}} \\
\frac{\overline{(\rho u)' T_t'}}{\overline{\rho u}\,\overline{T_t}} \\
\frac{\overline{(\rho v)' T_t'}}{\overline{\rho u}\,\overline{T_t}}
\end{pmatrix}
\tag{4.35}
$$

To obtain the terms in the "Favre Averaged" Navier-Stokes equations, the following relationships were be used (valid to second order)

$$
\begin{aligned}
\frac{\overline{u''}}{U} &= -\frac{\overline{\rho' u'}}{\overline{\rho u}} \\
\frac{\overline{v''}}{U} &= -\frac{\overline{\rho' v'}}{\overline{\rho u}} \\
\overline{u'' v''} &= \overline{u' v'}
\end{aligned}
\tag{4.36}
$$

where $(\,)''$ correspond to Favre (mass) averaged fluctuating components, and $U = \overline{\rho u}/\overline{\rho}$.

The assumption that $p' \approx 0$ is a controversial one. Kistler [54] demonstrated that this assumption was valid in boundary layers for $M_e \in (1.7,4.8)$. Kistler also suggested that p' is on the order of u'^2. Referring to the density fluctuation equation in Eqn. (4.34), the effects of p' can be seen. It is important to notice that the p' term is multiplied by a factor α, which is always less than 1, and is $\in (0.25,0.66)$ for the present study. Thus, even if p' is not equal to zero, the effects on separating the hot-wire variables may still be

small. It is also important to note, that if R_o is small (i.e. $\overline{v}$ is on the order of v'), then $(\rho v)'$ can be separated without the p' assumption.

4.2.5 Single Overheat Techniques

Many workers operate the normal-wire and/or the cross-wire at the largest possible overheat (without burning out the wires), to minimize the total temperature sensitivity, g in Eqn. (4.13). Figure 4.2 presents the hot-wire sensitivities as a function of the wire temperature, for the nominal conditions of T_t = 300 K and Re = 100. If the wire is operated at the minimum g, and the total temperature fluctuations are small compared to the mass flux fluctuations, then neglecting the total temperature terms should provide reasonable results. However, the error analysis in Ref. [55] indicated that this is not the case. Even for flows that are adiabatic in the mean, simply neglecting the total temperature terms can produce errors in the mass flux turbulence intensity on the order of 25%. Hence, the correction technique developed in [55] was generalized in order to be used with cross-wires as well as normal-wires.

This section presents a "Generalized" correction technique, which, unlike [55], is valid for both cross-wire and normal-wire probes. For many flow fields, one may expect only small mean total temperature gradients, which would imply that the total temperature fluctuations should be small, and mainly due to coupling with the mass flux fluctuations. If $d(T_t) = 0$ (adiabatic flow field) and Pr = 1, then the Crocco Analysis would imply [6] that, for a calorically perfect gas, $T = T(u_w)$. Therefore, it was postulated that $T' = T'(\overline{u},u_w')$, and with this, the energy equation can be used to obtain a correlation between the temperature and velocity fluctuations. First, if $T_t' = 0$, then

$$\frac{T'}{\overline{T}} = -(\gamma-1)M^2\left(\frac{u'}{\overline{u}} + R_o\frac{v'}{\overline{u}}\right) \tag{4.37}$$

which is the familiar "Strong Reynolds Analogy", presented by Morkovin [15] (note: Morkovin's results are typically presented in wind axes, but Eqn. (4.37) is equivalent). However, Pr ≠ 1, and, even for flow fields that are adiabatic in the mean, $T_t' \neq 0$. Thus, it was postulated that

$$\frac{T'}{\overline{T}} = -\kappa(\gamma-1)M^2\left(\frac{u'}{\overline{u}} + R_o\frac{v'}{\overline{u}}\right) \tag{4.38}$$

where κ is a correction factor, which was determined empirically, using data from the Refs. [54,55], as well as the present study. The value of κ was found to be 0.3-0.5. See Fig. 4.4(a) for the velocity temperature

correlation as a function of Mach number. Defining $\theta \equiv -k(\gamma-1)M^2$, (k=0.4) using Eqn. (4.34), and assuming $R_o^2\theta \ll 1$ and $R_o^2\theta^2 \ll 1-\theta$, then

$$\frac{u'}{\overline{u}} = \frac{1}{1-\theta}\left[\frac{(\rho u)'}{\overline{\rho u}} + R_o\theta\frac{(\rho v)'}{\overline{\rho u}}\right] \tag{4.39}$$

and

$$\frac{v'}{\overline{u}} = \frac{R_o\theta}{1-\theta}\frac{(\rho u)'}{\overline{\rho u}} + \frac{(\rho v)'}{\overline{\rho u}} \tag{4.40}$$

Therefore, the total temperature fluctuation equation becomes

$$\frac{T_t'}{\overline{T_t}} = \frac{\beta+\alpha\theta}{1-\theta}\left[\frac{(\rho u)'}{\overline{\rho u}} + R_o\frac{(\rho v)'}{\overline{\rho u}}\right] \tag{4.41}$$

where, again, $\alpha = [1 + \tfrac{1}{2}(\gamma-1)M^2]^{-1}$ and $\beta = (\gamma-1)\alpha M^2$. With Eqns. (4.38)-(4.41), the cross-wire response can be approximated as

$$\left[S_{ij}\right]\begin{pmatrix} \overline{\left(\frac{Reo_x'}{Reo_x}\right)^2} \\ \overline{\frac{Reo_x' Reo_y'}{Reo_x Reo_x}} \\ \overline{\left(\frac{Reo_y'}{Reo_x}\right)^2} \end{pmatrix} = \begin{pmatrix} \overline{\left(\frac{v_w'}{V_w}\right)_1^2} \\ \overline{\left(\frac{v_w'}{V_w}\right)_2^2} \\ \overline{\left(\frac{v_w'}{V_w}\right)_1\left(\frac{v_w'}{V_w}\right)_2} \end{pmatrix} \tag{4.42}$$

where the coefficients of the single overheat matrix, S, are given by

$$
\begin{aligned}
S_{11} &= f_1^2 B_{11}^2 + 2 f_1 g_1 R_{mT} R_{uT} B_{11} + g_1^2 R_{mT}^2 \\
S_{12} &= 2[f_1^2 B_{11} B_{21} + f_1 g_1 R_{mT}(R_{uT} R_o B_{11} + R_{vT} B_{21}) + g_1^2 R_{mT}^2 R_o] \\
S_{13} &= f_1^2 B_{21}^2 + 2 f_1 g_1 R_{mT} R_{vT} R_o B_{21} \\
S_{21} &= f_2^2 B_{12}^2 + 2 f_2 g_2 R_{mT} R_{uT} B_{12} + g_2^2 R_{mT}^2 \\
S_{22} &= 2[f_2^2 B_{12} B_{22} + f_2 g_2 R_{mT}(R_{uT} R_o B_{12} + R_{vT} B_{22}) + g_2^2 R_{mT}^2 R_o] \\
S_{23} &= f_2^2 B_{22}^2 + 2 f_2 g_2 R_{mT} R_{vT} R_o B_{22} \\
S_{31} &= f_1 f_2 B_{11} B_{12} + f_1 g_2 R_{mT} R_{uT} B_{11} + f_2 g_1 R_{mT} R_{uT} B_{12} + g_1 g_2 R_{mT}^2 \\
S_{32} &= f_1 f_2 (B_{11} B_{22} + B_{12} B_{21}) + f_1 g_2 R_{mT}(R_{uT} R_o B_{11} + R_{vT} B_{21}) \\
&\quad + f_2 g_1 R_{mT}(R_{uT} R_o B_{12} + R_{vT} B_{22}) + 2 g_1 g_2 R_{mT}^2 R_o \\
S_{33} &= f_1 f_2 B_{21} B_{22} + f_1 g_2 R_{mT} R_{vT} R_o B_{21} + f_2 g_1 R_{mT} R_{vT} R_o B_{22}
\end{aligned}
\tag{4.43}
$$

where

$$
\begin{aligned}
R_{mT} &= \frac{\beta + \alpha\theta}{1-\theta} \\
R_{uT} &= \frac{\overline{(\rho u)' T_t'}}{\sqrt{\overline{(\rho u)'^2}}\sqrt{\overline{T_t'^2}}} \\
R_{vT} &= \frac{\overline{(\rho v)' T_t'}}{\sqrt{\overline{(\rho v)'^2}}\sqrt{\overline{T_t'^2}}}
\end{aligned}
\tag{4.44}
$$

Most researchers agree that $R_{uT} \in [0.6, 0.9]$. However, there is no data in the literature concerning R_{vT}. However, the present study found that $R_{vT} \approx 0$ (see Chapter 5). Equation (4.43) reduces to the normal-wire results in Ref. [55], since $B_1' = 1$, $B_2' = 0$, and $R_o = 0$ (by definition). Also, setting R_{mT} equal to zero reduces Eqn. (4.43) to the typical method of neglecting the total temperature terms, or setting $R_{mT} = 1$ corresponds to the "Strong Reynolds Analogy" in Ref. [15].

4.3 Shadowgraph Image Processing

Researchers began extracting turbulence information from still Shadowgraphs and Schlieren photographs in the 1950's. However, with the exception of Clay, 1965 [69], in which Schlieren photographs were studied, the analysis of this type has not been extensively utilized. The present work brings the analysis of Shadowgraphs into the present, by using state-of-the art computer image processing equipment and modern two-dimensional spectra techniques to obtain density fluctuation levels.

4.3.1 Film Description

The film used for this study was Polariod Type 57 [70]. The characteristic curve for the film is given in Fig. 4.5(a). The image processing software (RIPS) stores the image in gray scales. Therefore, the characteristic curve density is transformed (via a linear transformation) into gray scales, see Fig. 4.5(b). Presented in Fig. 4.6(a) is a histogram of gray scale for a typical Shadowgraph used in the present study. As can be seen in Fig. 4.6(a), most of the Shadowgraph has a gray scale $\in$ [30,230]. Therefore, the simple curve fit in Fig. 4.6(b) can be used to convert the gray scale (G) to relative exposure (E/E_o).

4.3.2 Analysis

The contrast is defined as $h = (E-E_o)/E$, where E_o is an arbitrary reference. The contrast of a Shadowgraph is related to the second derivative of the index of refraction (n) by the following equation [71]

$$h = L\int_0^W \left(\frac{\partial^2 n}{\partial x^2} + \frac{\partial^2 n}{\partial y^2}\right) dz \tag{4.45}$$

where L is the distance from the centerline of the test section to the film plate and W is the width of the test section (see Fig. 3.2). It is important to note, that L should be made as small as possible in order to insure one-to-one correspondence between the Shadowgraph and the actual index of refraction field [71].

Replacing h, E and n by their mean and fluctuating component, it can be shown that

$$h' = L\int_0^W \left(\frac{\partial^2 n'}{\partial x^2} + \frac{\partial^2 n'}{\partial y^2}\right) dz \tag{4.46}$$

To analyze the Shadowgraph, a relation between the 2-D film contrast and the 3-D index of refraction field must be established. Taking the autocorrelation of both sides of Eqn. (4.46), one can show

$$R_{hh} = \alpha^* \int_{-\infty}^{\infty}\int_{-\infty}^{\infty} \left(f_x^4 + f_y^4\right) e^{2\pi i(f_y\zeta + f_y\eta)} \int_{-\infty}^{\infty} S_{nn} \frac{\sin^2(\pi W f_z)}{(\pi W f_z)^2} df_z df_x df_y \tag{4.47}$$

where $R_{hh} = R_{hh}(\zeta,\eta)$, $\alpha^* = (LW)^2(2\pi)^4$, $S_{nn} = S_{nn}(f_x,f_y,f_z)$, which is the 3-D, double sided, autospectra function of the index of refraction fluctuations, and f_i are frequencies in m^{-1}. The derivation of Eqn. (4.47) is similar to that of Ref. [69], except that in [69] the analysis is for Schlierens, where here it is for Shadowgraphs.

In order to solve Eqn. (4.47), it must be further simplified. Since, Shadowgraph photography inherently averages along the axis of the light path, the 3-D autospectra can be replaced by a 2-D, x-y planar, spectrum that is averaged along z. Therefore, denoting the 2-D, z-averaged, autospectrum, by $S_{nn}(f_x,f_y)$ and noting

$$\int_{-\infty}^{\infty} \frac{\sin^2(\pi W f_z)}{(\pi W f_z)^2} df_z \approx 4.37 \tag{4.48}$$

Eqn. (4.47) can be reduced to

$$R_{hh}(\zeta,\eta) = \alpha^{**} \int_{-\infty}^{\infty}\int_{-\infty}^{\infty} \left(f_x^4 + f_y^4\right) e^{2\pi i (f_y\zeta + f_y\eta)} S_{nn}(f_x,f_y)\, df_x df_y \tag{4.49}$$

where $\alpha^{**} = 4.37\alpha^{*}$.

For homogeneous gases, $\rho = Kn$, where K is the Gladstone-Dale constant [72] ($=2.38\times10^{-4}$ m^3/kg for air). Therefore, defining $\alpha = 4.37(KLW)^2(2\pi)^4$ ($=3.86\times10^{-4}(LW)^2$ m^{10}/kg^2), then from Eqn. (4.49), one can see that the film contrast autospectra and the density autospectra are related by the following

$$S_{\rho\rho}(f_x,f_y) = \frac{1}{\alpha} \frac{S_{hh}(f_x,f_y)}{f_x^4 + f_y^4} \tag{4.50}$$

Hence, the density autocorrelation function can be written as

$$R_{\rho\rho}(\zeta,\eta) \approx 2\int_o^{\infty}\int_o^{\infty} S_{\rho\rho}(f_x,f_y)\cos(2\pi(f_x\zeta + f_y\eta))\, df_x df_y \tag{4.51}$$

where the approximation is due to the averaging over z. Equations (4.50) and (4.51) can be combined to estimate the variance of the density fluctuations as

$$\sigma_\rho^2 = \frac{1}{\alpha}\int_0^{\infty}\int_0^{\infty} \frac{G_{hh}(f_x,f_y)}{f_x^4 + f_y^4} df_x df_y \tag{4.52}$$

where G_{hh} is the single sided autospectra function ($=2S_{hh}$), and is valid for $f_x,f_y \geq 0$.

Other information that can be obtained from the 2-D image processing are the microscale (λ) and integral scale (Λ) [1], in two dimensions. This differs from typical turbulence scale measurements currently in the literature. The length scales were obtained directly from the autocorrelation of h'.

A relatively simple and straight forward method for estimating the density fluctuation levels from a Shadowgraph has been developed. Due to the image processing method used, Ref. [69] had to make the assumption that the density fluctuation field is isotropic, in order to estimate σ_ρ from the Schlieren photograph, however, in this study, more modern image processing techniques were employed, and, the isotropic assumption was not needed. Secondly, microscale and integral scale lengths can be directly measured from the Shadowgraph.

The Shadowgraph analysis procedure, described above, has two possible sources of difficulty. First, the denominator in Eqn. (4.51) has the frequency raised to the fourth power, which may cause errors for low frequencies. However, the data is zero mean, therefore, the lower frequency results are not expected to cause any significant problems. Secondly, neglecting the z-dependence in Eqn. (4.47) is an assumption. Even if $S_{\rho\rho}$ is a function of z, $\sin^2 x/x^2$ rapidly collapses to zero, therefore, "pulling" $S_{\rho\rho}$ out of the integral should not cause significant errors (this is consistent with Ref. [69]).

4.4 Parallel-Wire and High Frequency Pitot

This section presents a method to estimate the flow structure angle [73,74] and turbulence length scales [1], based on the correlations obtained from a parallel wire probe. Secondly, a novel technique to extract density and Mach number fluctuation levels from Pitot pressure fluctuations (measured with the Kulite Pitot probe) is described.

4.4.1 Parallel-Wire

When a parallel-wire is subjected to a flow where there is a significant amount of organized structure, the angle of the this structure can be estimated from a cross correlation between the two wires. The structure angle associated with an average large-scale motion is given by [73]

$$\theta = tan^{-1}\left(\frac{w}{\overline{u}\tau}\right) \tag{4.53}$$

where w is the wire separation distance, $\overline{u}$ is the mean stream wise velocity, and τ is the time delay between the signals (which corresponds to the time at the peak on the cross correlation).

The integral scale (Λ) and the microscale (λ) of the turbulence [1] can be estimated from the normalized autocorrelation function (normalized by the variance), where the time axis, in correlation space, has been transformed into length by multiplying by the local mean velocity. The integral scale is found by

integrating the autocorrelation function from $\overline{u}\tau = 0$ to ∞. The microscale is the value of $\overline{u}\tau$ found by setting the "osculating" parabola, which is determined by fitting a parabola through the first few points of the autocorrelation, equal to zero [1].

4.4.2 High Frequency Pitot

The Pitot pressure fluctuation levels can be related to the density and Mach number fluctuation levels via the Rayleigh-Pitot formula, the thermally perfect gas relation, and the definition of the total temperature. The fluctuation equations can be found by replacing the properties by their mean plus the fluctuating component, and applying the binomial theorem, thus

$$\begin{aligned}
\frac{P_{t2}'}{\overline{P_{t2}}} &= \frac{p_1'}{\overline{p_1}} + \zeta(\overline{M})\frac{M'}{\overline{M}} \\
\frac{p'}{\overline{p}} &= \frac{\rho'}{\overline{\rho}} + \frac{T'}{\overline{T}} \\
\frac{T_t'}{\overline{T_t}} &= \frac{T'}{\overline{T}} + \beta(\overline{M})\frac{M'}{\overline{M}}
\end{aligned} \tag{4.54}$$

where $\zeta = 2\gamma/(\gamma\text{-}1)\{1\text{-}2M^2/[2\gamma M^2\text{-}(\gamma\text{-}1)]\}$, and $\beta = [(\gamma\text{-}1)M^2]/[1+\frac{1}{2}(\gamma\text{-}1)M^2]$. In order to estimate the Mach number fluctuation levels, the static pressure fluctuations were neglected (see Section 4.2.4). In addition, if the total temperature fluctuation levels are neglected, then the three equations in Eqn. (4.54) can be arranged to yield density fluctuation levels. With this, the high frequency Pitot pressure probe can yield important turbulence data.

CHAPTER FIVE
EXPERIMENTAL RESULTS

This chapter presents the experimental results of the present study. The free stream Mach number was measured as 3.8, where the total pressure ($P_{t\infty}$) and temperature ($T_{t\infty}$) were 12.5 atm and 290 K, respectively. The tangential injection model was operated at a slightly overexpanded condition in order to insure that the lower floor boundary layer had merged with the free mixing layer within the test section. The slot Mach number was measured as 1.8, where the stagnation pressure (P_{ts}) and temperature (T_{ts}) were 0.52 atm and 297 K, respectively. Table 3.1 presents a detailed summary of the present test conditions.

First, the composite Shadowgraph is qualitatively described. This is followed by the conventional mean probe data. Thirdly, the normal/cross-wire mean and turbulence results are given. Fourthly, the Shadowgraph image processing results are presented. Next, the parallel-wire and high frequency Pitot pressure data are given. As mentioned in Chapter 1, the free shear layer spreading rate has historically been considered a measure of compressibility. Hence, the last section gives various measures of the spreading rate. The profile results are sectioned by measurement type, however, they are also sub-divided by measurement station. The errors associated with the various measurement techniques can be found in the Appendix.

5.1 Qualitative Shadowgraph Analysis

A composite twenty nanosecond Shadowgraph is presented in Fig. 5.1, where the flow is from right to left, and the free stream and slot flow are clearly depicted. The fastest fluid particles only traveled about 5 μm in twenty nanoseconds, therefore, the flow was essentially "frozen" in the photograph. As can be seen in Fig. 5.1, the four profile measurement stations are marked on the composite shadowgraph.

The Shadowgraph allows qualitative and some limited quantitative results to be directly inferred. The slot flow was along the bottom wall, as indicated. The free stream boundary layer thickness (δ_∞), near the lip of the injector, was measured as 4.5 mm. The lip and slot over expansion shocks are clearly depicted on the Shadowgraph. Near the lip, the expansion fan can be seen, therefore, the free stream Mach angle can be estimated. Based on this, the free stream Mach number was found to be about 3.8±0.1. As can be seen, the shock-expansion pattern is similar to that of Fig. 1.1.

The free shear layer (mixing layer) can also be easily seen. The spreading rate was estimated as about 0.03. The eddy structures are clearly visible in the shear layer. The eddy sizes were measured to be about 0.1B to 0.3B, where B is the layer width. The eddy size appears to increase in the vertical direction, i.e. the eddies near the upper edge of the shear layer seem to be larger than those on the lower side. Intermittency [6] also appears to be more significant on the upper side of the free shear layer. The intermittent inviscid regions are about 20% of the layer width. Where, on the lower side the eddies seem to blend smoothly to the slot potential core region.

The lower floor boundary layer is difficult to see on the Shadowgraph. However, close examination of the last station indicates that the free shear layer has merged with the floor boundary layer.

5.2 Conventional Probes

The conventional probe data consisted of Pitot and cone-static pressure profiles, from which Mach number and static pressure profiles could be computed, at the four measurement stations marked on Fig. 5.1. The mean flow profiles add quantitative insight into the spatial progression of the flow field. The slot "potential" core decreases and the shear layer width increases as the flow progresses downstream.

Station 1 (x/H = 0.2) results are presented in Figs. 5.2 and 5.3. Figure 5.2(a) gives the Pitot pressure profile, normalized by the free stream total pressure measured at the same instant in time. This normalization eliminates linear errors due stagnation pressure control deviations. As mentioned earlier, all of the profiles are nondimensionalized by the slot exit height (H). The free stream and the slot "inviscid" core are clearly visible in the profile. The lip and over expansion shocks are noticeable in the profile near y/H = 1. Figure 5.2(b) presents the cone-static pressure profile. The "slot free stream" is clearly evident. However, the shocks near the lip distort the results in that region. The cone-static pressure approaches the free stream value at y/H ≈ 1.3. However, above this, as indicated by the increasing pressure, the probe has traversed into the nozzle design characteristic mesh.

The Mach number was computed from the ratio, p_c/P_{t2} (see Chapter 4). Figure 5.3(a) presents the Mach number profile. The slot Mach number was measured to be about 1.8. The free stream Mach number was found to be about 3.8. In the region near y/H = 1, the small probes were determined to be inadequate, therefore, the static pressure was set to the slot inviscid core value, and the Mach number was estimated with the Rayleigh-Pitot formula [25]. The Mach number profile also indicates that above y/H ≈ 1.3, the probes have traversed the last characteristic wave. The Rayleigh-Pitot formula was used to compute the

static pressure profile, which is presented in Fig. 5.3(b). As can be seen the slot was operated at a slightly overexpanded condition ($p_s/p_\infty \approx 1.3$). The mixing layer width (B/H) was estimated as about 0.25.

By station 2 (the data shown in Figs. 5.4 and 5.5), the slot upper wall and the free stream boundary layers appear to have dissipated into smoothly varying shear profile, indicating that the mixing layer has fully developed. The lip and reflected over expansion waves cause the profiles to appear jagged just above the shear layer (see Fig. 5.1). The floor boundary layer is also evident, and the boundary layer thickness is about 5 mm. The Mach number and static pressure profiles are presented in Fig. 5.6. The slot inviscid core Mach number has been "shocked" down to about 1.6. The slot static pressure has been shocked up to the free stream value. B/H was estimated as about 0.38.

By x/H = 15, the shear layer has grown significantly (B/H = 0.66), as can be seen in Figs. 5.6 and 5.7. The wall boundary layer has also grown to about 1 cm. The Pitot and cone-static profiles at this station have an interesting, yet not fully understood, phenomena just above the mixing layer. The profile increases, with increasing y, to a value at the edge of the layer, however, then the profiles decrease to a lower value, as y is increased.

The profiles at the last station (Figs. 5.8 and 5.9) are drastically different than the previous stations. The slot inviscid core is no longer evident from the profiles, nor is a separate floor boundary layer. Since the profiles start at a value of y that is less than the wall boundary layer thickness at the previous station (x/H = 15), it becomes obvious that the floor boundary layer and the mixing layer have merged somewhere between x/H = 15 and x/H = 19. Hence, the mixing and boundary layer widths cannot be determined.

5.3 Normal/Cross-Wire

The conventional probe results in the free stream and slot inviscid region were used to calibrate the normal-wire probes. Appendix A.1 presents the data reduction steps and a reduction algorithm comparison for a sample cross-wire data set. Based on those results, the GLS-Method was chosen. The normal-wire mean and fluctuating results will be present first, for the four measurement stations. This will be followed by the cross-wire results. It is important to note that most of the hot-wire profiles were obtained over multiple runs. This was necessary because of the short, nine second, tunnel run times.

5.3.1 Normal-Wire

Figures 5.10 through 5.17 present the normal-wire results for the four measurement stations. Figure 5.10(a) shows the mean mass flux profiles, nondimensionalized by the local free stream value, at x/H = 0.2. It should be noted that the normal-wire probe is not sensitive to flow angle, therefore, the results are in "wind coordinates". Figure 5.10(b) presents the mean total temperature profile. As can be seen, the slot total temperature was about 3% higher than the free stream total temperature. The peak near y/H = 1 is most likely due to the free stream and upper slot wall boundary layer total temperature profiles for a Prandtl number less than one, as described in Ref. [6].

Figure 5.11(a) gives the mass flux and total temperature turbulence intensity profiles. The low values in the slot inviscid core and the free stream indicate low incoming turbulence levels. The rms mass flux values peak at about 10% in the mixing layer. The total temperature turbulence intensity peaks at about 2.5%. This low value was expected since the flow is nominally adiabatic. Figure 5.11(b) presents the velocity and density turbulence intensity results. Recall from Chapter 4, that in order to decompose the mass flux and total temperature data into velocity and density, the static pressure fluctuations were neglected. Therefore, the results in 5.11(b) are approximate. However, the trends are expected to be valid. It is interesting to note that the density turbulence intensities are about twice the velocity values.

The mean normal-wire results at x/H = 5 are shown in Fig. 5.12. Similar trends mentioned about the conventional probe data can be seen here. For example, the smoothly varying total temperature and mass flux profiles indicate that the mixing layer has fully developed. Since shocks are adiabatic (for calorically perfect gases), the effects of the lip and reflected over expansion shocks can be seen, just above the mixing zone, only in the mass flux profiles. If the shocks were normal, then the effects would also be undetectable in the mass flux profiles. Figure 5.13 presents the turbulence intensity profiles in both conservative and primitive variables. The trends are similar to those of station 1, however, the mixing layer is significantly wider.

During the experiments, station 4 (x/H = 15) was the measurement techniques test location, which included probe independence validations. Hence, these profiles have more data points which were acquired with various similar probes. For example, the normal-wire results presented in Figs. 5.14 and 5.15 were acquired with four different normal-wire probes, over two separate test days. The trends in the mean normal-wire data are, again, identical to those of the conventional mean data. Some interesting trends can be seen in the turbulence intensity profiles, Fig. 5.15. This data set is unique in the sense that it contains features of

both the wall boundary layer and the free shear layer. The mass flux turbulence intensity rise to about 17% in the mixing layer, where, the total temperature fluctuation levels have remained nearly constant at about 2.5%. The floor boundary layer turbulence intensity profiles are similar to the boundary layer results presented in Ref. [54], and the mixing layer values are consistent with those of ref. [13].

The trend "reversal" demonstrated in figure 5.15(b) is particularly interesting. Notice that in the floor boundary layer region the density fluctuation levels are significantly smaller than the rms velocity values. However, immediately as the probe was traversed into the free shear layer the trend reversed, i.e. the density turbulence intensity levels increased, while the velocity levels decreased. There are two compounding factors that contribute to this phenomena. First, the effects of compressibility are excepted to be more important in free shear layers. Secondly, the local Mach number increases from one layer to the other. The effects of the increasing Mach number can be inferred by examining the free shear layer region of Fig. 5.15(b). Notice, that with increasing y (which implies increasing Mach number), the rms velocity levels decrease, where the density turbulence intensities increase.

Figure 5.16 presents the mean normal-wire results at the last station (x/H = 19). Again, the mean trends are identical to those of the conventional mean data. The turbulence intensity profiles are presented in Fig. 5.17. The rms mass flux level between the boundary layer and free layer only decreases to about 5% which supports the result that the layers have merged. The trend reversal, mentioned above, is also evident in Fig. 5.17(b).

5.3.2 Cross-Wire

Figures 5.18-5.53 present all of the cross-wire results for stations 1-4. It should be noted that, for station 1, the cross-wire probe volume is approximately 16% of the mixing layer width at this station, and the lip shocks are likely to contaminate the results. However, they will be presented for completeness. Also, at station 1, as well as the remaining stations, 3-D cross-wire data were acquired. A second benefit of the x-z data is the redundancy in the axial results (i.e. the cross-wire is sensitive to (ρu) in both the x-y and x-z orientations).

The mass flux flow angle ($\theta = \tan^{-1}R_o$, see Chapter 4) profile, at station 1, is given in Fig. 5.18(a). The large flow angles in Fig. 5.18(a), both x-y and x-z planes, are attributed to the lip shocks. Figure 5.18(b) shows the mean mass flux profiles, measured not only with the cross-wire, but the normal-wire and conventional probe results as well. The cross-wire temperature and pressure data were used in conjunction

with the Mach number data to compute the mean conventional probe mass flux profiles. As can be seen, the agreement between the various measurement techniques is excellent, except in the vicinity of the lip (near x/H=0.2 and y/H = 1).

Figure 5.19 gives the turbulence intensity profiles at x/H=0.2. The axial and total temperature results are similar to those measured with the normal-wire probe. However, the cross-wire also yields transverse ((ρv) or y) and spanwise ((ρw) or z) fluctuation levels. The transverse and spanwise mass flux turbulence intensities are about equal at about 75% of the axial values. The separated results are presented in Fig. 5.19(b). The axial and density results are nearly identical to those measured with the normal-wire. However, the v' and w' turbulence levels do not follow the same trend as the rms axial (u) values. In other words, the transverse and spanwise velocity turbulence intensities, which are about equal, are similar in magnitude to the density values, hence they are about twice the axial value. This contradicts the incompressible boundary layer results [6], where the axial turbulence intensity is the largest, followed by the spanwise, and the transverse levels are the lowest.

Figure 20 presents the cross-wire mass flux cross correlation, and the total compressible shear in transformed (or cross-wire variables) for the x-y plane (x/H=0.2). As can be seen, for thin layer type flows, the leading term in Eqn. (2.5) dominates the level of the shear. Figure 21 gives the same data for the x-z plane. Figure 22 shows the mass flux total temperature correlations and compressible heat flux data. The axial mass flux total temperature correlation is clearly the largest. The transverse and spanwise mass flux-total temperature correlation values are nearly zero, except near the lip. The axial heat flux is also the largest, however, for thin layer type flows, the important term is the transverse, or y component.

As was discussed in Chapter 4, the cross-wire results can be separated into primitive variables. Figure 5.23 presents the velocity-velocity and density-velocity correlations (x/H=0.2). The trends are difficult to distinguish at this station, however, as will be seen, they become much clearer at stations further down stream. The compressible (Eqn. (2.8)) and the typical turbulent kinetic energy profiles are given in Fig. 5.24, where the compressible TKE is about 50% larger than the incompressible value.

Figure 5.25 presents estimates of the Reynolds shear stress terms (Eqn. (2.3)), in both the x-y and x-z planes. The circles represent the incompressible term, the squares indicate the compressible term accounted for by Situ-Schetz (Eqn. (2.9) or Eqn. (2.14)), the triangles demonstrate the other second order term, and the hour glasses are the summation or total Reynolds shear. The third order term was neglected here. As

can be seen in Fig. 5.25, the apparent mass term (compressible term marked by the squares) is about 3 times the incompressible terms (circles). Therefore, the compressibility accounts for about 75% of the total level of the Reynolds shear. For completeness, the Favre (or mass averaged) data are presented in Figure 5.26. The Favre shear levels have the same magnitude as the incompressible Reynolds shear term. This is the expected results, since the apparent mass terms are inherently included in the mass averaged mean velocities.

Figures 5.27-5.35 present the cross-wire results for station 2. The trends discussed for station 1 carry over to station 2. The trends are more detectable at this station, than at station 1. Recall, that some of the trends were not distinguishable at station 1, hence, only those trends will be discussed hear. For example, the transverse heat flux results were difficult to interpret at station 1 (Fig. 5.22), however, the trends are much clearer here (see Fig.5.31). As for station 1, the axial heat flux component is the largest (and positive), however, the transverse heat flux is not zero, it has a finite negative value. The magnitude of transverse turbulent heat flux is about one-half the axial result. The separated correlation data is also easier to interpret at station 2 (Fig. 32). The x-y and x-z plane velocity-velocity correlations are similar in magnitude and sign. The transverse and spanwise velocity-density correlations are also similar.

Referring back to Fig. 5.28, an additional set of data appears, that was not included at station 1. The Shadowgraph image processing results (to be discussed in detail in the next section) are included for comparison. The density turbulence intensities measured off the Shadowgraph are in good agreement with those estimated from the cross-wire (recall the p' assumption) in the shear layer. However, Shadowgraph and cross-wire results diverge in both free streams. This is due to limited resolution from the Shadowgraph and the shocks appearing as turbulence to image processing routines.

Figures 5.36-5.44 present the cross-wire results at station 3. Figure 5.36(b) gives the mean mass flux profiles measure with the cross-wire, normal-wire, and the conventional probes. The agreement between the various measurements is considered excellent. Notice, that the "over shoot" in the axial mass flux profile (near y/H = 1.2) was measured by each method. The turbulence trends associated with Figs. 5.37-5.44 are identical with those discussed for stations 1 and 2. However, the trends are more prevalent at this station due both to the larger magnitudes of the turbulence and the increased resolution (recall that this station was the measurement technique evaluation station, hence the profiles contain more data points acquired over multiple runs). The relative magnitude of the various Reynolds averaged shear terms (Eqn. (2.3)) are particularly noticeable in Fig. 5.43(a).

Figs. 5.45-5.53 show the data for the last station. These data also reinforces the conclusion that the wall boundary layer and free mixing layer have merged. The slot potential core is not evident in mean axial mass flux profile given in Fig. 5.45. Also, the turbulence intensity levels (plotted in Fig. 5.46) on the lower side of the mixing layer do not decrease to the free stream value, hence, indicating that the layers have merged.

The image processing results Figs. 5.37 (x/H = 15) and 5.46 (x/H = 19) are in much better agreement with the cross-wire results than the x/H = 5 data (Fig. 5.28). This yields confidence not only in the Shadowgraph results, but also in the validity of the p' assumption at these conditions.

5.4 Shadowgraph Image Processing

Appendix A.2 shows the steps in computing the density turbulence intensity levels, as well as the length scale data. This section presents the final results of the analysis. Figure 5.54 presents the rms density fluctuation levels for stations 2-4. The lip shocks made it impossible to perform the analysis at the first station. As mentioned earlier, the agreement with cross-wire results yields confidence in both methods. In Fig. 5.55, the length scale results can be found for the last three stations. The effects of the lip and reflected shocks are clearly evident at x/H = 5 (near y/H = 1.1 and 1.5). Otherwise the micro-length scale is about 0.01H at all three stations, in both x and y. Similarly, the integral length scales are about 0.02H at all three stations.

5.5 Parallel-Wire and High Frequency Response Pitot Pressure

The parallel-wire and high frequency response Pitot pressure data are grouped together for two reasons. First, both are high frequency data sets from which spectra results were computed. Secondly, since the methods were being evaluated, they were only applied to only station 3 (the measurement technique evaluation station).

5.5.1 Parallel-Wire

Figures 5.56 and 5.57 present the parallel-wire auto/cross-correlation functions. The correlations are normalized by the variances, where the correlation time axis is nondimensionalized by multiplying by the local mean velocity (u) and dividing by the slot exit height. The correlations at y/H = 0.33 and 1.50 are indicative of instrumentation noise. This is the expected result, since these measurement locations are in the slot inviscid core and the free stream. The result at y/H = 0.5 is near the lower edge of the mixing

layer. The next three are in regions of relatively high turbulence, hence, the typical "looking" correlation functions.

The micro and integral length scales were estimated from the autocorrelation functions. The structure angles were estimated from the correlation space time of the cross-correlation peak. These results are presented in Fig. 5.58. The micro length scales appear to be constant across the shear layer (points between y/H = 0.5 and 1.0). The integral length scales decrease with increasing y/H (in the shear layer region), as does the structure angle. The error bars indicate sampling rate resolution.

Figure 5.59 illustrates the normalized frequency content of the turbulence, the rms mass flux values at each frequency is normalized by the mass flux variance. The frequency response of the system was estimated prior to the measurement as about 75 kHz. The "free stream" power spectra, or autospectra, (at y/H = 0.33 and 1.5) indicate that the frequency response was actually about 50 kHz. The normalized power spectra profiles in the mixing layer (y/H$\in$ [0.5,1.0]) are distinguishable from the free stream results because of the high power at low frequencies (i.e. for f less than about 4 kHz). The power decreases about one order of magnitude over a frequency range of near zero to about 4 kHz. Indicating that the larger eddies contribute most of the energy. The power then levels out until about 50 kHz, afterwards the power drops due to the frequency response of the anemometer. The results are practically identical for each wire on the probe, except at y/H = 1. Here, the lower wire (dashed line) appears to have been exposed to higher turbulence. Probably, the upper wire (solid line) was in an intermittent region.

Figure 5.60 presents the magnitude of the cross spectra, as well as the phase, recall that cross spectra are complex numbers. The cross spectra magnitude spectra indicate the same trends discussed for the power spectra. The phase results indicate the upper wire "leads" the lower wire by about 5 degrees in the free stream. However, in the mixing layer, the phase depends on frequency (or eddy size). The large eddies (low frequency) strike both wire almost simultaneously, thus the small phase shift. However, the small eddies strike the probes in succession, hence, the increasing phase shift.

5.5.2 High Frequency Pitot

Figure 5.61 presents the mean and rms Pitot pressure profiles. Figure 5.61(a) compares the Kulite Pitot probe and the conventional Pitot probe data. The agreement was found to be excellent. The pitot pressure turbulence intensity profile was used to estimate Mach number and density rms levels. Figure 5.62 shows the Pitot frequency content, again normalized by the variance of the P_{t2} fluctuations. A 100 kHz filter was

employed to minimize aliasing errors. The effects of aliasing can be seen by the dashed line at y/H = 0.89. Comparing the results at y/H = 1.64, one can see that the filtered results are accurate for frequencies lower than about 50 kHz. The power spectra results discussed for the parallel-wire probe carry over to the high frequency response Pitot pressure autospectra (i.e. the larger eddies seem to account for most of the turbulent energy content).

Subject to the assumptions mentioned in chapter 4, the rms Pitot pressure results can be related to the density and Mach number turbulence intensities. Figure 5.63(a) presents the rms density results. Also included are the cross-wire and Shadowgraph data. The agreement between the methods is very good. Once, again the p' assumption appears to be valid at these flow conditions. Figure 5.64(b) presents the Mach number fluctuation levels.

5.6 Shear Layer Spreading Rate

The shear layer spreading rate has historically been considered a measure of the effects of compressibility on the turbulent mixing zone. The "Langley Curve" (Fig. 1.2) , that was developed by Birch and Eggers [10], correlates the spreading rate (dB/dx) with the free stream Mach number for mixing layers or half-jets. In other words, the velocity of the secondary stream is zero. For a free stream Mach number of 4.0, the spreading rate, based on the Langley curve would be about 0.04. Reference [3] presents a spreading rate u_i/u_∞ correlation, for $M_\infty = 2.3$. For the present study $u_i/u_\infty = 0.73$, which, based on the correlation, should yield a spreading rate of about 0.02. Figure 5.66 presents the spreading rate for the present study, estimated by various methods. Ng and Brock [76] suggested that an entropy envelope could be used to estimate layer widths for numerical predictions, therefore, that method, as well as an entropy gradient technique (see Fig. 5.64), were compared to the results based on the velocity envelope and vorticity methods (see Fig. 5.65). To estimate the layer width with the envelope methods, a 99% criteria was employed. A 32% method was employed for the gradients. This was arrived at by assuming the gradient profile to be a square wave (equal to the maximum). Therefore, searching for the 32% level is crudely one standard deviation from the mean. Also presented are the results directly measured off the Shadowgraph. The best fit to all the methods yielded a spreading rate of 0.028, which is in fair agreement with two correlations in the literature, neither of which are directly applicable here.

CHAPTER 6
EXPERIMENTAL EVALUATION OF TURBULENCE MODELS

The turbulence models discussed in Chapter 2 will be experimentally evaluated with the data presented in Chapter 5. The mixing length formulations were evaluated with the conventional probe data (assuming a nominally adiabatic flow). In other words, the measured velocity and density profiles were used to evaluate the necessary model gradients. The value of L_m was based upon the shear spreading rate (Fig. 5.66) and an initial value of about 0.25H, which was estimated from the Shadowgraph.

6.1 Apparent Mass

In Chapter 2, it was suggested that compressible turbulence affects all of the conservation equations, starting with the continuity equation. Figures 6.1-6.4 present the measured apparent mass along with the compressible apparent mass mixing length model extension (Eqn. (2.13)) evaluations for the four axial stations. As can be seen the agreement between the model, the solid line, and the data, the squares, is excellent. Except at x/H=0.2, where the lip shocks contaminate both the cross-wire and mean flow probes.

6.2 Shear Stress

Figures 6.5-6.8 present the shear stress measurements and model evaluations at the four stations. The circular symbols presented in Figs. 6.5-6.8 represent the measured compressible shear, in transformed variables (i.e. no assumptions), where the squares are estimates to the incompressible (or first) Reynolds shear stress term (the ρ' assumption was applied here).

Looking at station 3, Fig. 6.3(a), for example, it can be seen that the Prandtl mixing length model agrees very well with the squares, which are the estimates of the incompressible Reynolds shear term. The compressible contributions were accounted for by multiplying the apparent mass by the axial velocity (i.e. including the term suggested by Situ and Schetz [4]). The agreement between the Situ-Schetz model, the dashed line, and the "total" compressible shear, the circles, is also excellent. Notice, that S was set to 1, as was implied in Chapter 2. The results are similar at all stations, except at x/H = 0.2. The conventional and the cross-wire probes both suffered errors there due to the lip shocks. Recall that the CAMMLE and SSML shear stress formulations are essentially identical.

The energy models were estimated using the cross-wire TKE and TKE_c (Eqn. (2.8)) results. Again, referring to station 3, Fig. 6.3 (b), it can be seen that the Prandtl energy formulation (Eqn. (2.6)), the solid line, predicts a shear stress slightly larger than the first Reynolds shear term. However, the incompressible Bradshaw TKE model, the short dashes, predicts a value much closer to the compressible shear. This result was surprising, since the Bradshaw model, like the Prandtl model, was based on incompressible boundary layer data [6]. The compressible Bradshaw extension (Eqn. (2.9)), the long dashes, performed practically identically to the incompressible formulation. The compressible Prandtl TKE model (Eqn. (2.9)), the dots, performs the best, and as the analysis of Chapter 2 implied, L should be set to L_m.

6.3 Heat Flux

Figures 6.9-6.12 present the measured heat flux and model evaluations, again at the four measurement stations. The circles represent the heat flux in cross-wire (transformed) variables, and the squares are the incompressible contribution. As can be seen the incompressible contribution is essentially zero. Thus, all of turbulent heat flux is due to compressibility at these conditions.

In order to correctly model the incompressible term, the total temperature gradient transport method (Eqn. (2.18)) was used over the existing incompressible methods (Eqn. (2.15a)). As discussed in Chapter 2, the typical incompressible gradient transport models are applied to Eqn. (2.15), thus the formulation is slightly different than Eqn. (2.18). To be specific, expanding the total enthalpy gradient, in Eqn. (2.18), into static enthalpy and velocities, both terms will be divided by the turbulent Prandtl number, where in the typical incompressible formulation, applied to Eqn. (2.15), only the static enthalpy term is divided by the turbulent Prandtl number (Eqn. (2.15a)). Therefore, the incompressible methods will not predict a zero contribution from the incompressible terms, for adiabatic flows unless the turbulent Prandtl number is set to 1. Since the flow field was assumed adiabatic, the total temperature gradients were zero, hence the model and the data agree. Care should be taken when using the incompressible formulation.

In order to model the compressible heat flux term (i.e. the second term in Eqn. (2.16)), the compressible apparent mass mixing length model formulation, Eqn. (2.13), was multiplied by the stagnation enthalpy, yielding the apparent mass mixing length extension heat flux model in Eqn. (2.18). Again, the model results, the solid line, are in excellent agreement with the data, the circles.

CHAPTER 7
NUMERICAL METHODS AND RESULTS

This Chapter details the numerical results generated by incorporating the compressible turbulence terms in all of the conservation equations through the compressible apparent mass mixing length extension formulation (Eqns. (2.13), (2.14), and (2.18)). The CFD set-up will be discussed first. The second section describes the turbulence model changes incorporated into GASP. The third section presents the numerical results. The last section examines the errors associated with the ad hoc eddy viscosity and thermal conductivity treatment of the energy equation.

7.1 CFD Set-Up and The Unit Problem

All of the numerical results were generated with GASP (Generalized Aerodynamics Simulation Program) [26,27]. The thin layer Navier-Stokes equations [77] were solved, where the PNS assumptions were enforced in the subsonic regions (very close to the lower wall and near the finite thickness lip). This allowed the solution to be space marched. The coordinate system was defined such that x was the marching direction, and y was the vertical direction, and z completed the right hand system as the span direction. The solution normalized residuals were converged to $1x10^{-4}$ (or four orders).

The problem was run single zone, block and group. Two grids were run, course (51x81) and fine (101x161). Both grids were generated with GRIDGEN2D [43], see Fig. 7.1. The numerical domain was a rectangle (0.5x0.14 m). The grids were uniform in x. However, the grids (in the vertical direction) were clustered near the lower wall and the injector lip. A GRIDGEN break point was placed at the injector lip (y = 0.0254 m), thus separating the grid into the slot flow region and the free stream zone. The hyperbolic sine method was used to stretch the grid in the areas near the lower floor and the lower side of the lip (i.e. the injection portion of the grid). For the fine grid, the first floor cell height was selected to be on the order of $y^+ = 1$, which was estimated for a $C_f = 0.0025$ as $5x10^{-5}$ m. For the course grid, the first cell height was about $y^+ = 2$. The stretching on the lower side of the lip was a reflection of the floor, in other words, the slot injection grid spacing was symmetric about the slot center line. The free stream portion of the grid, from the slot lip to the upper wall was clustered only near the lip, i.e. a boundary layer type grid. The hyperbolic sine was again used where the minimum cell height was set equal to the minimum used for the slot region, this insured a smoothly varying grid distribution. The 2-D grids were converted into 3-D grids,

as required by GASP (101x161x2 and 51x81x2). Grid convergence studies were performed with the course and fine grids.

Space marching of the parabolized Navier-Stokes equations is numerically efficient [78]. However, axial pressure gradients must be suppressed in subsonic regions of the flow in order to insure a numerically stable solution. Therefore, the effects of the PNS assumption were tested on a "unit" problem, i.e. the overexpansion shock-turbulent boundary layer region of the flow field (see Fig. 1.1) was tested. This region was tested because the PNS assumption has the largest effect here due to the large axial pressure gradients of the shocks in the subsonic portion of the boundary layer. The oblique shock pattern was generated by imposing the conditions prior and aft the shock on the inflow profile. This causes the initial shock and expansion, as well as a slip line, see Fig. 7.3.

Both global thin layer Navier-Stokes (TLNS) and space marched PNS solutions were generated on a course (51x51) and fine (101x101) grid, see Fig. 7.2 for the fine grid. Figure 7.3 presents the TLNS solution, where PNS solution is contoured in Fig. 7.4. Comparisons of the two contours indicate that the shock angles are identical for the two solution techniques. Hence, the PNS solution technique should yield accurate results in the free shear layer downstream of the reflected overexpansion shocks (see Fig. 1.1). Figure 7.5 presents the lower wall pressure and skin friction. The difference between the wall pressure downstream of the reflected shock for the fine grid PNS and TLNS solutions indicate that the static pressure between the two solutions agrees to within 0.25% (for q = 16800Pa and p_∞ = 6600Pa). The TLNS skin friction indicates that the wall boundary layer does not separate. Therefore, the only difference between the two solutions is the floor boundary layer thickness.

Based on the results of the unit problem, space marching was exploited. Euler implicit time integration with an exact LU decomposition of the linearized system was used. Second order full flux input flags were chosen (i.e. GASP inputs were set as: impl = 1 and invflxi = 4, with rkapi = -1) for the axial marching direction. Third order upwind biased approximate Riemann solver, Roe split flux difference splitting [20,79], was selected for the y or vertical plane (invflxj = 3 and rkapj = 1/3). Catastrophic limiting was used in the marching direction (limi = 1), and Min-Mod was chosen for the vertical plane.

The inflow boundary was prescribed, which corresponds to type 2 in the GASP input. The inflow profiles were generated by estimating the free stream and injector upper and lower wall boundary layer thicknesses at exit of the slot. These were estimated from the Shadowgraph. The velocity profiles were computed

using the typical power law relations (i.e. $u = U_\infty(y/\delta_\infty)^{1/n}$, where n was set to 7). The finite thickness of the lip was accounted for by enforcing the no slip condition over 0.762 mm region centered about y/H=1. The no-slip adiabatic boundary condition (type 9) was enforced along the lower wall; tangency (type 8) was used for the upper wall; and second order extrapolation (type 4) was incorporated for the exit boundary. First order extrapolation from the interior (type 3) was used for the two z walls, i.e. the values along the z walls were set to the value at the cell center.

The gas (air) was assumed to be thermally ($p=\rho RT$) and calorically (constant specific heats) perfect. The solution was run inviscid in i and k, and thin layer in j (visflxi = 0, visflxj = 0, and visflxk = -2). The laminar viscosity and thermal conductivity were computed with the Sutherland equation (modlmu = 2, modlk = 2).

Three mixing length formulations were incorporated into GASP for the present study (this is elaborated on in section 7.2), the Prandtl mixing length, the Situ-Schetz compressible mixing length and the new compressible apparent mass mixing length extension. All of the solutions were converged four relative orders of magnitude. The first twenty planes, for the fine grid, were the stiffest. For the Prandtl model the time step (GASP input dt) was set to 3 (really -3 in the input) for the first 20 planes, it was then increased to 10 for the remaining planes. The LU reuse was invoked to speed up convergence, starting after the residual was reduced one order. Ten iterations were performed with the frozen LU. The Situ-Schetz model was slightly stiffer. The time step was reduced by about a factor of 3. It should be noted here, that the viscous Jacobians were correct for both of these methods. The compressible apparent mass model was much stiffer than the other two formulations. The main reason for this that the viscous Jacobians were only correct for the momentum equations, and the incompressible turbulence terms of the energy equation. The apparent mass in the continuity equation, as well as the apparent mass multiplied by the stagnation in the energy equation, were treated as source terms. For the first twenty planes, the time step was set to 0.08. It was increased to 0.3 for remaining planes.

7.2 Turbulence Model Additions To GASP

GASP contains a variety of κ-ε models and a single zero equation model (the Baldwin-Lomax) which performs well for wall bounded flows [26]. For the present study, the Prandtl Mixing Length (PML, Eqn. (2.6)), the Situ-Schetz Compressible Mixing Length (SSML, Eqn. (2.9)), and the new Compressible Apparent Mass Mixing Length Extension (CAMMLE, Eqns. (2.13), (2.14), and (2.18)) models were all

incorporated into GASP. The models were formulated to exploit the marching PNS algorithms, therefore, no global solutions were obtained for the injection study.

The 2-D Reynolds averaged thin layer Navier-Stokes equations, in cartesian coordinates, can be written as

$$\frac{\partial Q}{\partial t} + \frac{\partial F}{\partial x} + \frac{\partial (G - G_v - G_v^T)}{\partial y} = 0 \tag{7.1}$$

where Q is the 2-D conservative variable vector, and F and G are the inviscid flux vectors, G_v is the laminar flux contributions [78], and G_v^T is the turbulence flux contributions given by

$$G_v^T = \begin{pmatrix} -\overline{\rho' v'} \\ -\bar{\rho}\overline{u' v'} - \bar{u}\overline{\rho' v'} \\ -\bar{\rho}\overline{v'^2} \\ -\bar{\rho}\overline{h_o' v'} - \overline{h_o}\overline{\rho' v'} \end{pmatrix} \tag{7.2}$$

where the incompressible terms were modeled with Prandtl mixing length model. In the boundary layer regions, the mixing length was evaluated by the typical incompressible methods [6]. The Van Driest mixing length model was used for the inner region ($L_m = \kappa[1-\exp(-y^+/A)]y$, where $\kappa = 0.4$, $A = 26$). For the outer region L_m was set equal to 0.09δ. For the mixing layer L_m was set equal to 0.07B. All of the these constants are typical for incompressible planar mixing [23]. The compressible or apparent mass terms were modeled as discussed in Chapter 2 (Eqns. (2.13), (2.14), and (2.18)), where S was set to 1, for all Mach numbers. The gradients were computed normal to the grid (to be consistent with generalized coordinates). Since this was a "proof of concept" effort, i.e. the effects of including the apparent mass terms was being studied, the floor boundary layer thickness and shear layer widths were "hard wired" in order to evaluate the mixing length. If the layer widths were computed as the solution progressed, then it would be difficult to identify the contributions of the compressible terms. In other words, the differences in the solutions would probably be dominated by the discrepancies in the mixing length determinations. The floor boundary layer thickness was set to $\delta/H = 0.05 + 0.025x$, where the free shear layer width was computed as $B/H = 0.25 + (db/dx)x$ ($db/dx = 0.028$). A solution was also obtained with the compressible apparent mass mixing length extension where the mixing lengths evolved with the solution. The 32% (one standard deviation) vorticity method was used to determine the layer widths (see Chapter 5).

Three mixing length model variations were tested, the PML, the SSML, and the CAMMLE. The only difference in the input deck between the three formulations was the turbulent Prandtl number. For the incompressible and Situ-Schetz compressible eddy viscosity model the turbulent Prandtl number was set to the typical value of 0.8. However, as discussed in Chapter 6, for an adiabatic flow field, the turbulent Prandtl number should be set to 1 or change the formulation to the total temperature gradient transport. Setting the Pr_T to one was chosen.

7.3 Results

Grid convergence studies were performed on the fine and course grids. The results are presented in Fig. 7.6. The solid line represents the fine grid solution with Lm fixed to the values used in the experimental turbulence model evaluations presented in Chapter 6, i.e. Lm = 0.25H + 0.028x. The short dashes represent the course grid solution, again with the "hard-wired" mixing length. Based on these results, the 51x81 (or course) grid is adequate to resolve the flow physics. The long dashed line represents a solution, on the course grid, where the mixing length evolved with the solution. The 32% (one standard deviation) method was employed. Figure 7.7 presents the spreading rate estimated from the vorticity solution. As can be seen the spreading rate was slightly over predicted.

Figures 7.8-7.11 presents Mach number profiles at the four experimental measurement stations computed on the fine grid with the mixing lengths hard-wired. The third station (Fig. 7.10) presents the comparisons of the three model variations (recall, all were computed with the same values of L_m). As can be seen, the compressible apparent mass mixing length extension, the solid line, agrees the best with the data. The agreement appears to very good for all the stations, except near the upper edge of the shear layer, where the numerical results are diffused higher into the free stream. A possible reason for this difference may by the effects of intermittency, which based on the Shadowgraph are more prevalent on the upper side of the mixing layer. No numerical intermittency corrections were included. The Prandtl model also works pretty well, however, it deviates from the data slightly sooner than the apparent mass method. The Situ-Schetz formulation over predicted the shear layer spreading (recall L_m was fixed for all three model evaluations). The relatively poor performance of the Situ-Schetz model will be addressed in section 7.4.

Figures 7.12-7.14 present line contours of the mixing length apparent mass turbulence model solution for the fine grid with the hard-wired mixing lengths. The qualitative results agree nicely with those of the composite Shadowgraph. The waves are clearly evident in the density and pressure contours (Figs. 7.12

and 7.13). The velocity contours (Fig. 7.14) present the development of the mixing layer and floor boundary layer.

7.4 Examination of the Energy Equation Turbulence

The poor performance of the Situ-Schetz compressible eddy viscosity method was unexpected since the results reported by Situ and Schetz [4] were in excellent agreement with the data of Gilreath and Schetz [11]. However, the over prediction of the free mixing layer width can be seen by close examination of the experimental results and CFD comparison presented of the Hyde et. al. data [13] in ref. [4]. This phenomena may be explained by considering the energy equation turbulent heat flux formulation. In other words, does the Situ-Schetz compressible eddy viscosity correctly represent the turbulent heat flux (incompressible) formulation. With the compressible eddy viscosity, the typical incompressible heat flux formulation would be expressed as

$$q_y^T = -\frac{C_p \mu_T^S}{Pr_T}\frac{\partial \overline{T}}{\partial y} - \overline{u}\mu_T^S\frac{\partial \overline{u}}{\partial y} \tag{7.3}$$

where μ_T^S is the compressible Situ-Schetz eddy viscosity (Eqn. (2.10)), which can be written as

$$\mu_T^S = \mu_T + \frac{\overline{u}}{S}\left|\frac{\partial \overline{\rho}}{\partial y}\right| L_m^2 \tag{7.4}$$

where μ_T is the Prandtl eddy viscosity (Eqn. (2.7)). Note, the absolute values were slightly redefined, this is more consistent with the apparent mass model. Substituting the formulation in Eqn. (7.4) into Eqn. (7.3), then

$$q_y^T = -\left[k_T\frac{\partial \overline{T}}{\partial y} + \overline{u}\mu_T\frac{\partial \overline{u}}{\partial y}\right] - \left[\frac{\overline{u}}{S}\left|\frac{\partial \overline{\rho}}{\partial y}\right| L_m^2\left(\frac{\overline{\rho}C_p}{Pr_T}\frac{\partial \overline{T}}{\partial y} + \overline{u}\frac{\partial \overline{u}}{\partial y}\right)\right] \tag{7.5}$$

The term in the first set of brackets represents the "correct" gradient transport formulation for the incompressible term (consistent with Eqn (2.15a)), where the second group are additional terms due to the compressible eddy viscosity. This "compressible" formulation is drastically different than that of the CAMMLE model (Eqn. (2.18)). As can be inferred from Fig. 7.10, these extra terms increase the diffusion of the mixing layer, recall that all three formulations use the same value of L_m.

In order to quantify the effects of the second bracketed term in Eqn. (7.5), the formulations where evaluated for the idealized injection profile given in Fig. 7.15 for the Gilreath and Schetz data, the Hyde et. al. adiabatic results and the present study. Tables 7.1-7.3 summarize the parameters for each case. Tables 7.4-7.6 use the data in Tables 7.1-7.3 to evaluate the turbulent flux vector (Eqn. (7.2)) for the PML, SSML, and the CAMMLE models (see Chapter 2). Based on the results from Chapter 6, the CAMMLE model results can be used as a standard to evaluate the SSML and PML formulations. Hence, the error estimates are relative to the CAMMLE model results. Therefore, based on the results in Tables 7.4-7.6, the PML model estimates are consistently low for each term. The SSML and the CAMMLE models have identical shear (term 2 in the tables) formulations. However, the SSML neglects the apparent mass in the continuity equations and the results for the energy equation are extremely under predicted. The CAMMLE model consistently predicts a positive turbulent energy flux due to compressibility. However, the SSML formulation consistently predicts a negative value, which is similar in magnitude to the positive CAMMLE value (if $\partial p/\partial y = 0$ and $Pr_T = 1$, then the magnitude would be identical). The Situ-Schetz model under predicts the heat flux by about 140%, see Tables 7.4-7.6. The relatively small static temperature gradient for the Gilreath-Schetz case may explain why the SSML model preformed satisfactorily for this case. Even though the SSML model correctly predicts the shear level, perhaps the errors associated with the energy equation treatment are a poorer approximation than neglecting the compressible terms in all of the conservation equations. The numerical results of Fig. 7.10 seem to reinforce this hypothesis.

CHAPTER 8
DISCUSSION

The goal of the present research was to obtain insight into the complicated physics associated with high speed compressible turbulence. The a rigorous experimental, theoretical, and numerical study was undertaken. This Chapter presents a brief summary of the study, detailed discussion and conclusions, and finally, some future research areas.

8.1 Summary

As discussed in Chapter 1, compressible turbulence modeling remains the controlling factor in the accuracy of all high speed, high Reynolds number viscous computational boundary layer and Navier Stokes predictions. There are many reasons for the current dismal state of compressible turbulence modeling. The complicated physics, lack of compressible turbulence data (or experimental methods), and the separate CFD and experimental fluid dynamic disciplines are obvious contributors. The present study addresses this issue in the classical systematic approach that has historically been applied to incompressible flows.

The first step in the analysis was to formulate the problem, thus, identifying the terms that need to be measured and modeled. Based on the discussion presented in ref. [5], the Reynolds averaged form of the Navier-Stokes equations was studied. These equations were derived in a form that was experimentally convenient and also consistent with current numerical algorithms (see Chapter 2). The Reynolds shear stress and heat flux (Eqn. (2.3)) contains terms that cannot be directly measured. Hence, a transformation was developed, in Chapter 2, such that the sum or total Reynolds shear level could be measured (Eqn. (2.5)) via multiple overheat cross-wire anemometry, image processing of Shadowgraph photographs, and conventional mean flow data. Multiple overheat cross-wire anemometry has not received a great deal of attention. This is probably due to the complicated experimental set-up and intricate data reduction (must simultaneously solve for six turbulence unknowns at a single probe location). Chapter 4 details the development of the cross-wire routines, as well as improving current normal-wire methods. A Technique to uncouple the cross-wire data into apparent masses, Reynolds shear stresses, and Reynolds heat fluxes is also presented in Chapter 4. Chapter 3 describes the TTL multiple overheat scanning circuit developed to facilitate the measurements. Also presented in Chapter 4 is the derivation of the Shadowgraph image processing algorithms.

Chapter 2 also summarizes current incompressible turbulence models [6] (Eqn. (2.6)), as well as the Situ-Schetz [4] compressible eddy viscosity formulation (Eqn. (2.9)). All of the current models concentrate on the momentum equation shear stress formulation, thus, treating the energy equation in an ad hoc fashion (i.e. the effective eddy viscosity and thermal conductivity), and neglecting the turbulence effects on the continuity equation. Developed, in Chapter 2, is a new *Compressible Apparent Mass Mixing Length Extension* (CAMMLE), which accounts for the compressible turbulence in all of the conservation equations. The method generalizes the gradient transport methods of Situ and Schetz [4]. Finally, a new compressible turbulent kinetic energy formulation was developed to generalize the Prandtl and Bradshaw energy formulations [6] to compressible flows.

The literature review, presented in Chapter 1, indicated that a supersonic free shear layer is an attractive flow field in order to study the effects of compressibility on turbulence. More specifically, the effects of compressibility are significant at lower Mach numbers for free mixing layer as apposed to wall boundary layers. Unfortunately, the existing compressible turbulence data, in free mixing layers, does not include Reynolds shear stresses or density-velocity correlations. Hence, the experimental goal of the present study was to obtain the crucial compressible turbulence data using the methods developed in Chapter 4. The experimental set-up was designed to maximize both the compressibility effects and probe effectiveness. This flow field is not only valuable as turbulence study, but it has many practical applications (e.g. SCRAMjet fuel injection and wall film cooling).

Detailed data profiles were compiled at four strategically located measurement stations. The purpose of the first station was to document the initial conditions. The second station was chosen to be near the beginning of the fully developed region. Third station was chosen to be just prior to the merging of the shear layer and wall boundary layer. The last station was chosen to be aft of the layer merging. Flow visualization was accomplished with Shadowgraph photography. Chapter 5 presents all of the experimental data.

The experimental data, presented in Chapter 5, was used to evaluate the various turbulence models, see Chapter 6. The mean flow data was used in the turbulence model formulations, and the results were compared to the measured turbulence data. This is consistent with the classical turbulence modeling approach applied to incompressible wall bounded flows [6]. The zero equation, mixing length formulations were then numerically tested in Chapter 7.

8.2 Discussion and Conclusions

The present study was successful in implementing a theoretical/experimental/numerical program to gain a better understanding of the complicated physics associated with compressible turbulence. With the turbulence transformation, derived in Chapter 2, cross-wire anemometry and image processing of Shadowgraphs, developed in Chapter 4, became very powerful research tools in achieving this end. The $p' = 0$ assumption, necessary to uncouple the cross-wire turbulence data into velocity-velocity and velocity-density correlations, was validated for the present case, by comparing the uncoupled cross-wire rms density fluctuation levels to the results of the Shadowgraph image processing analysis. The high frequency response Pitot probe methods (again restricted by the p' assumption) were also found to yield accurate density and Mach number rms fluctuation levels.

The compressibility effects on the shear were found, experimentally, to be more than significant; they were dominant (3-4 times the incompressible term for the present study); for example see Fig. 5.43. The x-z plane turbulence measurements were found to be nearly as large and the x-y plane results, see Fig. 5.43. This was not to surprising, since turbulence is a 3-D phenomena.

Three mixing length model variations, the incompressible Prandtl mixing length (PML, Eqn. (2.6)), the Situ-Schetz [4] compressible eddy viscosity mixing length model (SSML, Eqn. (2.9)), and the newly developed, compressible apparent mass mixing length extension (CAMMLE, Eqns. (2.13), (2.14), and (2.18)), were experimentally and numerically evaluated. Four turbulent kinetic energy (TKE) formulations were experimentally tested, the Prandtl and Bradshaw incompressible planar mixing formulations [6], and the newly developed compressible TKE extensions (see Chapter 2), which were based upon the compressible turbulent kinetic energy (TKE_c), see Eqn. (2.8), developed in the present study.

Experimentally, the Prandtl mixing length model was found to yield accurate predictions of the incompressible Reynolds shear stress term (first term in Eqn. (2.3)). However, this term only accounts for about 25% of the total Reynolds Shear level (see Fig. 6.7, for the x/H = 15 results). The Prandtl incompressible TKE formulation was also successful in predicting the incompressible term (see Fig. 6.7). However, the Bradshaw incompressible formulation predicted the full compressible shear stress level (see Fig. 6.7). This result was surprising since the Bradshaw formulation was founded on incompressible wall boundary layer data. The Situ-Schetz compressible mixing length model (Eqn. (2.9)) and the CAMMLE model (Eqn. (2.14)) are essentially the same for the shear stress. Figure 6.7 indicates that the model

accurately represented the physics of the compressible turbulence. The TKE_c formulations also performed very well (again see Fig. 6.7).

The CAMMLE model differs from all other because it accounts for compressible turbulence in all of the governing conservation equations (see Chapter 2). Compressibility affects the continuity equation via an apparent mass. A gradient transport mixing length model was employed for the vertical plane (or y) apparent mass (Eqn. (2.13)); the data Fig. 6.3 (x/H = 15) demonstrates that this is an adequate model. All turbulence models treat the energy equation terms via an effective eddy viscosity and thermal conductivity. However, the CAMMLE model incorporates a consistent gradient transport formulation (Eqn. (2.18)) directly to the compressible Reynolds heat flux formulation making the typical thin layer approximations (Eqn. (2.16)). The model and the data are in excellent agreement (see Fig. 6.11 for the x/H = 15 results).

Numerically, the new apparent mass model was found to perform the best. The results agreed excellently with the data, except near the upper edge of the free mixing layer, see Fig. 7.10 for the x/H = 15 results. A possible reason, for the error near the upper edge of the mixing layer, may be due to the intermittency that was noticeable on the Shadowgraphs. The Prandtl model also performed well (Fig. 7.10). However, it deviated from the data more than the apparent mass method. The Situ-Schetz compressible eddy viscosity model over predicted the free shear layer width (Fig. 7.10). At first sight, this was a surprising result, since SSML and CAMMLE are identical representatives for the compressible turbulent shear stress, and the mixing length was hard-wired to the experimental value for both cases (solutions were also obtained where the mixing length developed with the solution). However, by close examination of the turbulent flux vector (Eqn. (7.2)), evaluated for the various turbulence models, the cause of the SSML over prediction of the shear layer width can be found. This phenomena is most likely due to the errors incorporated into the energy equation as detailed in Chapter 7. Therefore, the compressible apparent mass mixing length extension model should be the first choice. However, based on the performance of the SSML results compared to the PML, the compressible effects should be accounted for in all of the conservation equations, or none. In other words, the use of an effective compressible eddy viscosity and thermal conductivity are not consistent representatives of the physics associated with the energy equation. Therefore, care should be taken if using a "compressible" κ-ε model. If the model predicts the correct compressible shear level, and typical energy equation formulations (Eqn. (2.15a)) are used, then the results will be similar to those of the SSML.

8.3 Future Research

High speed compressible turbulence is an extremely complicated phenomena. The present study just barely touched the "tip of the ice berg". Many more experiments are needed. A couple of variations on the present experiment are easily identified. For example, heating the injectant would add insight to the turbulent heat flux phenomena. Secondly, if a different gas were injected (for example Helium), then the multi-species apparent masses could be studied.

The apparent mass model agreed with the experimental data very well, except near the upper edge of the mixing zone. The precise reason for this is unknown. However, examination of the Shadowgraphs implied that the upper edge of the free shear layer was much more intermittent than the lower side. Perhaps an intermittency correction is needed. This requires future study.

The present study suggested two compressible turbulent kinetic energy models, both of which show potential. Thus, the next logical step would be to develop a differential equation(s), for the compressible TKE, or even the leading term in the transformed shear stress, i.e. develop one and two equation models for the compressible shear. In addition, an equation for the apparent mass would be required.

This study measured 3-D turbulence, however, no three dimensional modeling was attempted. Therefore, future research may concentrate on 3-D turbulence modeling. This could lead to a necessity for turbulence measurements in a three dimensional flow. For example, the present cross-wire techniques could be applied to a flow where the turbulence was generated by low angle injection circular nozzles. Circular axial injection could also be incorporated.

A final area of future research would be to study the turbulence quantities in a chemically reacting flow. This would be invaluable for SCRAMjet analysis and design.

BIBLIOGRAPHY

1. Cebeci, T., and Smith, A.M.O.,Analysis of Turbulent Boundary Layers, Academic Press, 1974.

2. Harris, R.V. Jr.,"On the Threshold-The Outlook for Supersonic and Hypersonic Aircraft," AIAA Journal of Aircraft, Vol. 29, No. 1, 1992.

3. Marvin, J.G., and Coakley, T.J.,"Turbulence Modeling for Hypersonic Flows," NASA TM 1087, 1989.

4. Situ, M. and Schetz, J.A.,"New Mixing-Length Model For Turbulent High-Speed Flows," AIAA-89-1821.

5. Liou, W.W and Shih, T.-H.,"On the Basic Equations for the Second Order Modeling of Compressible Turbulence," NASA TM 105277, 1991.

6. Schetz, J.A.,Foundations of Boundary Layer Theory for Momentum, Heat Transfer, and Mass Transfer, Prentice Hall, Englewood Cliffs, 1984.

7. Bradshaw, P.,"Compressibility Effects on Free-Shear Layers,"The 1980-81 AFOSR-HTM-Stanford Conference on Complex Turbulent Flows: Comparison of Computation and Experiment, Vol.I, 1980, Stanford, California.

8. Papamoschou, D. and Roshko, A.,"Observations of Supersonic Free Shear Layers," AIAA-86-0162.

9. Schlicting, H.,Boundary Layer Theory,McGraw-Hill, New York, 1942; 7TH ed., 1979.

10. Birch, S.F. and Eggers, J.M.,"A Critical Review of the Experimental Data for Developed Free Turbulent Shear Layers," NASA SP-321, 1973, pp. 11-37.

11. Gilreath, H.E. and Schetz, J.A.,"Transition and Mixing in the Shear Layer Produced by Tangential Injection in Supersonic Flow," Journal of Basic Engineering, December 1971, pp. 610-618.

12. Walker, D.A., Cambell, R.L. and Schetz, J.A.,"Turbulence Measurements for Slot Injection in Supersonic Flow," AIAA-88-0123.

13. Hyde, R., Smith, B., Schetz, J. and Walker, D.,"Turbulence Measurements for Heated Slot Injection in Supersonic Flow," AIAA-89-1868.

14. Baldwin, B.S. and Lomax, H.,"Thin Layer Approximation and Algebraic Model for Separated Turbulent Flows," AIAA-78-257.

15. Morkovin, M.,"Fluctuations and Hot-Wire Anemometry in Compressible Flow," AGARDOGRAPH 24, 1956.

16. Li, T.Y. and Nagamatsu, H.T.,"Effects of Density Fluctuations on the Turbulent Skin Friction of an Insulated Flat Plate at High Supersonic Speeds," ALCIT Hypersonic Wind Tunnel Memorandum No. 5, May, 1951.

17. Jones, W.P. and Whitelaw, J.H.,"Calculation Methods for Reacting Turbulent Flows: A Review,"COMBUSTION AND FLAME, Elsevier Science Publishing Co., Inc., New York, New York, 48, pp. 1-26, 1982.

18. Huang, P.G. and Coakley, T.J.,"An Implicit Navier-Stokes Code for Turbulent Flow Modeling," AIAA-92-0547.

19. Marvin, J.G.,"Turbulence Modeling for Computational Aerodynamics (Invited)," AIAA-82-0164.

20. Roe, P.L.,"Approximate Riemann Solvers, Parameter Vectors, and Difference Schemes," Journal of Computational Physics, Vol.43, 1981, pp.357-372.

21. Van Driest, E.R.,"Turbulent Boundary Layer in a Compressible Fluid," J. Aeronautical Sci., Vol.13, No.3, 1951, pp.145-160.

22. Owen, F.,"Transition and Turbulence Measurements in Hypersonic Flows," AIAA-90-5231.

23. Lauder, B.E. and Spalding, D.B.,Mathmatical Models of Turbulence, Academic Press London and New York, 1972, pp.27-29.

24. Hyde, C.R.,"Turbulence Measurements of Heated Supersonic Injection Into a Supersonic Stream," Master Thesis-VPI&SU Aerospace Engineering Dept., Feb.,1989.

25. Anderson, J.D.,Modern Compressible Flow With Historical Perspective,2ND ed., Mcgraw-Hill Series in Mechanical Engineering, 1990.

26. McGrory, W., Slack, D., Applebaum, M., and Walters, R.,GASP Version 2, Aerosoft Inc., Blacksburg, Virginia, 1992.

27. Walters, R., Slack, D., Cinnella, P., Applebaum, M., and Frost, C.,"A User's Guide to GASP," NASA Langley Research Center, Hampton, Virginia, 1991.

28. Data Acquisition & Control, Keithley Metrabyte/ASYST/DAC, Vol.29, 1990.

29. Complete Temperature Measurement Handbook and Encyclopedia, 1986, Omega Engineering Inc., USA, 1985.

30. Bowersox, R.D.W.,"Meanflow and Turbulence Measurements in the Wake of a Supersonic Through-Flow Cascade," Master Thesis-VPI&SU Aerospace Engineering Dept., Jan. 1990.

31. Horowitz, P. and Hill, W.,The Art of Electronics, Cambridge University Press, 1980.

32. Waveform-Catalyst,Multichannel Digital Oscilloscope and Instrument Control Systems User's Manual, Version 2.3, 1986.

33. Volluz, R.J.,Handbook of Supersonic Aerodynamics, Section 20,"Wind Tunnel Instrumentation and Operations,",NAVORD Report 1988, vol.6, 1961.

34. DISA 55M System with 55M12 CTA Symmetrical Bridge, DISA ELECTRONIK A/S, DK-2730, Herlev, Denmark.

35. Probe Catalog, Dantec Electronik, Denmark, 1982.

36. Lancaster, D.,TTL Cookbook,Howard W. Sams & Co., Inc., Indianapolis, Indiana, USA.

37. Signetics Data Book, Digi-Key Corporation, Thief River Falls, MN.

38. Perpeptics Resident Image Processing Software (RIPS) Version 4.00. ***

39. Bendat, J. and Piersol, A.,Random Data Analysis and Measurement Procedures,2ND ed.,John Wiley & Sons, 1986.

40. Kay, S.M.,Modern Spectral Estimations: Theory and Application, Prentice Hall, Englewood Cliffs, 1988.

41. Parker, R. and Shure, L.,"PLOTXY-A Versatile Plot Program," 1987.

42. CRAY Mini Manual, NASA Langley Research Center, Hampton VA, 1991.

43. Stienbrenner, J., Chawner, J. and Fouts, C..The GRIDGEN 3D Multiple Block Grid Generation System, General Dynamics Corporation, Fort Worth Texas, WRDC-TR-90-3022.

44. Walatka, P., Bunning, R., Pierce, L. and Elson, P.,PLOT3D User's Manual Version 3.6, NASA, Fluid Dynamics Division Numerical Aerodynamic Simulation Division, TM-1010667, 1990.

45. Ames Research Staff,"Equations, Tables, and Charts for Compressible Flow,",NACA TR 1135, 1953.

46. Kovaszney, L.S.G.,"The Hot-Wire Anemometer in Supersonic Flow,"Journal of Aeronautical Sciences, vol.17, 1950, pp.565-584.

47. Spagenberg, W.G.,"Heat-Loss Characteristics of Hot-Wire Anemometers at Various Densities in Transonic and Supersonic Flow," NACA TN 3381, 1955.

48. Holman, J.P.,Heat Transfer, 6TH ed., McGraw-Hill Book Co., 1986.

49. Swokowski, E.,Calculus with Analytic Geometry, Alt. ed., Prindle Wever & Schmidt, 1983.

50. Fischer, M., Maddalon, L., and Wagner, R.,"Boundary-Layer Pitot and Hot-Wire Surveys at $M_\infty \approx 20$,"AIAA Journal, Vol.9, No.5, 1971, pp.826-834.

51. Smits, A., Hayakawa, K. and Muck, K.,"Constant Temperature Hot-Wire Anemometry in Practice in Supersonic Flow,"Experiments in Fluids 1, 83-92, Springer-Verlag, 1983.

52. Kovaszney, L.S.G.,"Turbulence in Supersonic Flow",Journal of the Aeronautical Sciences, Vol.20, No.10, 1953.

53. Wagner, R.D. and Weinstein, L.M.,"Hot-Wire Anemometry in Hypersonic Helium Flow," NASA TN D-7465, 1974.

54. Kistler, A.,"Fluctuation Measurements in a Supersonic Turbulent Boundary Layer,"Physics of Fluids,2,220,1959.

55. Bowersox, R.D.W., Ng, W.F. and Schetz, J.A.,"Hot-Wire Techniques Evaluated in the Wake of 2-D Supersonic Compressor Cascade,"Yokohama International gas Turbine Conference, IGTC-84, 1991, pp.303-309.

56. Laufer, J. and McLellan, R.,"Measurements of Heat Transfer from Fine Wires in Supersonic Flows," Journal of Fluid Mechanics, 1,276,1956.

57. Walker, D., Ng., W. and Walker, M.,"Hot-Wire Anemometry in Supersonic Shear Layers,"AIAA Journal, Vol.27, No.8, 1988.

58. Owen, F., Horstman, C. and Kussoy, M.,"Mean and fluctuating measurements of a fully-developed, non-adiabatic, hypersonic boundary layer,"Journal of Fluid Mechanics, Vol.70, part 2,pp.393-413,1975.

59. Rose, W.C.,"Turbulence Measurements in a Compressible Boundary Layer," AIAA Journal, Vol.12, No.8, 1974.

60. Settles, G., Williams, B., Baca, B. and Bogdonoff, S.,"Reattachment of a Compressible Turbulent Free Shear Layer,"AIAA-80-1408R.

61. Laderman,A. and Demetriades, A.,"Turbulent Shear Stresses in a Compressible Boundary Layer," AIAA Journal, Vol.17, No.7, 1979.

62. Barre, S., DuPont, P. and Dussauge, J.,"Hot-wire measurements in a turbulent transonic flows," European Journal of Mechanics, B/FLUIDS, Vol.11, No.3, 1992.

63. Champagne, F., Sleicher, C. and Wehrmann, O.,"Turbulence measurements with inclined hot-wires: Part 1. Heat transfer experiments with inclined hot-wires,"Journal of Fluid Mechanics, vol.1, part 1, pp.153-175,1967.

64. Chew, Y. and Simpson, R.,"The non-real-time explicit data analysis method of crossed hot-wire anemometer measurements including tangential cooling velocity correction,"Journal of Physics, E: Sci. Instrum. 21, 1988, pp.310-316.

65. Sandborn, V. and Laurence, J.,"Heat Loss from Yawed Hot Wires at Subsonic Mach Numbers," NACA TN 3563.

66. Demetriades, A. and Laderman, A.,"Reynolds Stress Measurements in a Hypersonic Boundary Layer,"AIAA Journal, Vol.11, No.11, 1973.

67. Laderman, A.J.,"New Measurements of Turbulent Shear Stresses in Hypersonic Boundary Layers," AIAA Journal, Vol. 14, No. 9, 1975.

68. Lowell, H.,"Design and Applications of Hot-Wire Anemometers for Steady-State Measurements at Transonic and Supersonic Airspeeds,"NACA TN 2117, 1950.

69. Clay, W., Herrmann, J. and Slattery, R.,"Statistical Properties of the Turbulent Wake Behind Hypervelocity Spheres,"The Physics of Fluids, Vol.8, No.10, 1965.

70. Polaroid High Speed Film Type 57, Data Sheet, PP479, Printed in the USA, 1983.

71. Kovaszney, L.S.G.,"Optical Techniques,"Physical Measurements in Gas Dynamics and Combustion, Princeton University Press, Princeton, New York, 1954.

72. Liepmann, H.W. and Roshko, A.,Elements of Gas Dynamics, GALCIT Aeronautical Series, John Wiley & Sons, Inc.,1957.

73. Clark, R., Ng., W., Rettew, A., Walker, D., and Schetz, J.,"Turbulence Measurements in a High-Speed Shear Flow Using a Dual-Wire Probe,"AIAA-88-3055A.

74. Donovan, J. and Smits, A.,"Large-Scale Motions in a Supersonic Turbulent Boundary Layer on a Curved Surface,"AIAA-90-0019.

75. Spina, E., Donavan, J. and Smits, A.,"Convection velocity in supersonic turbulent boundary layers,"Physics of Fluids A, Vol.3, No.12, 1991.

76. Brock, J. and Ng., W.,"The Baldwin-Lomax Model for Separated and Wake Flows Using an Entropy Envelop Concept",AIAA-92-0148.

77. Newsome, R., Walters, R., and Thomas, J.,"An Efficient Iteration Strategy for Upwind/Relaxation Solutions to the Thin Layer Navier-Stokes Equations," AIAA-87-1113.

78. Thomas, J. and Walters, R.,"Upwind Relaxation Algorithms for the Navier-Stokes Equations,", AIAA-85-1501.

79. Walters, R., Cinnella, P., Slack, D. and Halt, D.,"Characteristic-Based Algorithms for Flows in Thermochemical Nonequilibrium,"AIAA Journal, Vol.30, No.5, 1992.

80. Burden, R. and Faires, J.,Numerical Analysis 4TH ed., PWS-KENT Publishing Company, Boston, 1989.

APPENDIX

The appendix is divided into two sections. The first section presents the detailed data reduction procedures for both the cross-wire and Shadowgraph methods. The cross-wire sub-section also compares the various reduction algorithms (see Chapter 4). The cross-wire was chosen as an example over the normal-wire since, the normal-wire reduction steps are a sub-set of those of the cross-wire.

The second section presents an experimental error analysis. The conventional probe errors will be discussed first since those errors effect the anemometry results, through calibration. Also, the hot-wire linearization errors will be examined. Thirdly, the errors associated with the high frequency response probes (Kulite Pitot and Parallel-wire) will be discussed. The last section analyzes the Shadowgraph errors.

A.1 REDUCTION PROCEDURES

This section details the reductions procedures for both the cross/normal-wire anemometry and Shadowgraph image processing via example data sets

A.1.1 Cross-Wire Anemometry

The first step, in the data reduction, was the wire calibration. The primary and slot free streams (where the turbulence levels were essentially zero) were used for this purpose. A diffuser type thermocouple was found to yield the same total temperature as the free stream settling chamber and slot total temperatures (when in those regions of the flow). Therefore, with the conventional probe profiles, slot and primary flow total temperatures and pressures (measured during the cross-wire traverse), along with the mean cross-wire voltages, the Reynolds number calibration constants could be determined.

While paused at a vertical measurement station, the overheat scanning circuit rapidly changed the wire temperature. The data acquisition computer digitized the anemometer output. Figure A.1 presents the "raw" voltages for wire 1 on the cross-wire probe at two vertical locations (in a typical tunnel run, 10-20 vertical locations of data were acquired). The cross-wire probe was near the upper edge of the free mixing layer in Fig. A.1(a). The intermittency is evident by the varying levels of the peaks. The probe was near the center of the mixing layer in Fig. A.1(b). Figure A.2 presents the same traces for the second wire on the cross-wire probe. The eight wire temperatures are evident by the steps in the traces.

The signal conditioning techniques discussed in Chapter 3 were applied to each of the steps in the trace. This particular data set had fifteen vertical locations. Figure A.3 presents the resulting mean, cross/auto correlation results.

Figures A.4(a) - A.4(c) present the results of GLS - Method (see Chapter 4) for the two wires on the cross-wire probe. However, in Chapter 4, five different reduction techniques were derived. The two multiple overheat (GLS and QLS) and the three single overheat (Crocco, Morkovin, and no total temperature correction) methods. Figures A.4(d) - A.4(f) present the results for all five methods in tunnel axes. The results indicate that the GLS and QLS methods agree very well (with in about 5%). The relaxed Crocco correction technique ($\kappa = 0.4$, $R_{uT} = 0.7$, and $R_{vT} = 0$) performs slightly better that the Morkovin method ($R_{mT} = 1$, $R_{uT} = 0.7$, and $R_{vT} = 0$). The typical single overheat method of simply neglecting the total temperature terms under estimates the axial mass flux turbulence intensity (Fig. A.4(d)) by about a factor of 2. However, all three single overheat methods correctly predicted the rms vertical mass flux fluctuation levels (Fig. A.4.(e)), as well as the cross-wire shear term (Fig. A.4(f)). Since the GLS - Method is the popular normal-wire technique, and the results are virtually identical with the QLS - method, it was chosen for all normal/cross-wire data.

A.1.2 Shadowgraph Image Processing

The Shadowgraphs were digitized as discussed in Chapter 4. The camera was zoomed such that the spatial resolution was about 0.125 mm. The vertical profiles were generated by processing 32x32 pixel squares (yielding 4x4 mm "probe" areas) along a measurement station line (13 or 14 data sets were reduced at each station). The 2-D signal processing techniques, discussed in Chapter 3, were applied to the 32x32 arrays. Figure A.5 presents the 2-D film contrast autospectra (where frequency has the unusual units of m^{-1}) for two vertical locations: (a) is in the free stream, and (b) is near the center of the free shear layer. From these results and the analysis derived in Chapter 4, the 2-D autospectra of density was computed. The rms density fluctuation level, at a particular y location, was computed by integrating for the volume under the curve. Simpson's rule was incorporated. This procedure was repeated for each of the 13 or 14 vertical locations in a single profile presented in Chapter 5.

A second type of information that was extracted from the Shadowgraphs was the integral and micro length scales, see Chapter 4. Figure A.7 presents the autocorrelations at the three axial locations (13 or 14 per location). The length scales were computed from these results.

A.2 Error Analysis

Error, or scatter, is an inherent facet of experimental research. This section attempts to identify sources, and estimate the magnitude, of these errors. Since, for any given measurement technique, there are many sources of scatter. The present study uses the L_2 (or Euclidean) [80] norm as the measure of the error. The L_2 norm is given by

$$e_x = \left[\sum_{i=1}^{n} e_i^2\right]^{1/2} \tag{A.1}$$

where i indexes the various errors associated with the measurement of x. The conventional probe errors will be discussed first.

A.2.1 Conventional Probes

The settling and slot total pressure and temperature probe errors can be attributed to calibration standard deviations. Therefore, $e_{Pt1} = 0.02$ atm, $e_{Pts} = 0.0047$ atm, and $e_{Tt1} = e_{Tts} = 1$ K.

All of the probes were 7.62 ± 0.25 cm long. The probes "flexed" back about 0.02 cm. Hence, the error in the axial location (e_x) was about 0.25 cm. The vertical calibrations were repeatable to 0.05 mm. The probe flexing yielded and additional uncertainty of about 0.05 cm. Therefore e_y was approximately 0.05 cm.

Three sources of error infected the Pitot and cone-static results. The calibration standard deviations were both about 0.0047 atm. Reference [32] reports that errors associated with the turbulence would be about 0.0068 atm, for both probe types. The uncertainty in the vertical location, coupled with the spatial Pitot and cone-static gradients create the third source of error. These errors were estimated as 0.034 and 0.00068 atm for the Pitot and cone-static pressures, respectively. Hence, $e_{Pt2} = 0.035$ atm, and $e_{pc} = 0.0083$ atm. The effects of the Pitot and cone-static pressure errors on the Mach number and static pressure could be estimated with a perturbation analysis. The results of which are summarized in Table A.1.

A.2.2 Cross/Normal-Wire Anemometry

Since 512 data points were acquired at each overheat ratio, the statistical error estimates are negligible. The dominant error is expected to be associated with the calibration. Therefore, the errors in the conventional probe data carry over to the hot-wire analysis. Assuming the total temperature errors (e_{Tt}) to be mainly due

to calibration, and continuing the perturbation analysis, the calibration errors can be estimated. The results are summarized in Table A.2. From Table A.1, it can be seen the error in mass flux (or Reynolds number) was found to be $e_{\rho u} \approx 2\%$, and $e_{Tt} \approx 0.3\%$. Hence, the errors in the hot-wire sensitivities were about $e_f = 1\%$ and $e_g = 0.3\%$. Applying a perturbation analysis to the GLS - Method, the correlation errors were found to be $e_{0'0'} \approx 8.33\%$ (i.e. the errors in the cross-wire shear and total temperature-mass flux correlation terms. Since, the turbulence intensity is the square root of the autocorrelation, the errors are reduced by about a factor of 2 (i.e. $e_{TI} \approx 4.17\%$). The perturbation analysis found that the effects of probe misalignment were negligible. This is mainly due to the fact that the probe was calibrated for each run, hence accounting for any misalignment.

A.2.3 Hot-Wire Linearization

To arrive at the hot-wire response equations, the hot-wire response equation was linearized via the Binomial theorem [49]. This section investigates the errors associated with this approximation. In order to estimate the magnitude of the neglected terms, the second order term in the binomial expansion were included, thus

$$\left[\frac{v_w'}{V_w}\right](1+e_V) = +f\left[\frac{Reo'}{Reo}\right](1+e_R) + fg\left[\frac{Reo'T_t'}{Reo\ T_t}\right](1+e_C) + g^2\left[\frac{T_t'}{T_t}\right](1+e_T) \qquad \text{(A.2)}$$

where the errors are given by

$$
\begin{aligned}
e_V &= \frac{1}{4}\left(\frac{v_w'}{V_w}\right)^2 \\
e_R &= \frac{1}{16}\left(\frac{Reo'}{Reo}\right)^2 \\
e_T &= \frac{I^2}{g^2}\left(\frac{T_t'}{T_t}\right)^2 \\
e_C &= \frac{-\frac{H}{4g}\left(\frac{Reo'}{Reo}\right)^3\frac{T_t'}{T_t} - \frac{I}{4g}\left(\frac{Reo'}{Reo}\right)^2\left(\frac{T_t'}{T_t}\right)^2 + \frac{H^2}{2fg}\left(\frac{Reo'}{Reo}\frac{T_t'}{T_t}\right)^2 + \frac{HI}{fg}\left(\frac{Reo'}{Reo}\right)^3\left(\frac{T_t}{T_t}\right)^3}{\left(\frac{Reo'}{Reo}\frac{T_t'}{T_t}\right)} \\
&\approx -\frac{H}{4g}\left(\frac{Reo'}{Reo}\right)^2 + \left(\frac{H^2}{2fg} - \frac{I}{4g}\right)\left(\frac{Reo'}{Reo}\frac{T_t'}{T_t}\right) + \frac{HI}{fg}\left(\frac{T_t'}{T_t}\right)^2
\end{aligned}
\tag{A.3}
$$

where I and H are defined for convenience as

$$
\begin{aligned}
H &= 2f\left[n_k - \frac{n_\mu}{2} - g^*\right] \\
I &= \frac{1}{2}\left[\frac{n_k(n_k-1)}{2} - n_\mu f\left(2n_k - 1 + \frac{n_\mu}{2}\right) - g^*(2n_k - 4fn_\mu)\right]
\end{aligned}
\tag{A.4}
$$

where $g^* = g - n_k/2 + n_\mu f$. Equation (A.3) implies that the linearization errors are second order. To get a quantitative estimate, some typical values can be substituted into Eqns. (A.3) and (A.4). For $f \approx 0.3$ and $g \approx -0.5$, then $H \approx 0.5$ and $I \approx -0.25$. The following numbers are typical of the peak values in the free shear layer

$$\left(\frac{v_w'}{V_w}\right)^2 = 0.002$$

$$\left(\frac{Reo'}{Reo}\right)^2 = 0.06$$

$$\left(\frac{T_t'}{T_t}\right)^2 = 0.0009$$

$$\left(\frac{Reo'}{Reo}\frac{T_t'}{T_t}\right)^2 = 0.0025$$

Therefore, the linearization error, e_{Lin} sums to less than 0.5%. Hence, combining this error with the calibrations error (Eqn. (A.1)), then the total estimated hot-wire error is about 8.5 %. Table A.2 includes the linearization errors.

A.2.4 High Frequency Response Probes

The Kulite Pitot pressure and parallel-wire probes were used to acquire frequency spectra. Hence, relatively high sampling rates were employed (500 kHz). One hundred and twenty-five blocks, record length of 1024 data points, were acquired. The statistical errors, in the spectra results, can be estimated by the methods discussed in Ref. [39]. Applying these techniques, then $e_{Gff} \approx 9\%$ and $e_{Gfg} \approx 10\%$. The cross and auto correlation, as well as the length scale, errors, are expected to be very small (<1%) for 125 averages (based on Chi-Square distribution).

The errors in the turbulence intensity results are expected to be much smaller. The only source of error, assuming the p' assumption is valid, is due to calibration, which was estimated as $e_{cal} = 1\%$.

There are three causes for error in the structure angle estimates. The main one is due to time resolution of τ_{max} (i.e. time between data samples). The second is due to the uncertainty in the mean velocity (e_u), which was estimated as approximately 10 m/s. The last, and least significant, is due to the statistical errors in the cross correlation. These errors are presented as error bars on the structure angle plots (Chapter 5). An average error would be about ±10°.

A.2.5 Shadowgraph Processing

Two sources of uncertainty, other than the assumptions discussed in Chapter 4, existed in the Shadowgraph data. Due to the inherent averaging across the flow field, the statistical errors, in the estimated spectra, are assumed to be very small. The second source of uncertainty is the determination of L, the distance the photographic plate was from the center of the test section. The error in L was estimated as about 1 cm (or about 2%). However, this term is squared, hence, the expected error is about 5.7%. As was found with the hot-wire methods, the linearization errors are expected to be small.

TABLE 3.1: Measured Free Stream and STIM Flow Field Characteristics

M_∞	3.8
$P_{t\infty}$(atm)	12.5
$T_{t\infty}$(K)	290
u_∞(m/s)	658
Re_∞/m	$67x10^6$
M_s	1.8
P_{ts}(atm)	0.49
T_{ts}(K)	297
u_s(m/s)	484
Re_s/m	$7x10^6$
M_c	0.39
ρ_s/ρ_∞	0.32

TABLE 7.1: Idealized Injection Flow Field Parameter - Present Case.

M_1	3.8
u_1(m/s)	660
ρ_1(kg/m^3)	0.5
T_1(K)	77
M_2	1.8
u_2(m/s)	485
ρ_2(kg/m^3)	0.15
T_2(K)	182

TABLE 7.2: Idealized Injection Flow Field Parameter - Hyde et. al. [13] un heated case.

M_1	3.0
u_1(m/s)	620
ρ_1(kg/m^3)	0.6
T_1(K)	110
M_2	1.7
u_2(m/s)	470
ρ_2(kg/m^3)	0.3
T_2(K)	190

TABLE 7.3: Idealized Injection Flow Field Parameter - Gilreath-Schetz [11] Case.

M_1	2.85
u_1(m/s)	610
ρ_1(kg/m^3)	0.016
T_1(K)	115
M_2	2.0
u_2(m/s)	520
ρ_2(kg/m^3)	0.0095
T_2(K)	167

TABLE 7.4: Idealized Turbulent Flux Evaluations (Normalized by the local mean) - Present Case.

	App.Mass	τ^T_{xy}	q^T_y	e_q
CAMMLE	0.0017	0.0022	0.0017	****
SSML	0.0000	0.0022	-0.00061	140%
PML	0.0000	0.0005	-0.0001	110%

TABLE 7.5: Idealized Turbulent Flux Evaluations (Normalized by the local mean) - Hyde et. al. [13] Case.

	App.Mass	τ^T_{xy}	q^T_y	e_q
CAMMLE	0.00092	0.0013	0.00092	****
SSML	0.0000	0.0013	-0.00025	130%
PML	0.0000	0.0004	-0.00007	110%

TABLE 7.6: Idealized Turbulent Flux Evaluations (Normalized by the local mean) - Gilreath-Schetz [11] Case.

	App.Mass	τ^T_{xy}	q^T_y	e_q
CAMMLE	0.00041	0.00054	0.00041	****
SSML	0.0000	0.00054	-0.00015	130%
PML	0.0000	0.00013	-0.00004	110%

TABLE A.1: Conventional Probe Errors.

e_x	2.5mm	****
e_y	0.005 mm	****
e_{Pt1}	0.02 atm [1]	0.2%
e_{Tt1}	1 K	0.3%
e_{Pt2}	0.04 atm	2.3%
e_{pc}	0.01 atm	5.4%
e_M	0.2	6.0%
e_p	0.01	10.0%

[1]All error estimates are based on a nominal Mach number of 3.3, total pressure of 12.5 atm, and a stagnation temperature of 290K.

TABLE A.2: Hot-Wire Errors.

e_T	7 K [1]	7.6%
e_ρ	0.015 kg/m^3	3.6%
e_u	10 m/s	1.5%
$e_{\rho u}$	5.75 kg/m^{2}s	2.1%
e_f	0.0025	1.0%
e_g	0.005	1.0%
e_V	0.0008 [2]	0.08%
e_R	0.004	0.4%
e_T	0.0002	0.02%
e_C	0.013	1.3%
e_{Lin}	0.0058	0.4%
$e_{0'0'}$	0.0053	8.4%
e_{TI}	0.0027	4.3%

[1]Same as TABLE A.1.

[2]Typical values presented in section A.2.2.

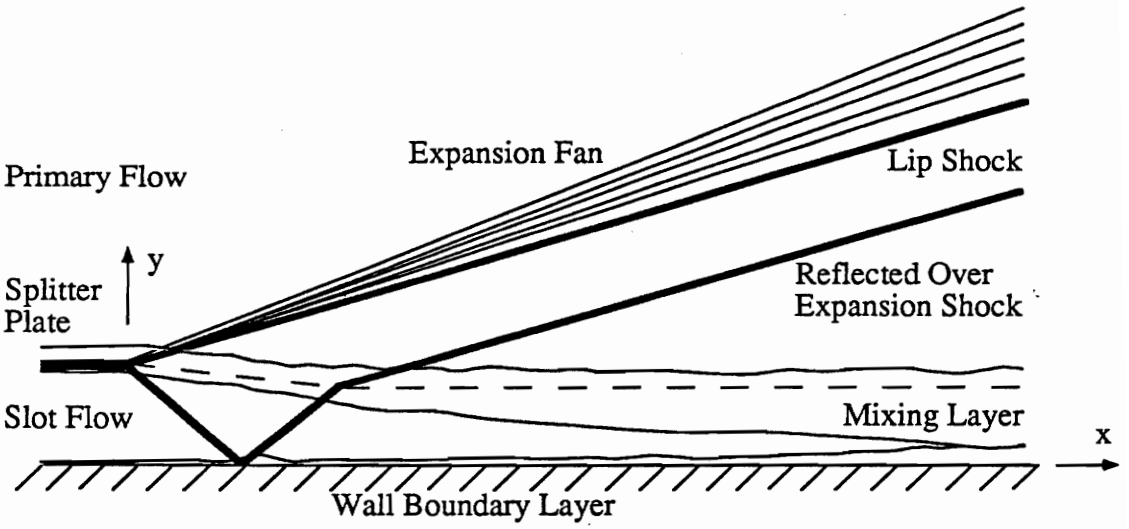

FIGURE 1.1: Schematic of supersonic mixing flow field.

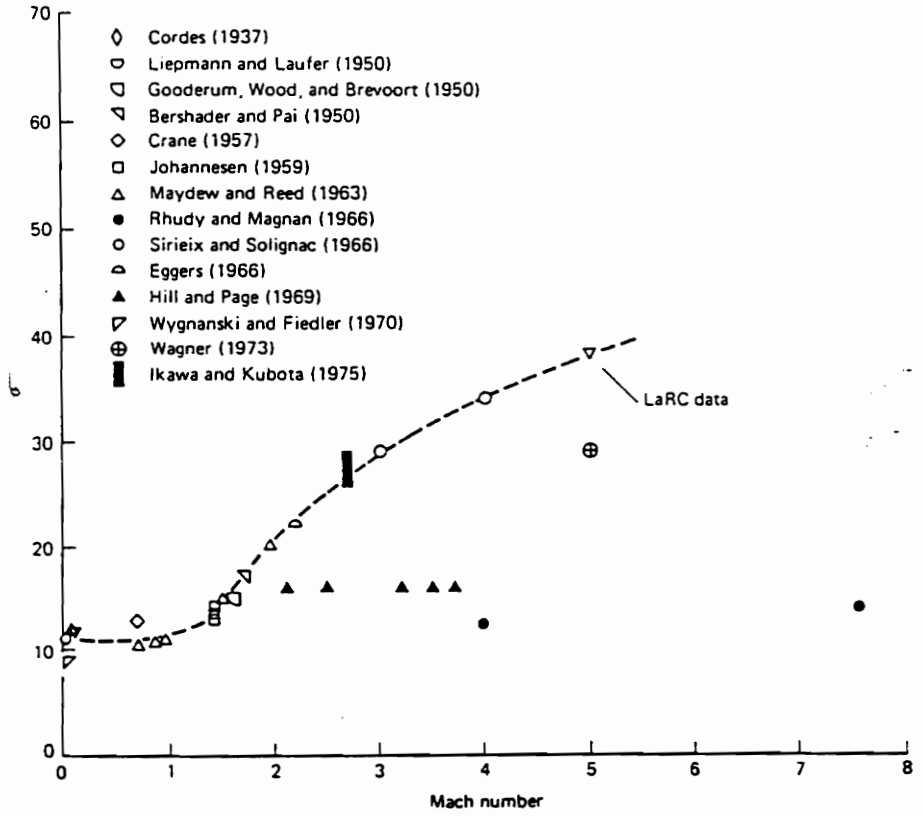

(a) Spreading Parameter

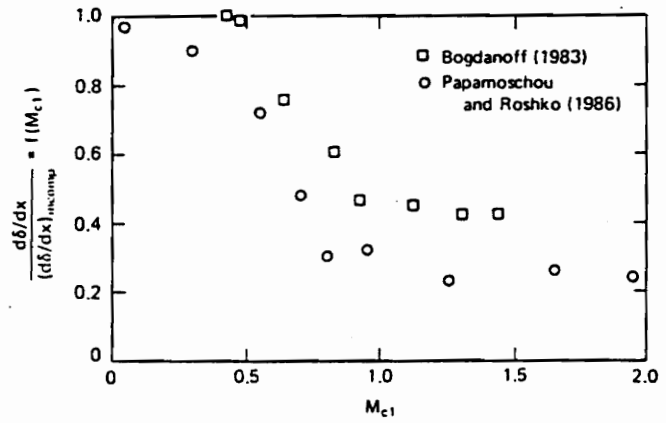

(b) Convective Mach Number

FIGURE 1.2: (a) Free shear layer spreading parameter as a function of Mach number (Birch and Eggars [10], reproduced from Schetz [6] with additional data). (b) Free shear layer spreading rate as a function of convective Mach Number (Papamoschou and Roshko [8], Bogdanoff data included by Schetz [6]).

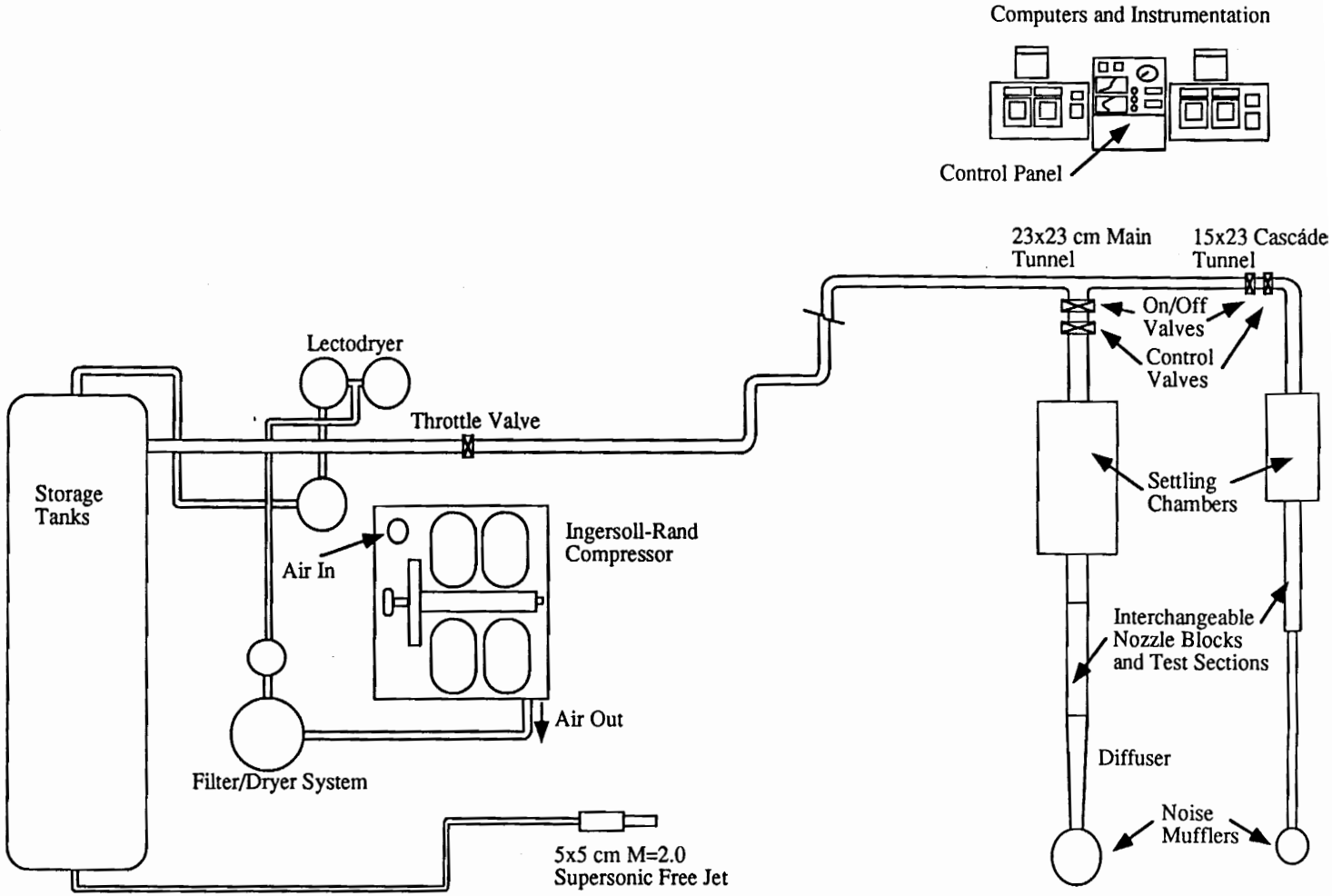

FIGURE 3.1: Schematic of the Virginia Tech Supersonic Wind tunnel Facilities.

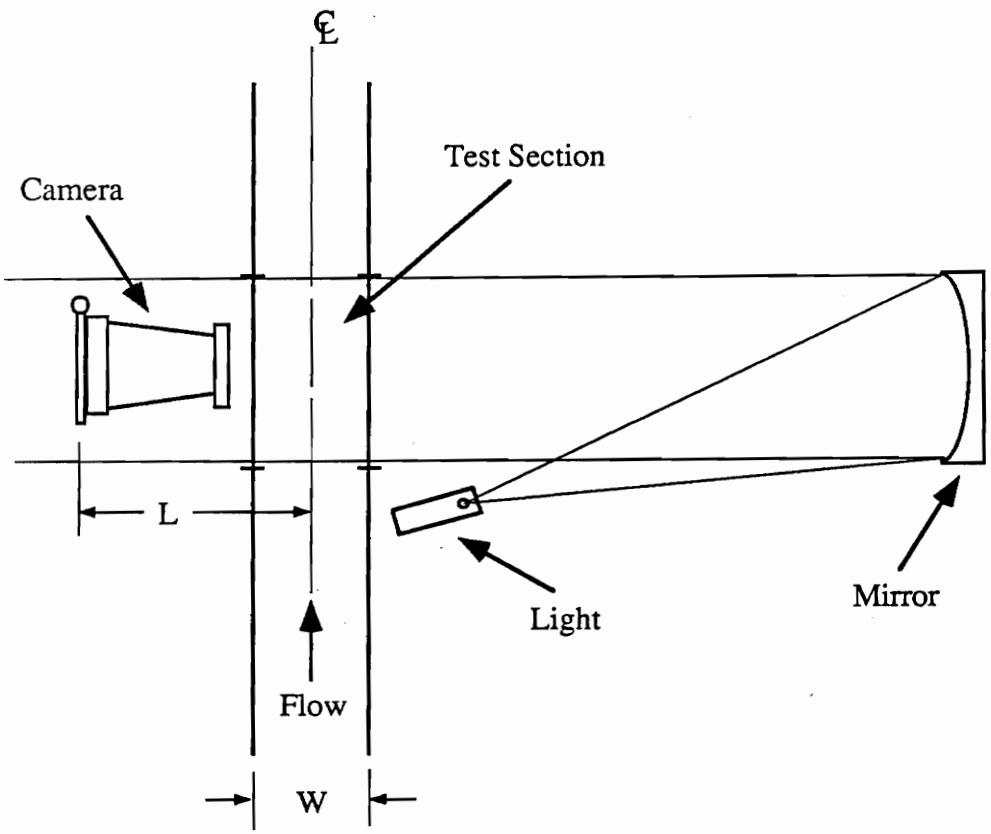

FIGURE 3.2: Schematic of the Shadowgraph optics.

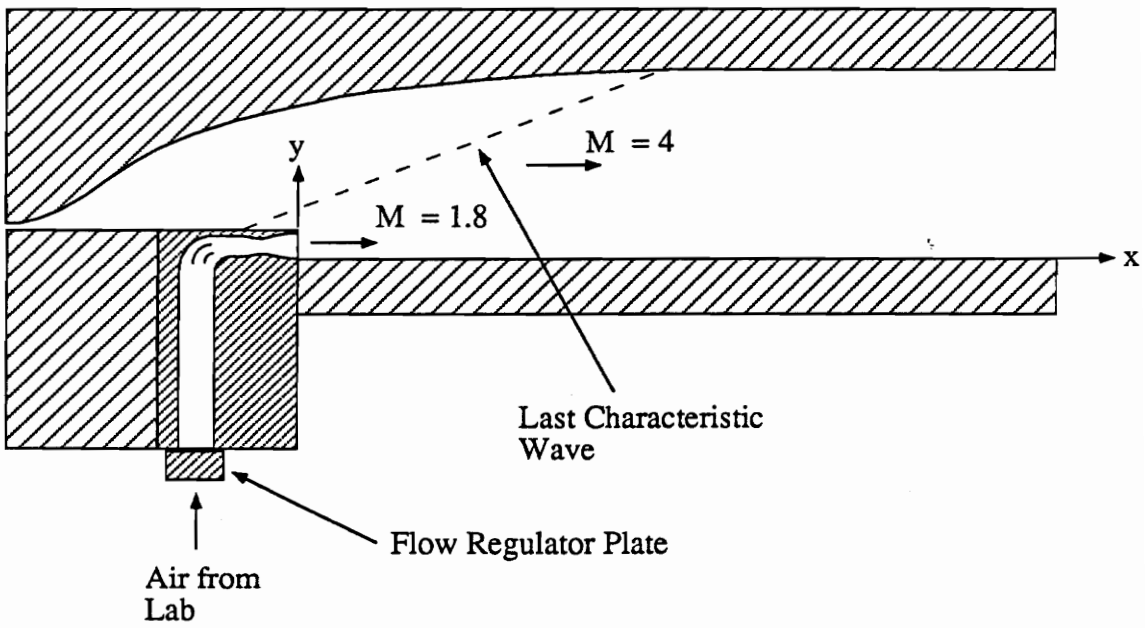

FIGURE 3.3: Sketch of the experimental arrangement.

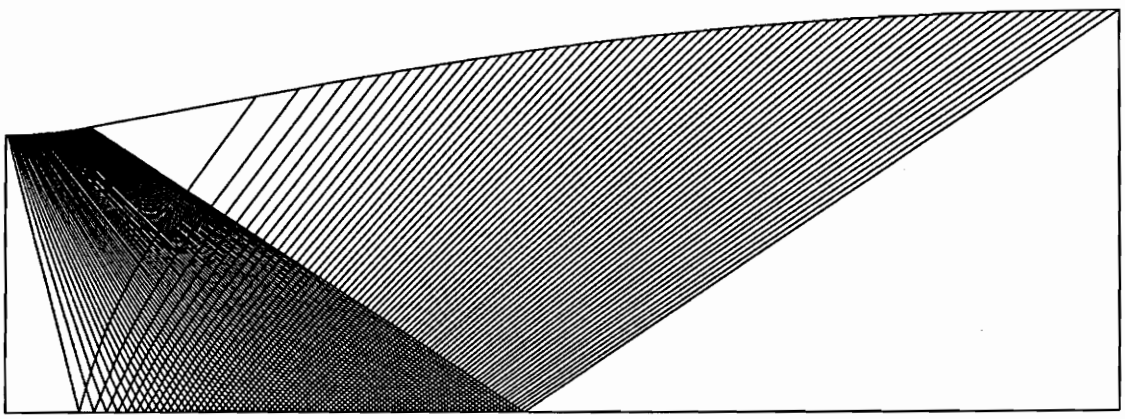

FIGURE 3.4: (a) Mach 1.8 injection model Method of Characteristics design mesh (70 waves).

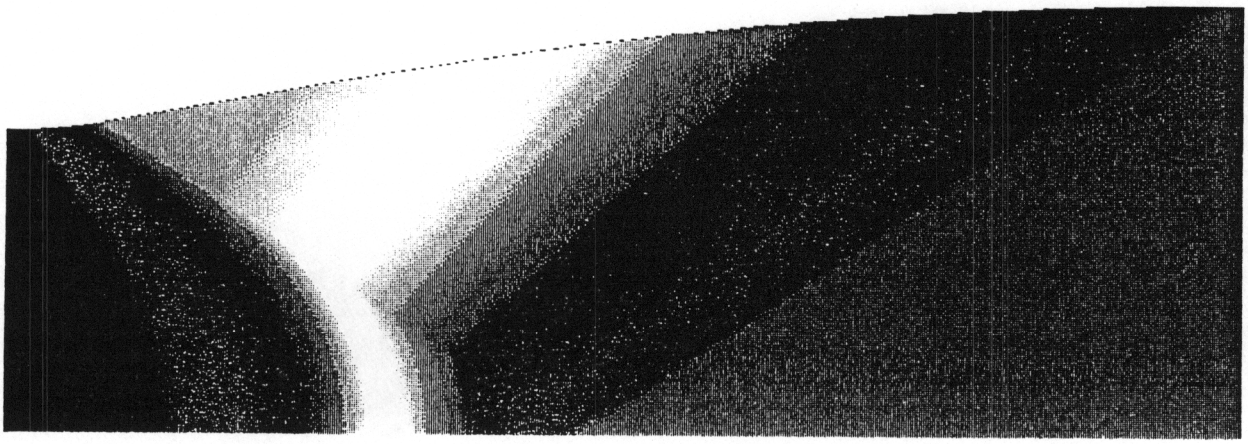

FIGURE 3.4: (b) Mach 1.8 Method of Characteristics Mach number contours.

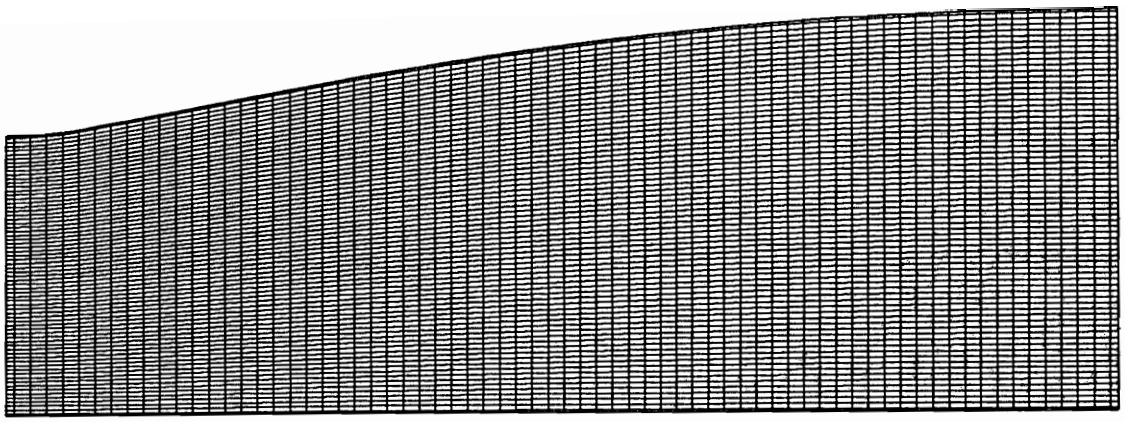

FIGURE 3.4: (c) Structured CFD grid (70x70).

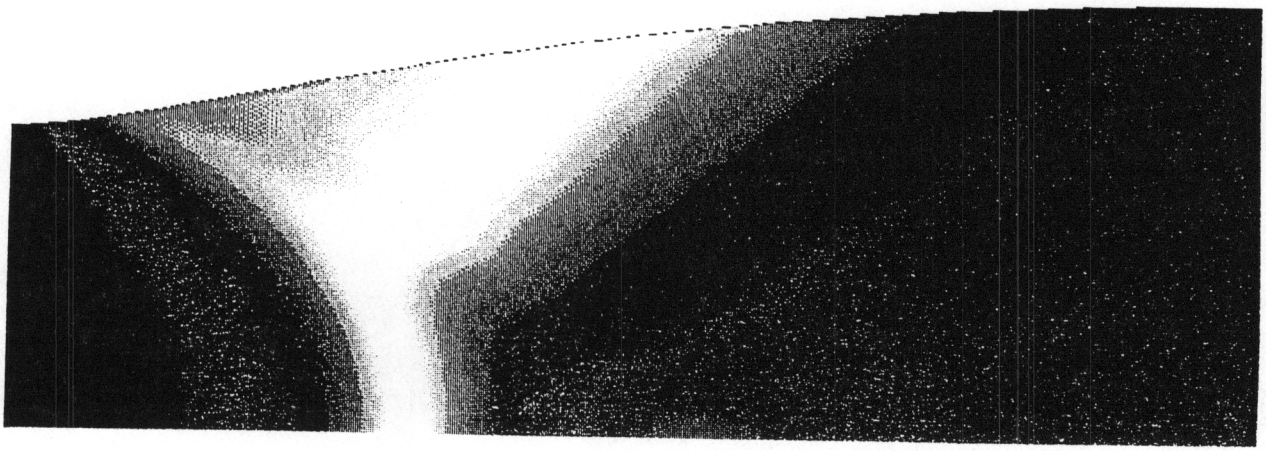

FIGURE 3.4: (d) Inviscid GASP Mach number contours.

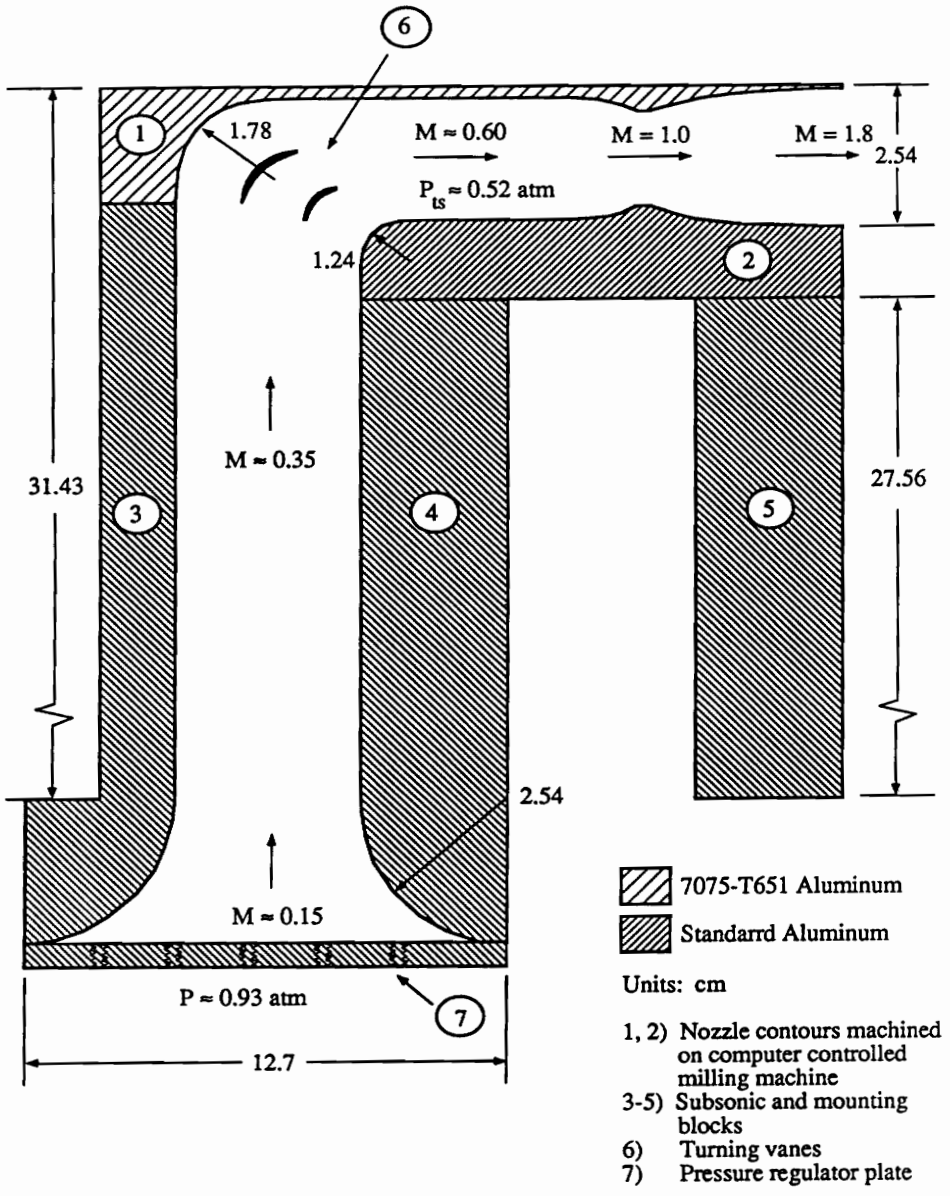

FIGURE 3.5: Sketch of the supersonic tangential injection model.

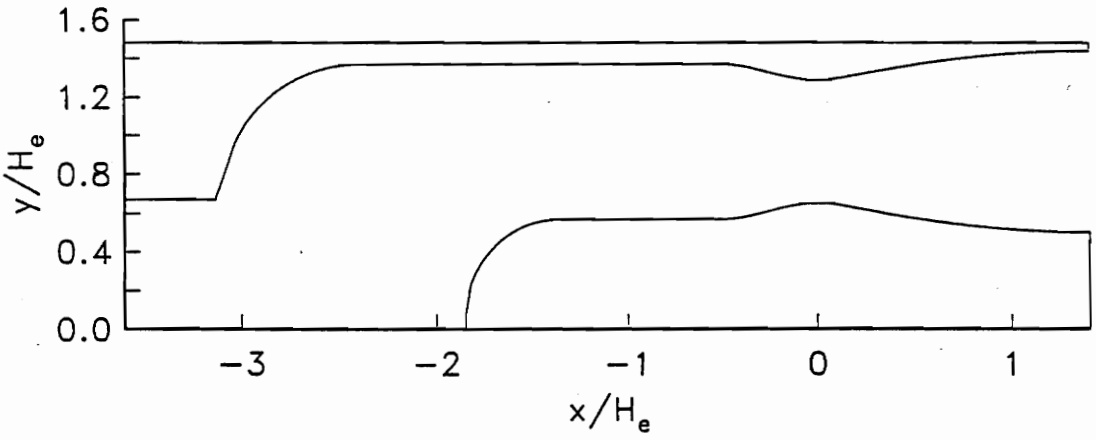

FIGURE 3.6: Plot of the two nozzle pieces (machined on a computer controlled milling machine).

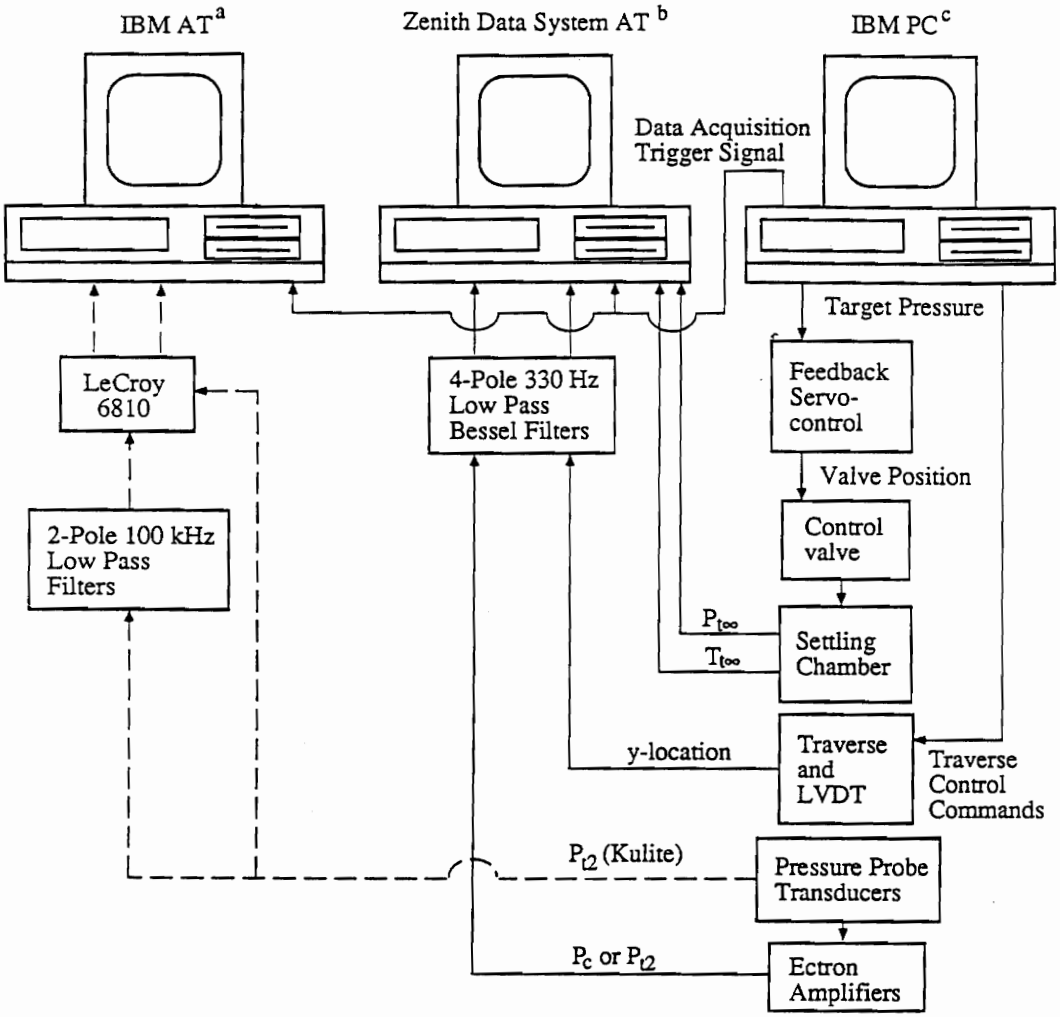

[a]Equipped with a Metrabyte DAS-16 A/D Interface and STREAMER data acquisition package.

[b]Equipped with a Metrabyte DAS-20 A/D Interface and LABTECH NOTEBOOK data acquisition package.

[c]Wind tunnel control computer, equipped with a Metrabyte DAS-16 A/D Interface and in house tunnel and acquisition control software.

FIGURE 3.7: Diagram of the mean flow data acquisition.

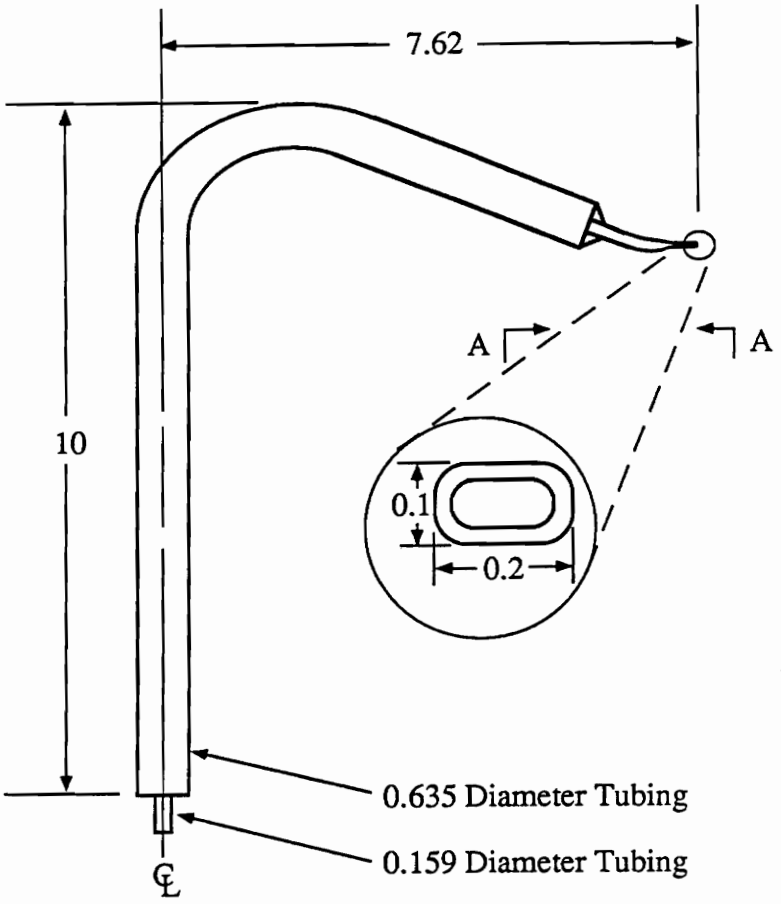

Units: cm
Material: Stainless Steel
Not to Scale

FIGURE 3.8: (a) Sketch of conventional Pitot pressure probe.

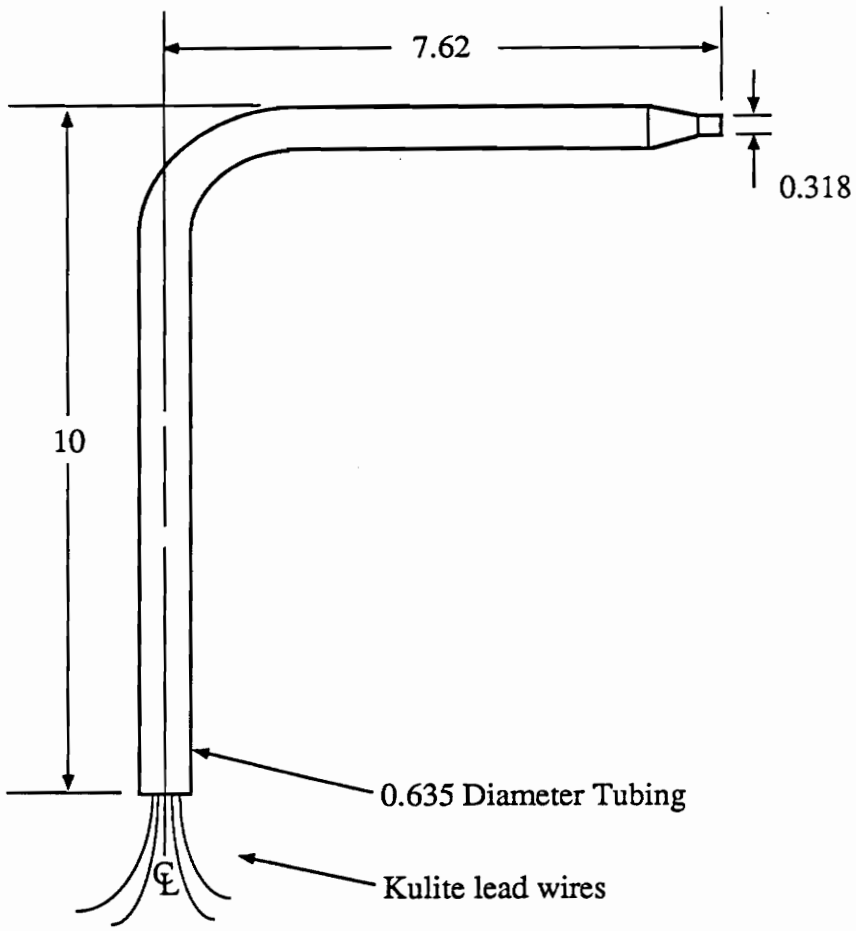

Units: cm
Material: Stainless Steel
Not to Scale

FIGURE 3.8: (b) Sketch of high frequency response Kulite Pitot pressure probe.

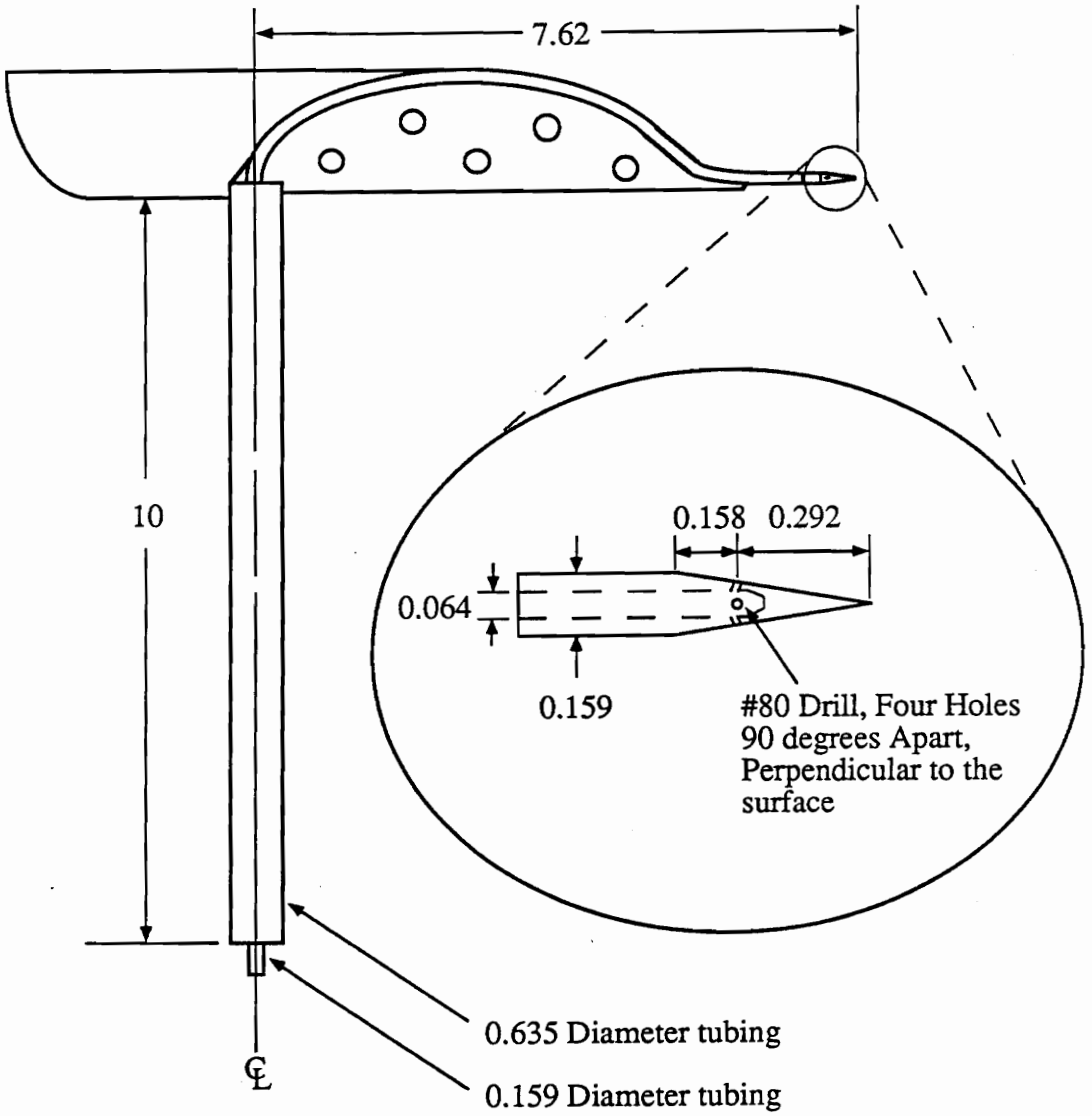

Units: cm
Material:
(1) Housing: Stainless Steel
(2) Cone tip: Brass
Not to Scale

FIGURE 3.8: (c) Sketch of the 10° semivertex angle cone-static pressure probe.

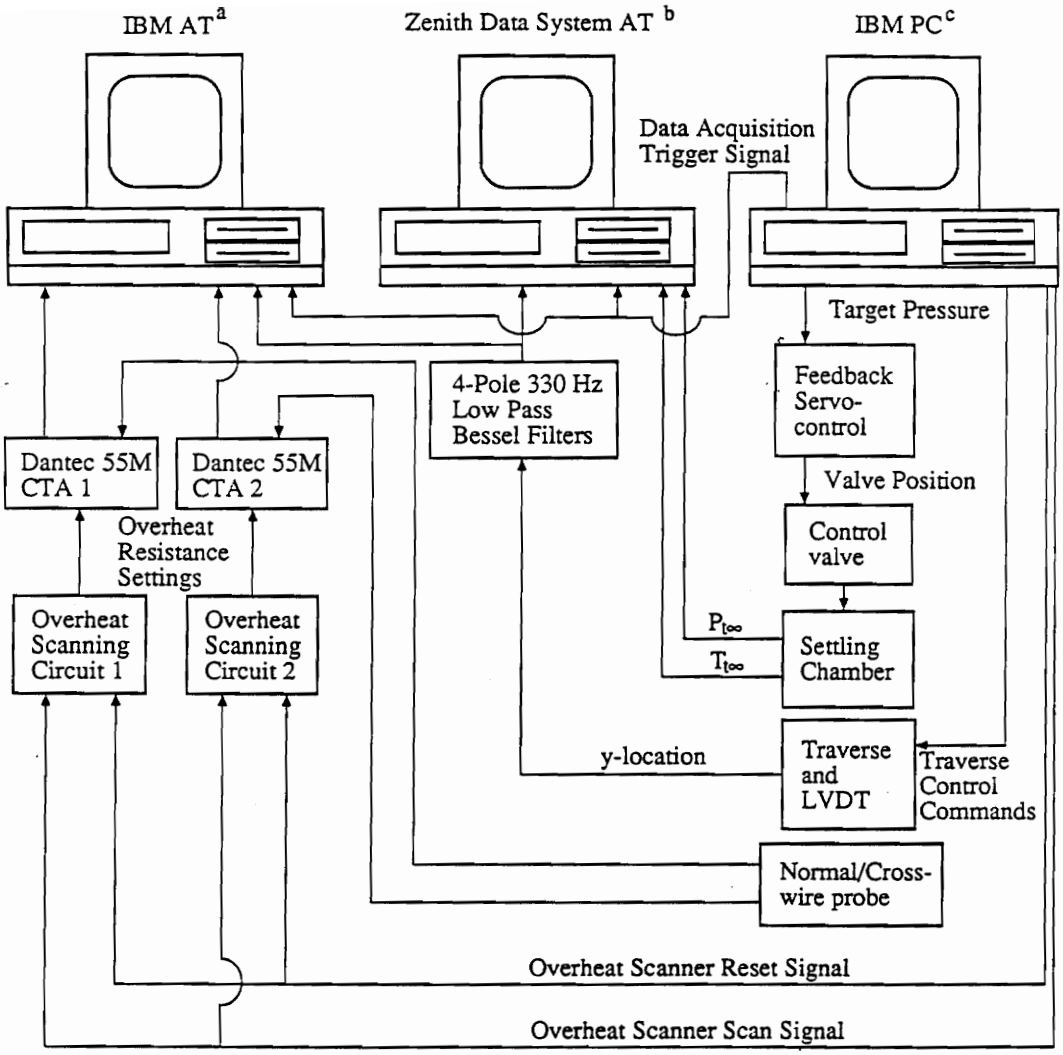

[a] Equipped with a Metrabyte DAS-16 A/D Interface and STREAMER data acquisition package.

[b] Equipped with a Metrabyte DAS-20 A/D Interface and LABTECH NOTEBOOK data acquisition package.

[c] Wind tunnel control computer, equipped with a Metrabyte DAS-16 A/D Interface and in house tunnel and acquisition control software.

FIGURE 3.9: Diagram of the hot-wire data acquisition.

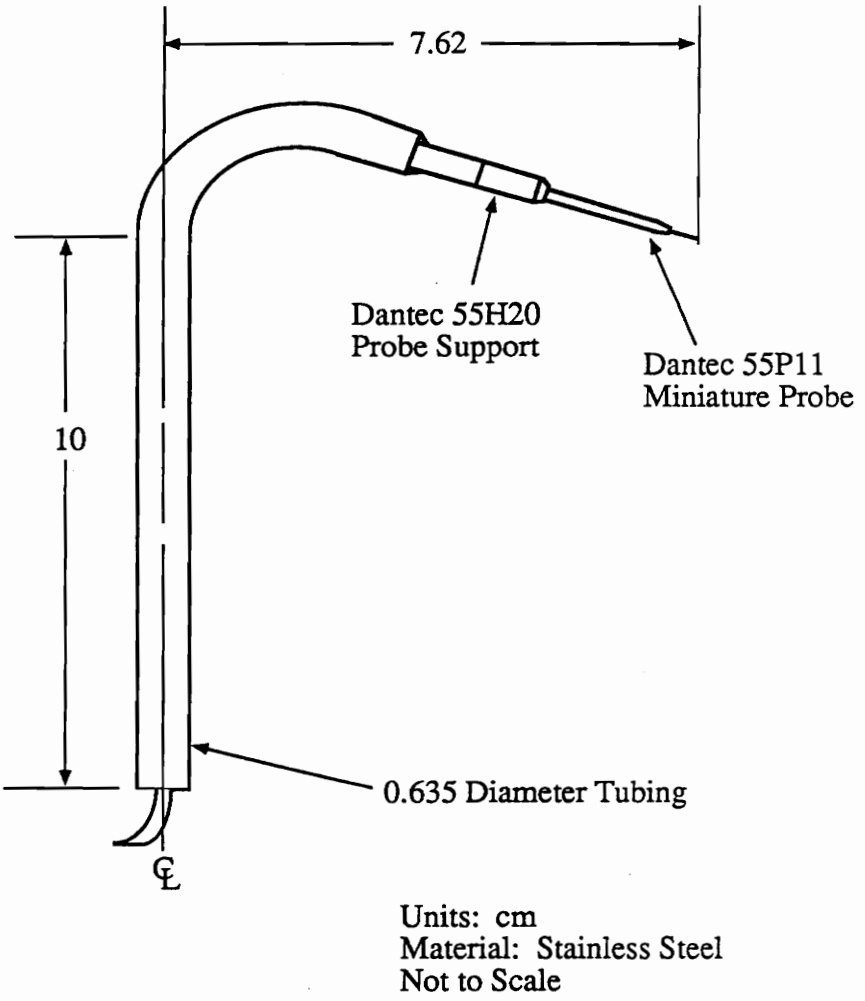

FIGURE 3.10: (a) Sketch of the normal-wire probe.

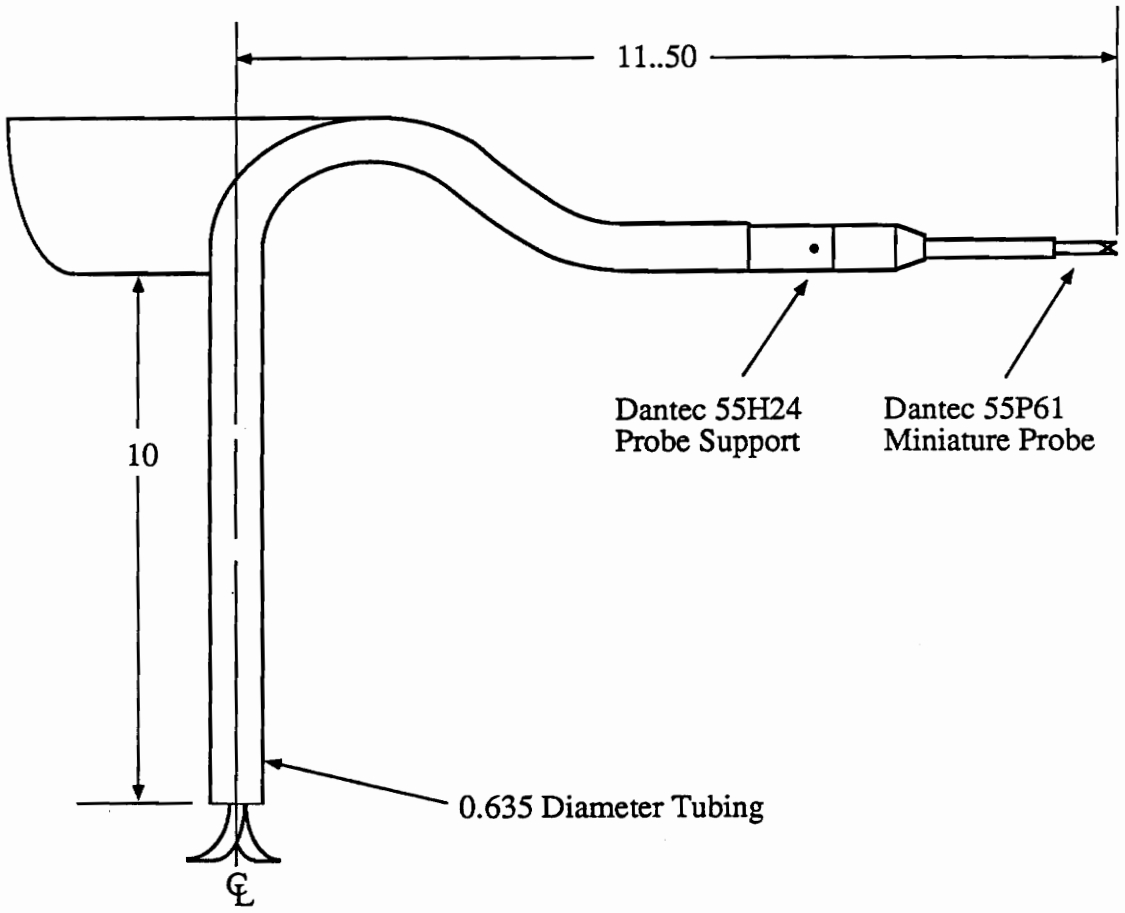

FIGURE 3.10: (b) Sketch of the cross-wire probe.

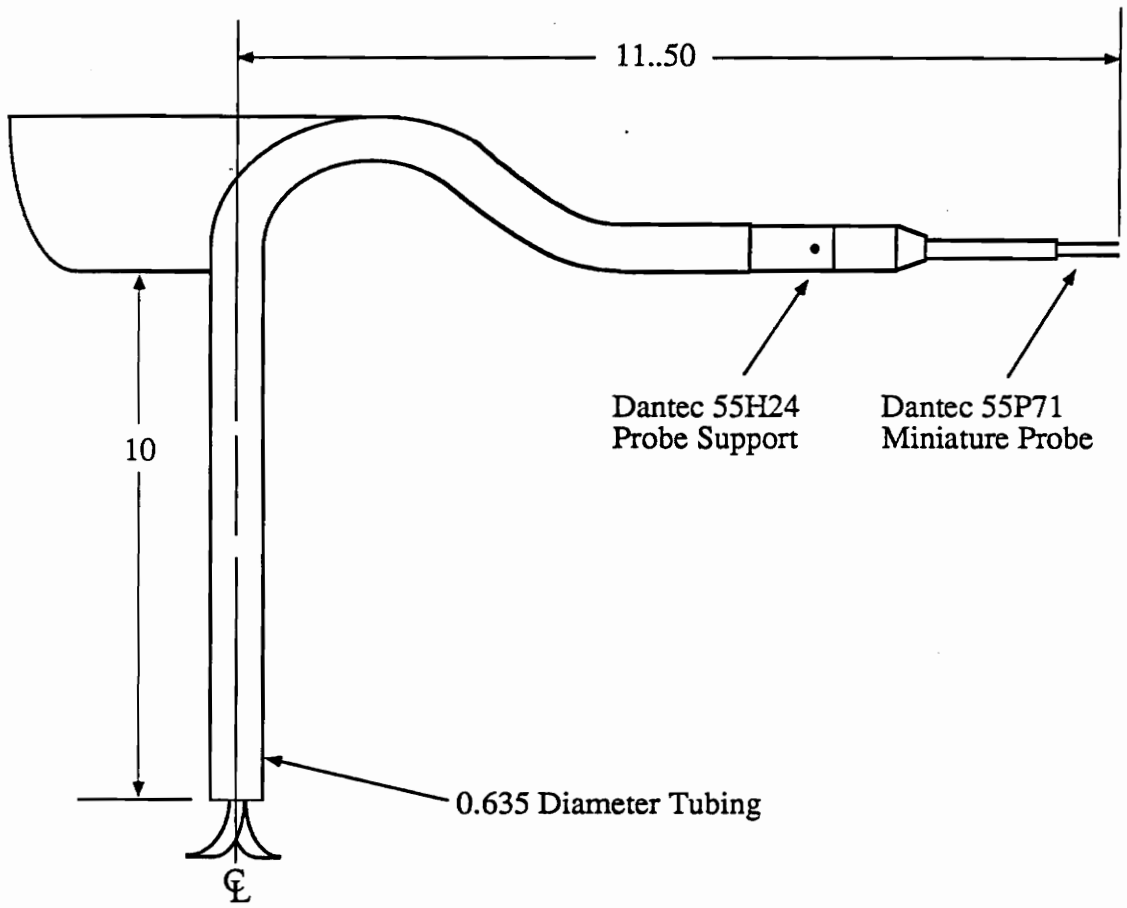

Units: cm
Material: Stainless Steel
Not to Scale

FIGURE 3.10: (c) Sketch of the parallel-wire probe.

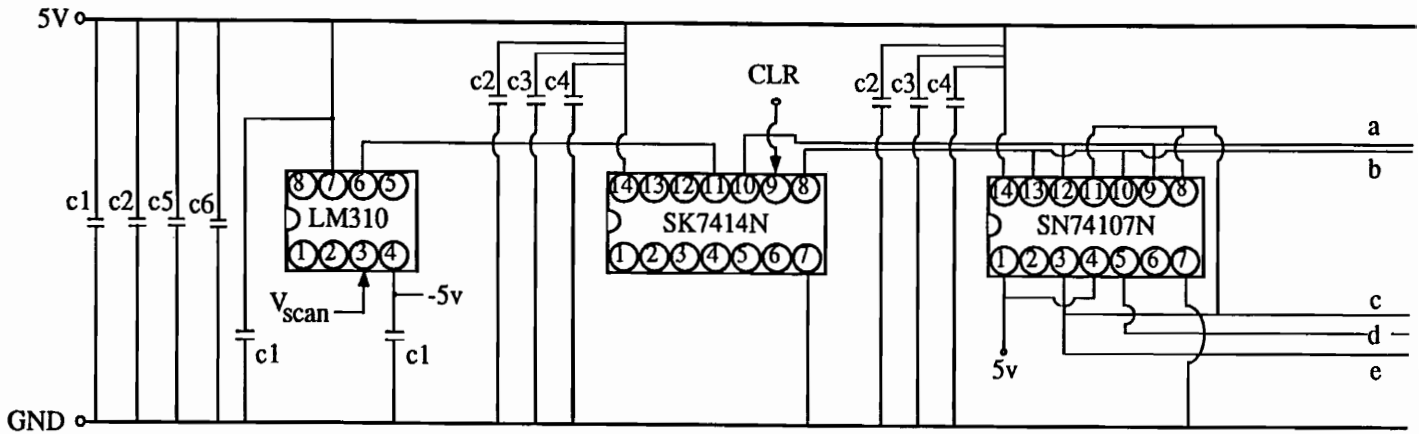

c	µF
1	220 E
2	0 .01
3	1 T
4	100 E
5	470 E
6	10 E

R = 110 Ohms

All 16 Volt

FIGURE 3.11: (a) Schematic of buffer and TTL counter multiple overheat scanning circuit.

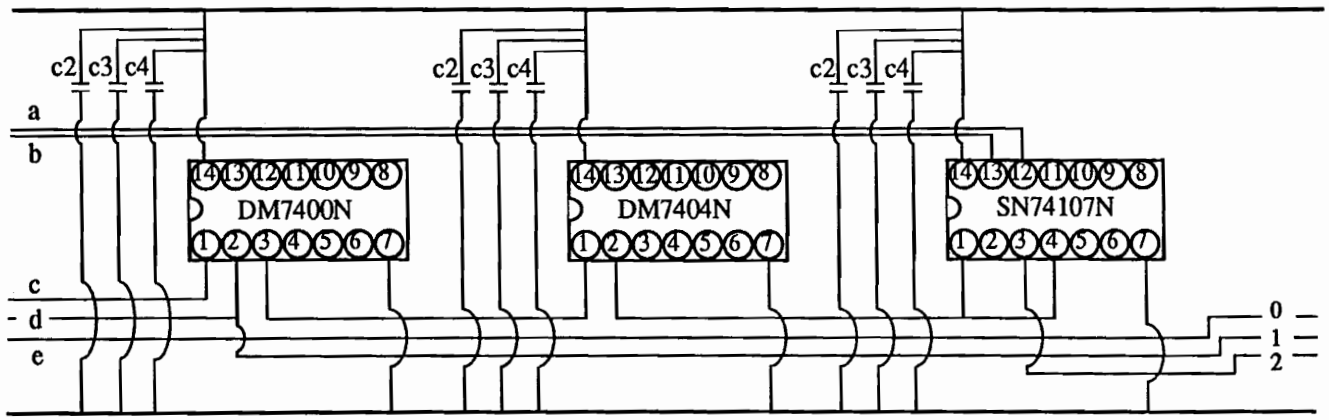

FIGURE 3.11: (a) continued.

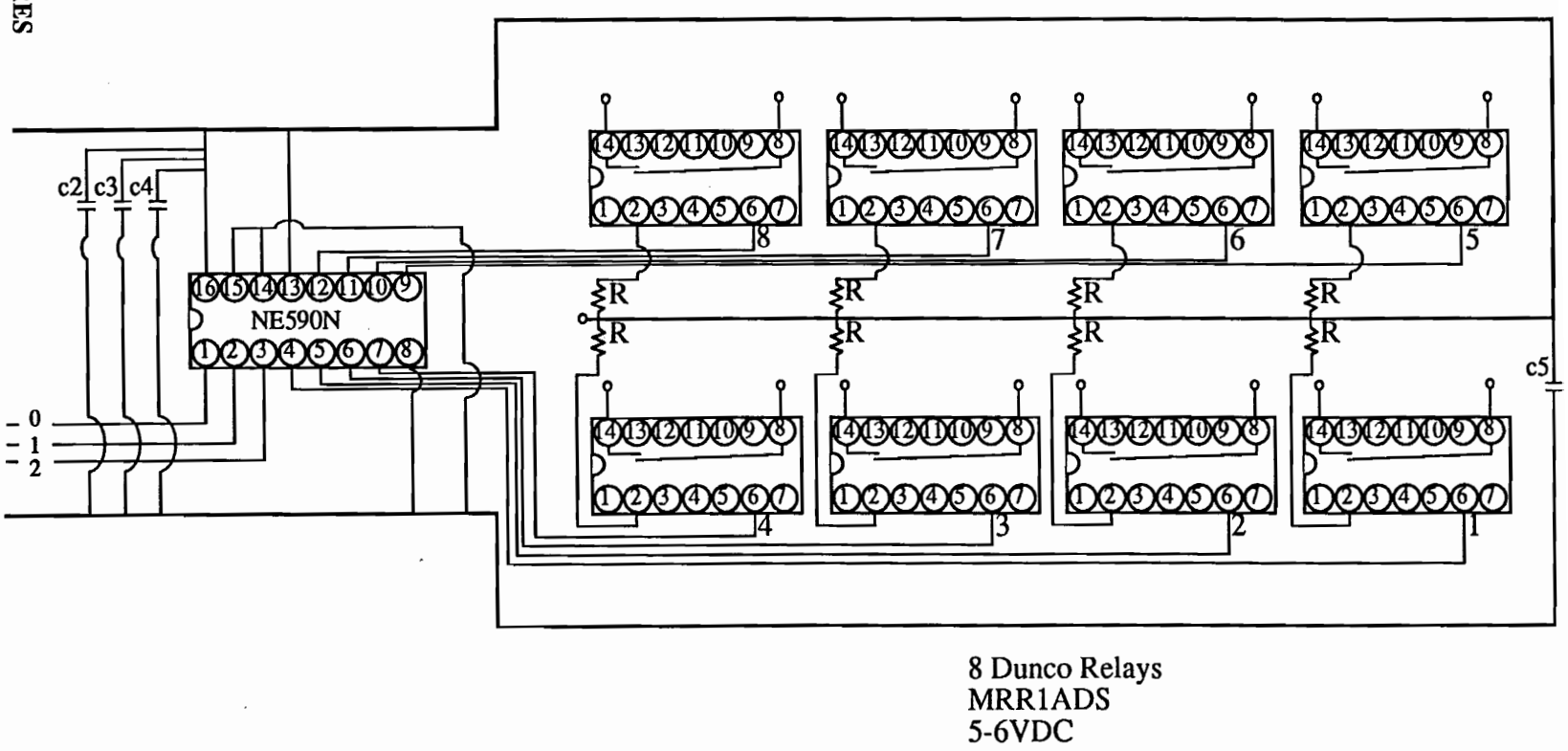

FIGURE 3.11: (b) Multiple overheat scanner peripheral driver and relay schematic.

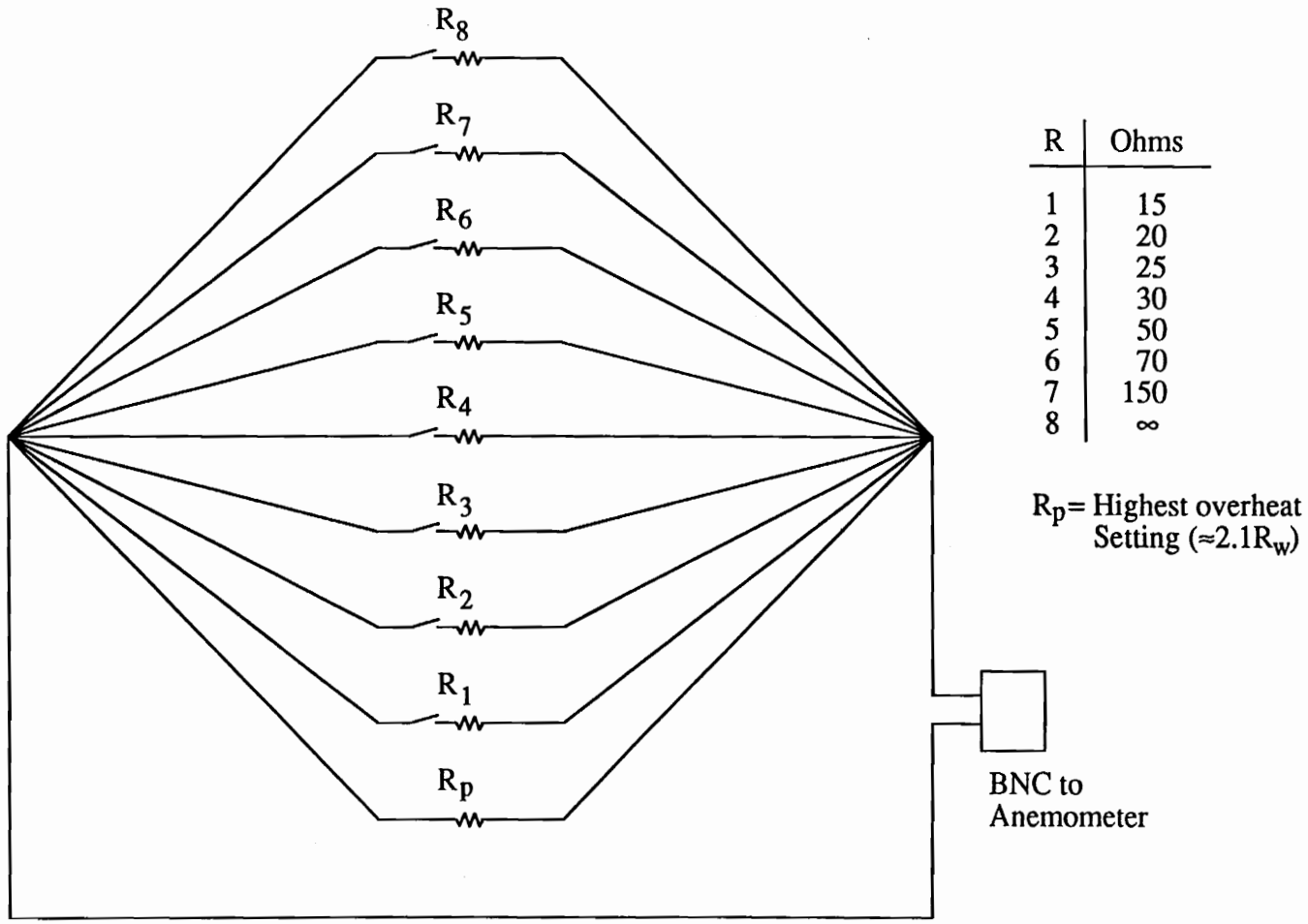

FIGURE 3.11: (c) R_p parallel resistor "pull down" schematic.

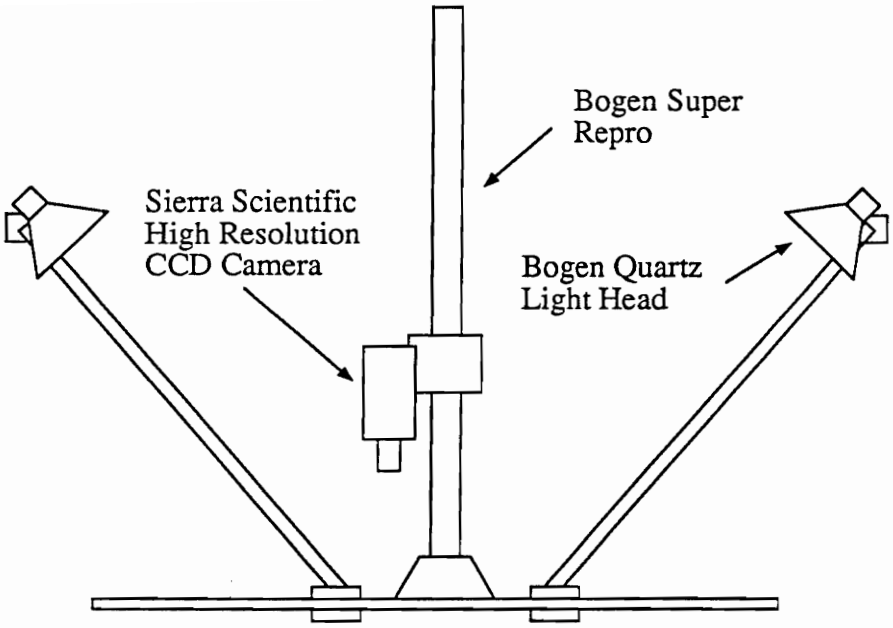

Front View

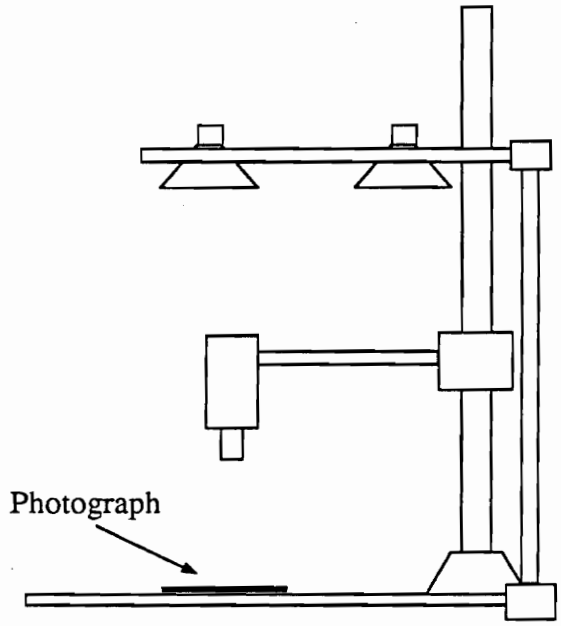

Side View

FIGURE 3.12: Schematic of SDA image processing hardware.

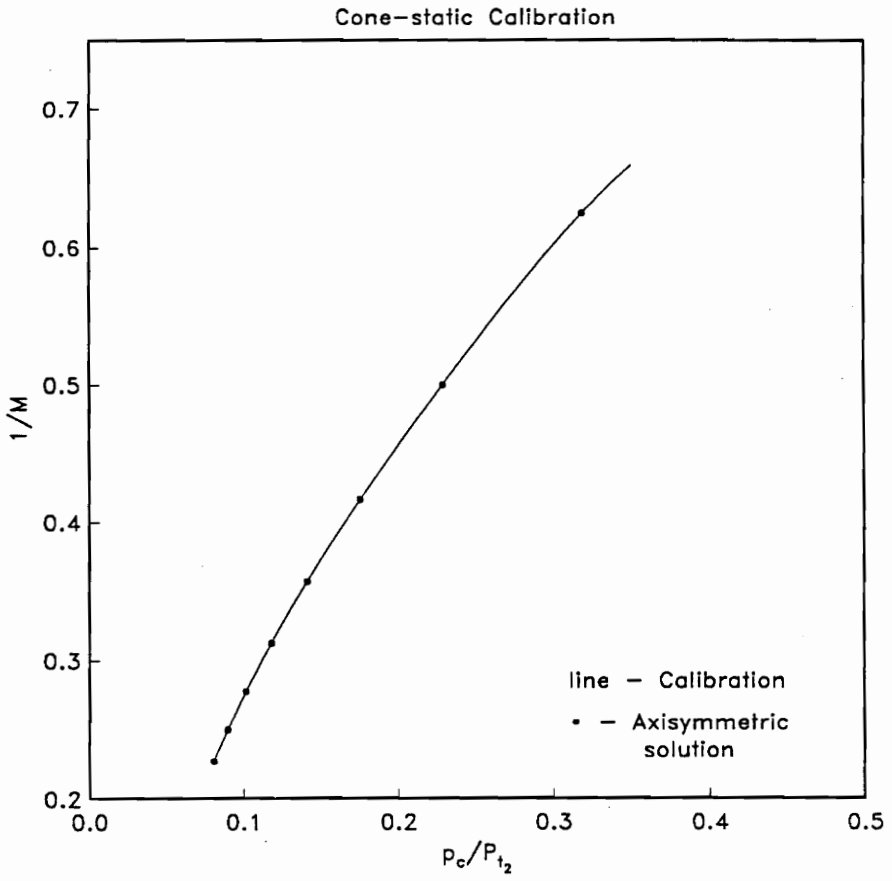

FIGURE 4.1: Cone-static/Pitot pressure verses Mach number (calibration Eqn. (4.1)).

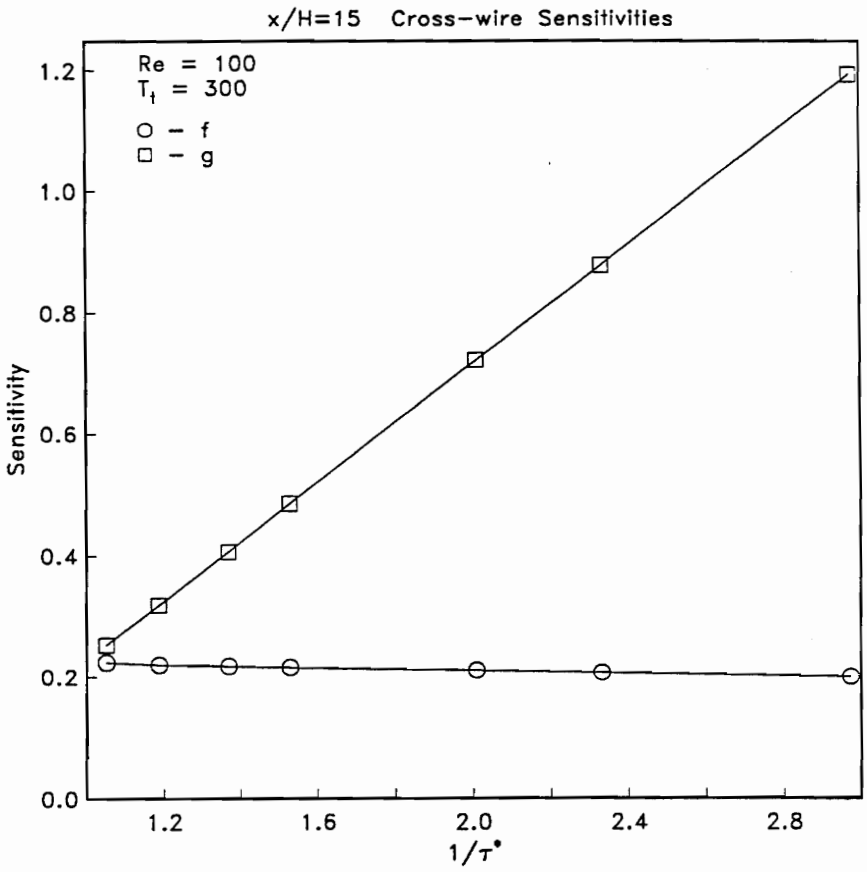

FIGURE 4.2: Cross-wire sensitivities versus the "new" equilibrium temperature wire loading for nominal conditions.

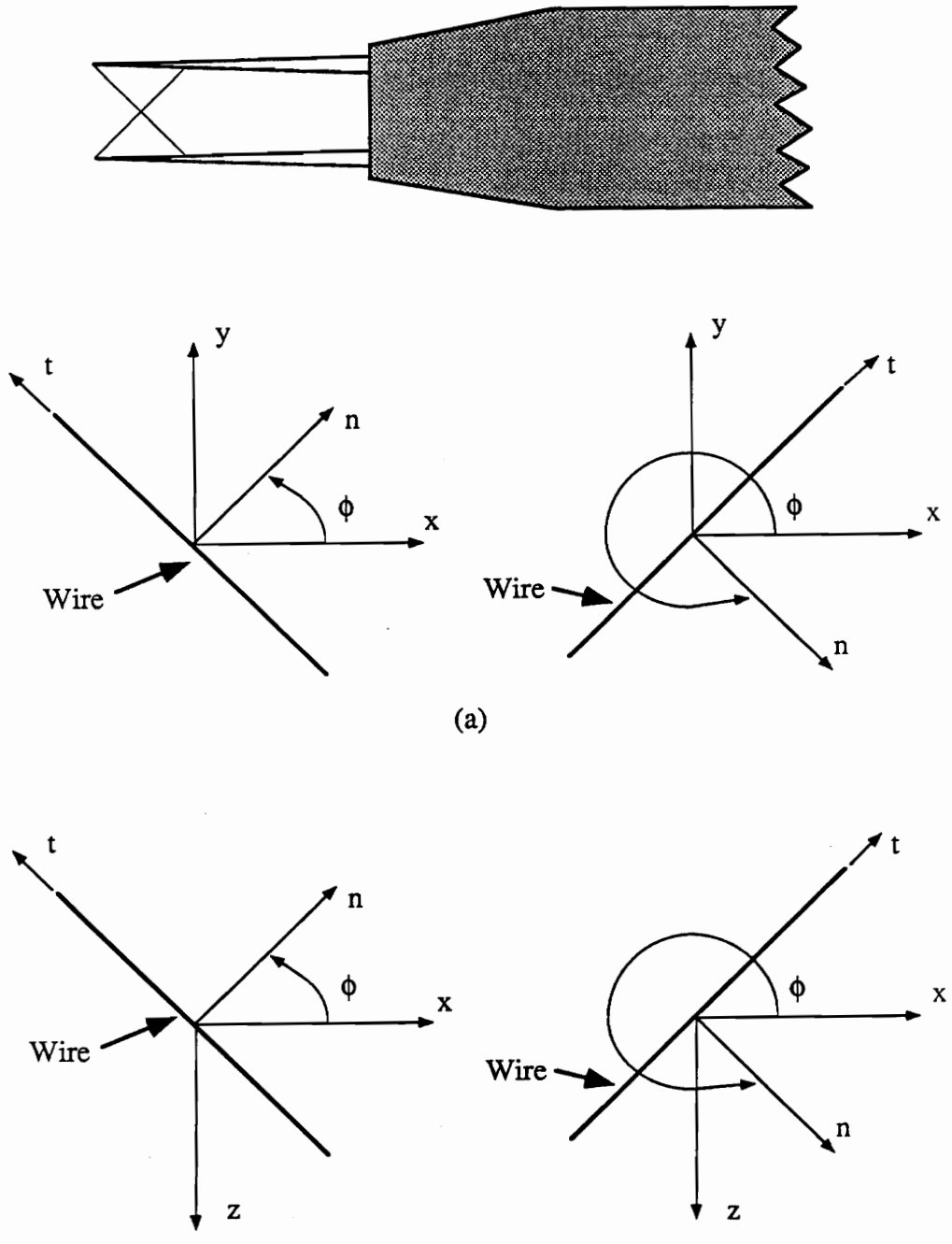

FIGURE 4.3: Cross-wire angle definitions.

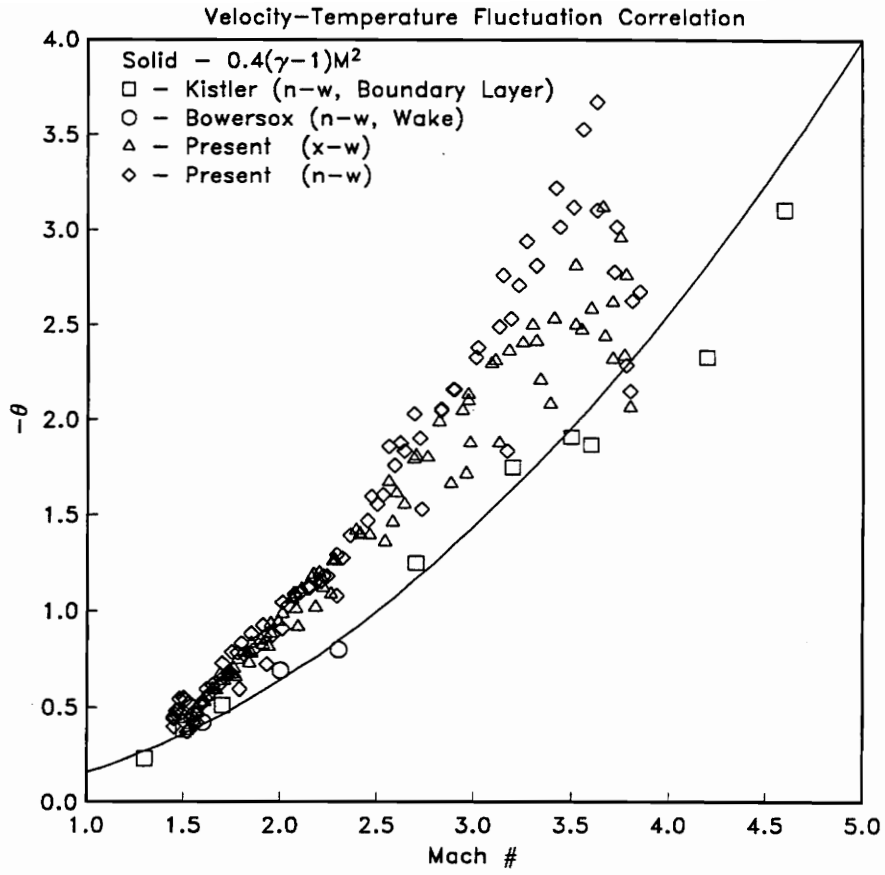

FIGURE 4.4: Single overheat hot-wire relaxed Crocco total temperature correction technique temperature-velocity correlation (Bowersox [55] with the addition of the present study data).

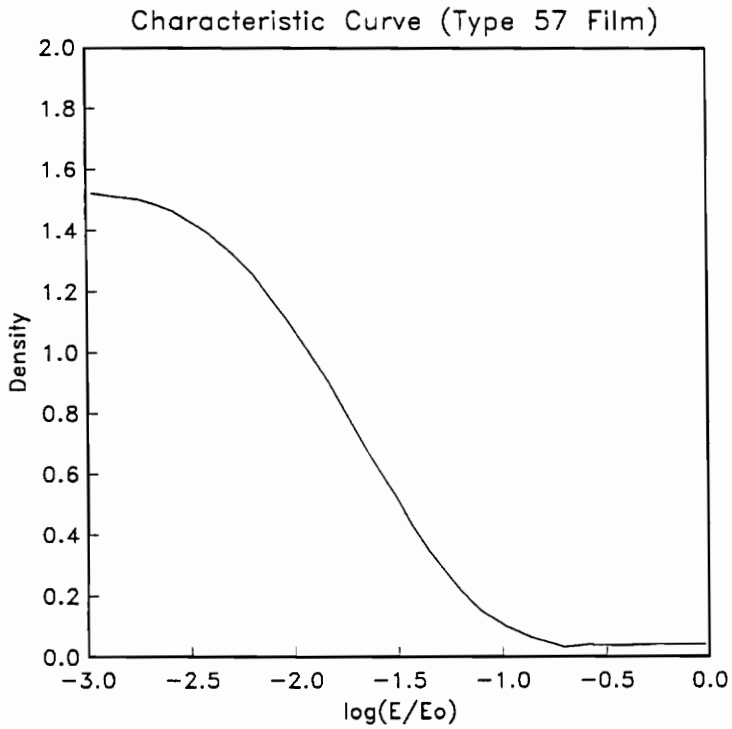

FIGURE 4.5: (a) Characteristic Curve (Polaroid Type 57 [70]).

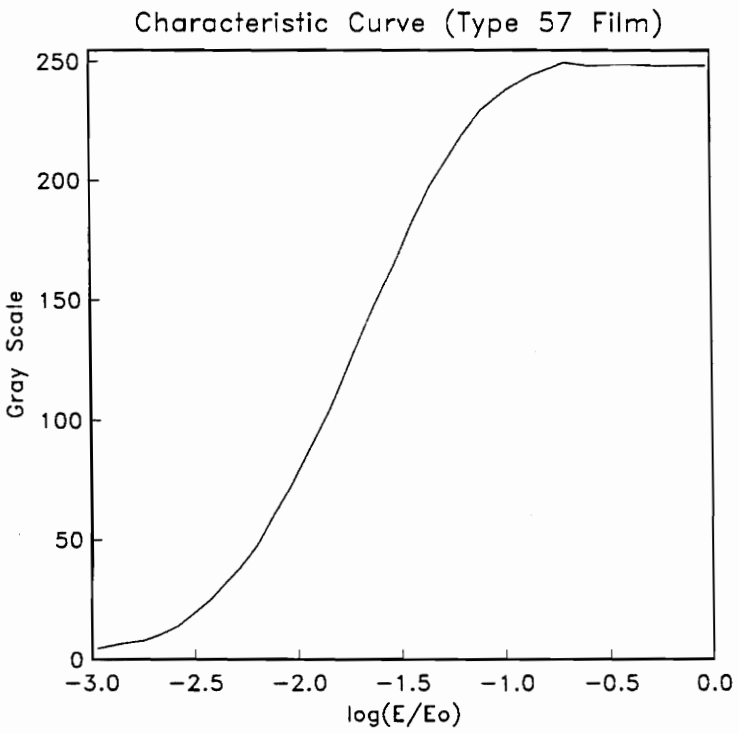

FIGURE 4.5: (b) Gray scale "Characteristic" curve (converted from Fig. 4.5(a)).

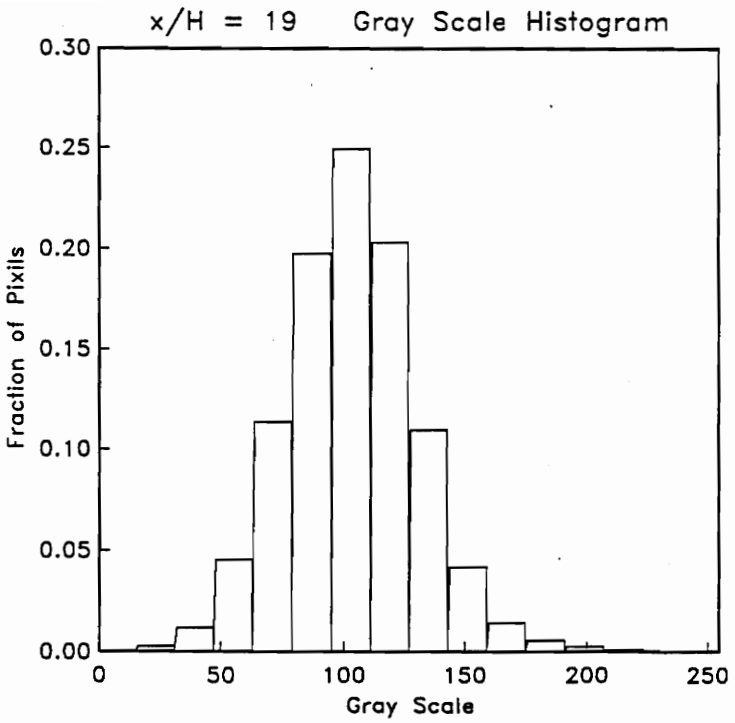

FIGURE 4.6: (a) Typical Shadowgraph gray scale histogram (x/H = 19).

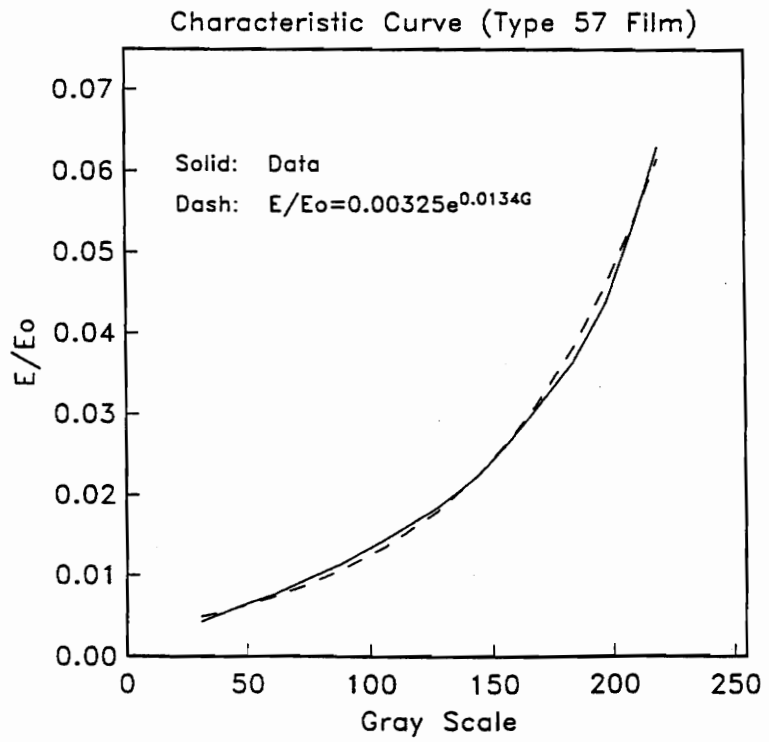

FIGURE 4.6: (b) Exponential curve fit to the gray scale characteristic curve.

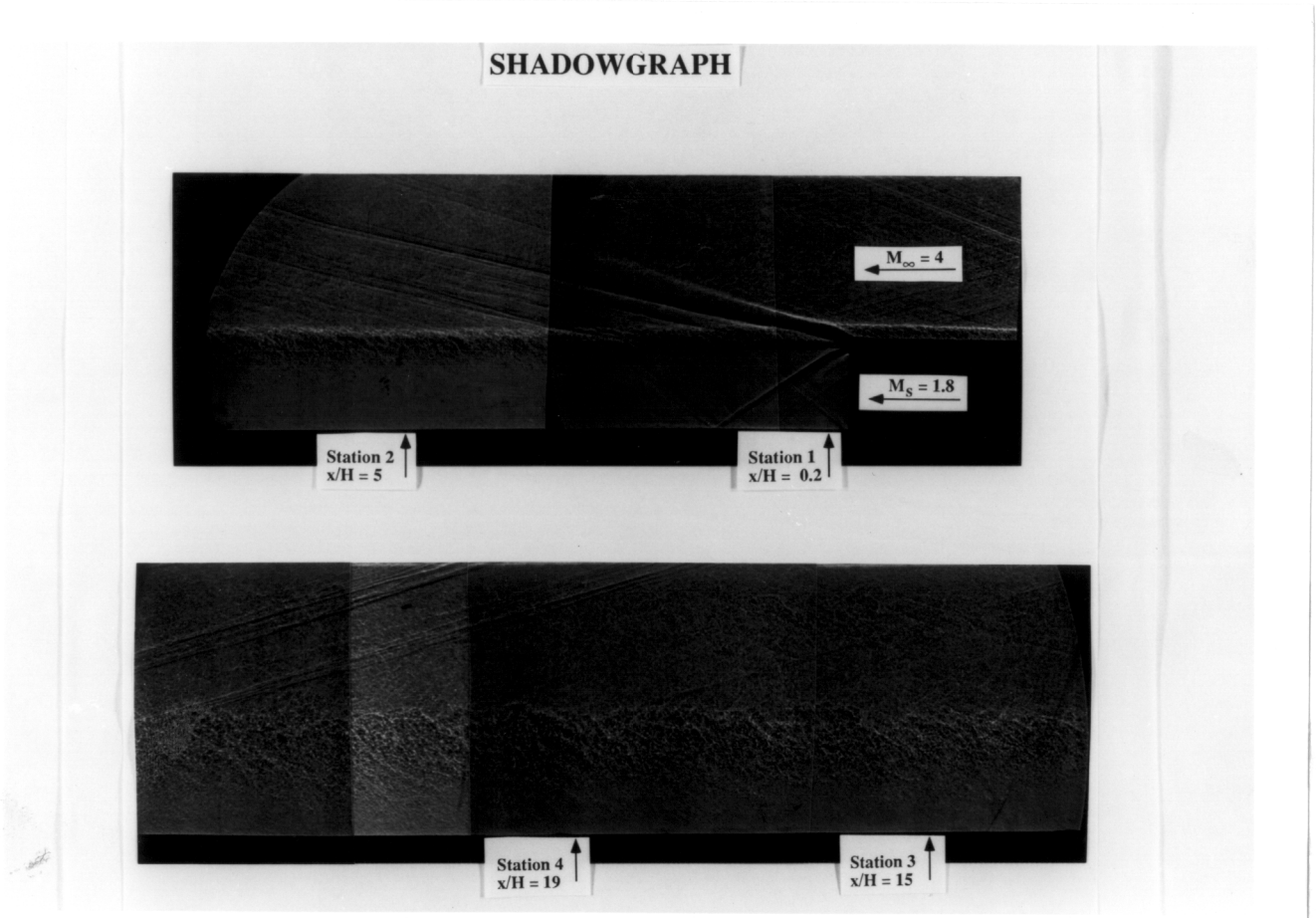

FIGURE 5.1: 20 nanosecond composite Shadowgraph.

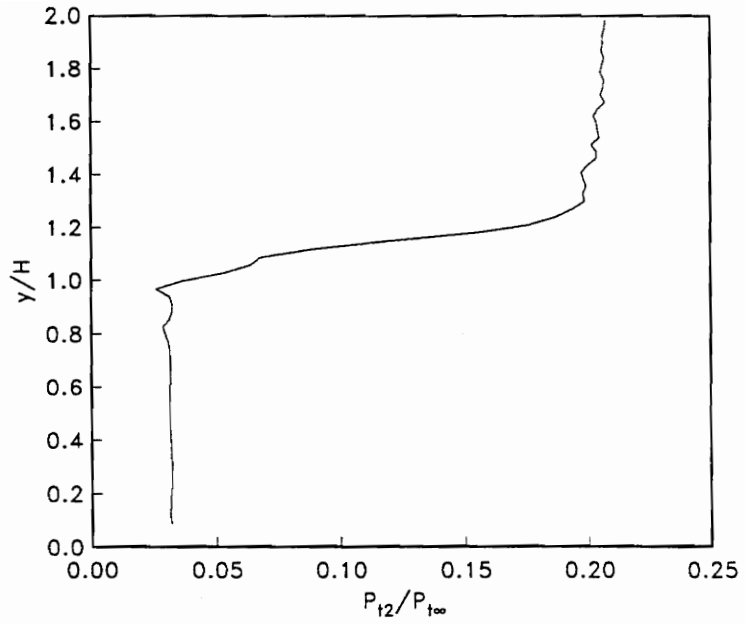

(a) Pitot Pressure

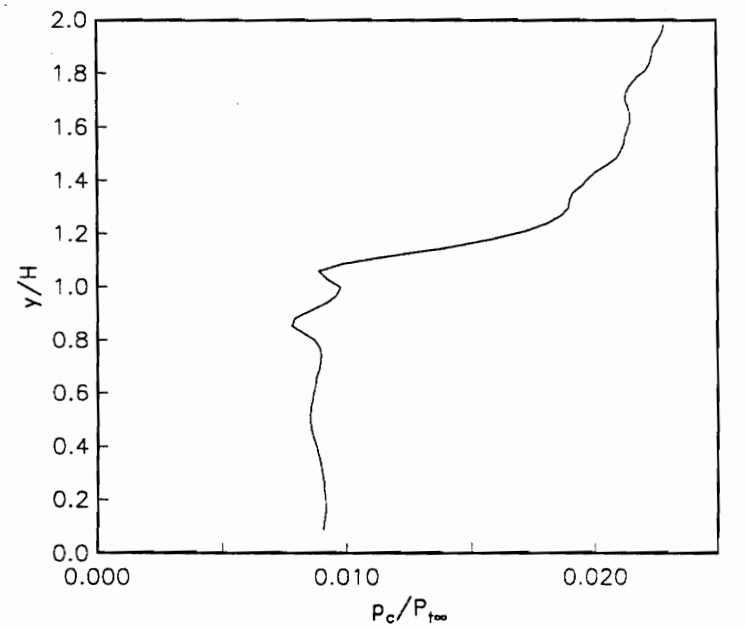

(b) Cone–Static Pressure

FIGURE 5.2: Conventional mean flow Pitot and cone-static pressure data (x/H = 0.2).

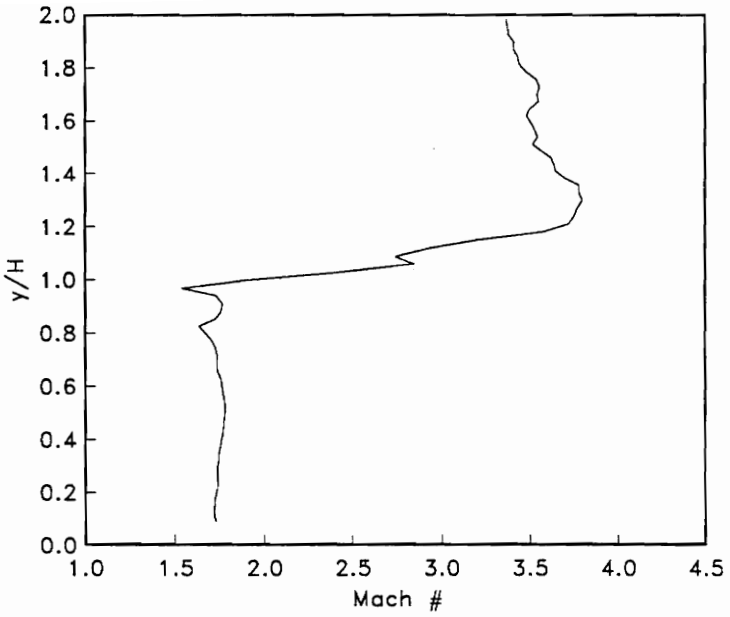

(a) Mach Number

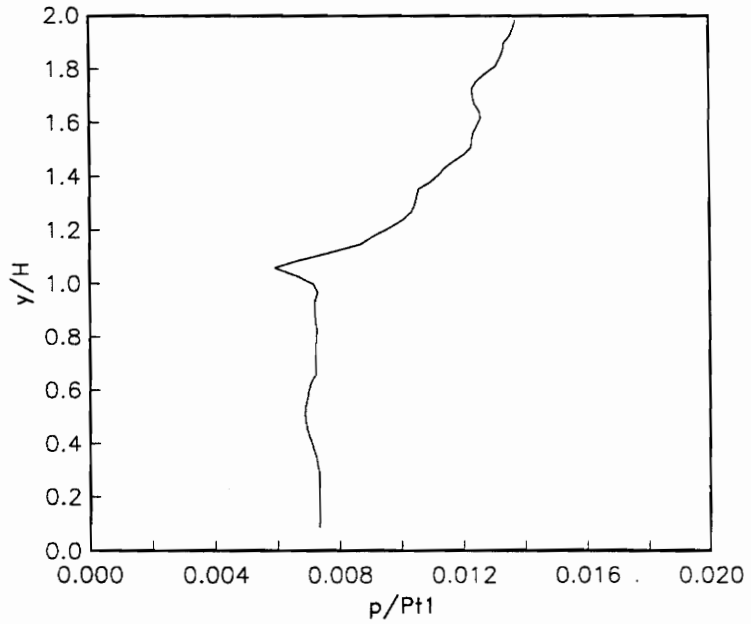

(b) Static Pressure

FIGURE 5.3: Conventional mean flow Mach number and static pressure data (x/H = 0.2).

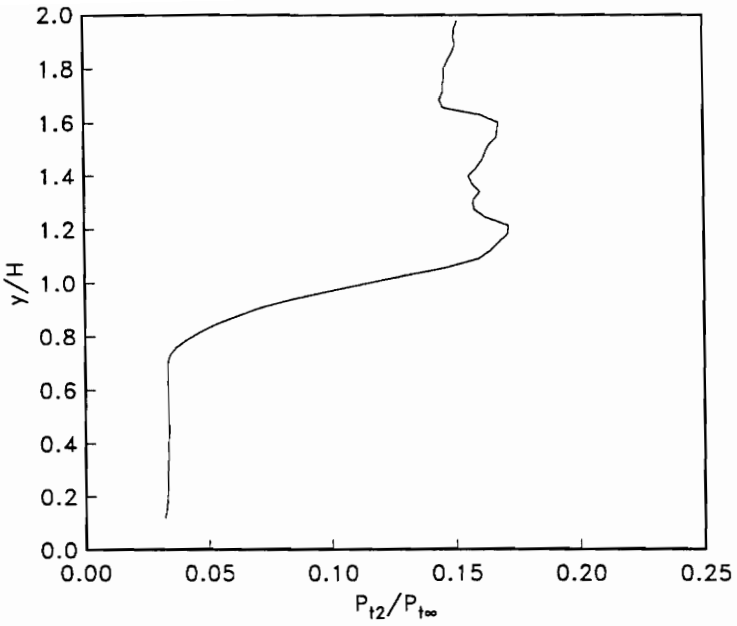

(a) Pitot Pressure

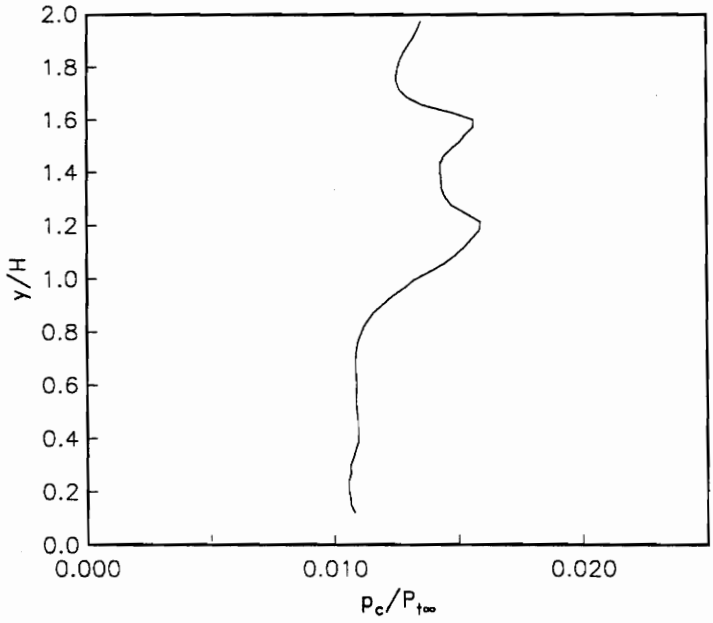

(b) Cone–Static Pressure

FIGURE 5.4: Conventional mean flow Pitot and cone-static pressure data (x/H = 5).

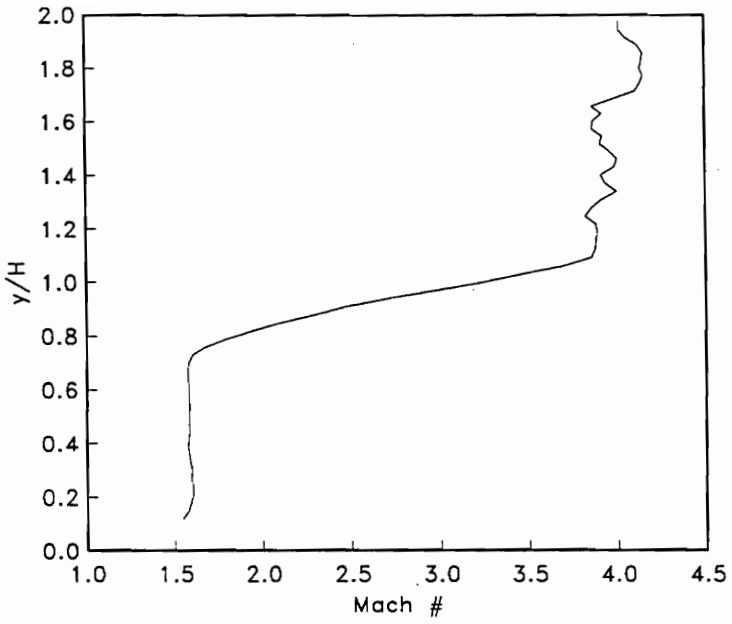

(a) Mach Number

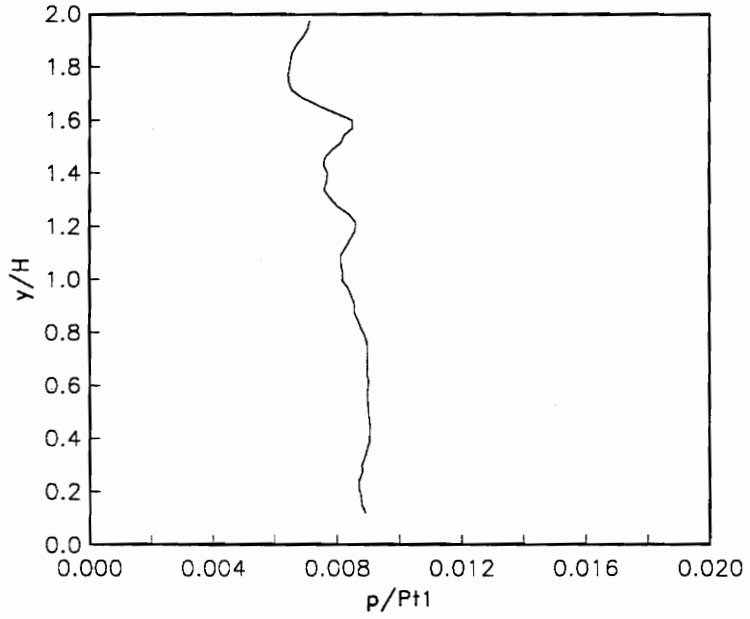

(b) Static Pressure

FIGURE 5.5: Conventional mean flow Mach number and static pressure data (x/H = 5).

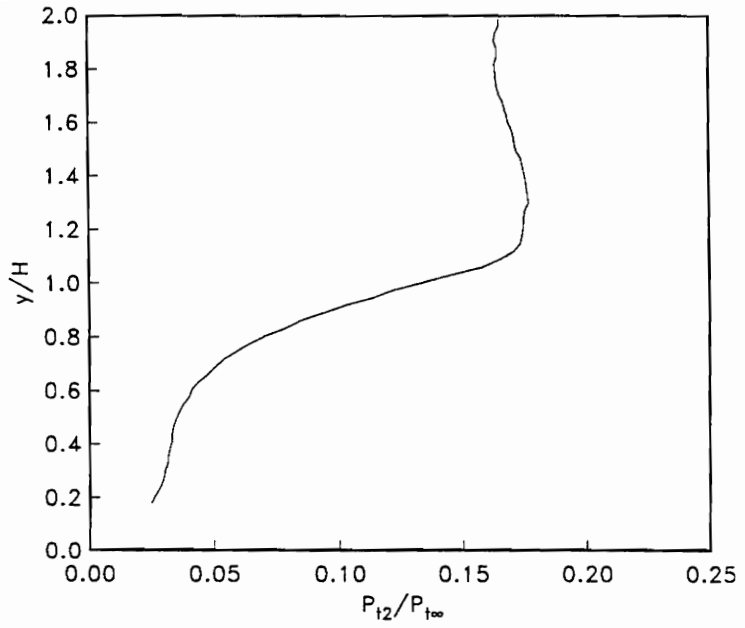

(a) Pitot Pressure

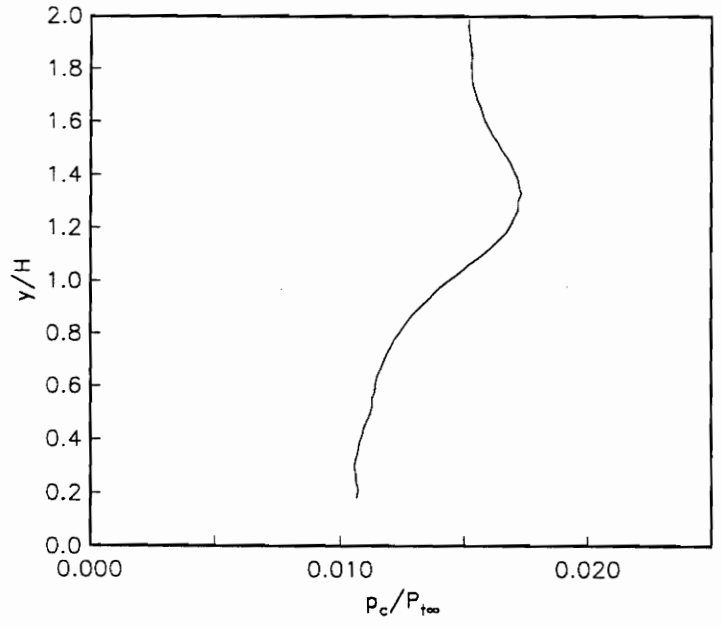

(b) Cone–Static Pressure

FIGURE 5.6: Conventional mean flow Pitot and cone-static pressure data (x/H = 15).

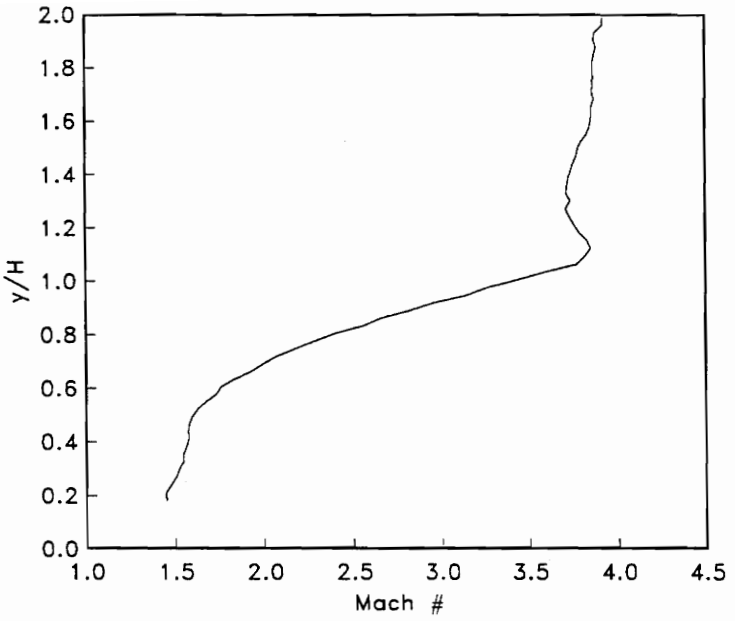

(a) Mach Number

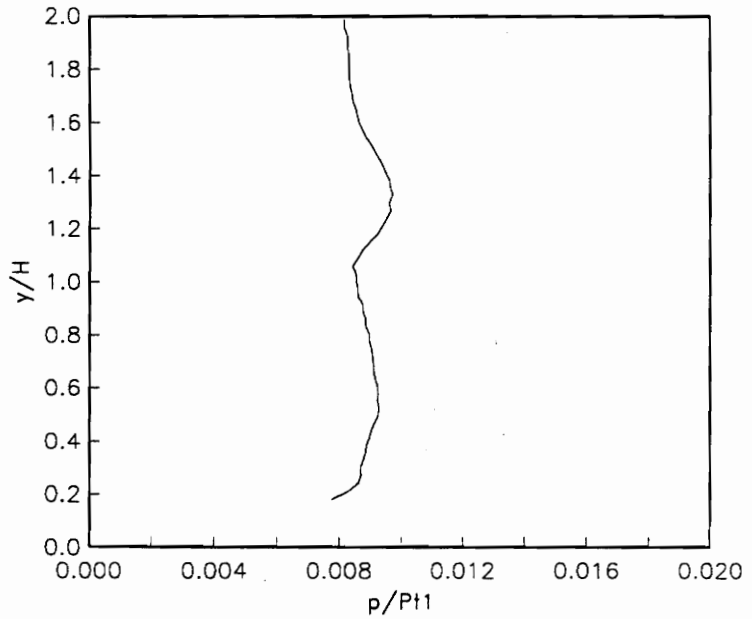

(b) Static Pressure

FIGURE 5.7: Conventional mean flow Mach number and static pressure data (x/H = 15).

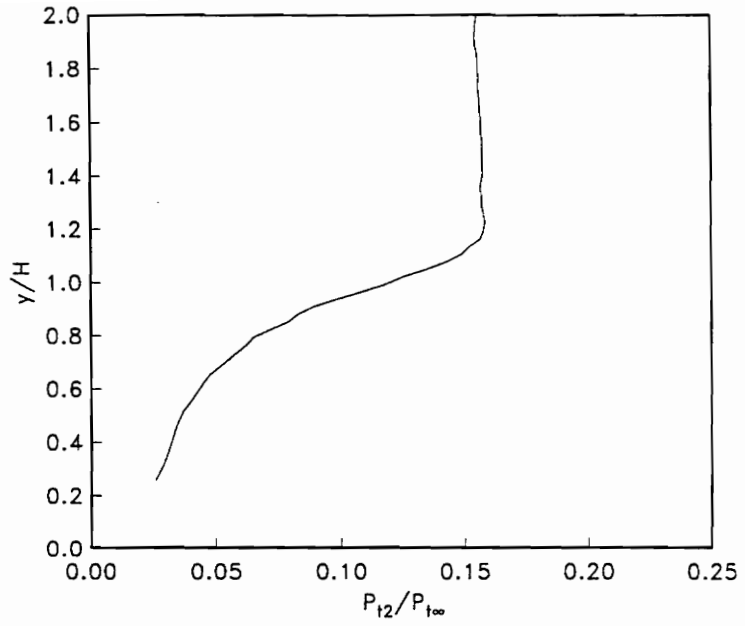

(a) Pitot Pressure

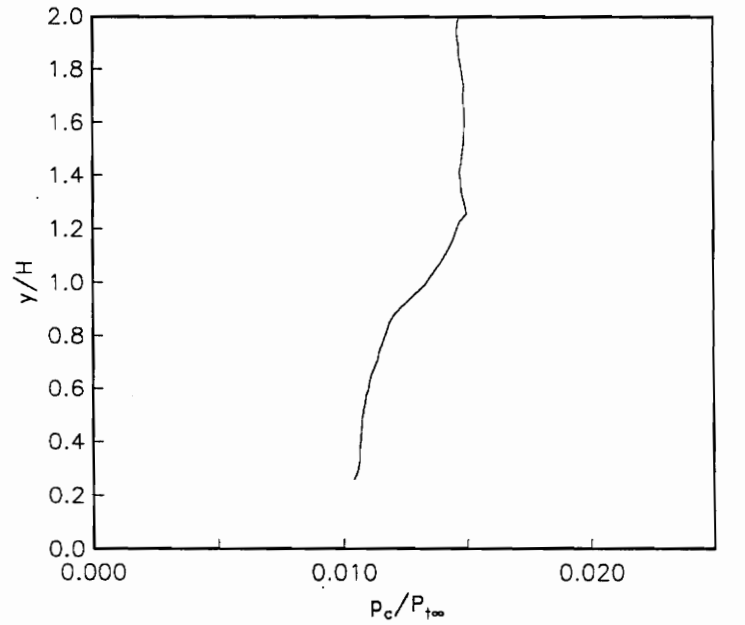

(b) Cone–Static Pressure

FIGURE 5.8: Conventional mean flow Pitot and cone-static pressure data (x/H = 19).

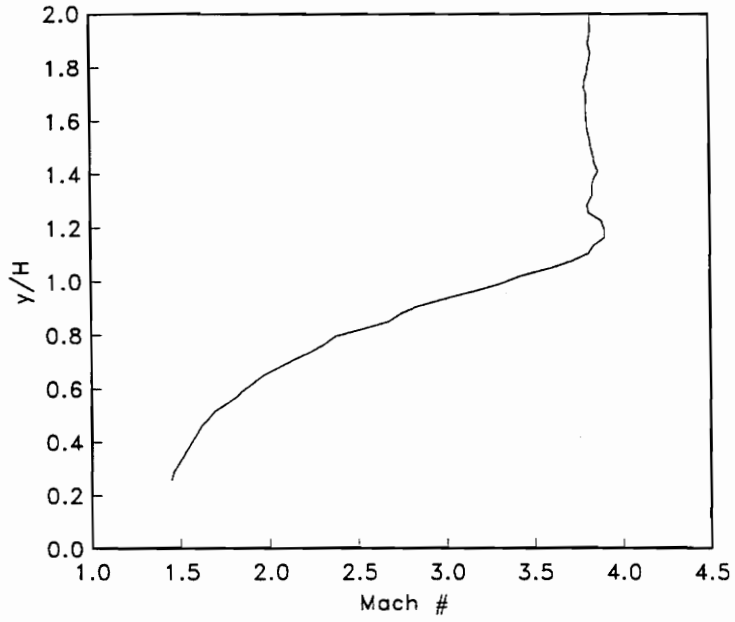

(a) Mach Number

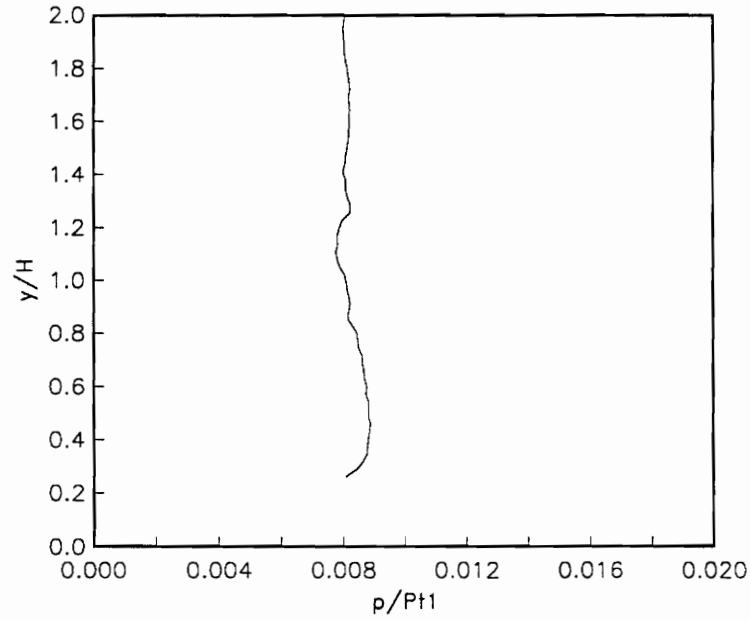

(b) Static Pressure

FIGURE 5.9: Conventional mean flow Mach number and static pressure data (x/H = 19).

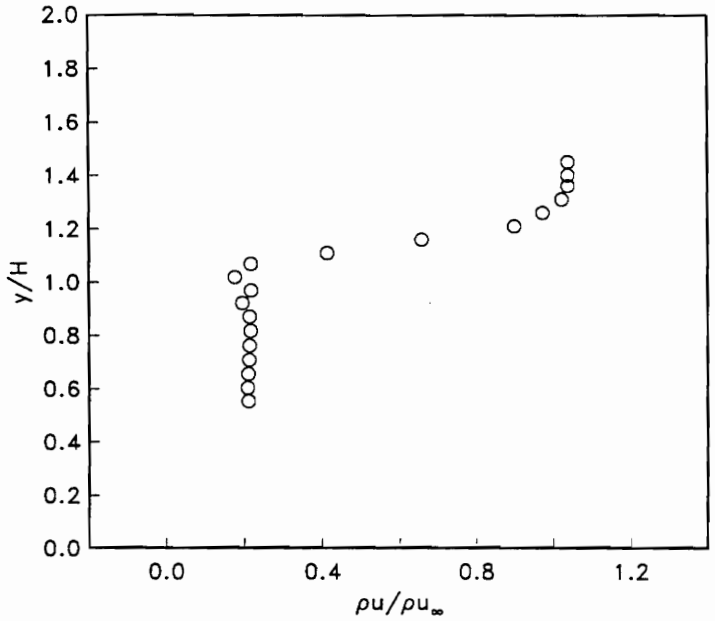

(a) Mass Flux (Wind Axes)

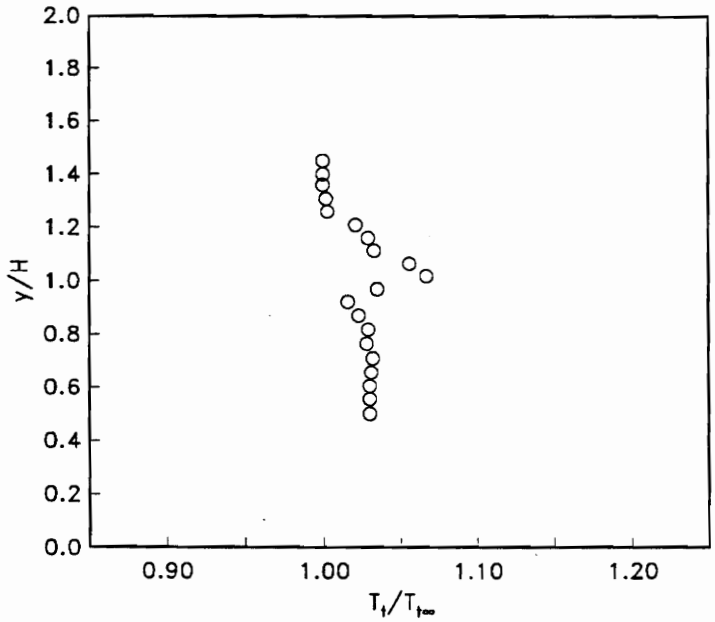

(b) Total Temperature

FIGURE 5.10: Normal-Wire mean mass flux and total temperature data (x/H = 0.2).

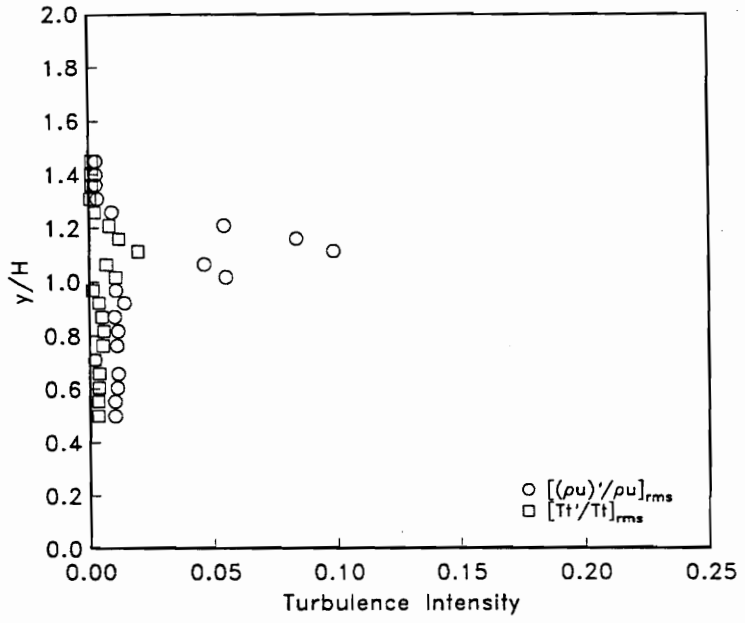

(a) Turbulence Intensity

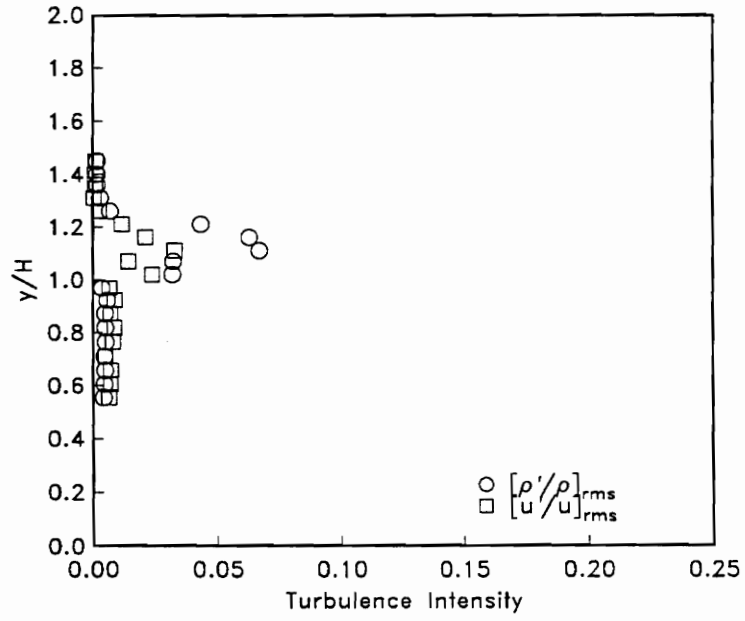

(b) Separated Turbulence Intensity

FIGURE 5.11: Normal-Wire turbulence intensity data (x/H = 0.2).

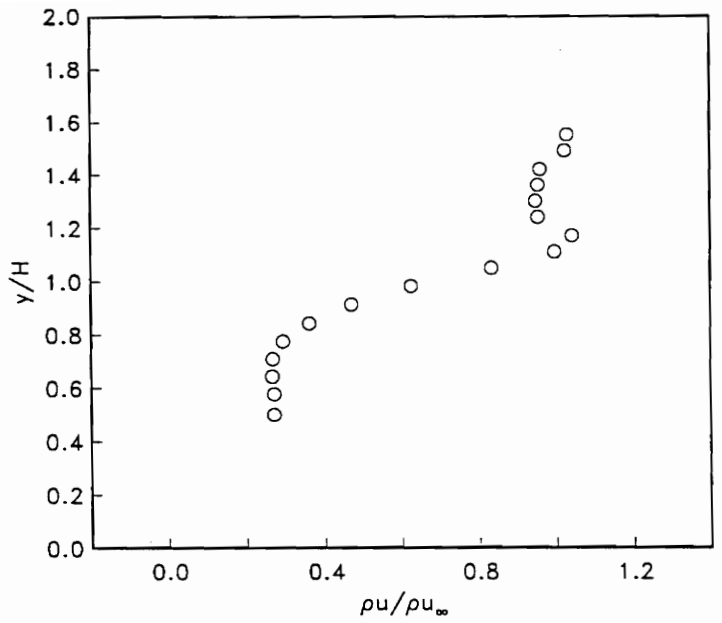

(a) Mass Flux (Wind Axes)

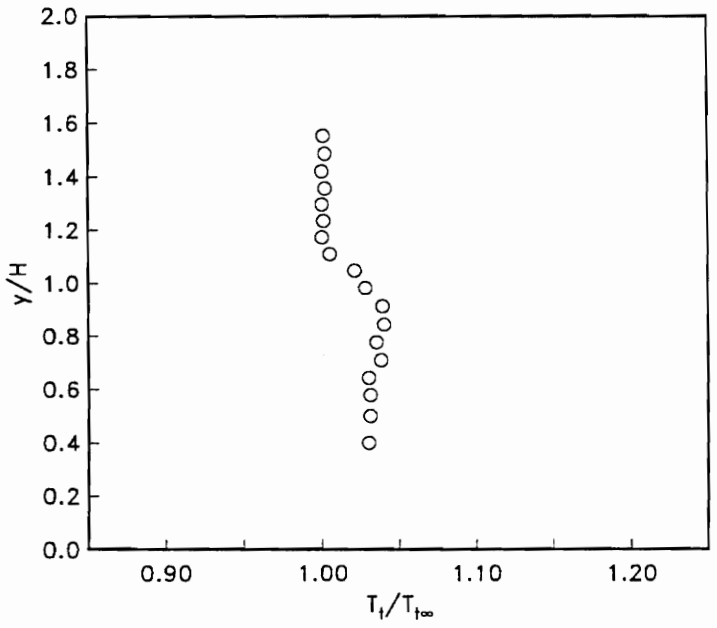

(b) Total Temperature

FIGURE 5.12: Normal-Wire mean mass flux and total temperature data (x/H = 5).

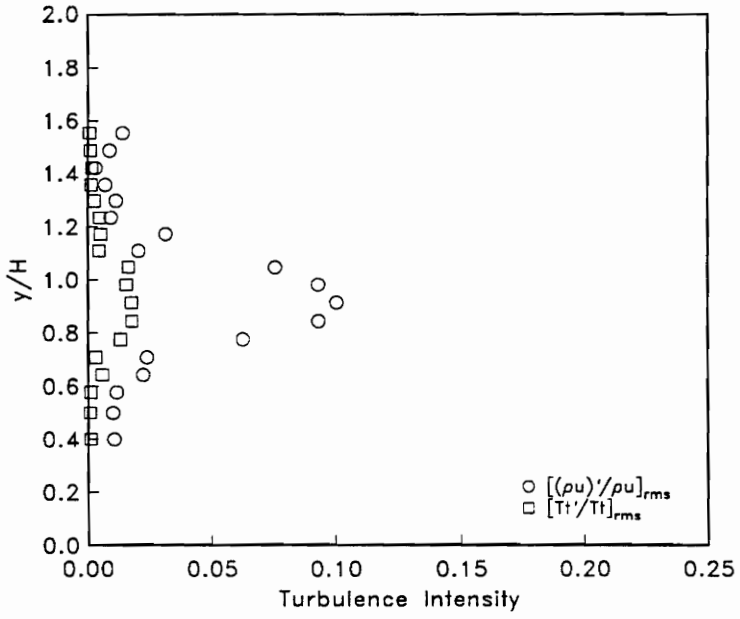

(a) Turbulence Intensity

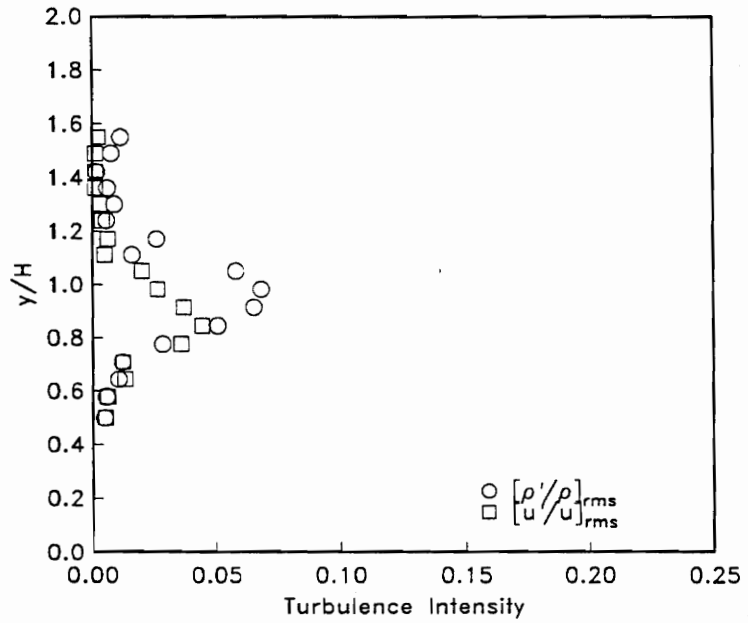

(b) Separated Turbulence Intensity

FIGURE 5.13: Normal-Wire turbulence intensity data (x/H = 5).

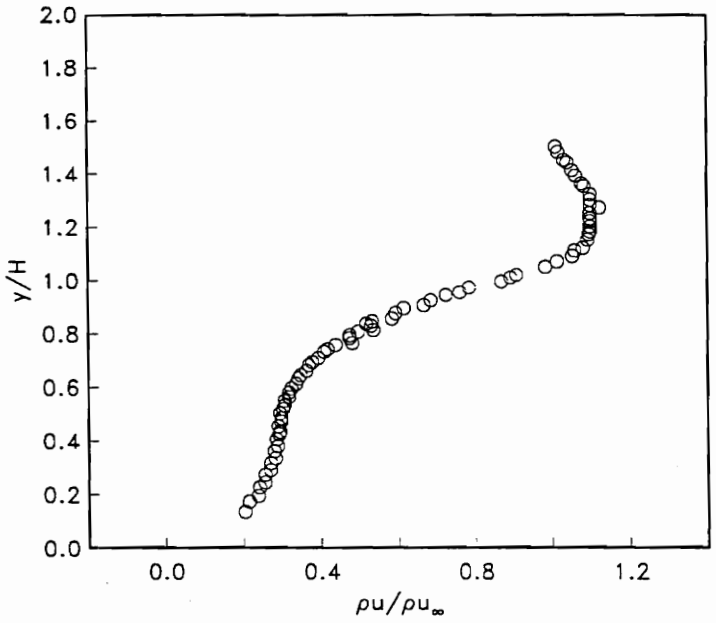

(a) Mass Flux (Wind Axes)

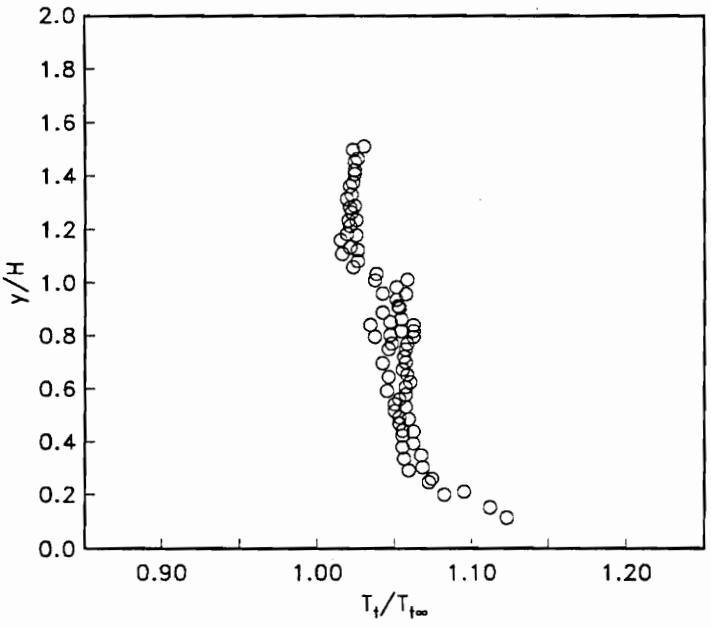

(b) Total Temperature

FIGURE 5.14: Normal-Wire mean mass flux and total temperature data (x/H = 15).

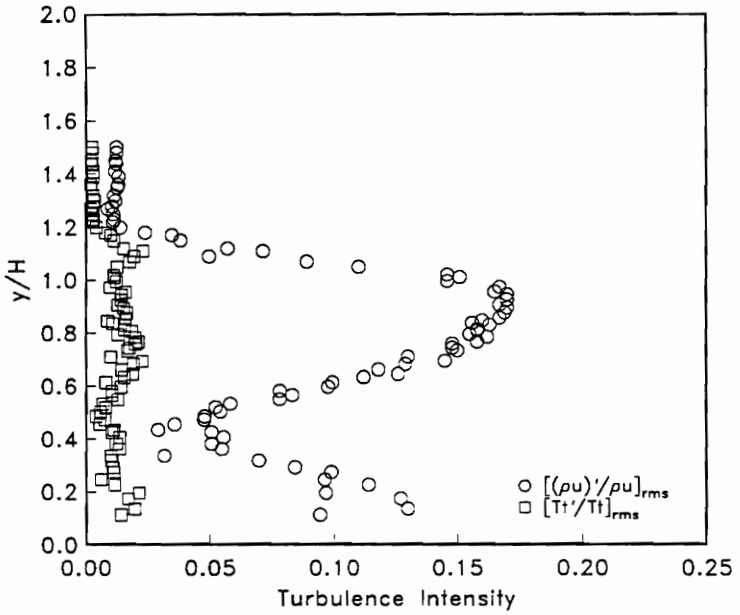

(a) Turbulence Intensity

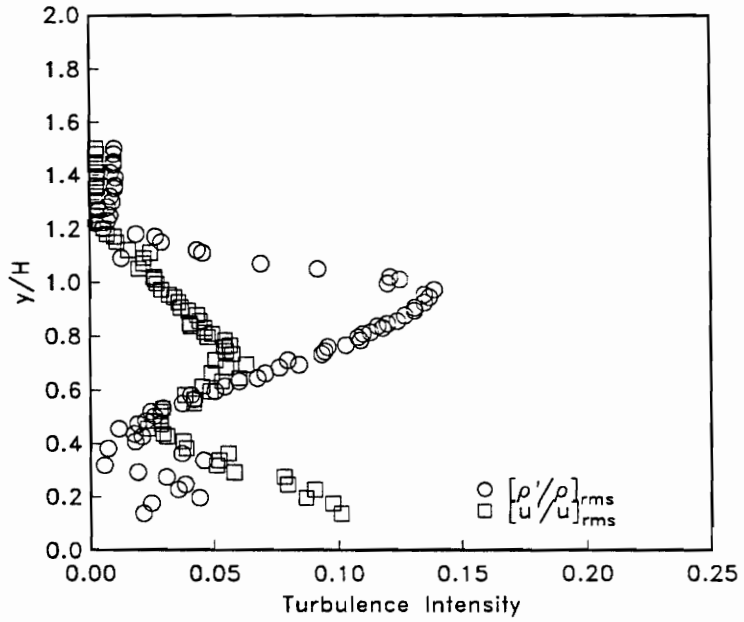

(b) Separated Turbulence Intensity

FIGURE 5.15: Normal-Wire turbulence intensity data (x/H = 15).

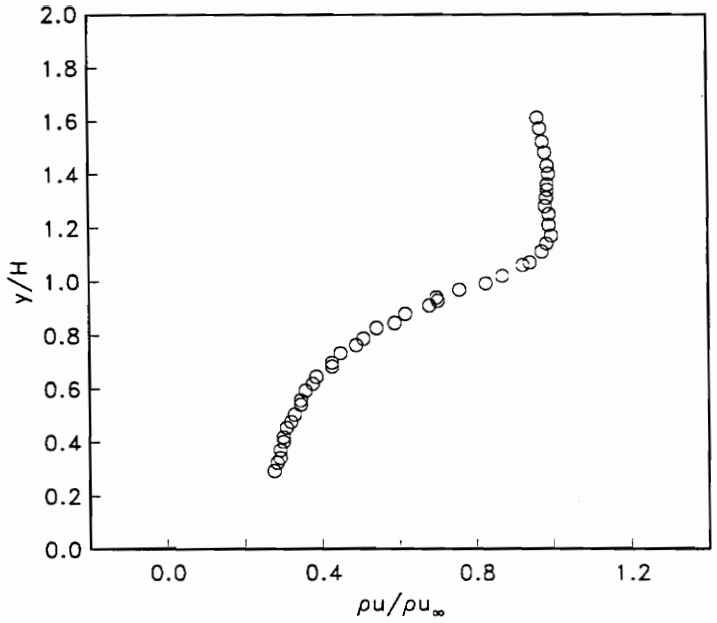

(a) Mass Flux (Wind Axes)

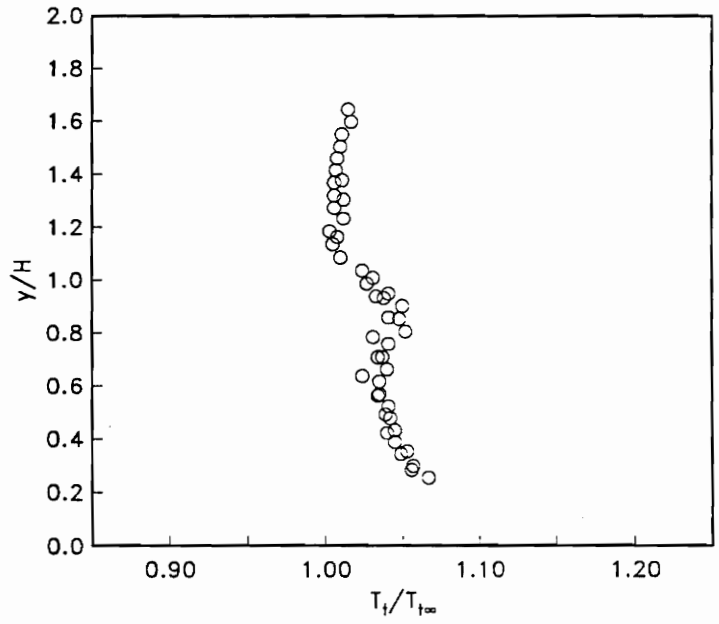

(b) Total Temperature

FIGURE 5.16: Normal-Wire mean mass flux and total temperature data (x/H = 19).

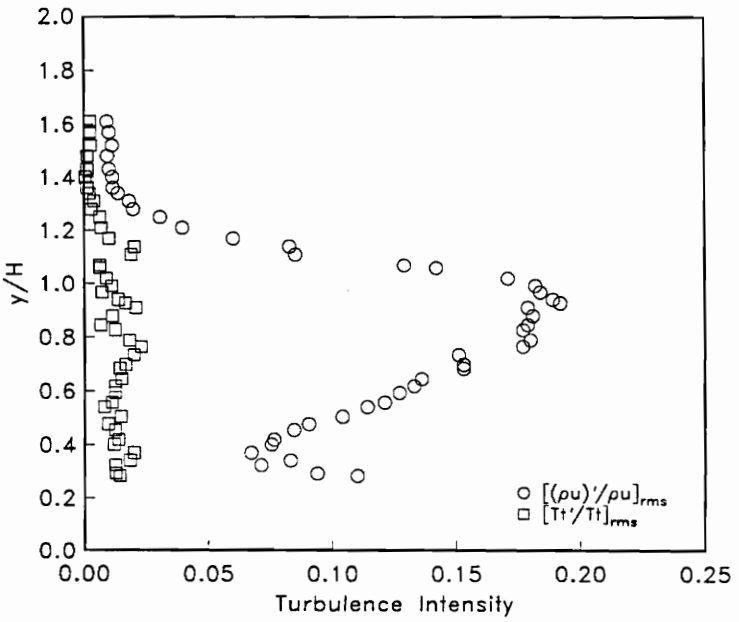

(a) Turbulence Intensity

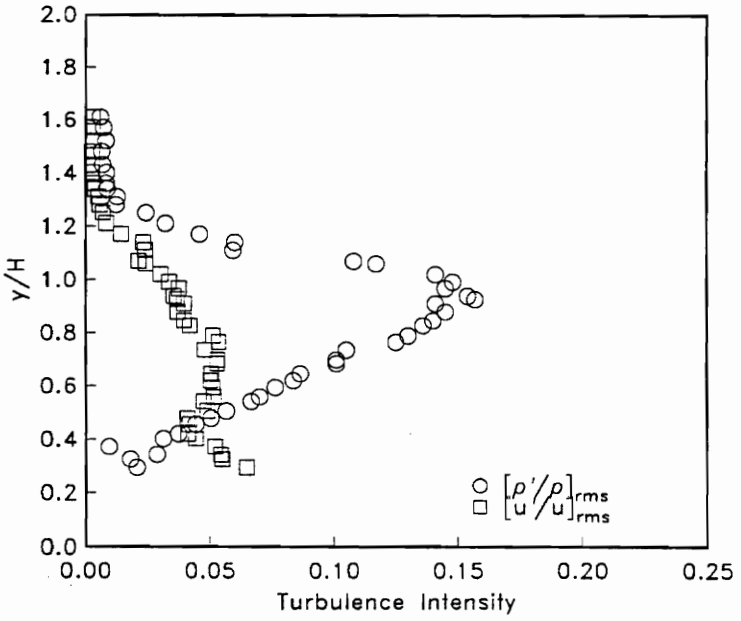

(b) Separated Turbulence Intensity

FIGURE 5.17: Normal-Wire turbulence intensity data (x/H = 19).

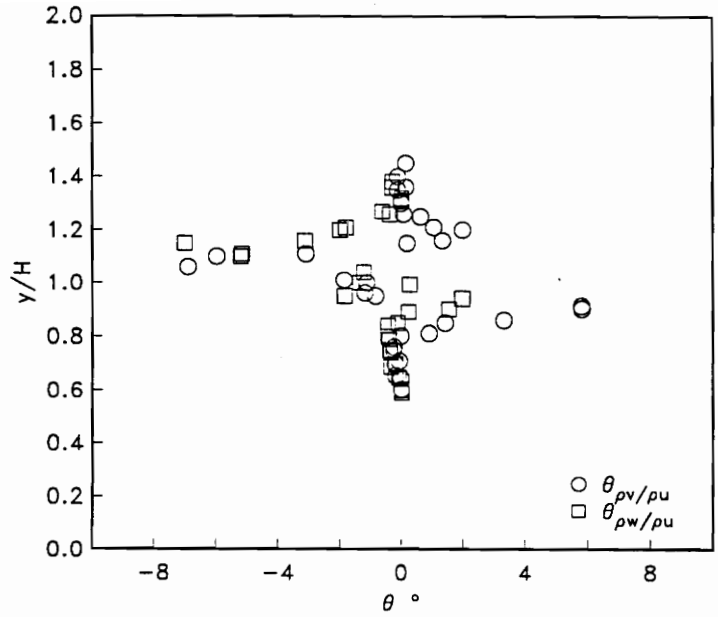

(a) Mass Flux Flow Angle

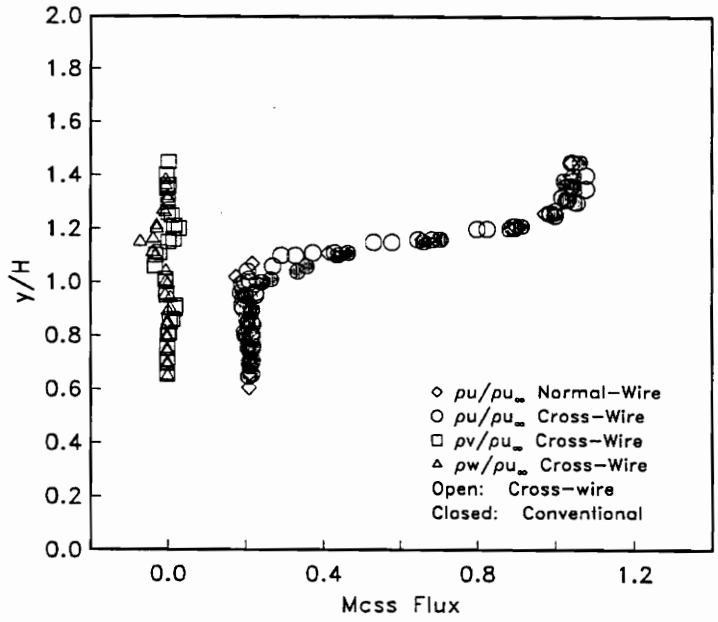

(b) Mass Flux

FIGURE 5.18: Cross-Wire mean flow angle and mass flux data (x/H = 0.2).

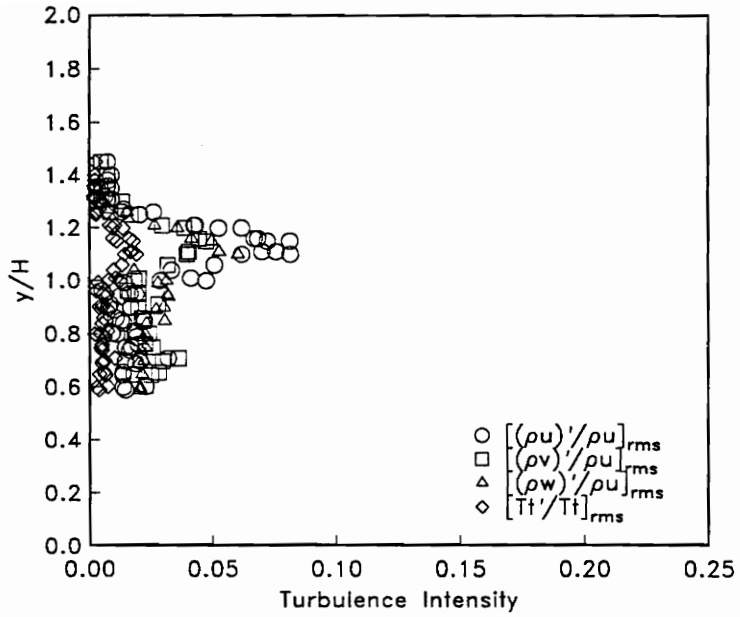

(a) Turbulence Intensities

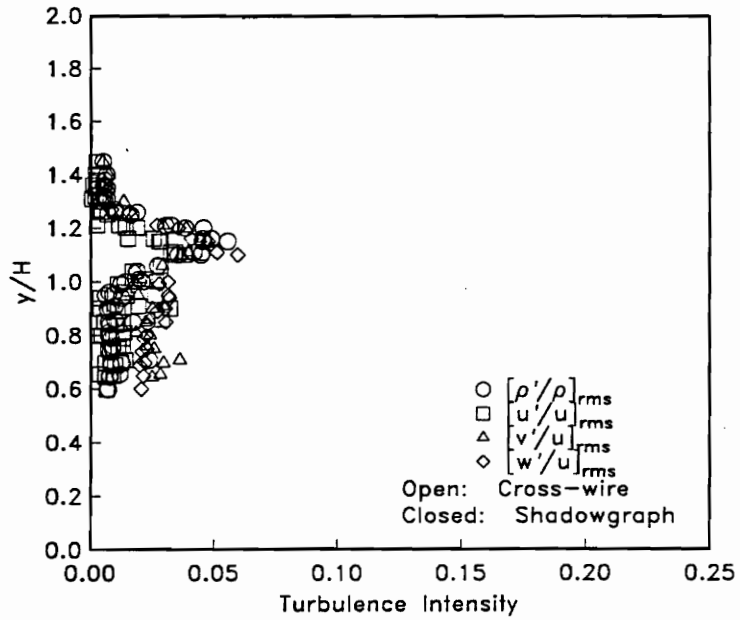

(b) Separated Turbulence Intensities

FIGURE 5.19: Cross-Wire turbulence intensity data (x/H = 0.2).

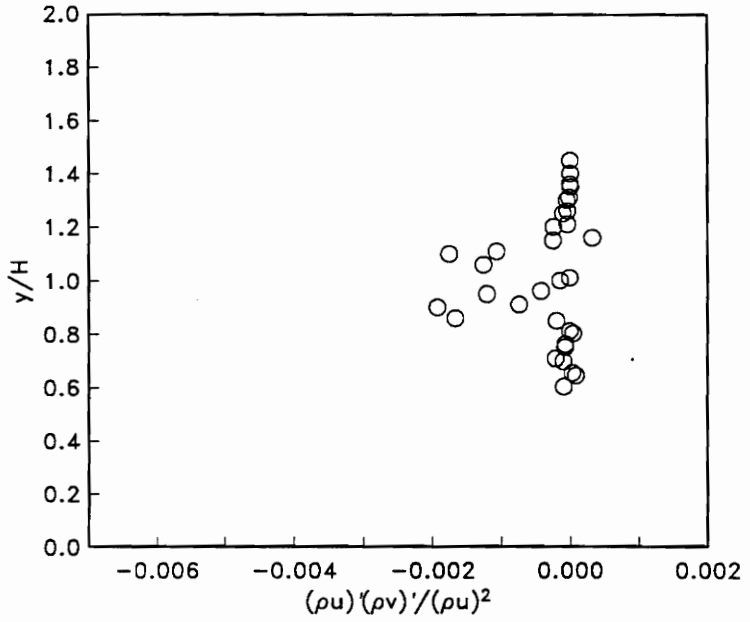

(a) Cross−Wire Shear Term

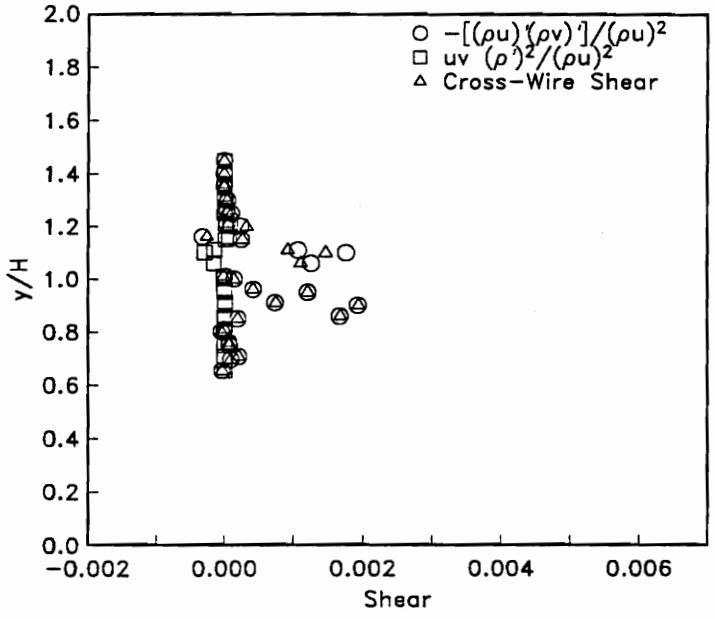

(b) Compressible Shear Terms

FIGURE 5.20: Cross-Wire transformed turbulent x-y shear data (x/H = 0.2).

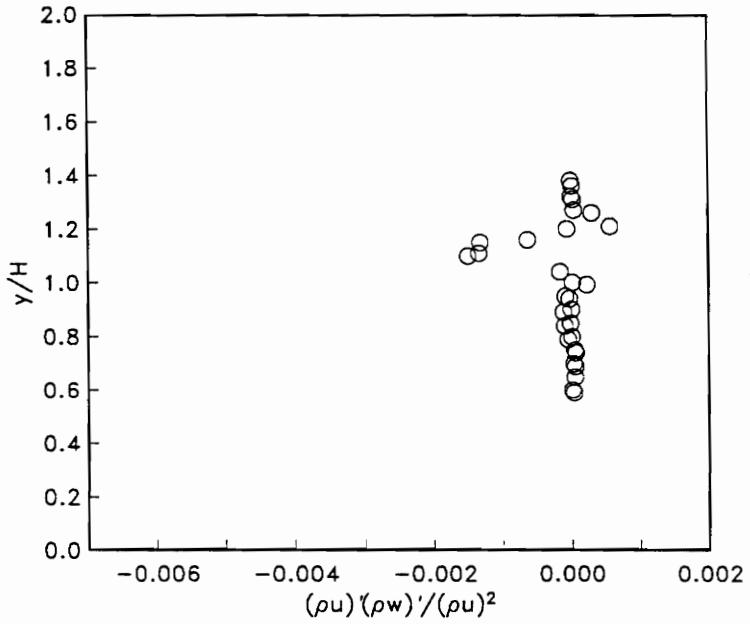

(a) Cross−Wire Shear Term

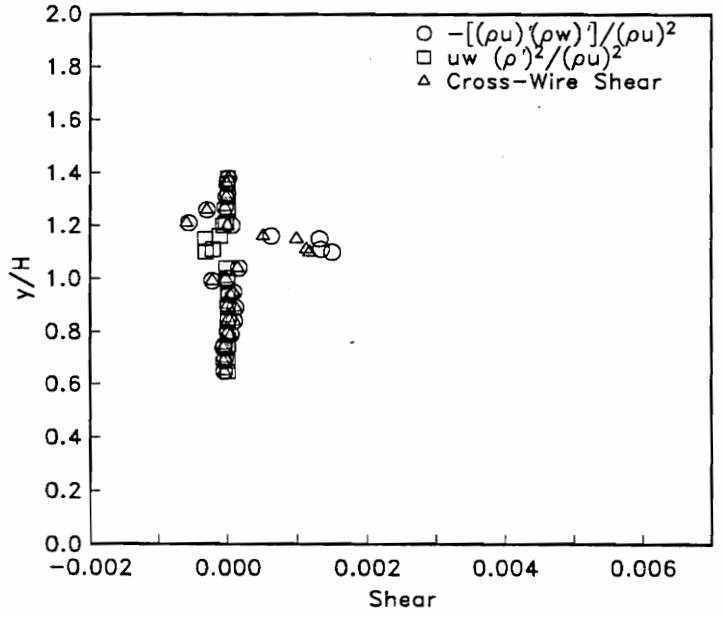

(b) Compressible Shear Terms

FIGURE 5.21: Cross-Wire transformed turbulent x-z shear data (x/H = 0.2).

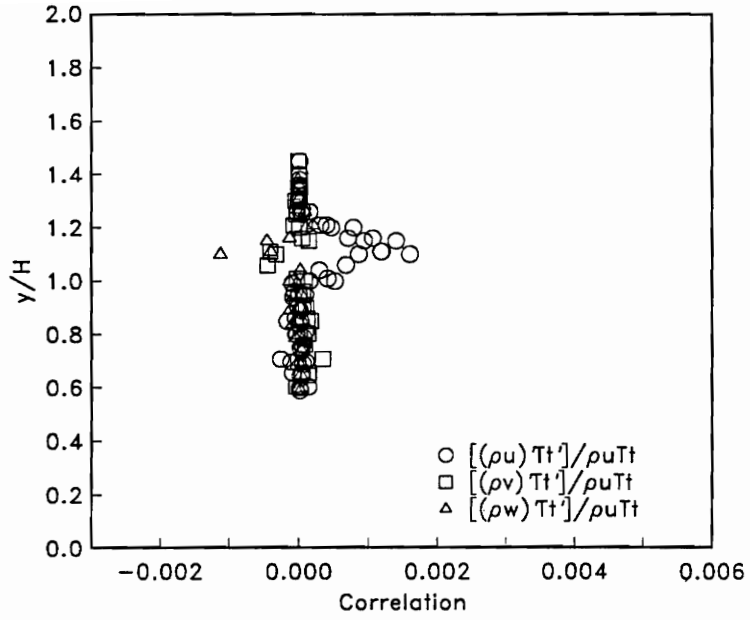

(a) Mass Flux–Total Temperature Correlations

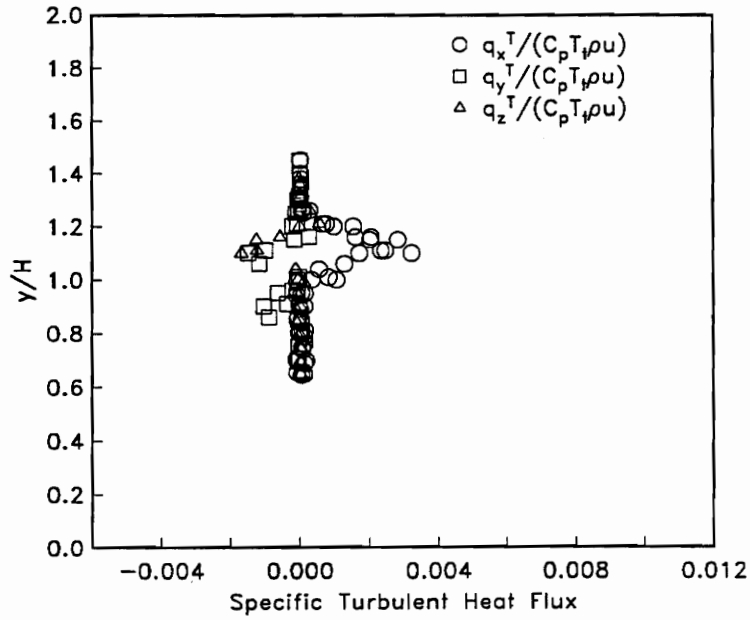

(b) Specific Turbulent Heat Flux

FIGURE 5.22: Cross-Wire turbulent heat flux data (x/H = 0.2).

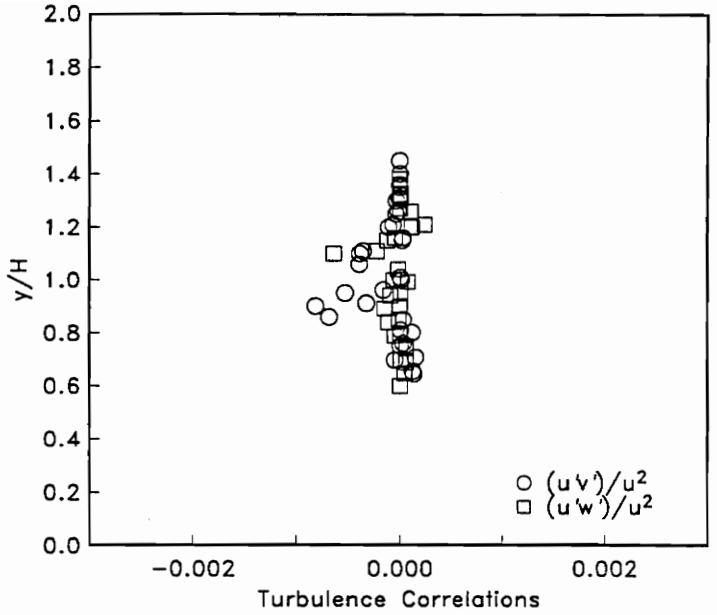

(a) Velocity–Velocity Correlations

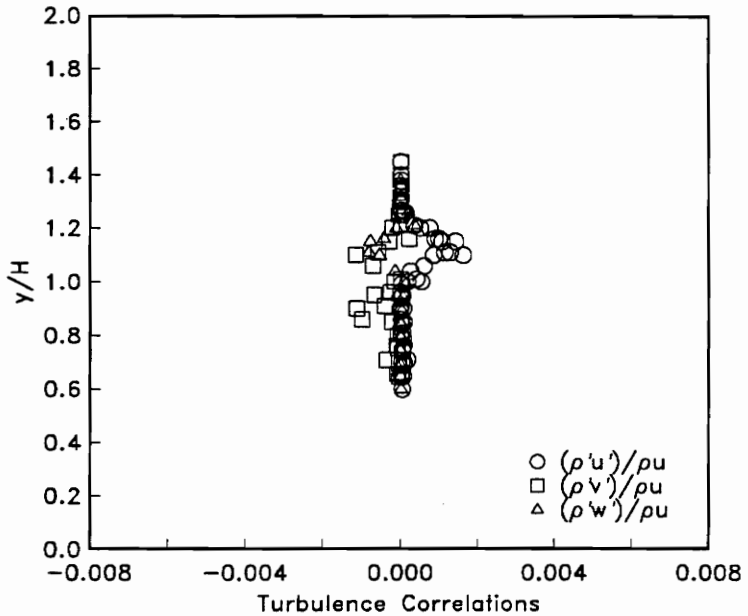

(b) Velocity–Density Correlations

FIGURE 5.23: Cross-Wire velocity-velocity and density-velocity correlation data (x/H = 0.2).

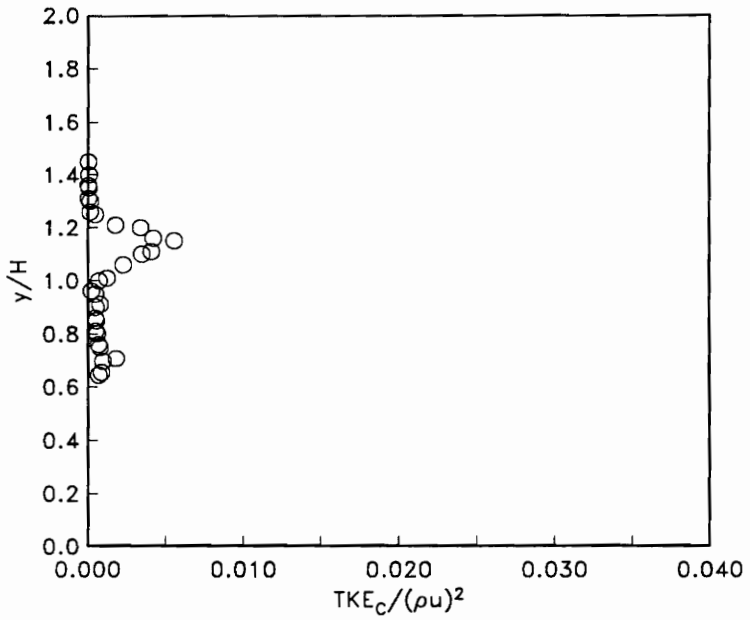

(a) Compressible TKE

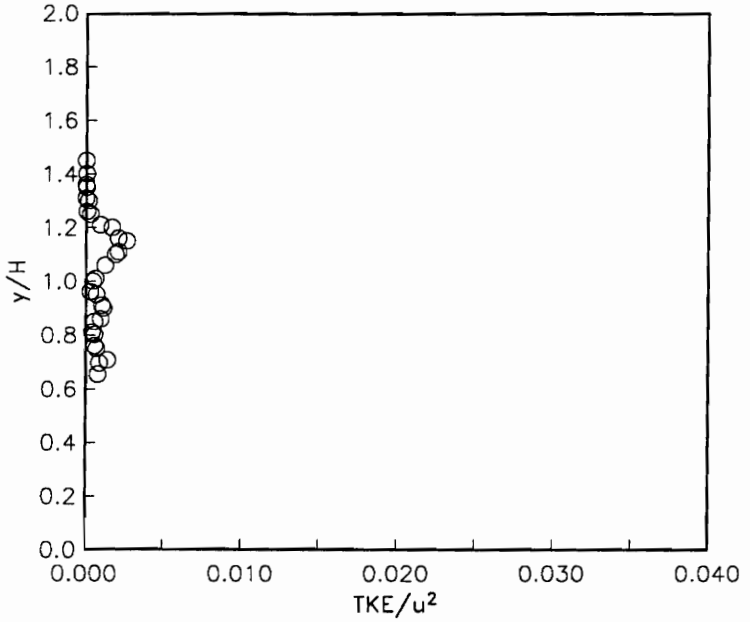

(b) Conventional TKE

FIGURE 5.24: Cross-Wire typical and compressible TKE data (x/H = 0.2).

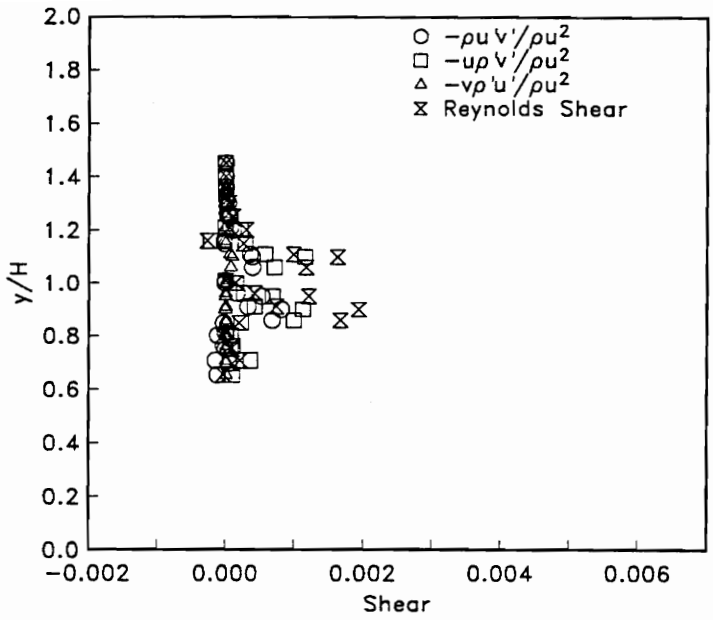

(a) Separated Reynolds Shear (xy)

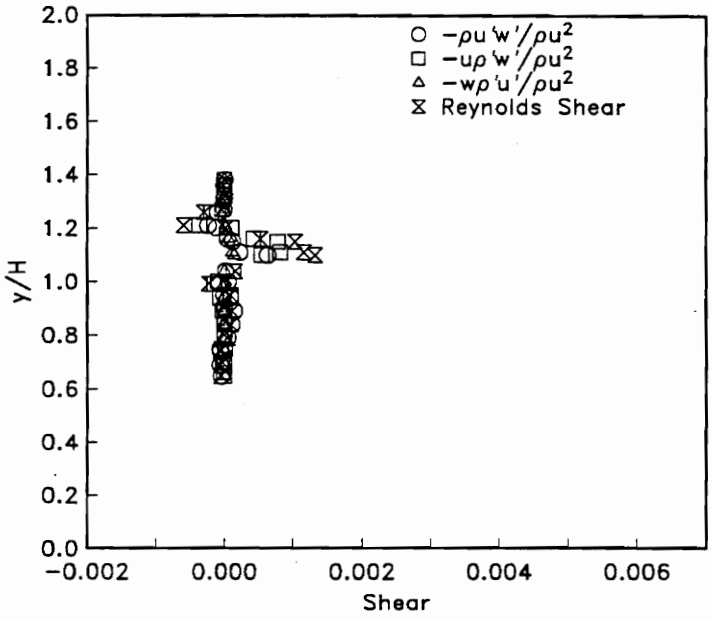

(b) Separated Reynolds Shear (xz)

FIGURE 5.25: Cross-Wire x-y and x-z plane Reynolds shear stress data (x/H = 0.2).

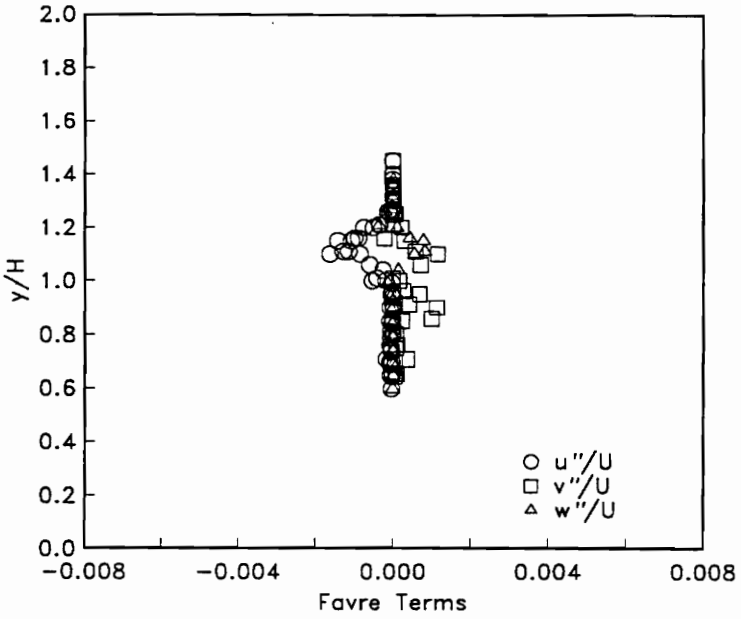

(a) Favre Terms

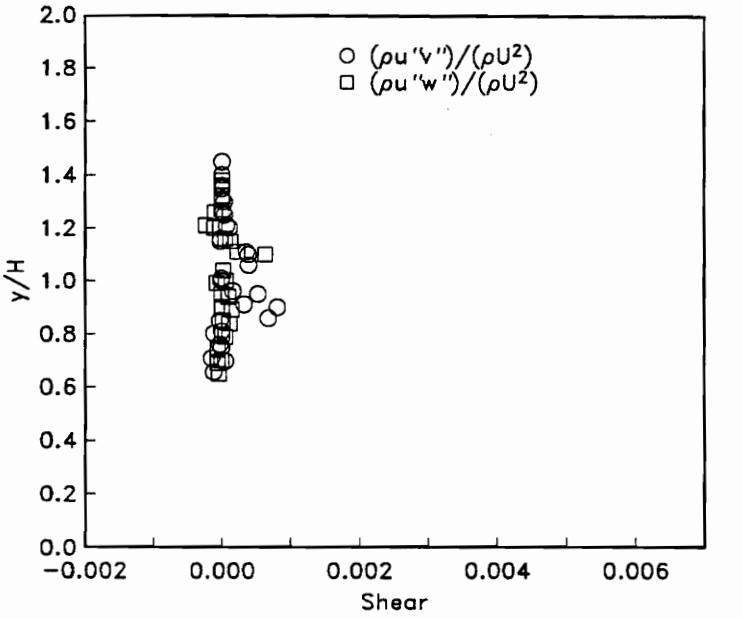

(b) Favre Shear

FIGURE 5.26: Cross-Wire Favre variable data (x/H = 0.2).

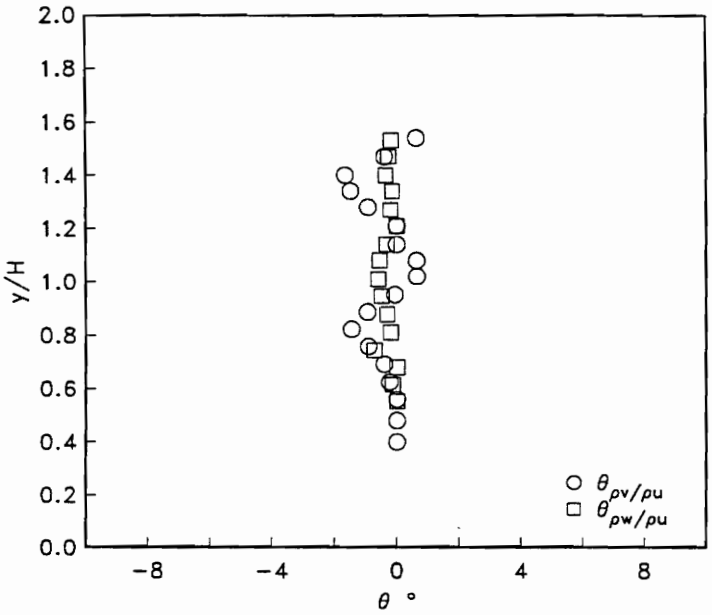

(a) Mass Flux Flow Angle

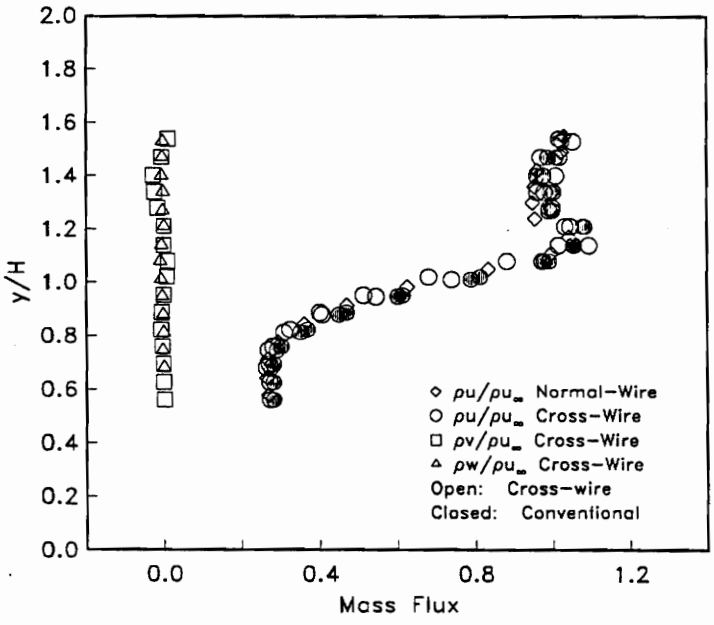

(b) Mass Flux

FIGURE 5.27: Cross-Wire mean flow angle and mass flux data (x/H = 5.0).

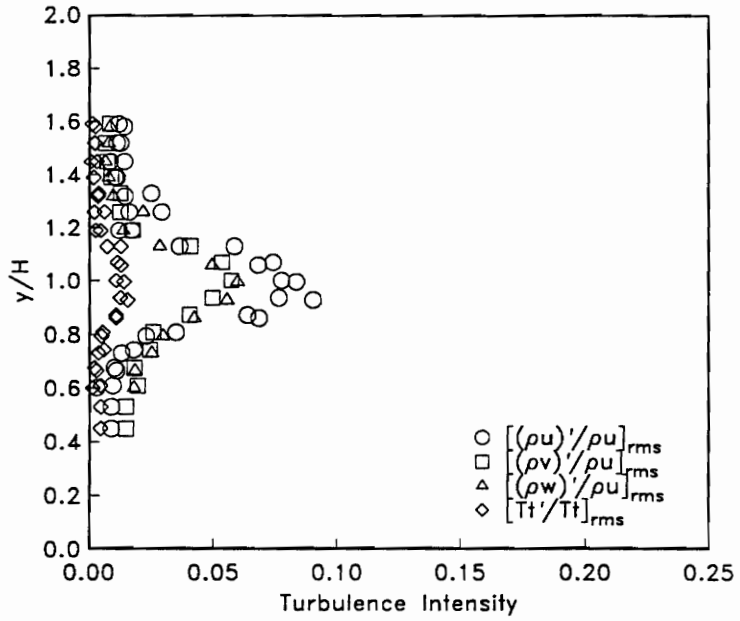

(a) Turbulence Intensities

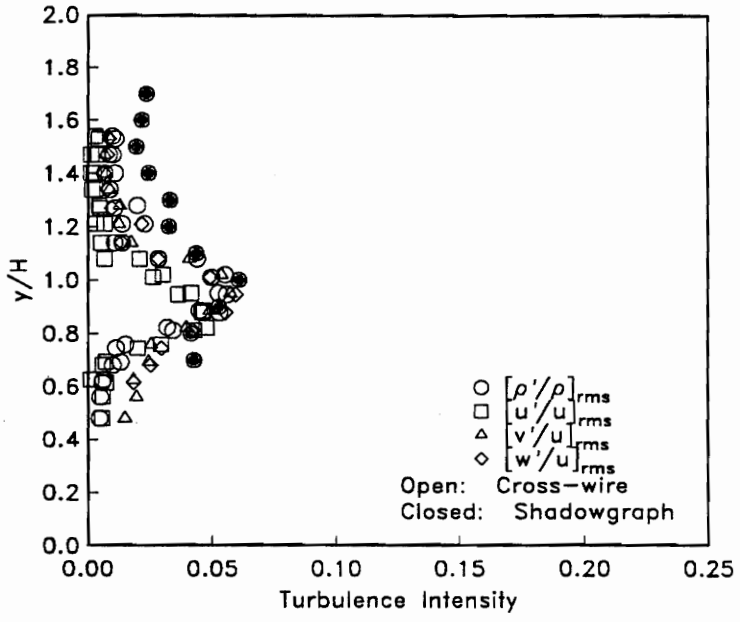

(b) Separated Turbulence Intensities

FIGURE 5.28: Cross-Wire turbulence intensity data (x/H = 5.0).

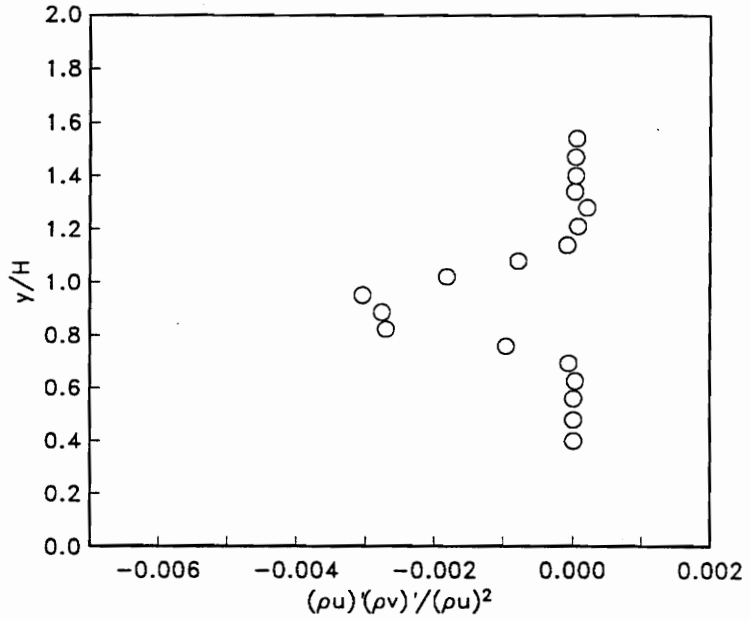

(a) Cross-Wire Shear Term

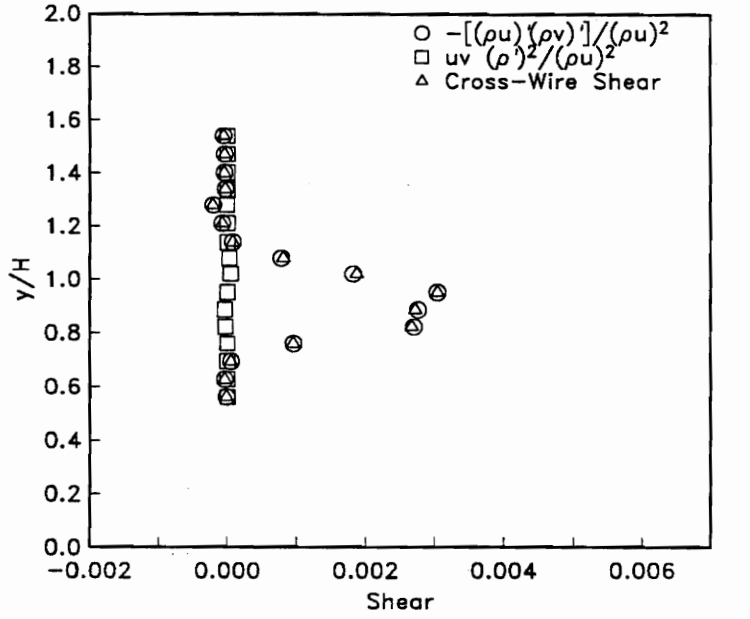

(b) Compressible Shear Terms

FIGURE 5.29: Cross-Wire transformed turbulent x-y shear data (x/H = 5.0).

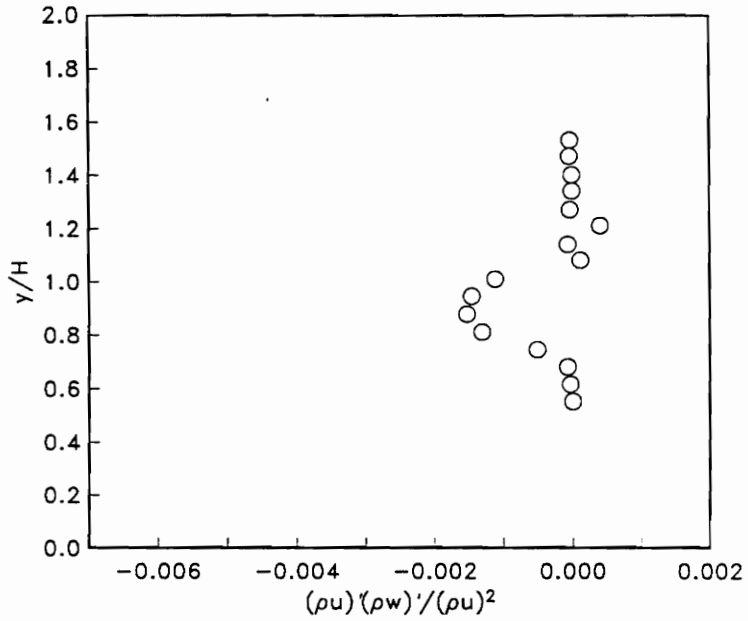

(a) Cross–Wire Shear Term

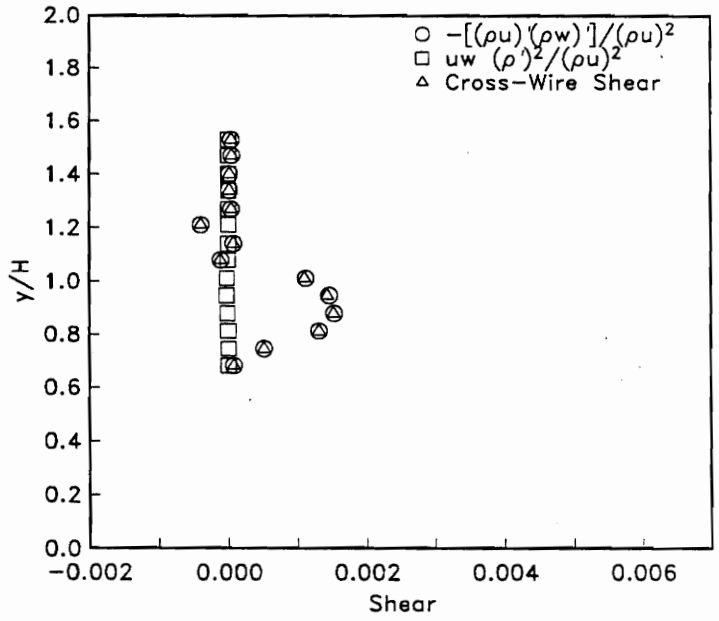

(b) Compressible Shear Terms

FIGURE 5.30: Cross-Wire transformed turbulent x-z shear data (x/H = 5.0).

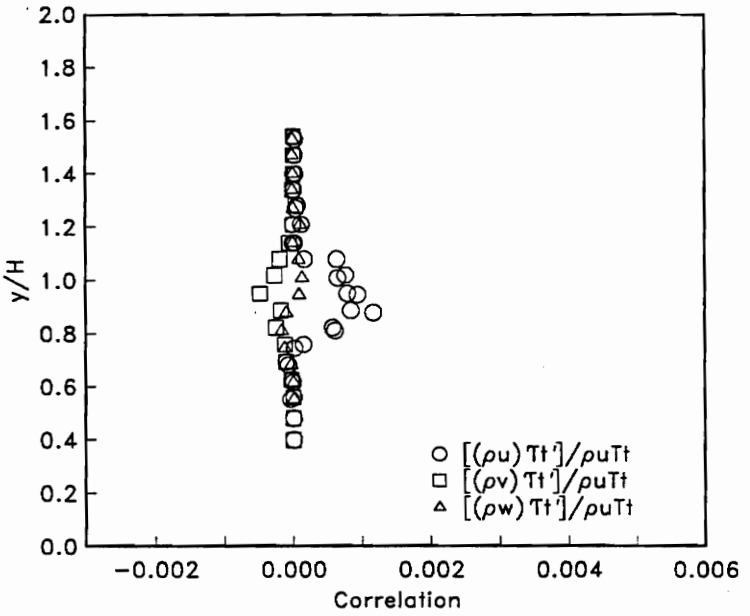

(a) Mass Flux–Total Temperature Correlations

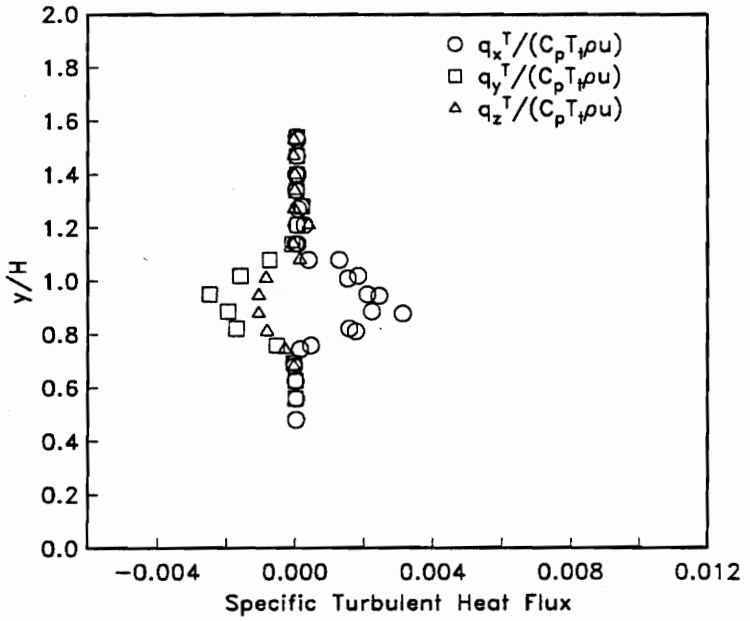

(b) Specific Turbulent Heat Flux

FIGURE 5.31: Cross-Wire turbulent heat flux data (x/H = 5.0).

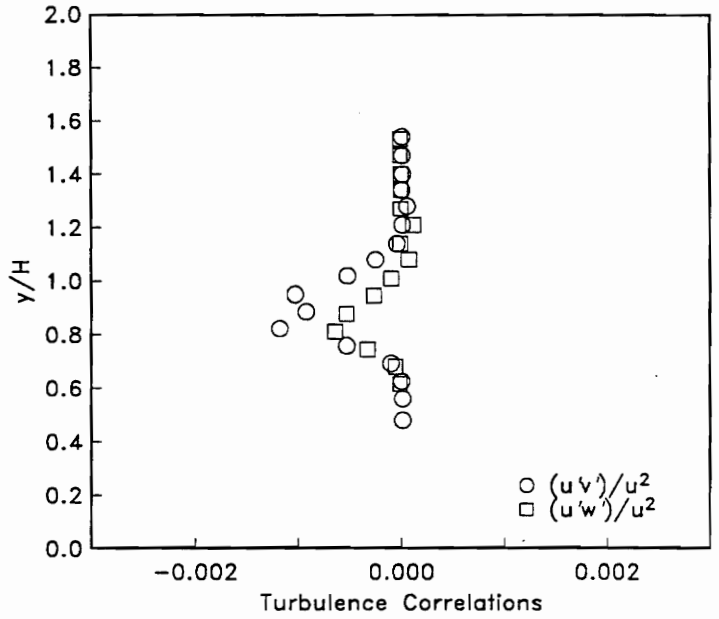

(a) Velocity–Velocity Correlations

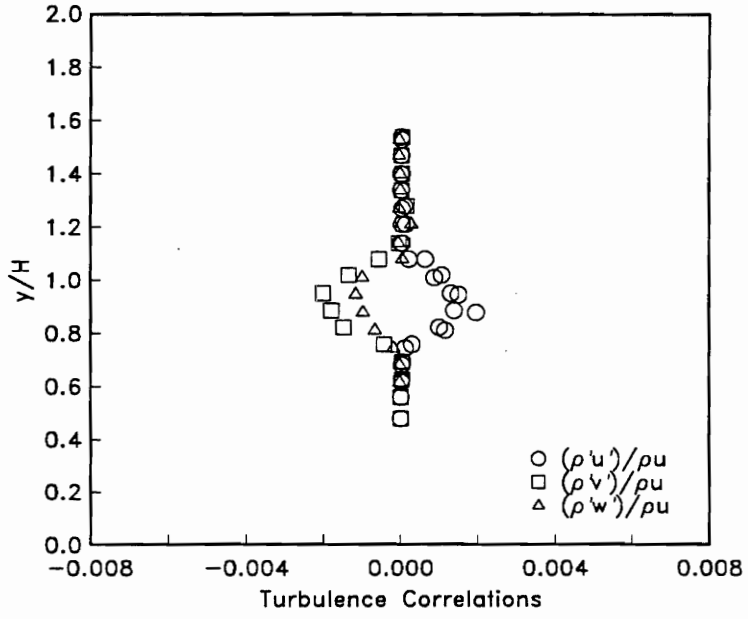

(b) Velocity–Density Correlations

FIGURE 5.32: Cross-Wire velocity-velocity and density-velocity correlation data (x/H = 5.0).

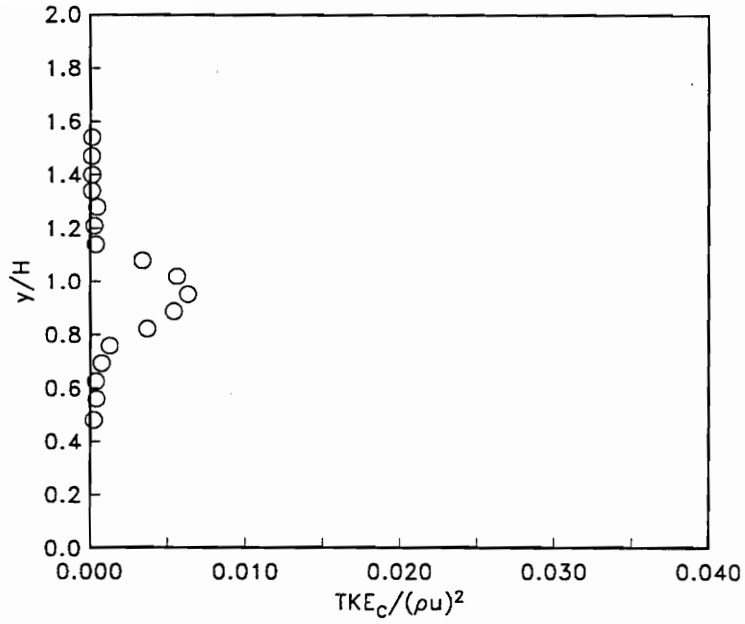

(a) Compressible TKE

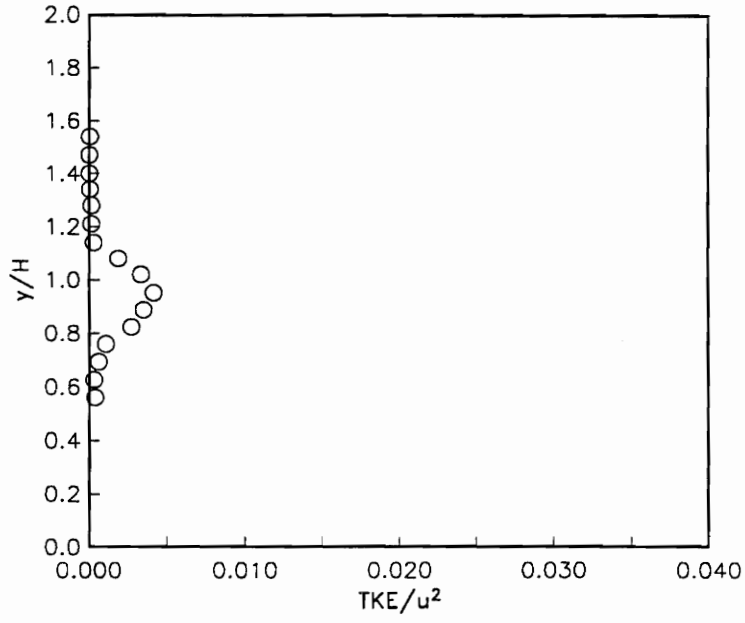

(b) Conventional TKE

FIGURE 5.33: Cross-Wire typical and compressible TKE data (x/H = 5.0).

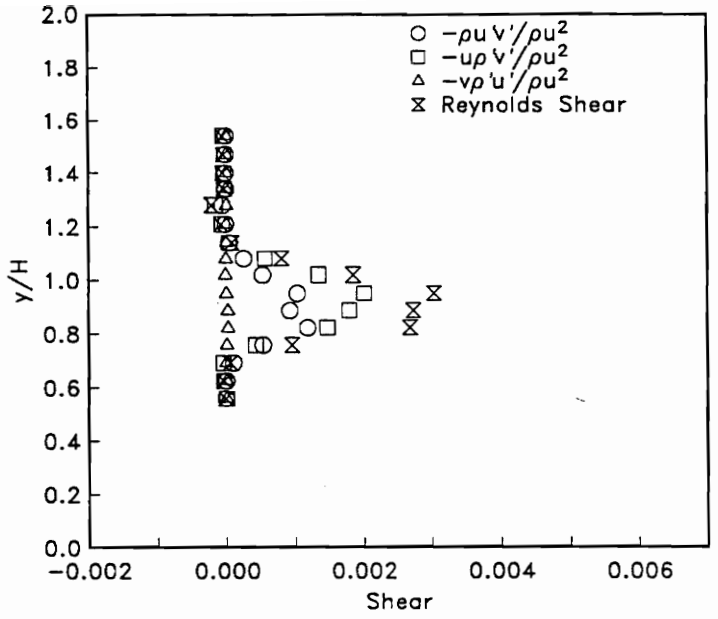

(a) Separated Reynolds Shear (xy)

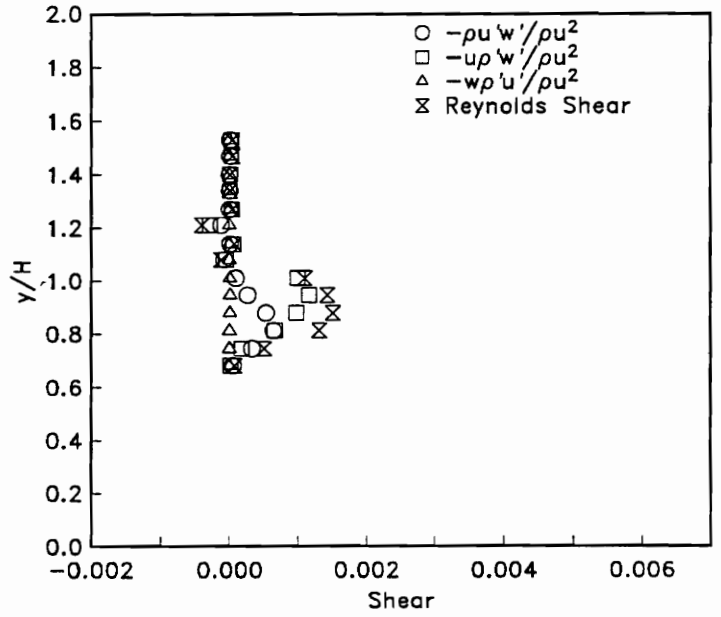

(b) Separated Reynolds Shear (xz)

FIGURE 5.34: Cross-Wire x-y and x-z plane Reynolds shear stress data (x/H = 5.0).

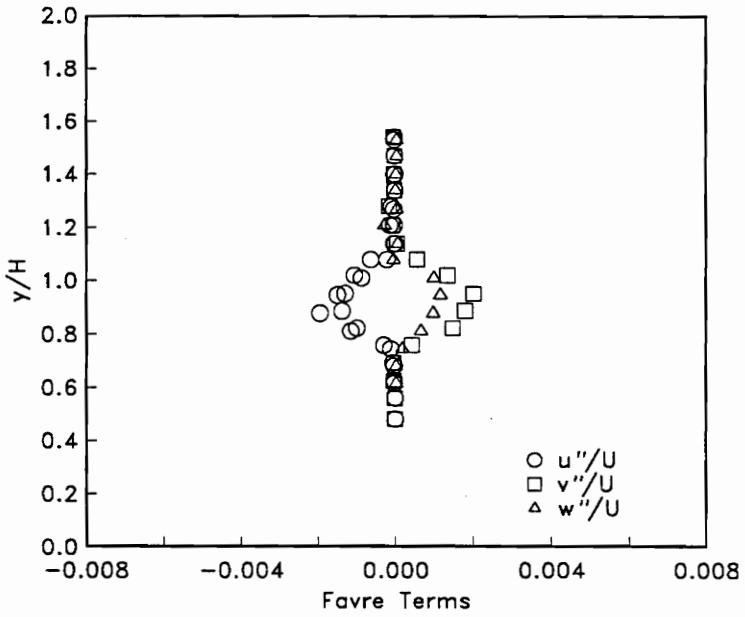

(a) Favre Terms

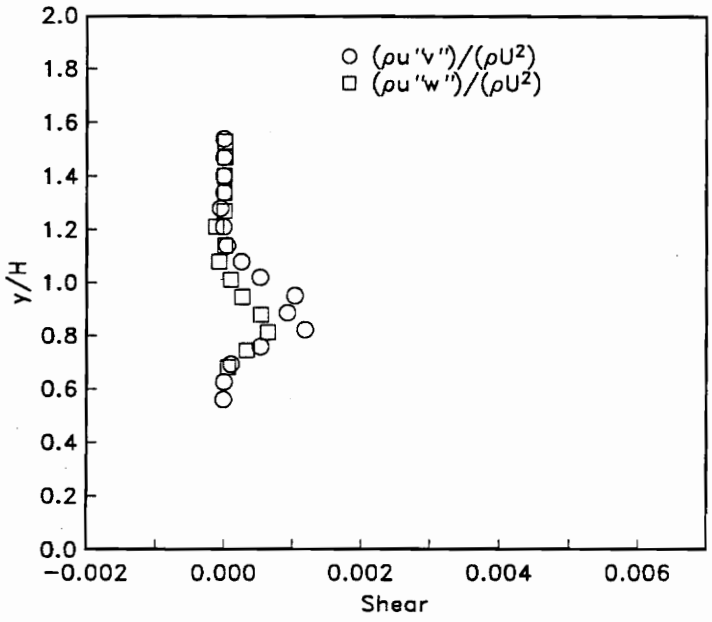

(b) Favre Shear

FIGURE 5.35: Cross-Wire Favre variable data (x/H = 5.0).

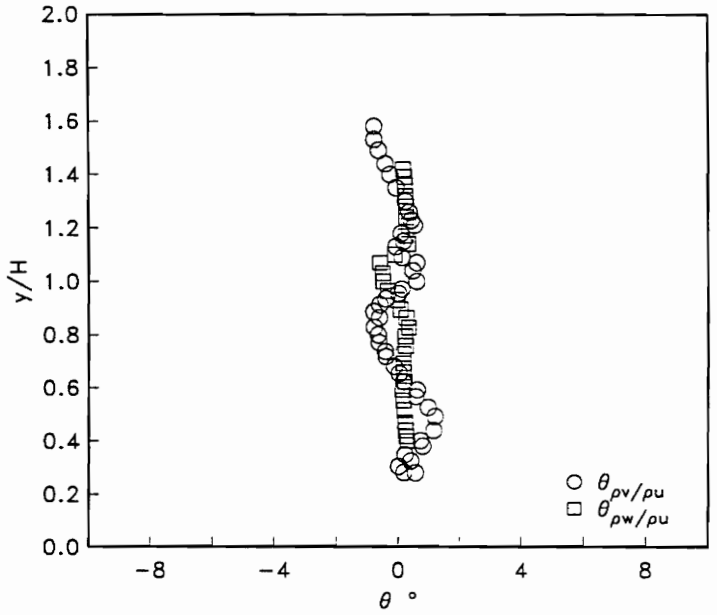

(a) Mass Flux Flow Angle

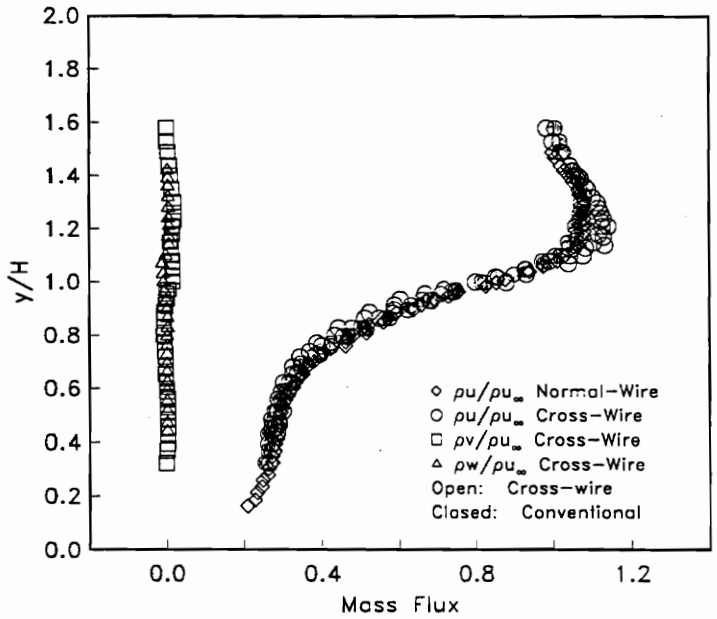

(b) Mass Flux

FIGURE 5.36: Cross-Wire mean flow angle and mass flux data (x/H = 15.).

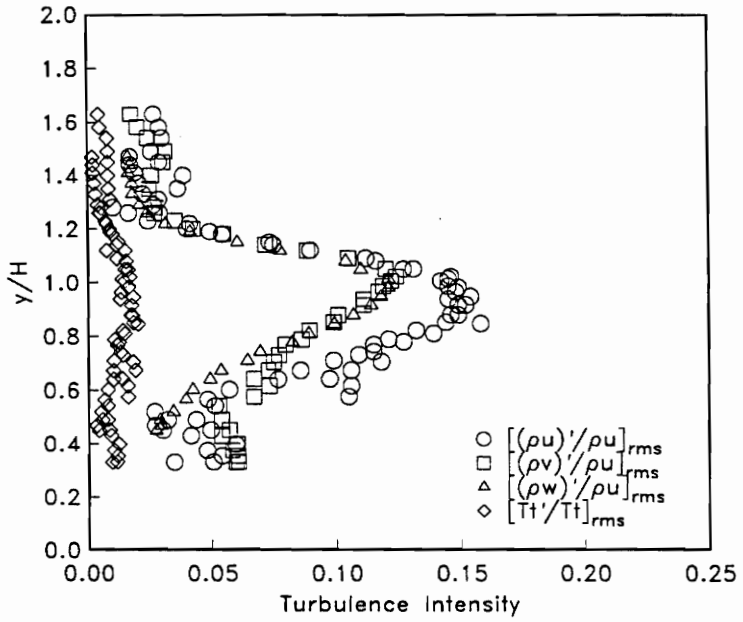

(a) Turbulence Intensities

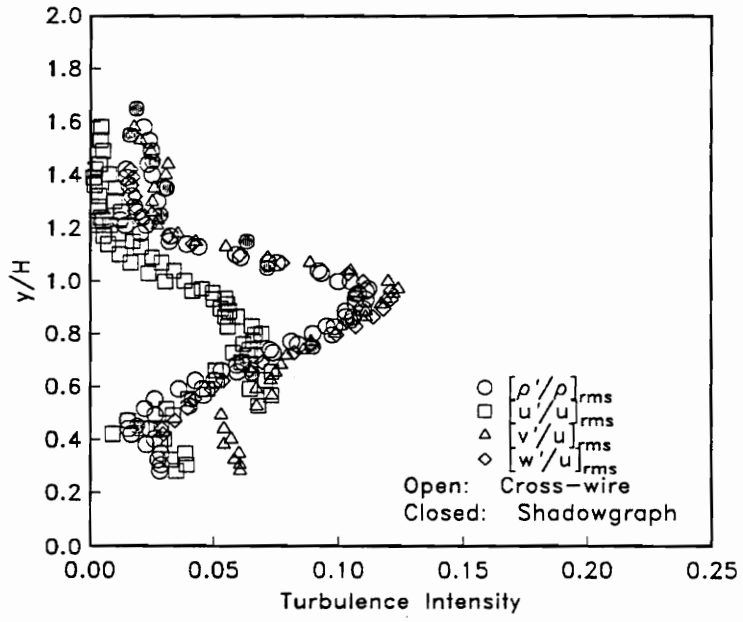

(b) Separated Turbulence Intensities

FIGURE 5.37: Cross-Wire turbulence intensity data (x/H = 15.).

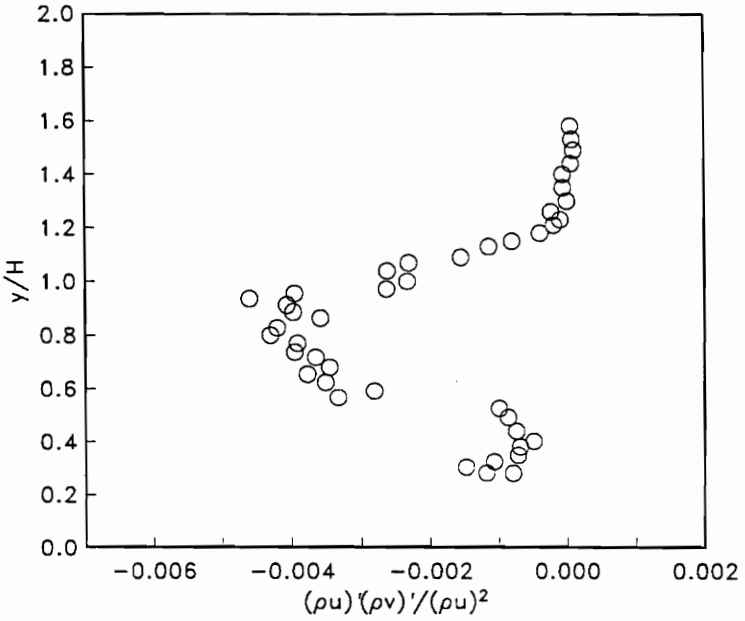

(a) Cross−Wire Shear Term

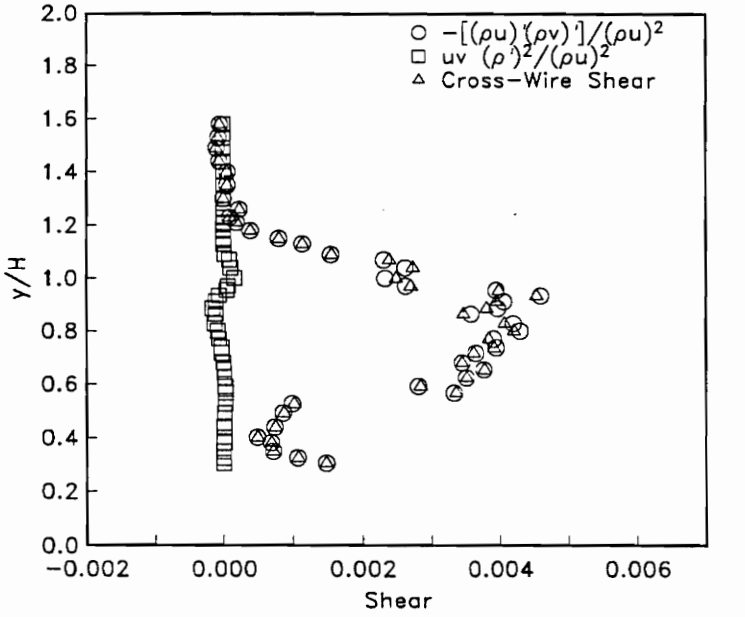

(b) Compressible Shear Terms

FIGURE 5.38: Cross-Wire transformed turbulent x-y shear data (x/H = 15.).

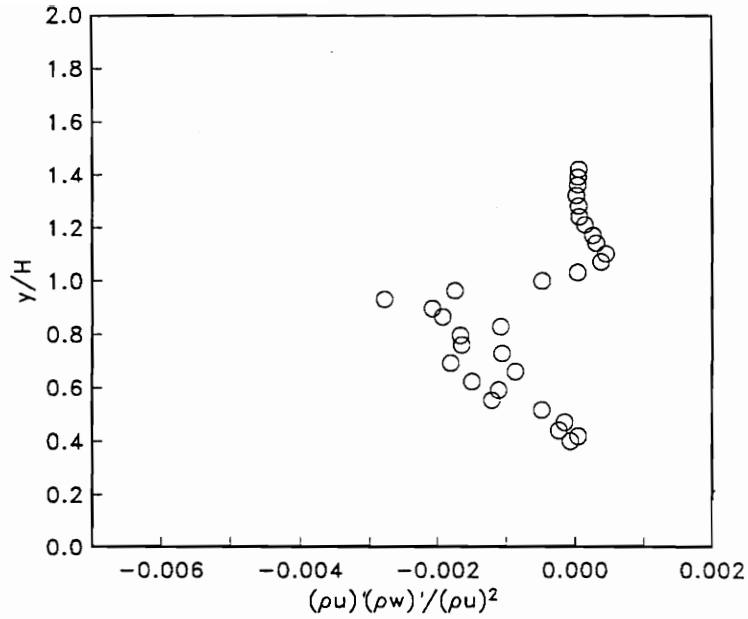

(a) Cross-Wire Shear Term

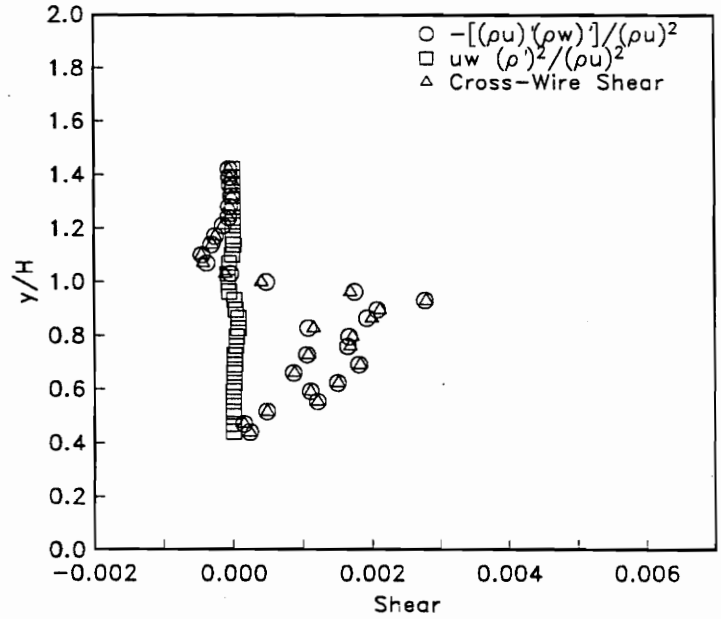

(b) Compressible Shear Terms

FIGURE 5.39: Cross-Wire transformed turbulent x-z shear data (x/H = 15.).

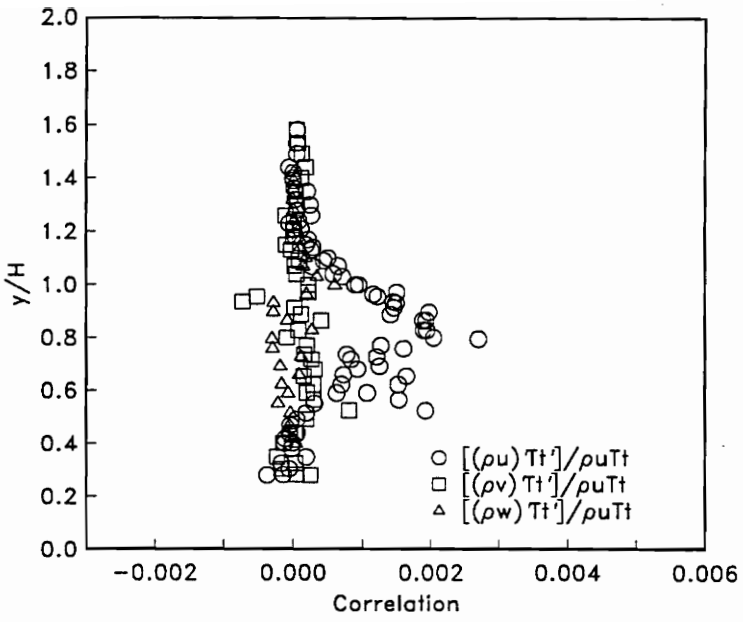

(a) Mass Flux–Total Temperature Correlations

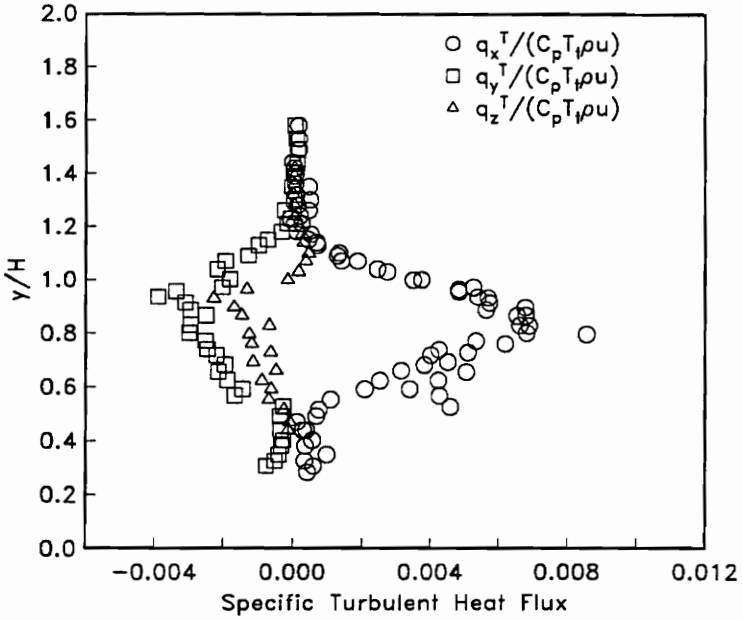

(b) Specific Turbulent Heat Flux

FIGURE 5.40: Cross-Wire turbulent heat flux data (x/H = 15.).

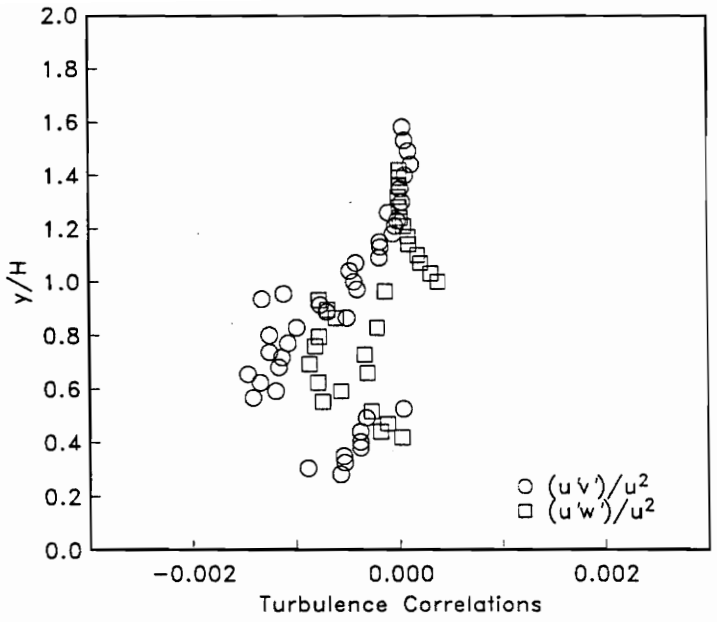

(a) Velocity–Velocity Correlations

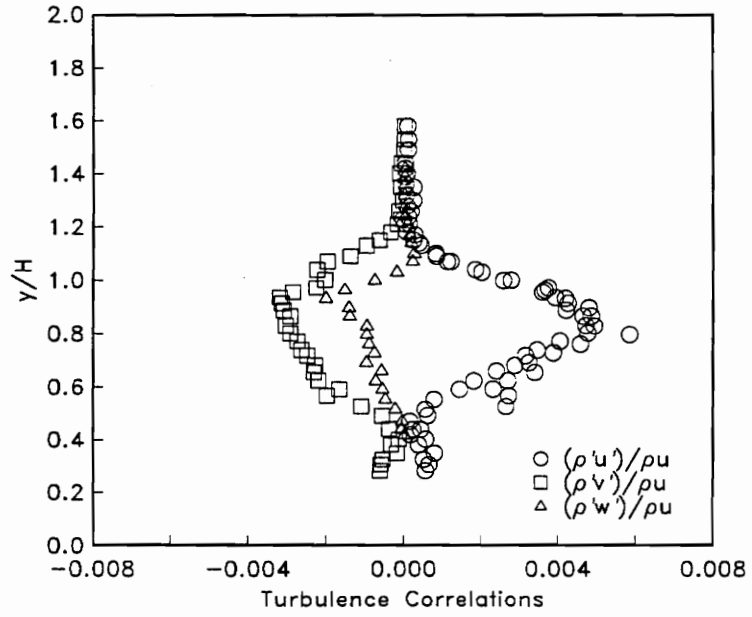

(b) Velocity–Density Correlations

FIGURE 5.41: Cross-Wire velocity-velocity and density-velocity correlation data (x/H = 15.).

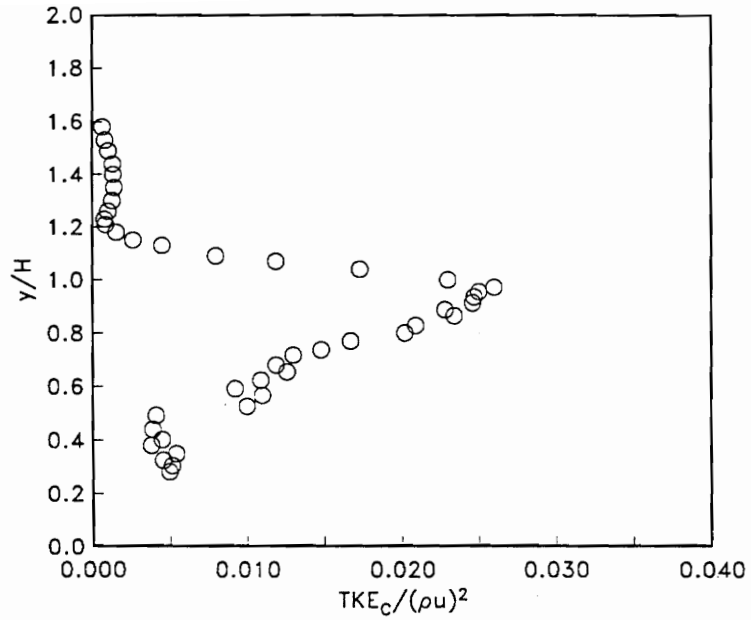

(a) Compressible TKE

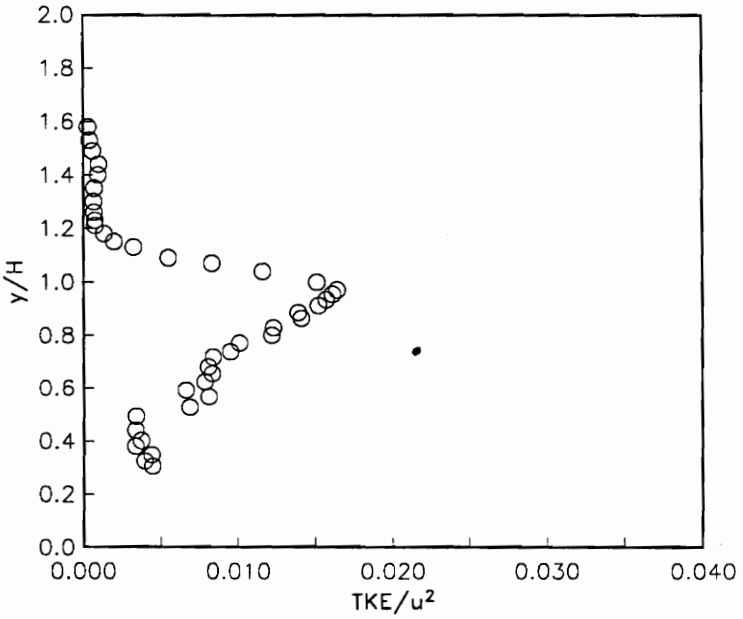

(b) Conventional TKE

FIGURE 5.42: Cross-Wire typical and compressible TKE data (x/H = 15.).

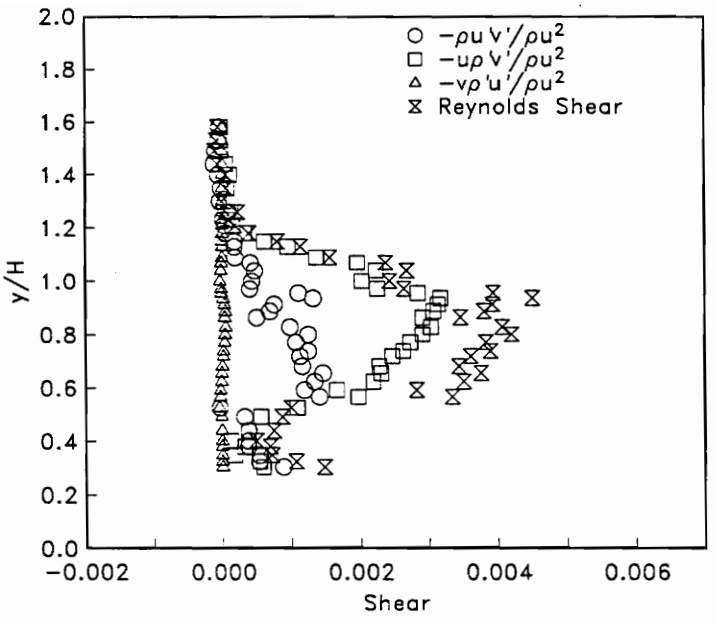

(a) Separated Reynolds Shear (xy)

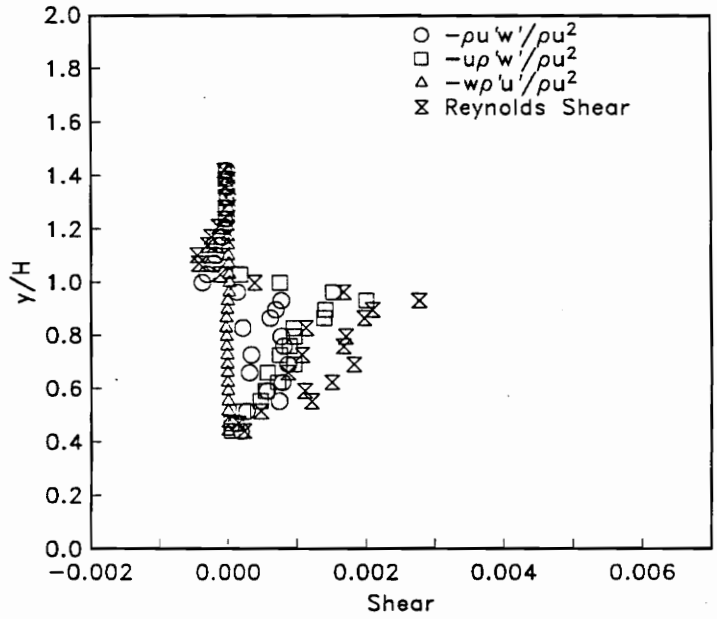

(b) Separated Reynolds Shear (xz)

FIGURE 5.43: Cross-Wire x-y and x-z plane Reynolds shear stress data (x/H = 15.).

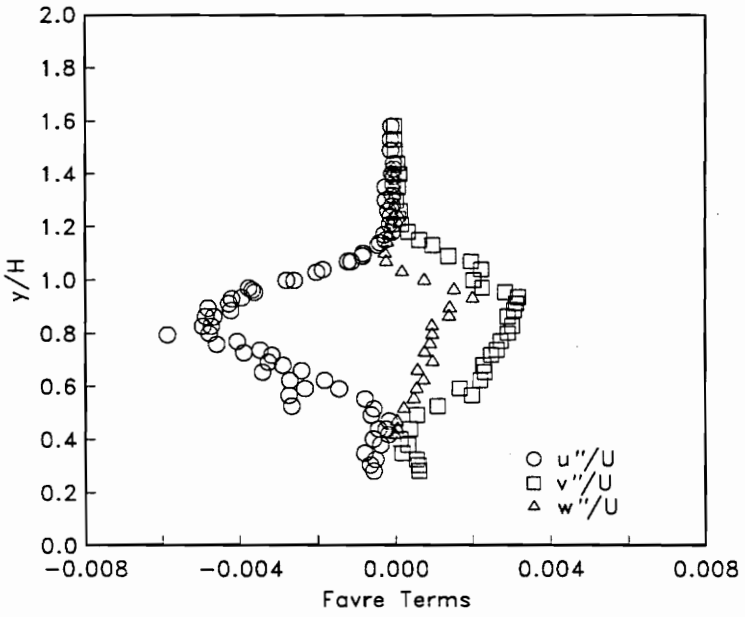

(a) Favre Terms

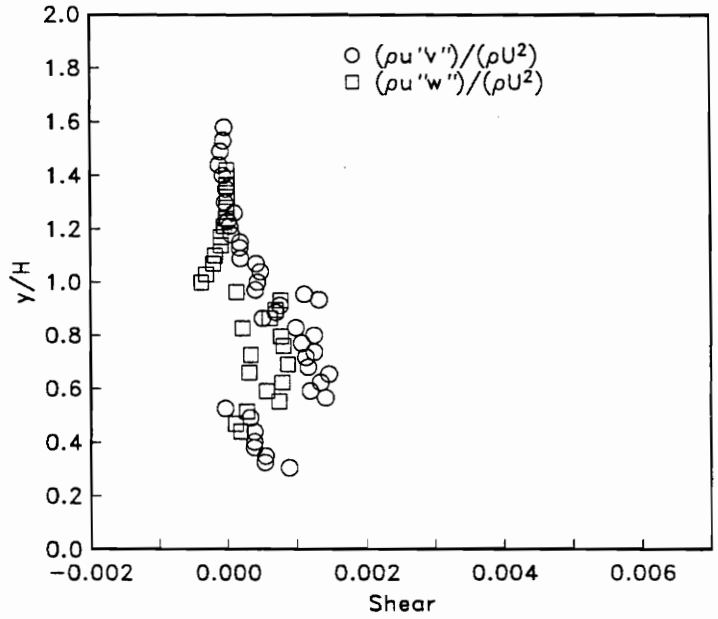

(b) Favre Shear

FIGURE 5.44: Cross-Wire Favre variable data (x/H = 15.).

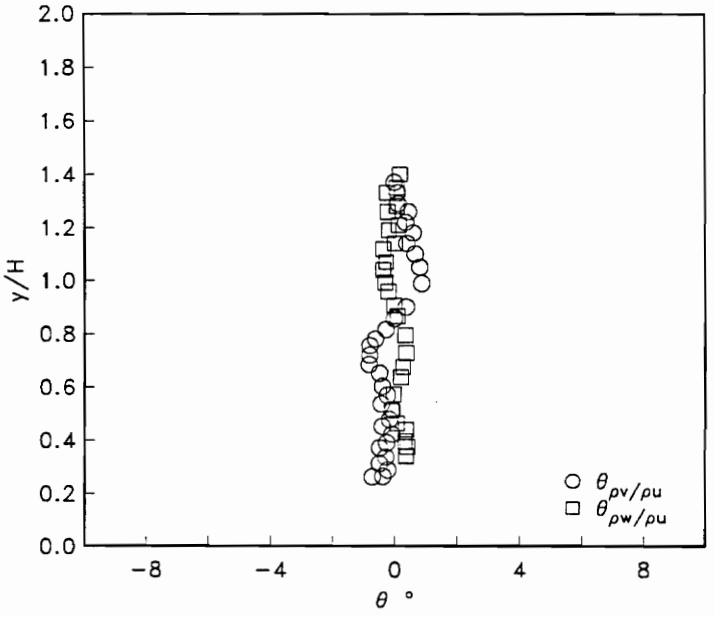

(a) Mass Flux Flow Angle

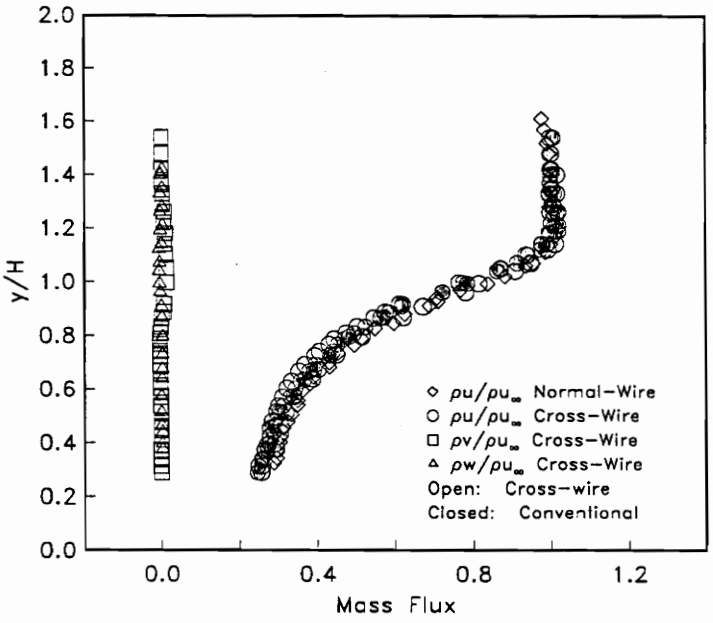

(b) Mass Flux

FIGURE 5.45: Cross-Wire mean flow angle and mass flux data (x/H = 19.).

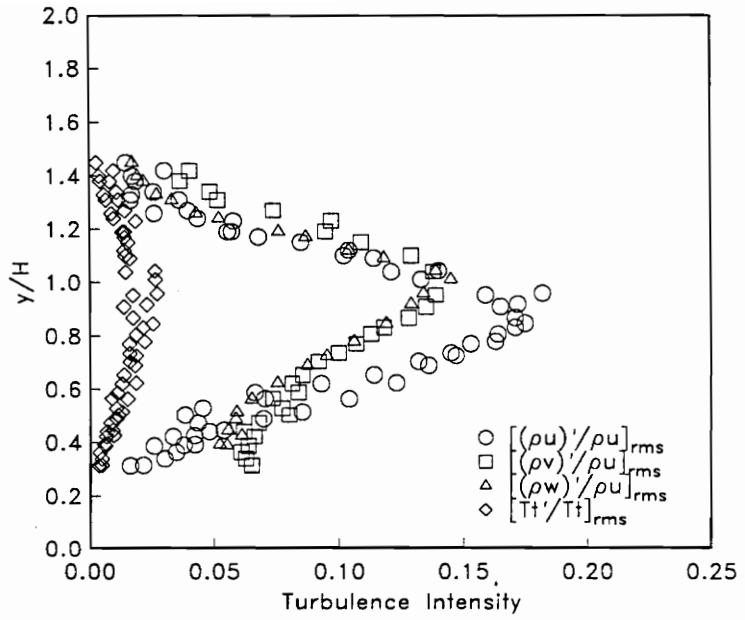

(a) Turbulence Intensities

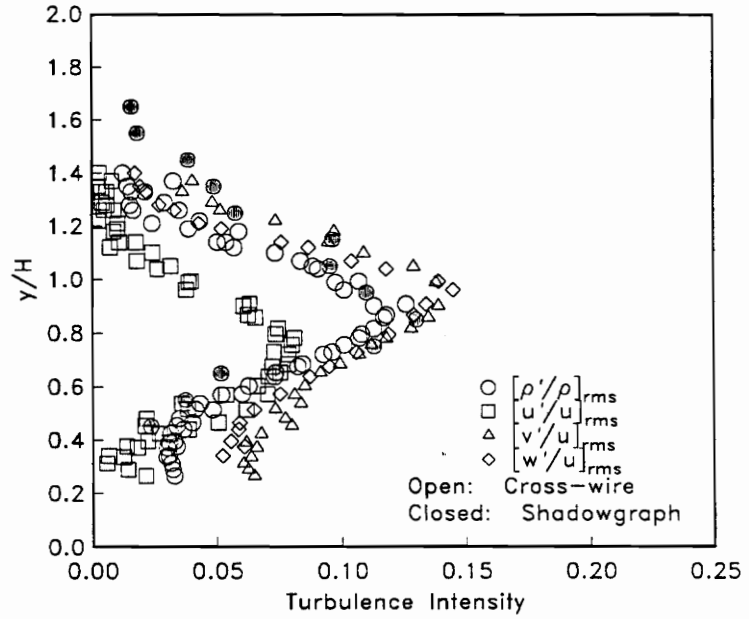

(b) Separated Turbulence Intensities

FIGURE 5.46: Cross-Wire turbulence intensity data (x/H = 19.).

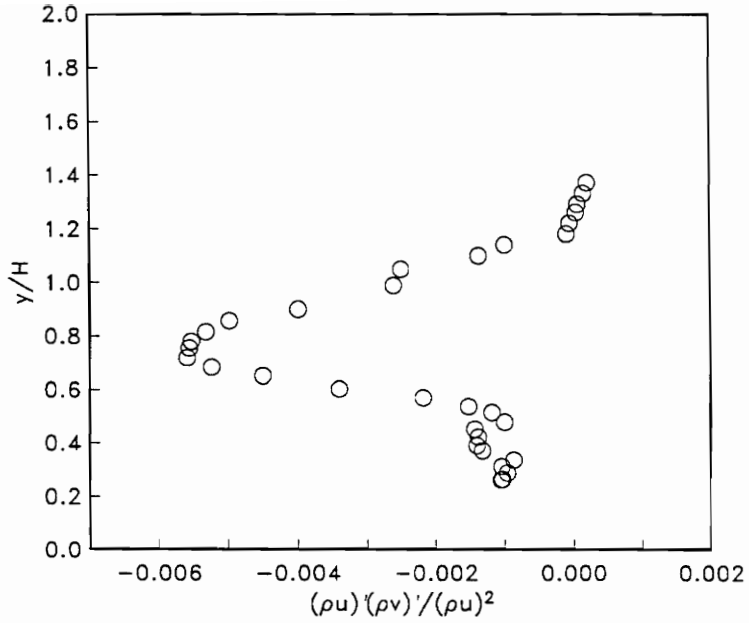

(a) Cross−Wire Shear Term

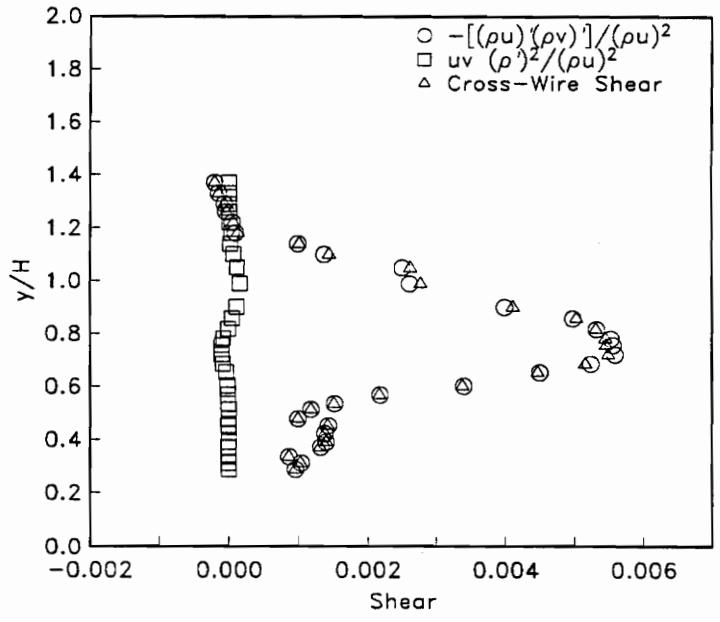

(b) Compressible Shear Terms

FIGURE 5.47: Cross-Wire transformed turbulent x-y shear data (x/H = 19.).

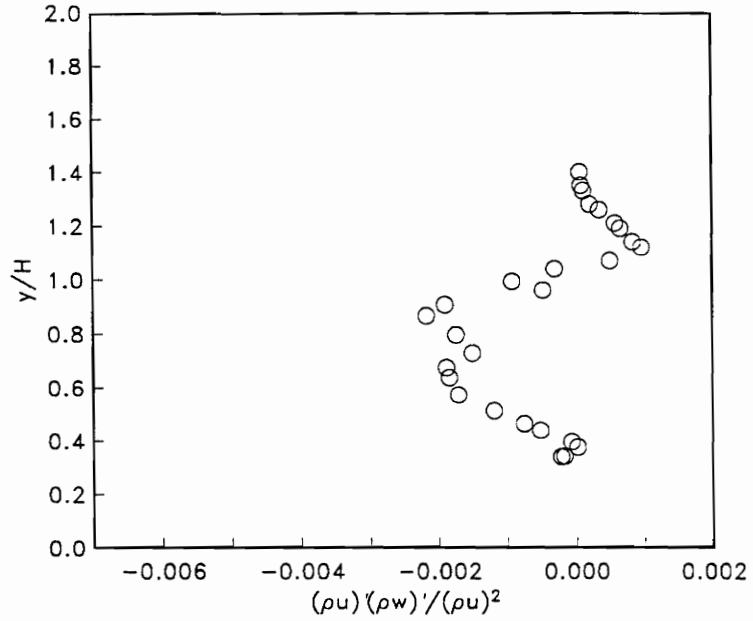

(a) Cross-Wire Shear Term

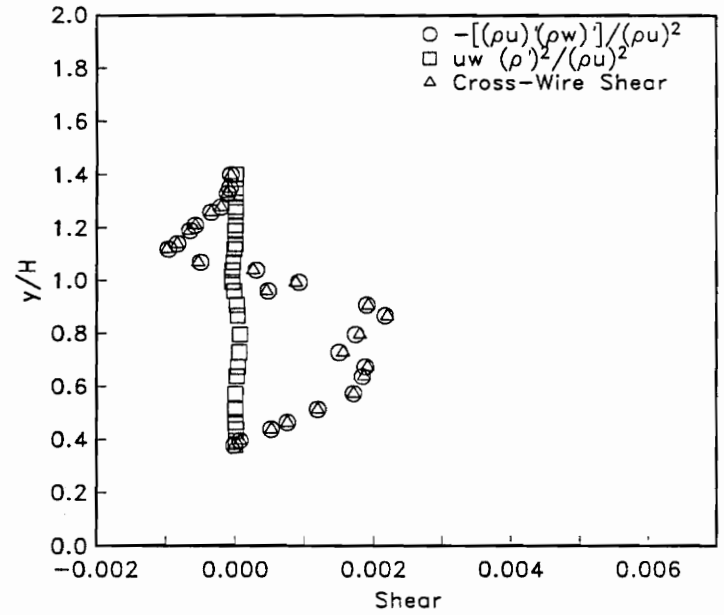

(b) Compressible Shear Terms

FIGURE 5.48: Cross-Wire transformed turbulent x-z shear data (x/H = 19.).

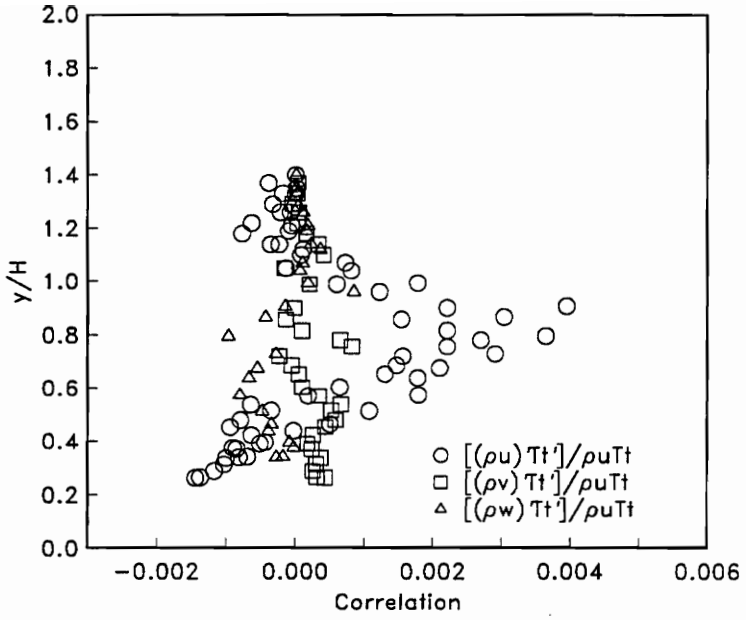

(a) Mass Flux–Total Temperature Correlations

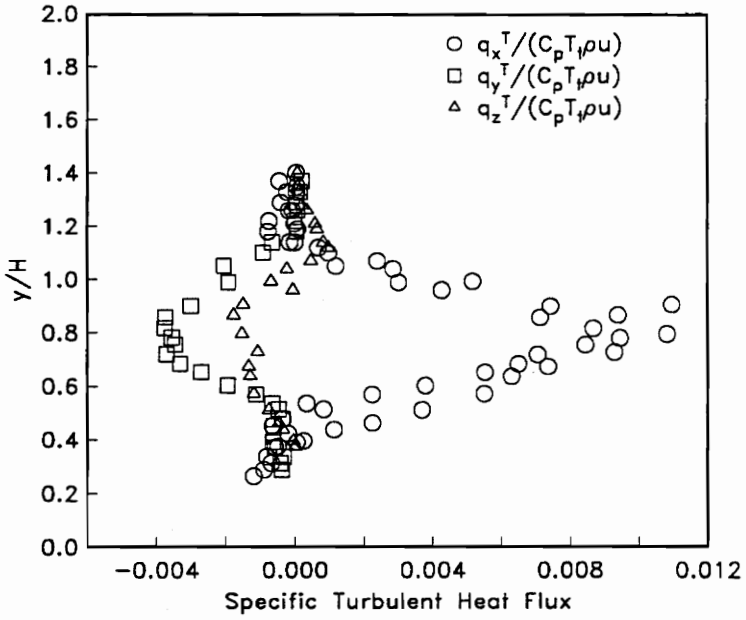

(b) Specific Turbulent Heat Flux

FIGURE 5.49: Cross-Wire turbulent heat flux data (x/H = 19.).

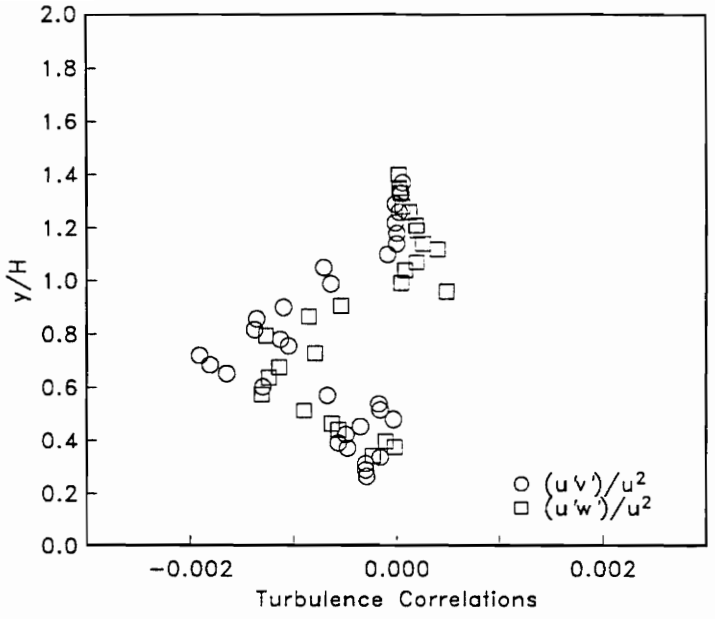

(a) Velocity–Velocity Correlations

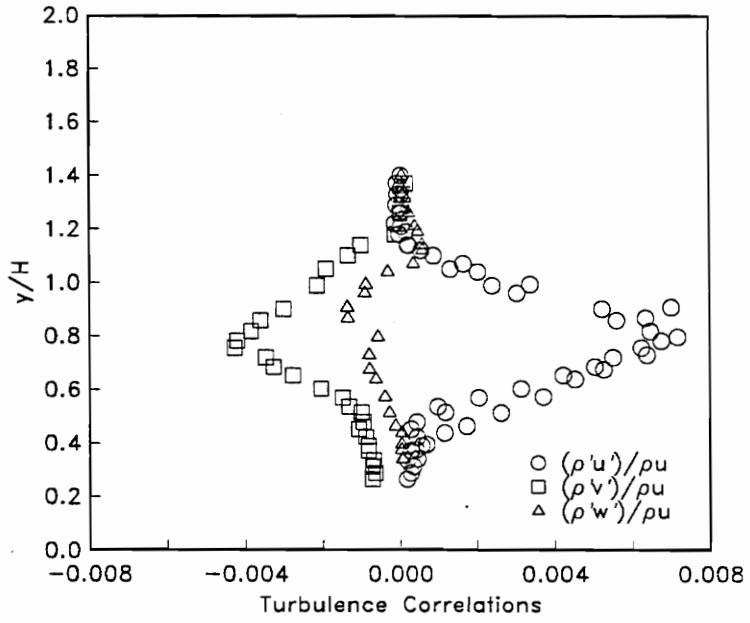

(b) Velocity–Density Correlations

FIGURE 5.50: Cross-Wire velocity-velocity and density-velocity correlation data (x/H = 19.).

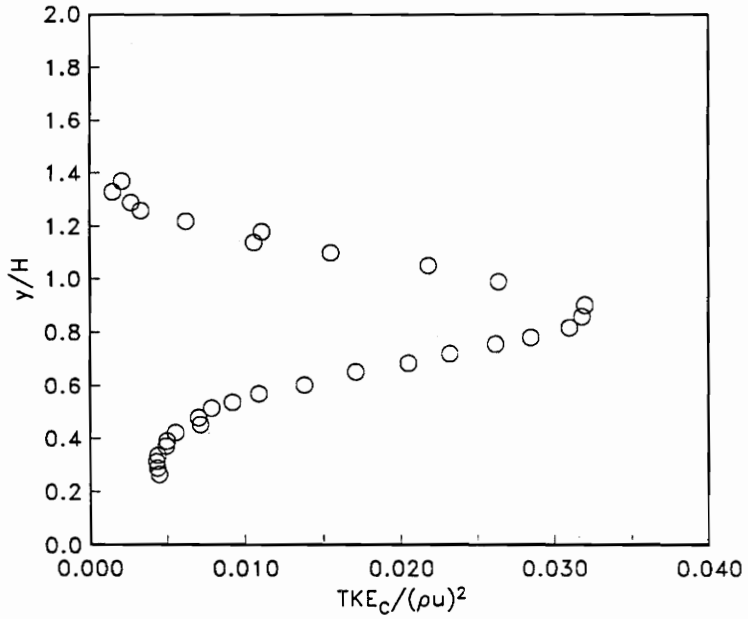

(a) Compressible TKE

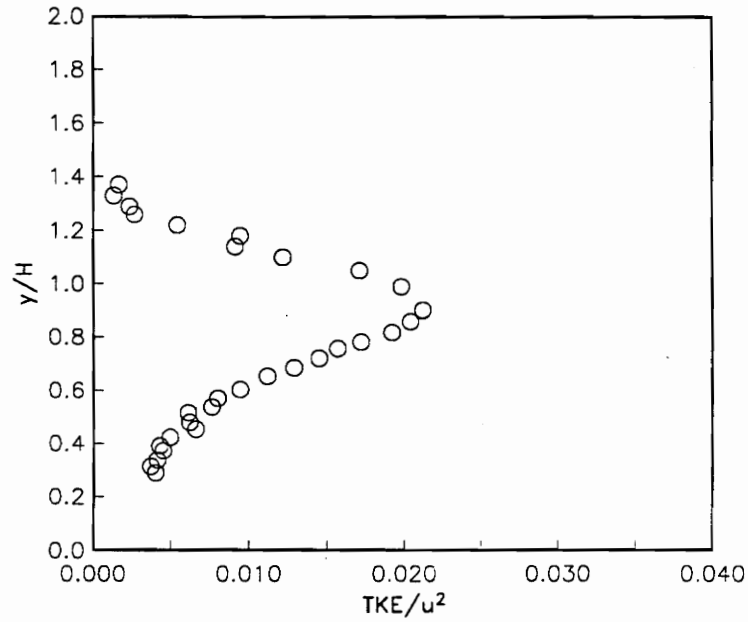

(b) Conventional TKE

FIGURE 5.51: Cross-Wire typical and compressible TKE data (x/H = 19.).

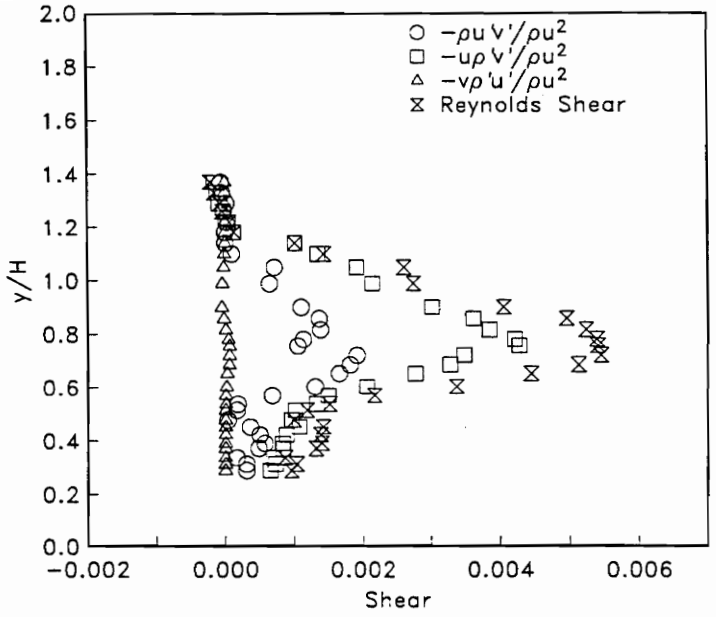

(a) Separated Reynolds Shear (xy)

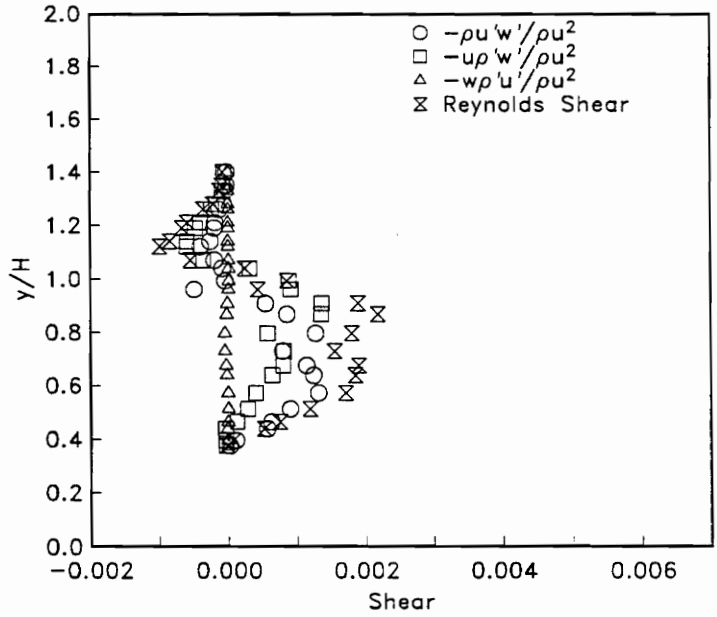

(b) Separated Reynolds Shear (xz)

FIGURE 5.52: Cross-Wire x-y and x-z plane Reynolds shear stress data (x/H = 19.).

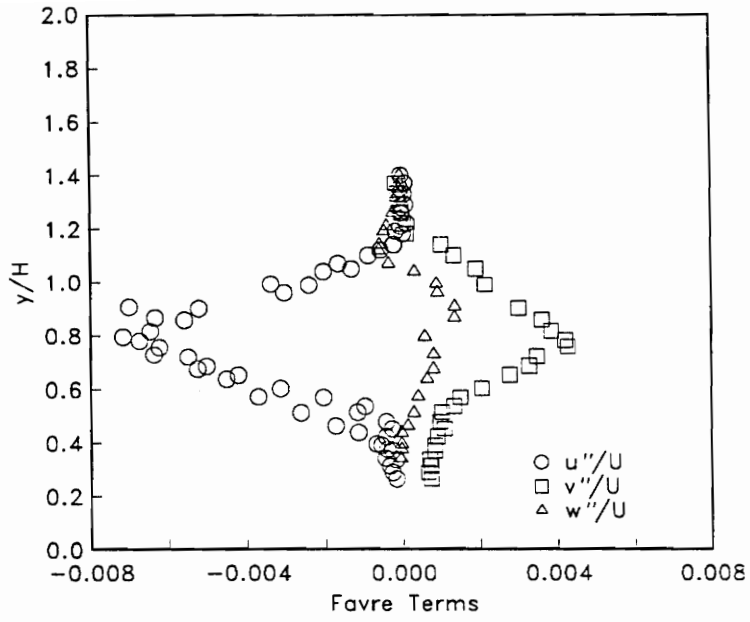

(a) Favre Terms

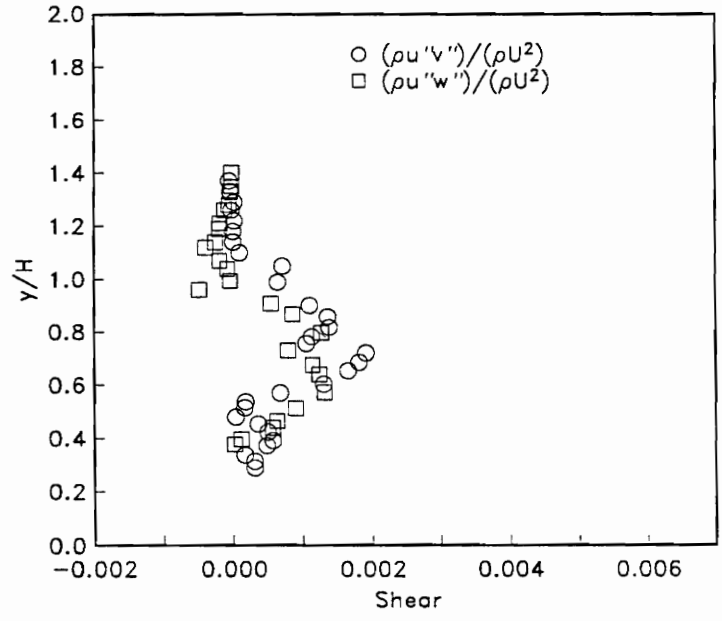

(b) Favre Shear

FIGURE 5.53: Cross-Wire Favre variable data (x/H = 19.).

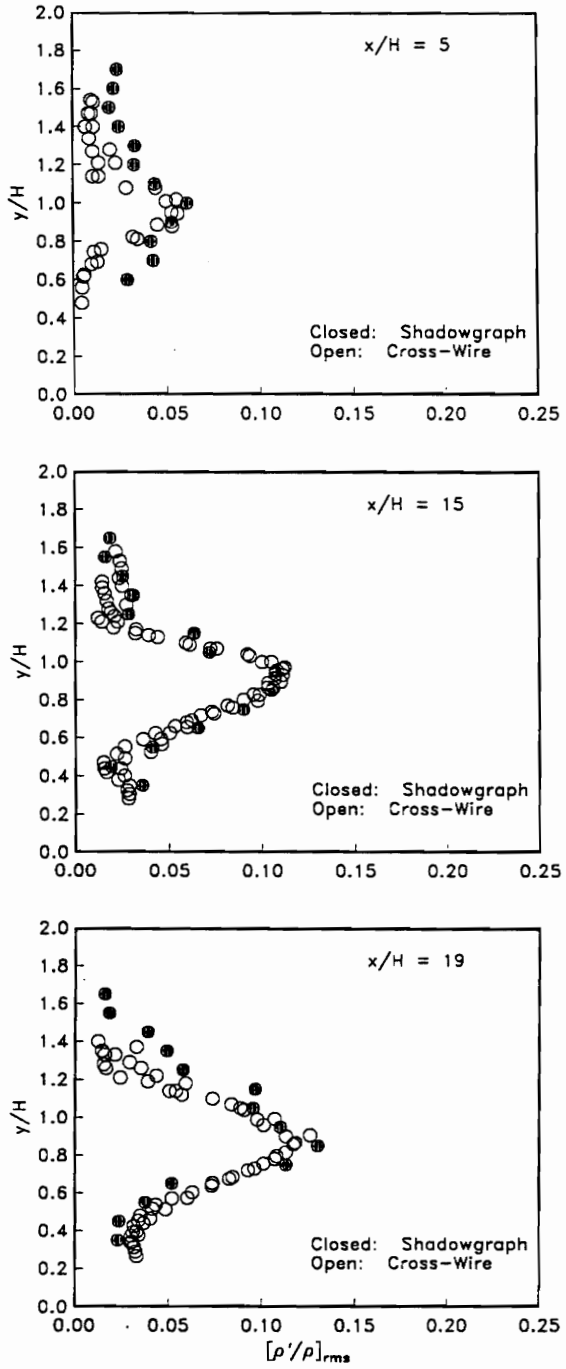

FIGURE 5.54: Shadowgraph density turbulence intensities.

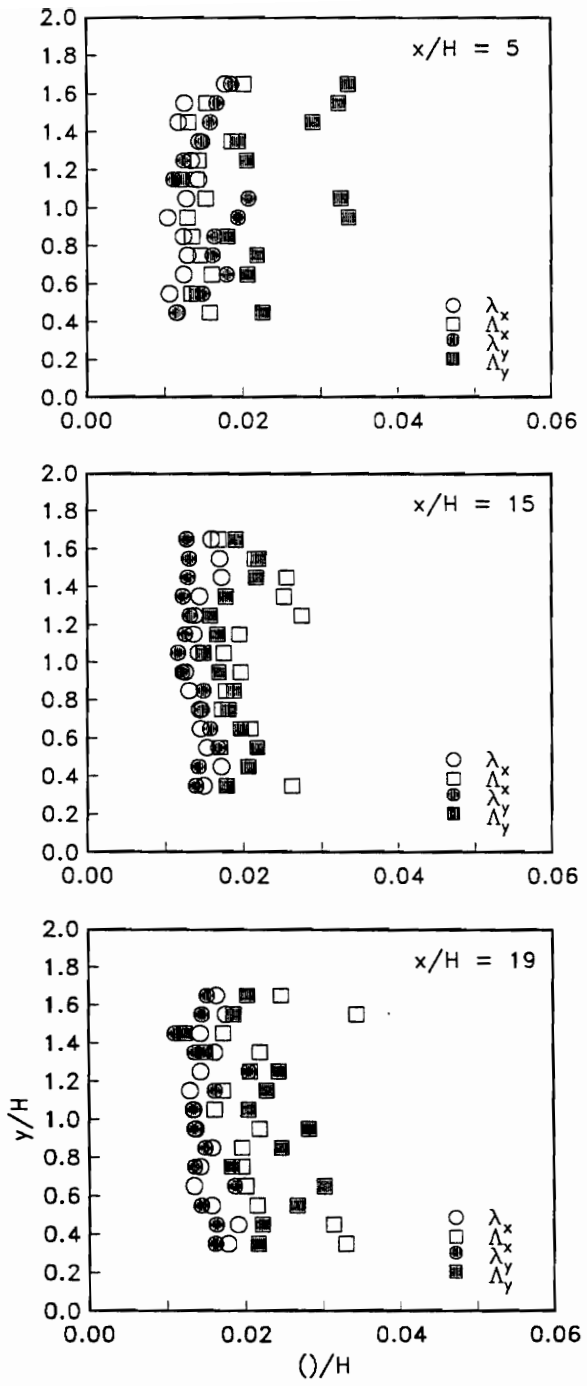

FIGURE 5.55: Shadowgraph length scales.

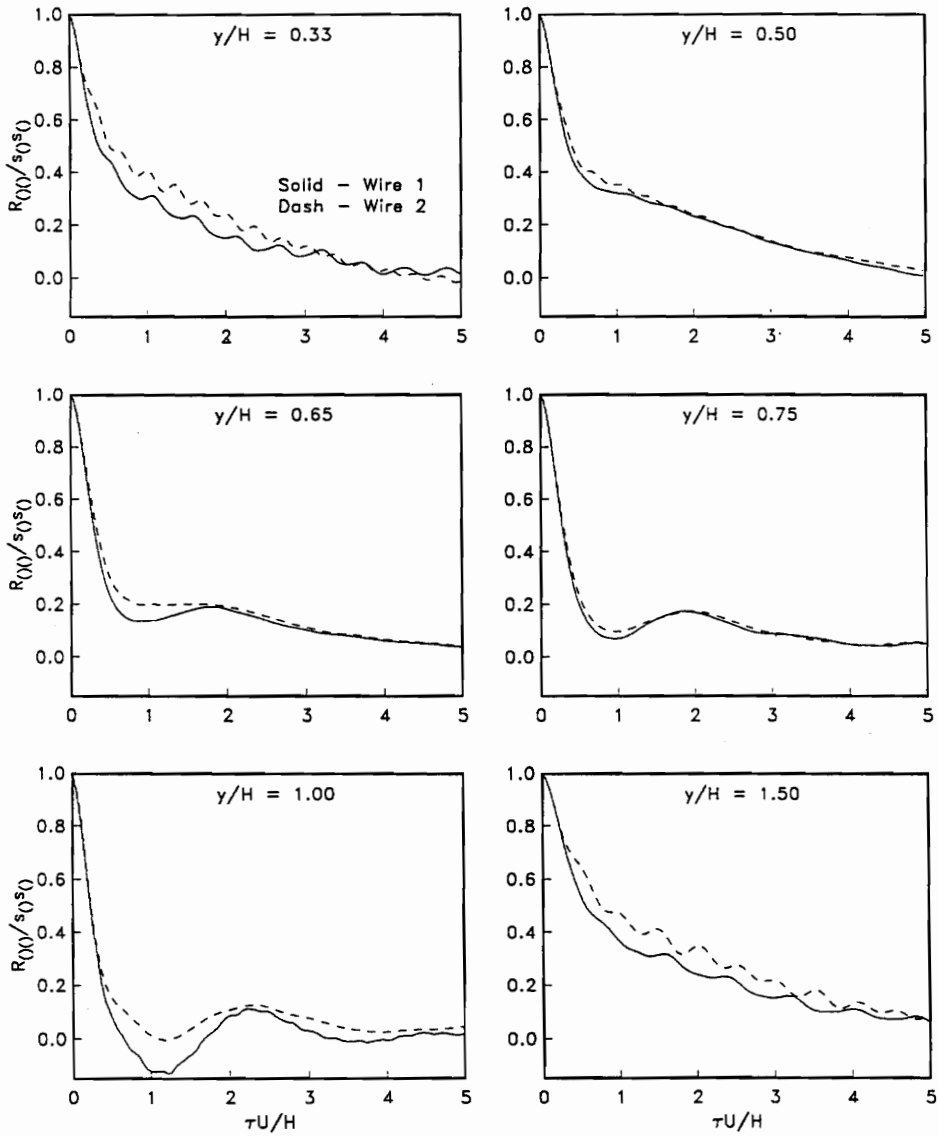

FIGURE 5.56: Parallel-wire auto correlations (x/H=15).

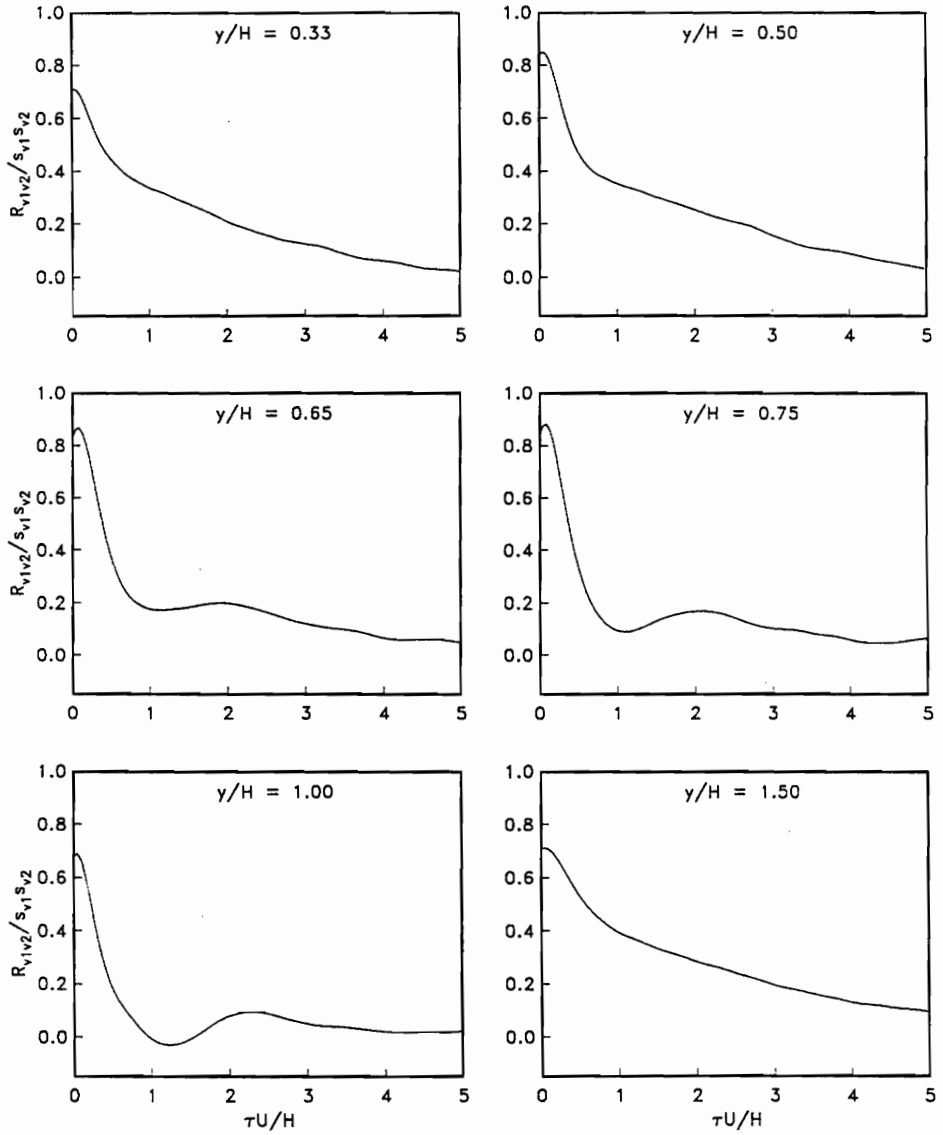

FIGURE 5.57: Parallel-wire cross correlations (x/H=15).

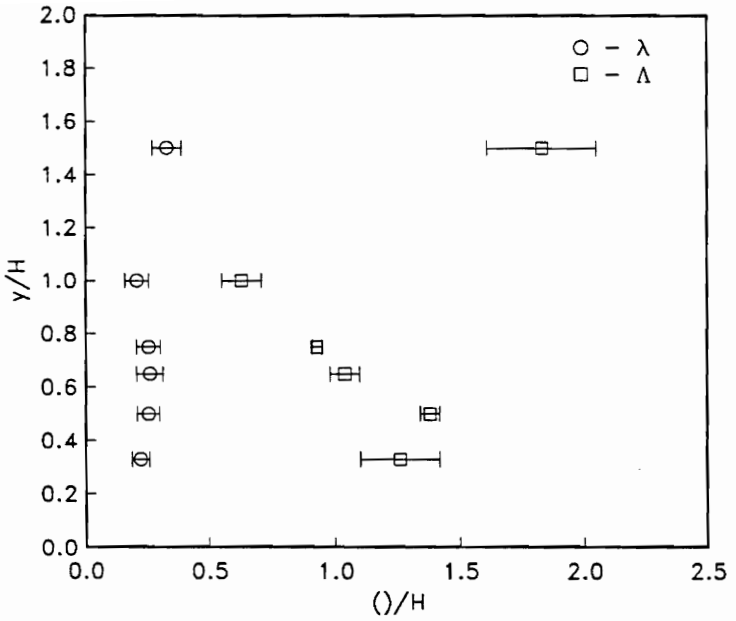

(a) Length Scales

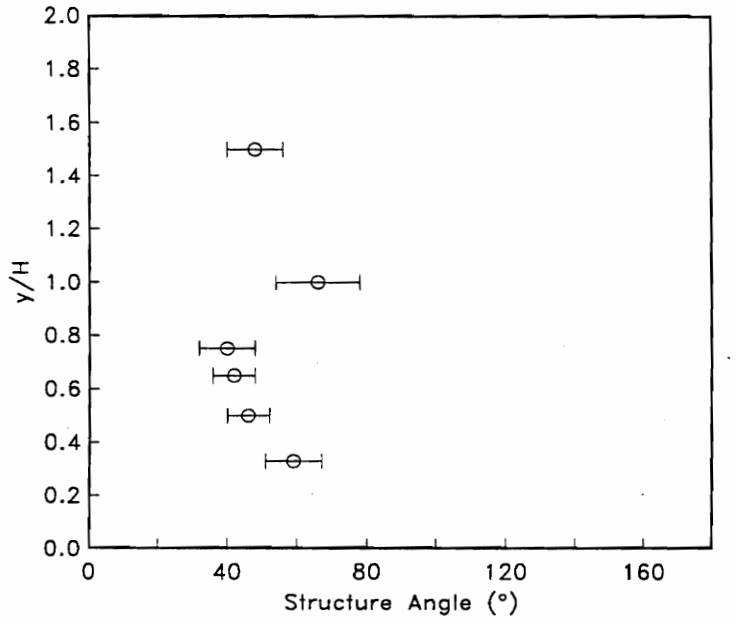

(b) Structure Angle

FIGURE 5.58: Parallel-wire length scales and structure angle (x/H=15).

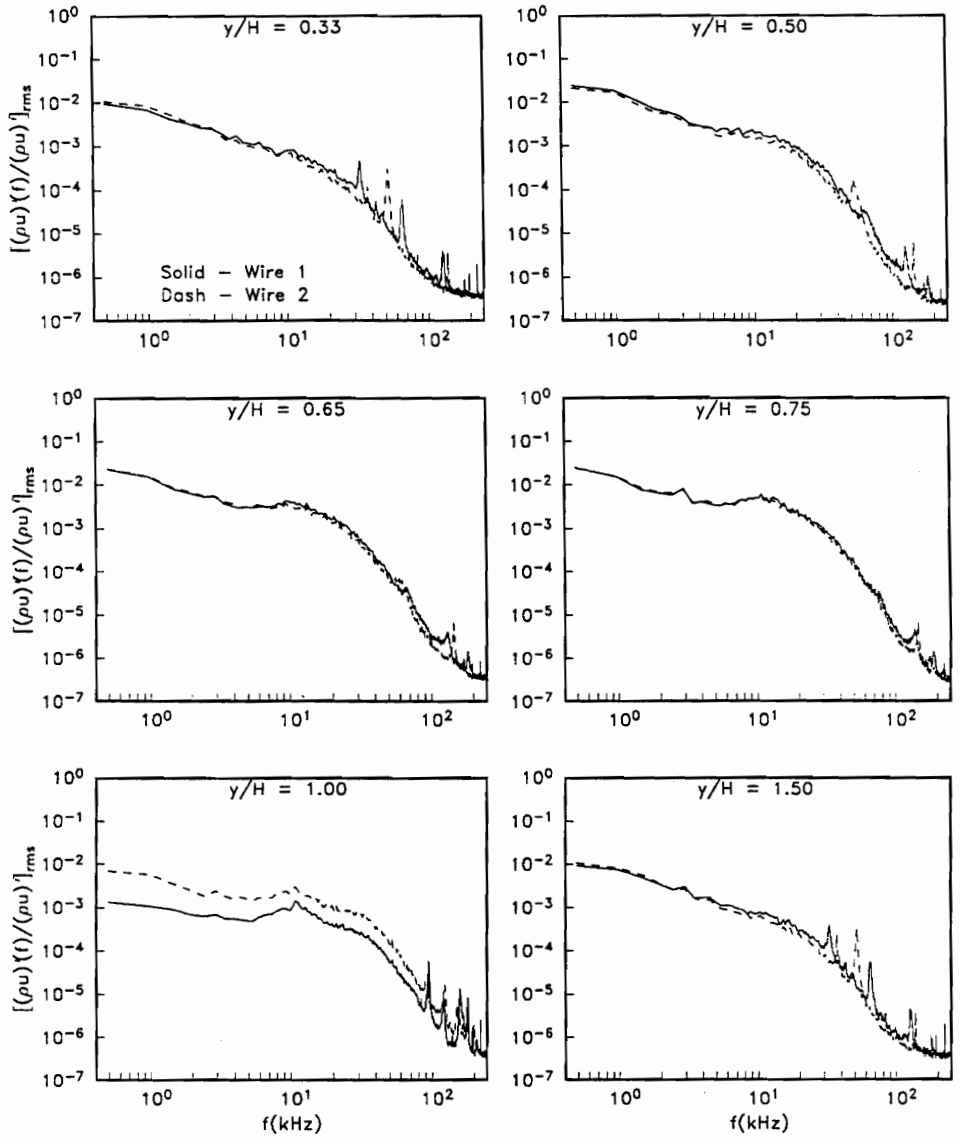

FIGURE 5.59: Parallel-wire power spectra (x/H=15).

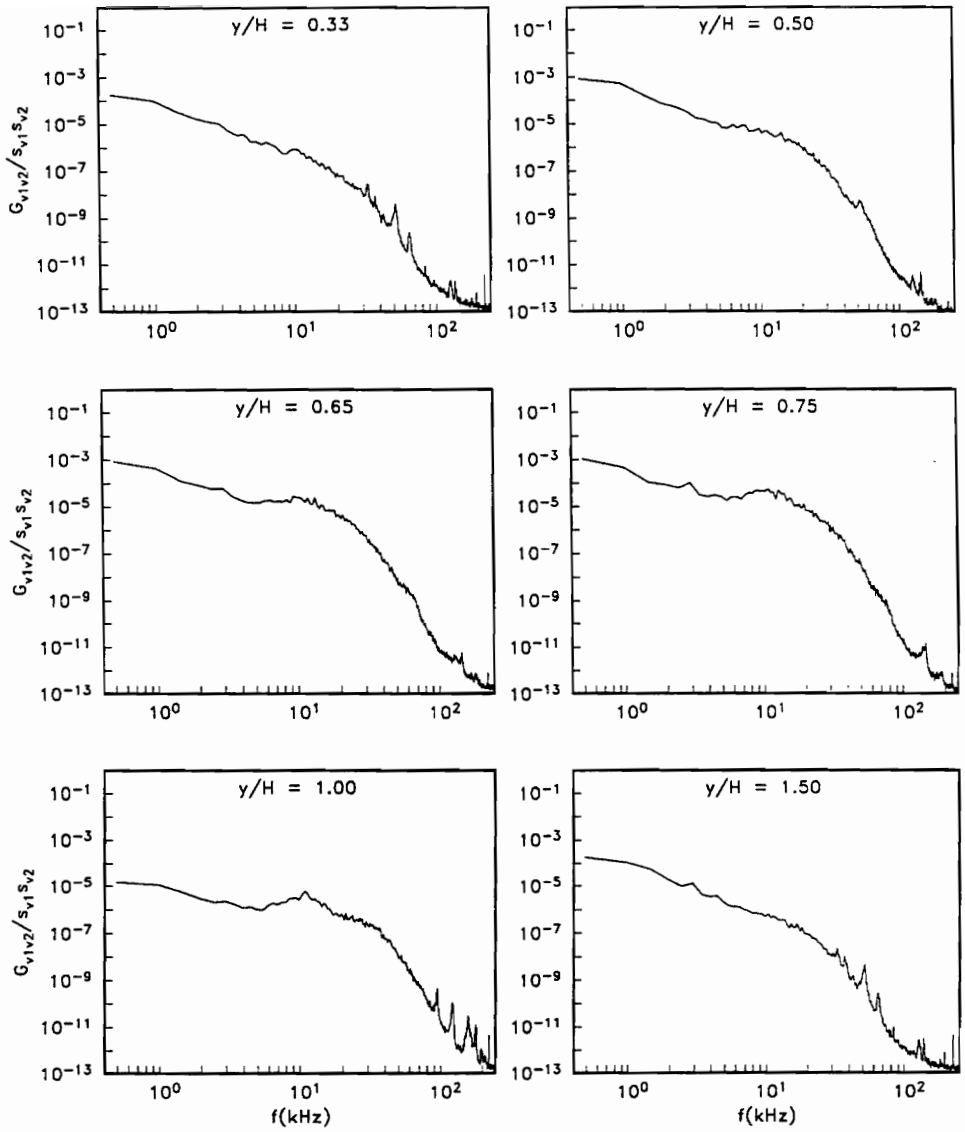

FIGURE 5.60: (a) Parallel-wire cross spectra magnitude (x/H=15).

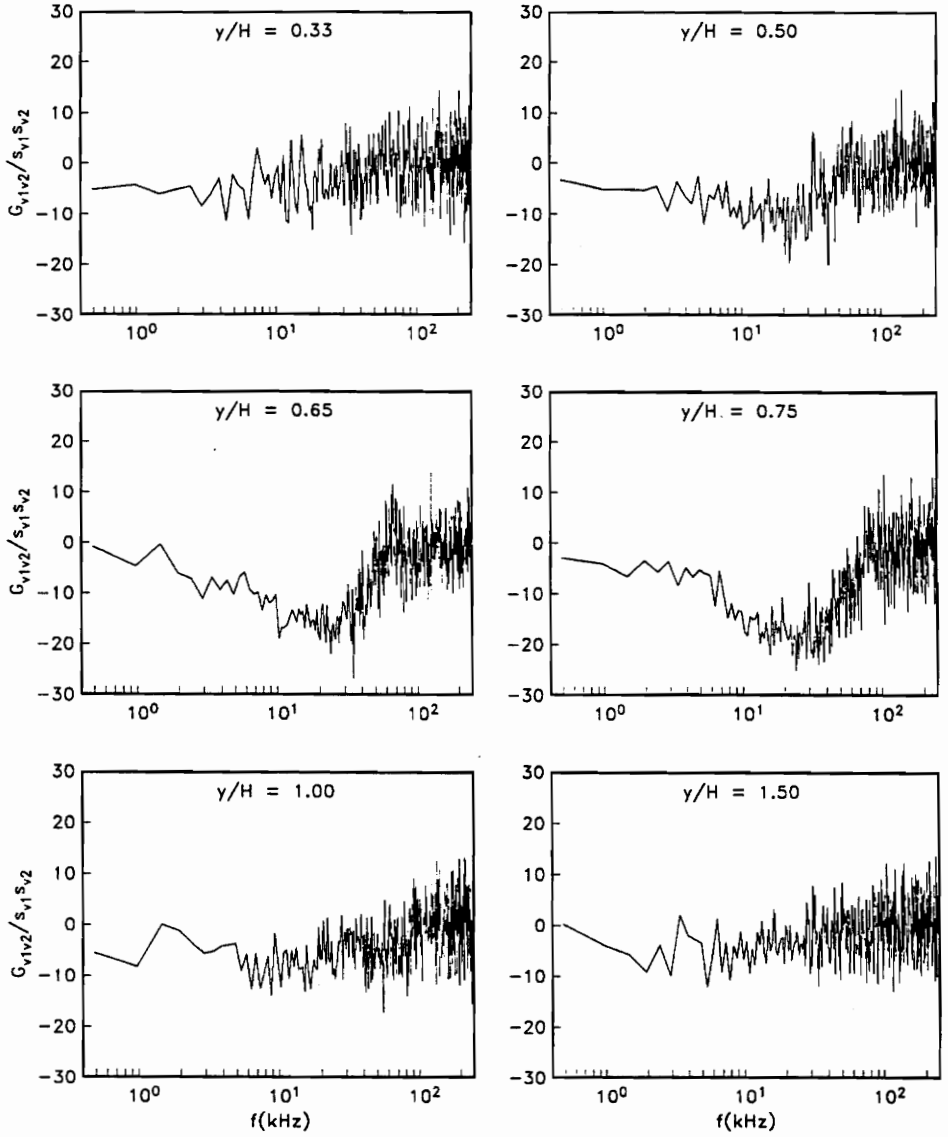

FIGURE 5.60: (b) Parallel-wire cross spectra phase (x/H = 15).

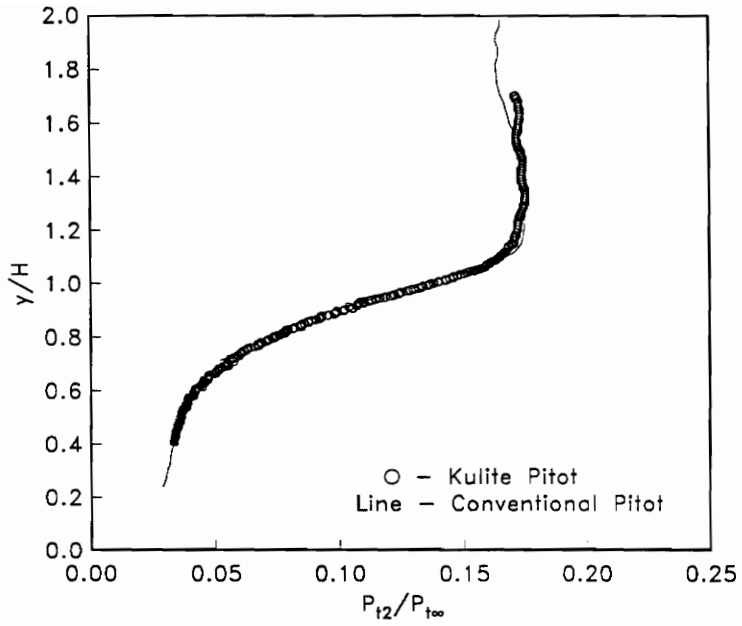

(a) Kulite Pressure

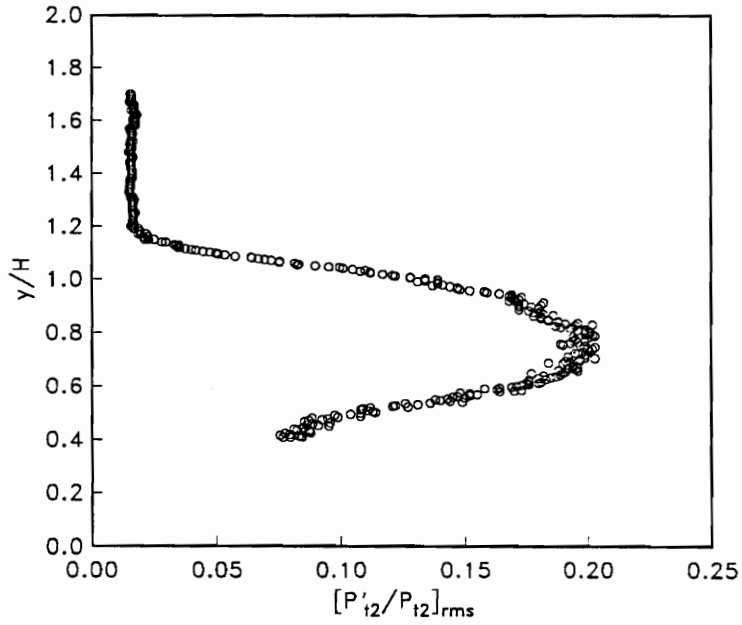

(b) Turbulence Intensity

FIGURE 5.61: Kulite Pitot probe mean and rms data (x/H = 15).

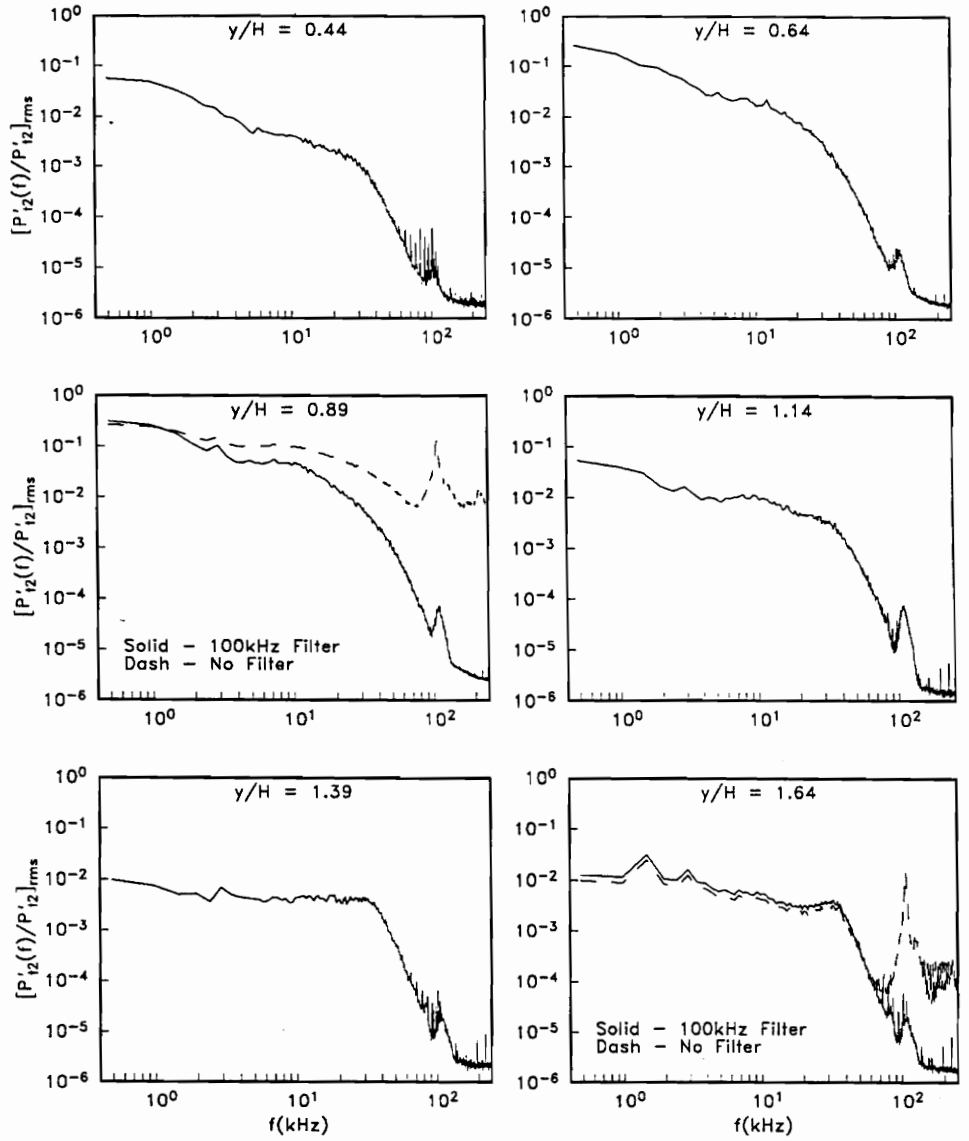

FIGURE 5.62: Kulite Pitot pressure power spectra (x/H = 15).

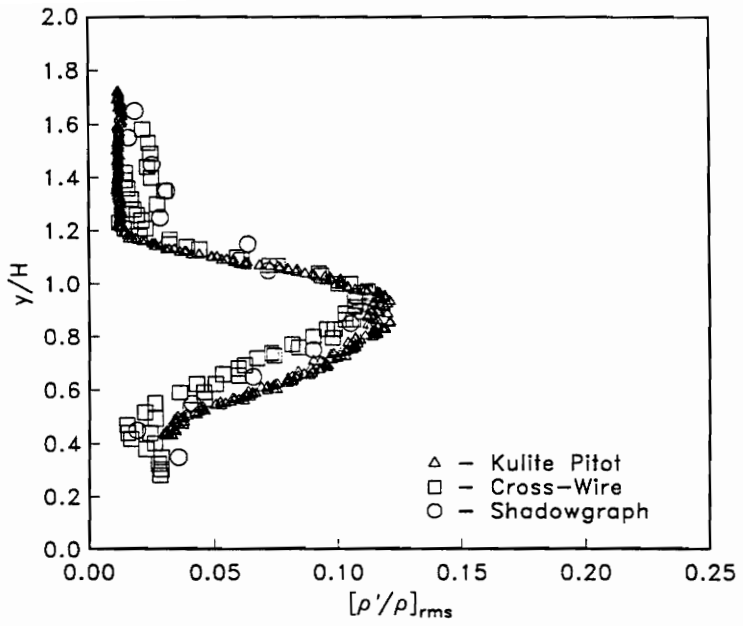

(a) Density Turbulence Intensity

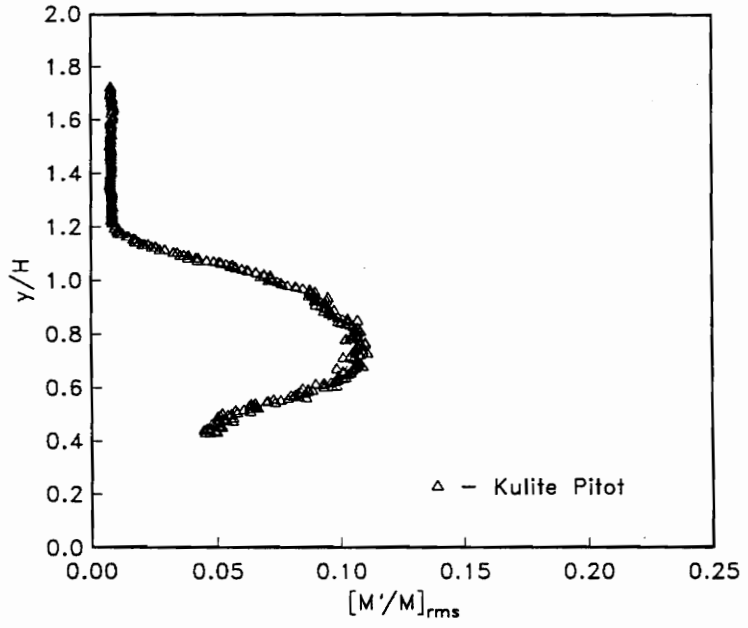

(b) Mach Number Turbulence Intensity

FIGURE 5.63: Kulite Pitot probe density and Mach number turbulence intensities (x/H = 15).

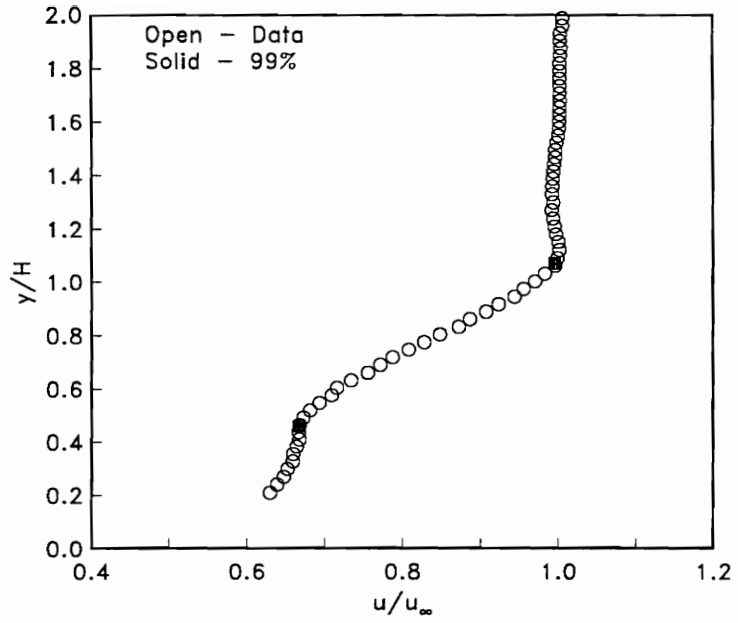

(a) Velocity Profile

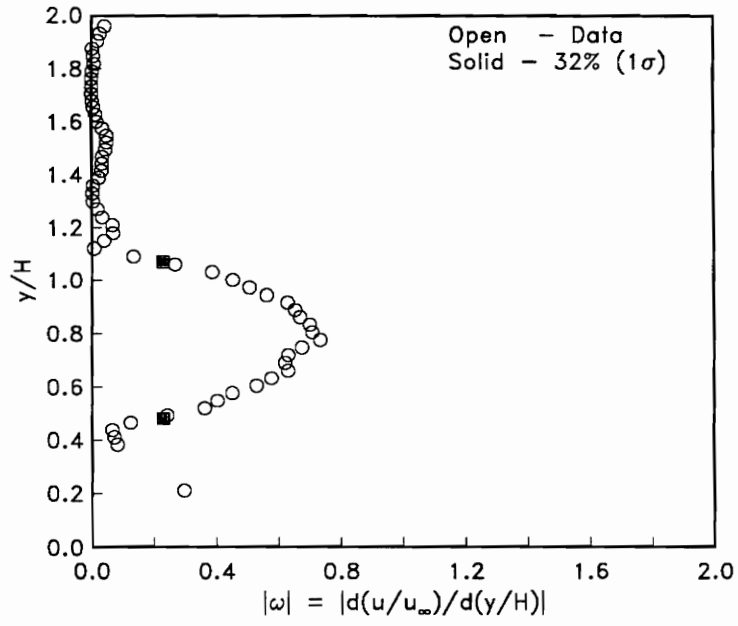

(b) Vorticity

FIGURE 5.64: (a) Velocity edge search (99%). (b) Vorticity edge search (32%).

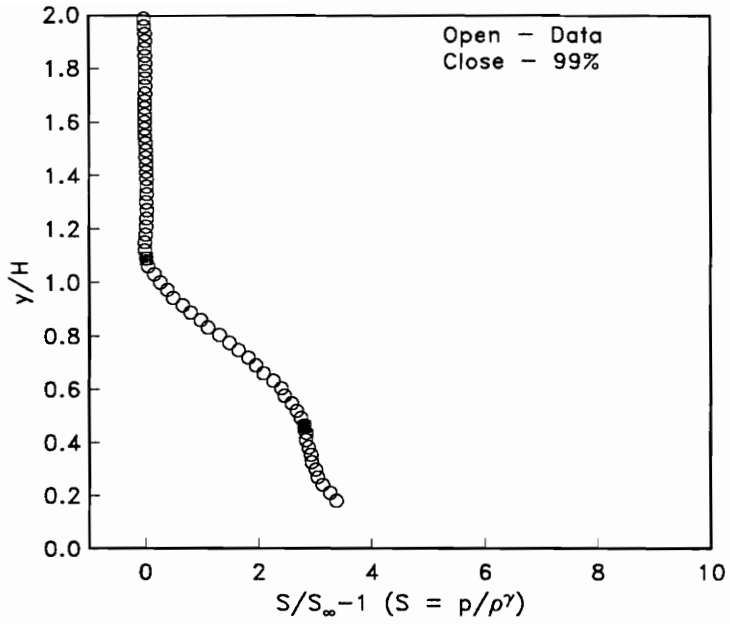

(a) Entropy

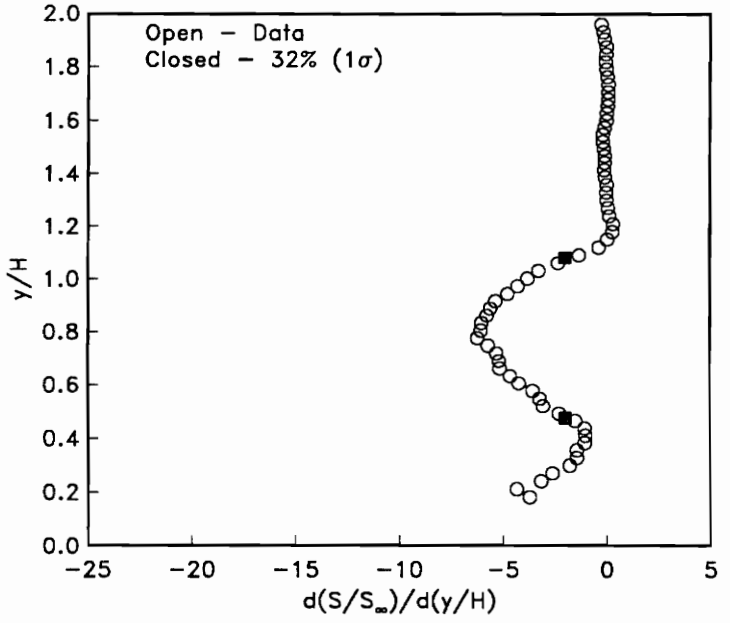

(b) Entropy Gradient

FIGURE 5.65: (a) Entropy edge search (99%). (b) Entropy gradient edge search (32%).

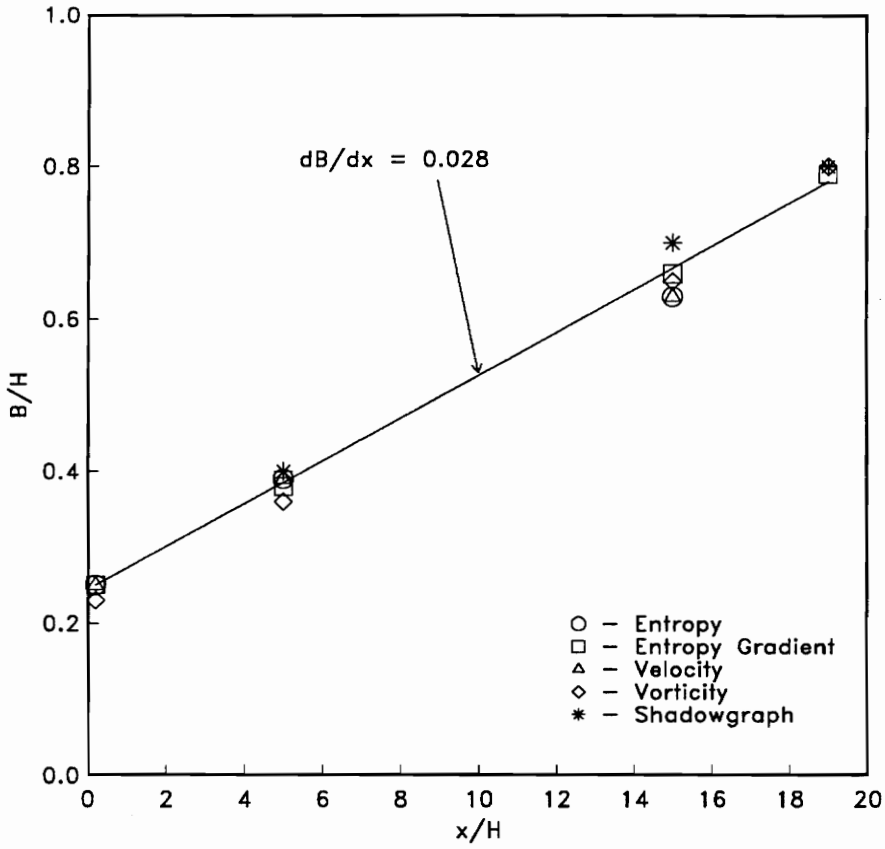

FIGURE 5.66: Shear layer spreading rate.

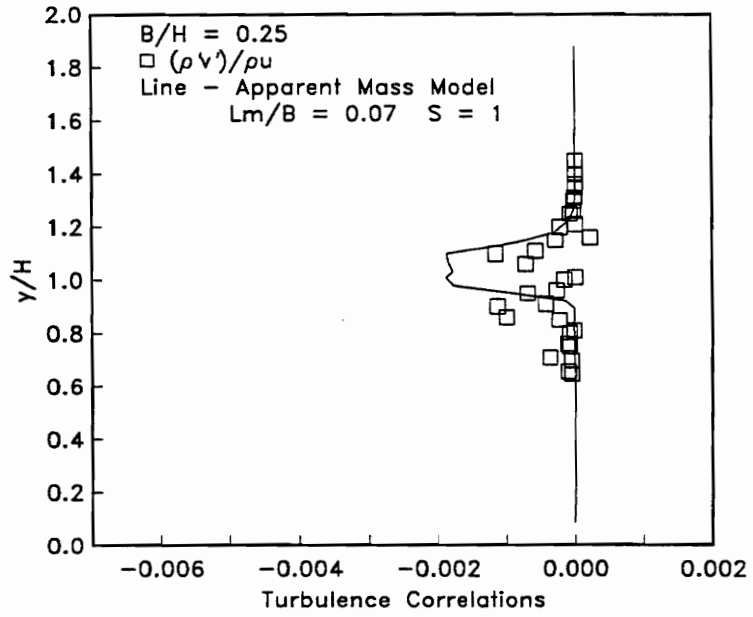

(a) Mixing Length Apparent Mass Model

FIGURE 6.1: CAMMLE model apparent mass (Eqn. (2.13)) evaluation (x/H = 0.2).

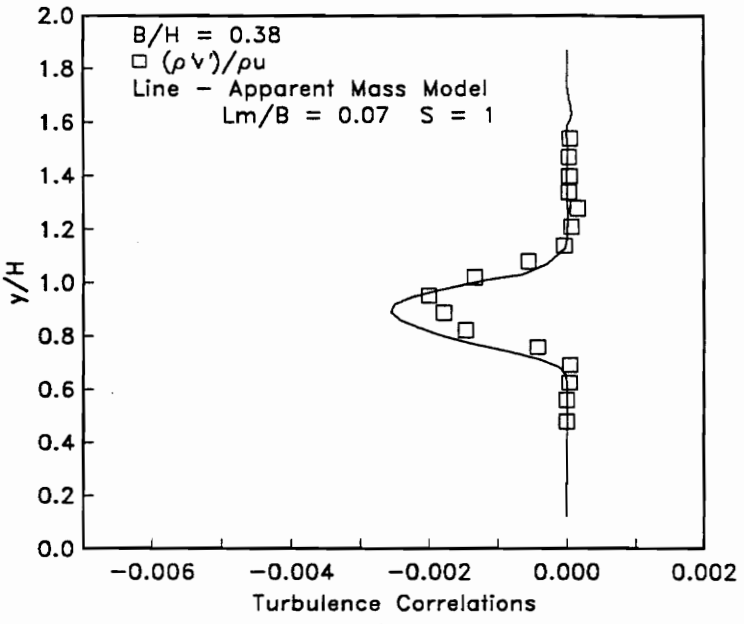

(a) Mixing Length Apparent Mass Model

FIGURE 6.2: CAMMLE model apparent mass (Eqn. (2.13)) evaluation (x/H = 5.0).

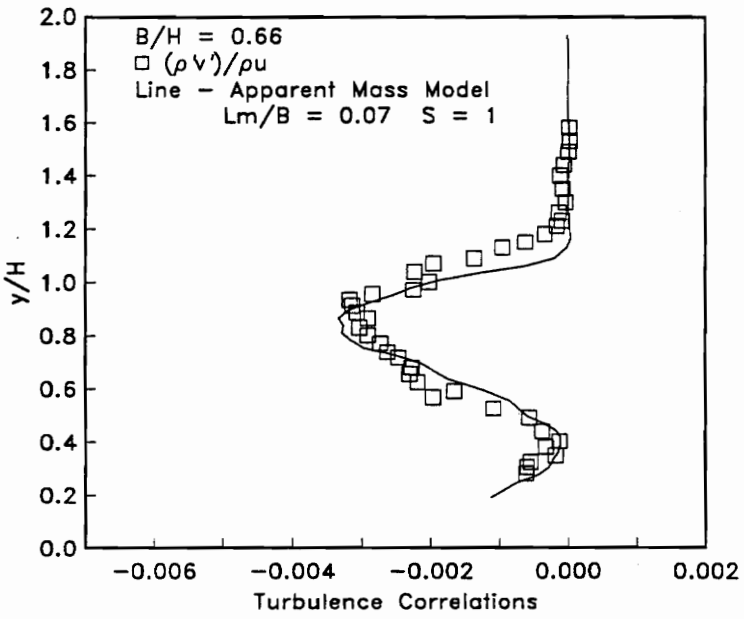

(a) Mixing Length Apparent Mass Model

FIGURE 6.3: CAMMLE model apparent mass (Eqn. (2.13)) evaluation (x/H = 15.).

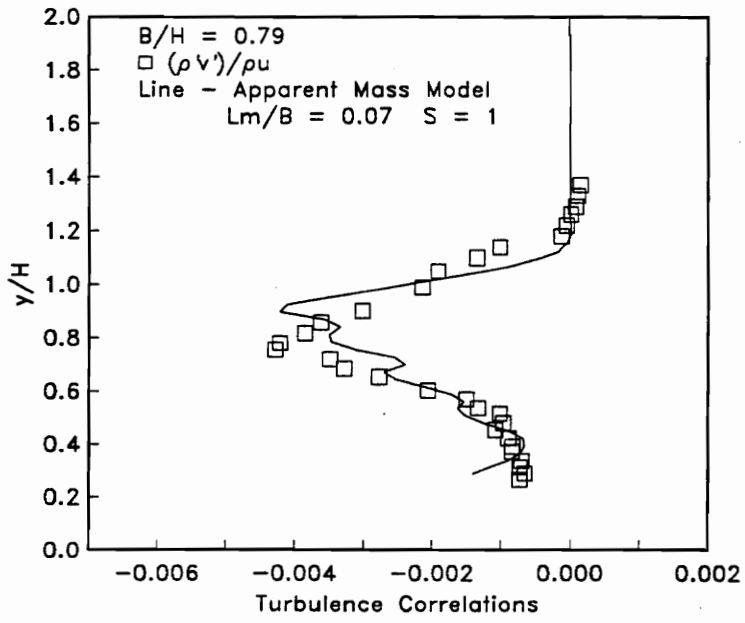

(a) Mixing Length Apparent Mass Model

FIGURE 6.4: CAMMLE model apparent mass (Eqn. (2.13)) evaluation (x/H = 19.).

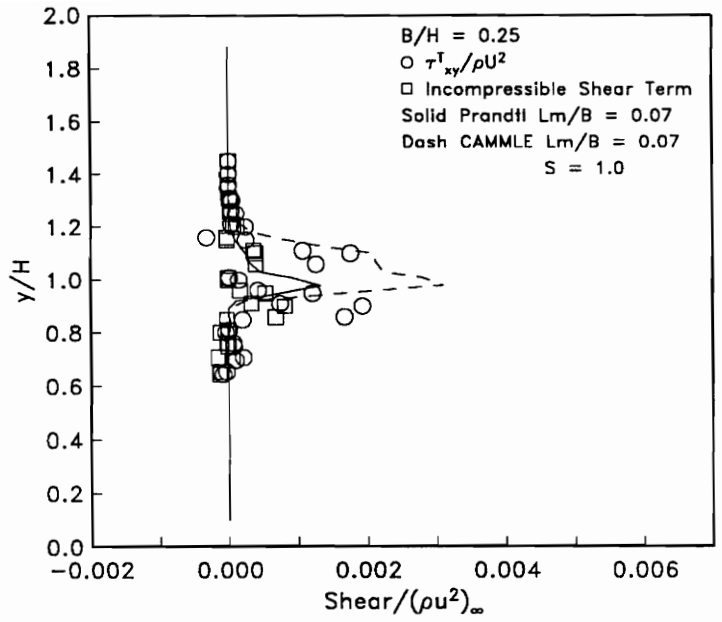

(a) Mixing Length Models

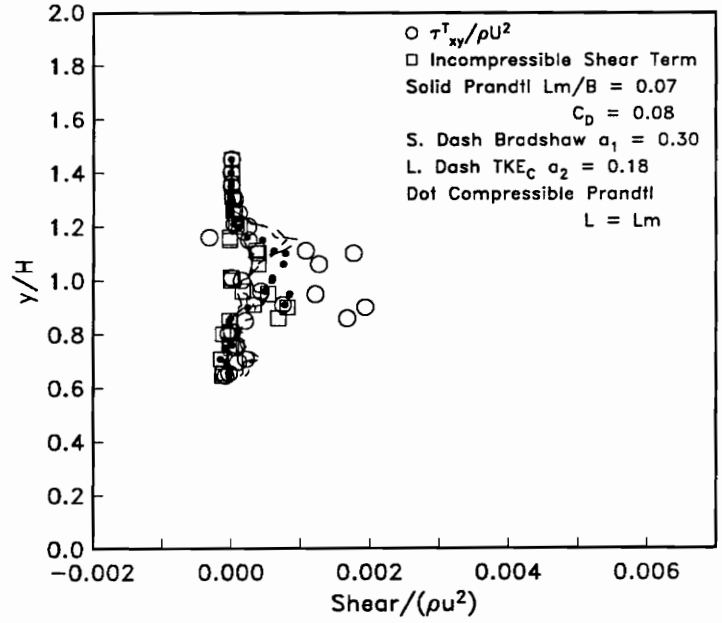

(b) Energy Models

FIGURE 6.5: (a) Prandtl (Eqn. (2.6)) and the Situ-Schetz (= CAMMLE) mixing length shear stress (Eqns. (2.9) or (2.14)) evaluations. (b) Prandtl and Bradshaw incompressible TKE (Eqn. (2.6)), and the new TKE_c (Eqn. (2.8)) evaluations (x/H = 0.2).

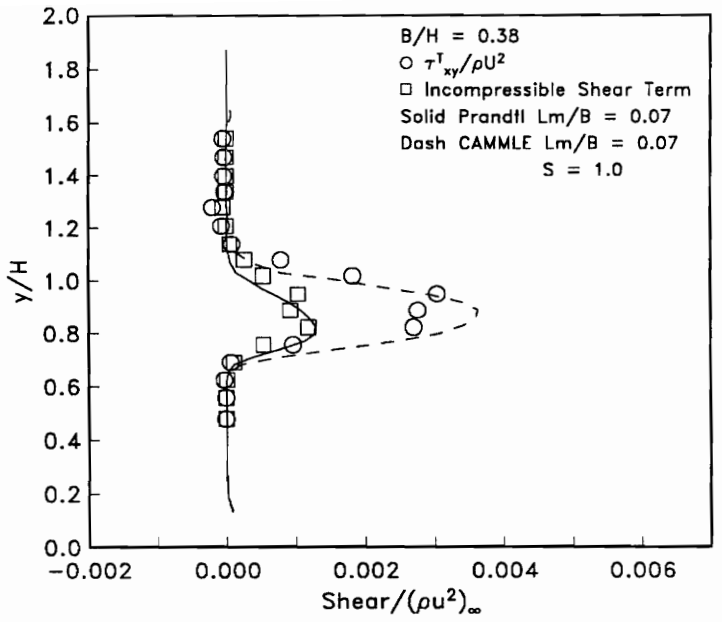

(a) Mixing Length Models

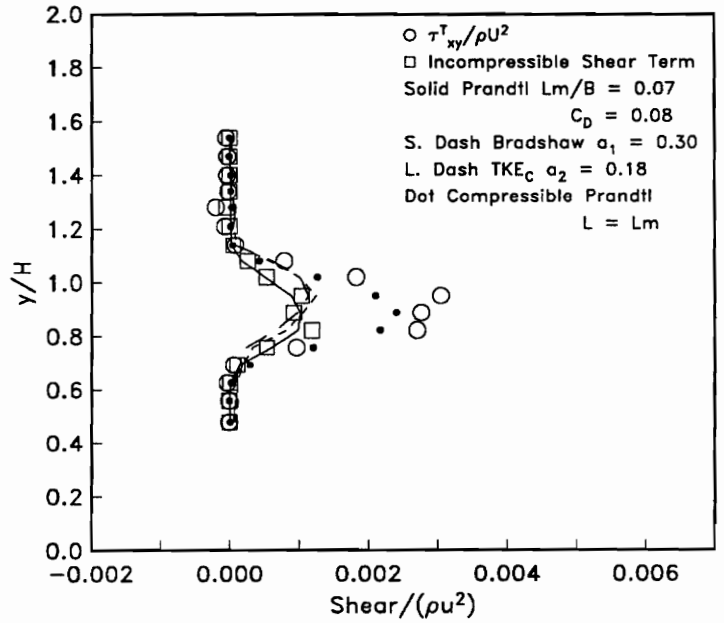

(b) Energy Models

FIGURE 6.6: (a) Prandtl (Eqn. (2.6)) and the Situ-Schetz (= CAMMLE) mixing length shear stress (Eqns. (2.9) or (2.14)) evaluations. (b) Prandtl and Bradshaw incompressible TKE (Eqn. (2.6)), and the new TKE_c (Eqn. (2.8)) evaluations (x/H = 5.0).

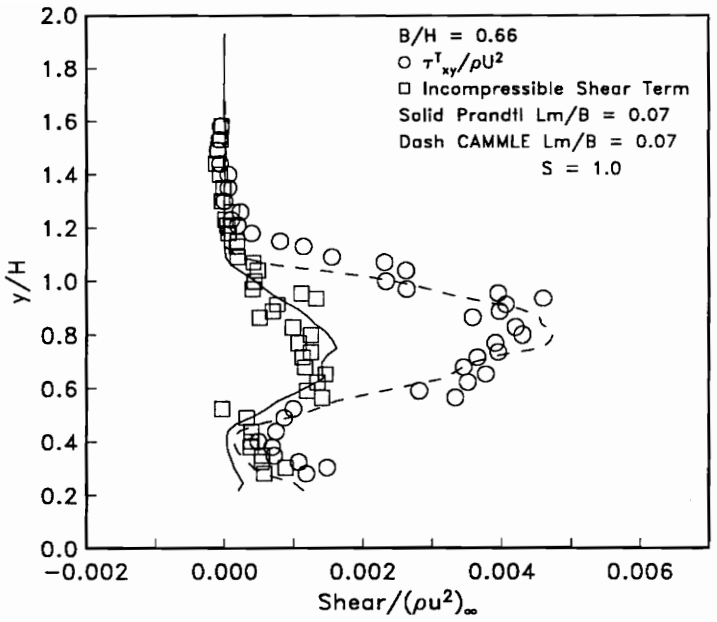

(a) Mixing Length Models

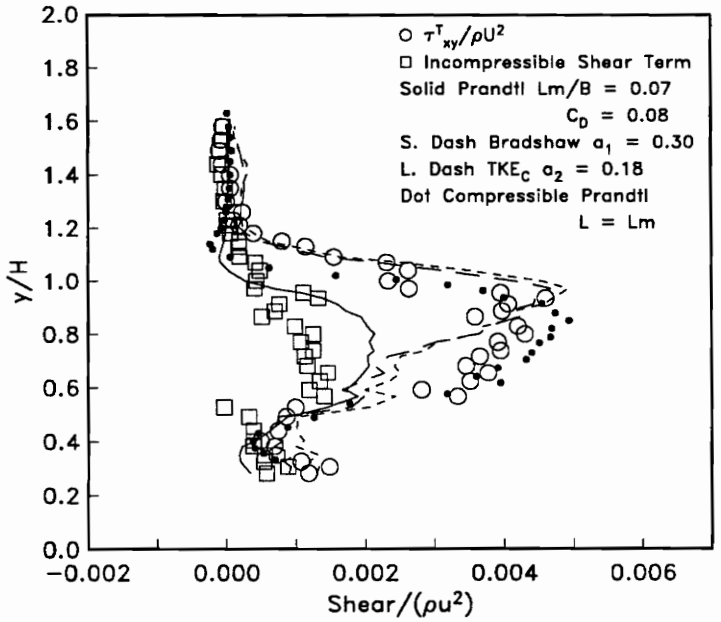

(b) Energy Models

FIGURE 6.7: (a) Prandtl (Eqn. (2.6)) and the Situ-Schetz (= CAMMLE) mixing length shear stress (Eqns. (2.9) or (2.14)) evaluations. (b) Prandtl and Bradshaw incompressible TKE (Eqn. (2.6)), and the new TKE_c (Eqn. (2.8)) evaluations (x/H = 15.).

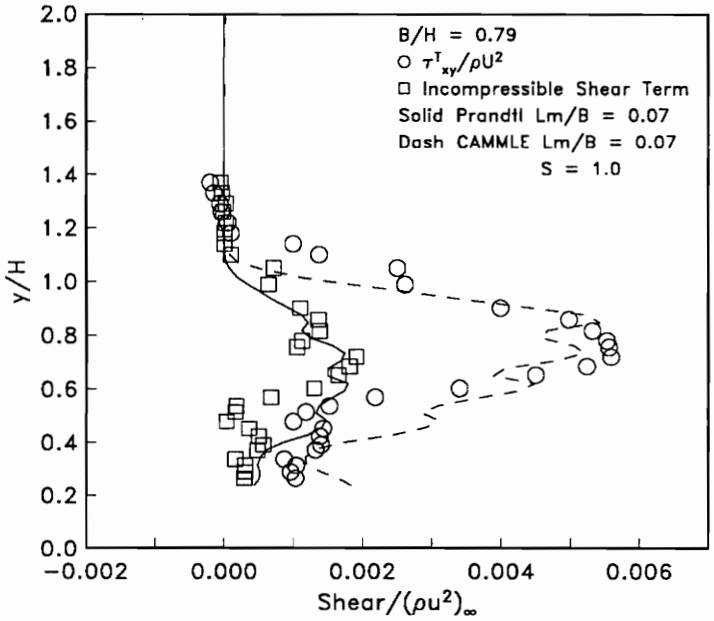

(a) Mixing Length Models

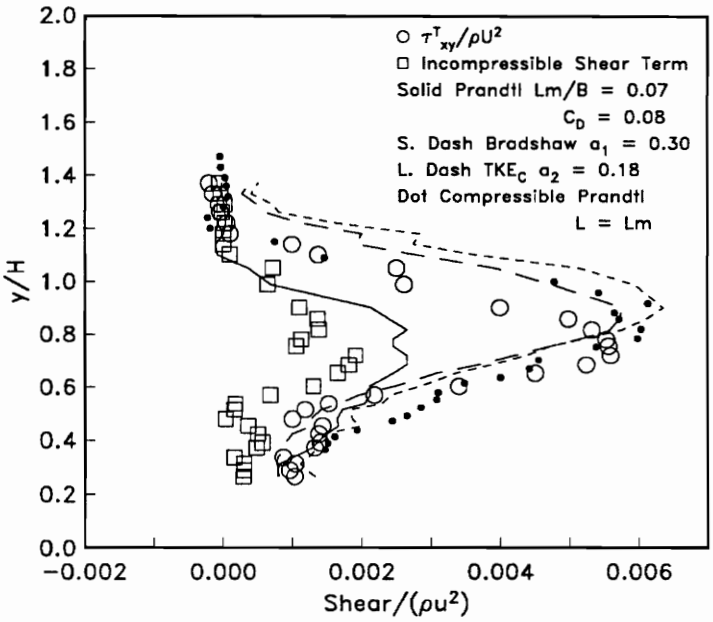

(b) Energy Models

FIGURE 6.8: (a) Prandtl (Eqn. (2.6)) and the Situ-Schetz (= CAMMLE) mixing length shear stress (Eqns. (2.9) or (2.14)) evaluations. (b) Prandtl and Bradshaw incompressible TKE (Eqn. (2.6)), and the new TKE_c (Eqn. (2.8)) evaluations (x/H = 19.).

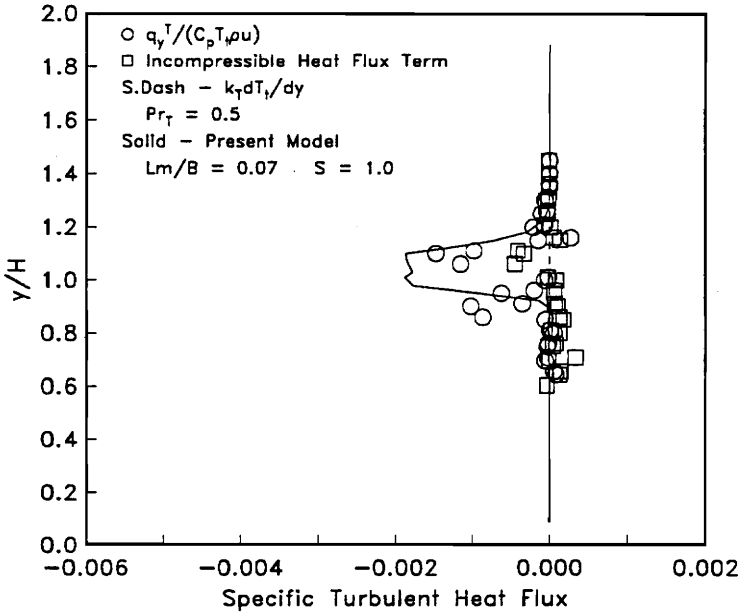

FIGURE 6.9: CAMMLE (Eqn. (2.18)) heat flux evaluations (x/H = 0.2).

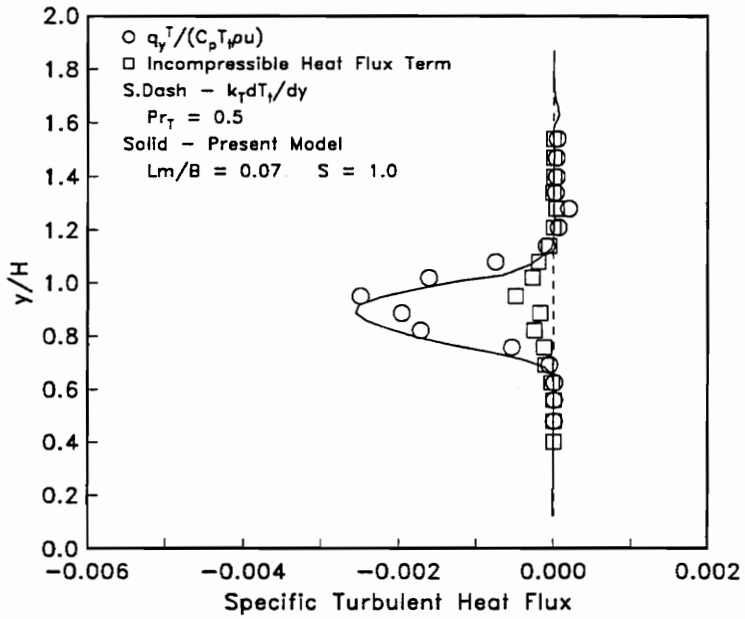

FIGURE 6.10: CAMMLE (Eqn. (2.18)) heat flux evaluations (x/H = 5.0).

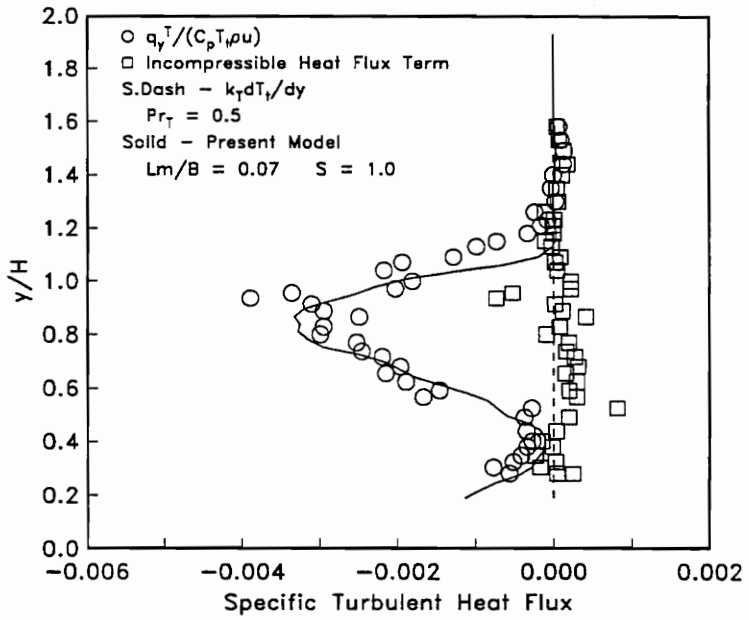

FIGURE 6.11: CAMMLE (Eqn. (2.18)) heat flux evaluations (x/H = 15.).

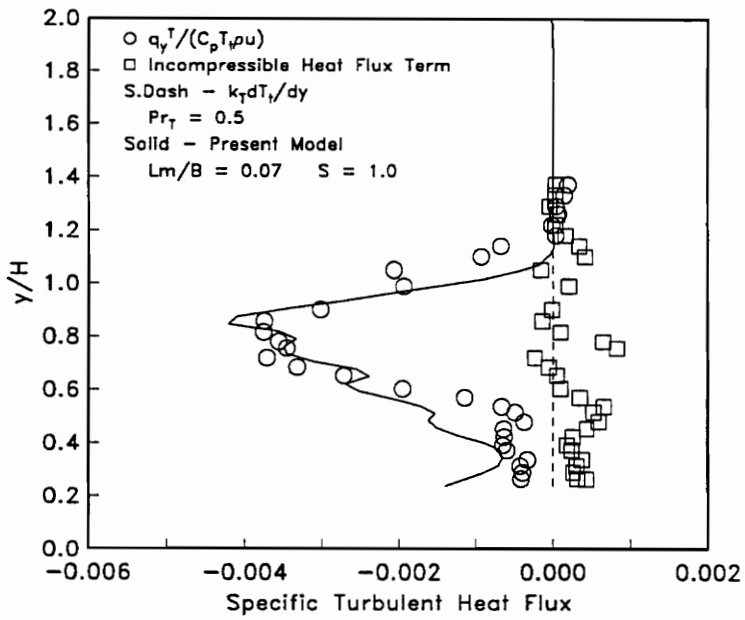

FIGURE 6.12: CAMMLE (Eqn. (2.18)) heat flux evaluations (x/H = 19.).

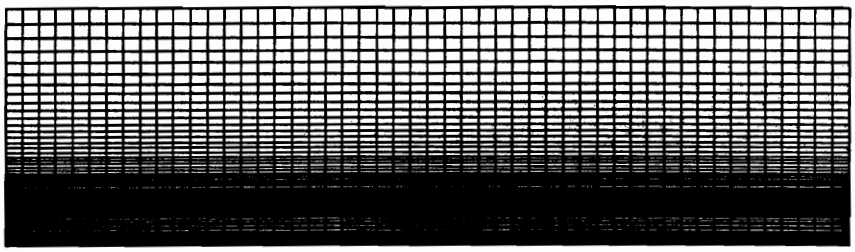

(a)

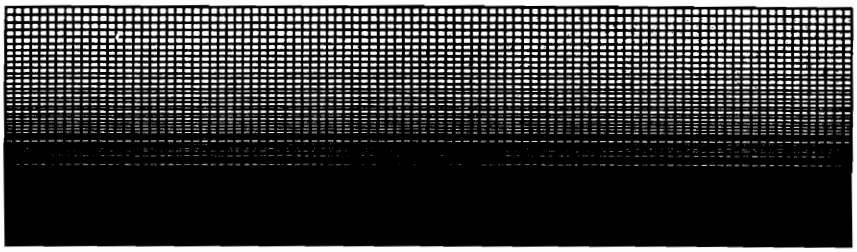

(b)

FIGURE 7.1: (a) Course grid (51x81). (b) Fine grid (101x161).

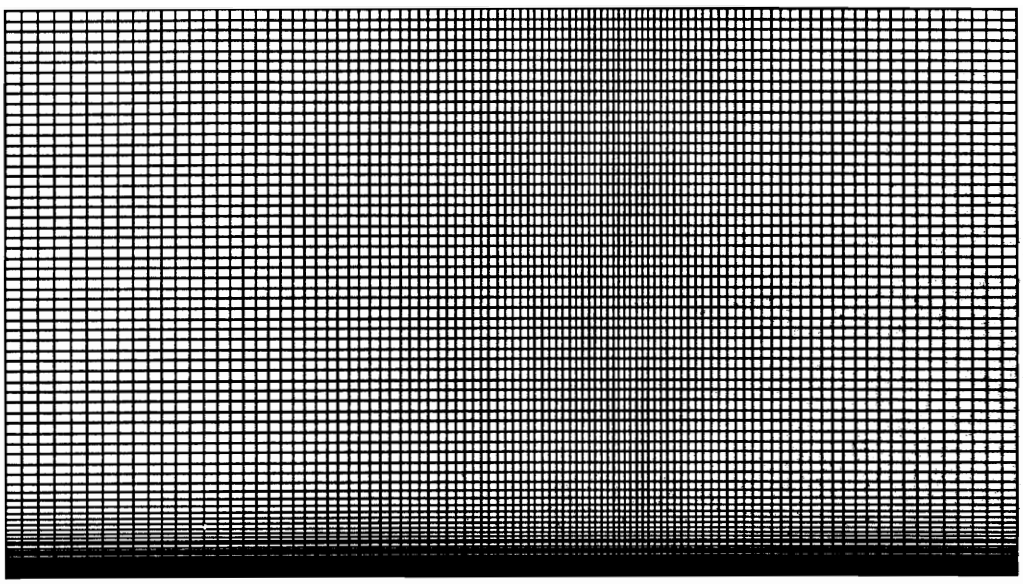

FIGURE 7.2: Shock-boundary layer unit problem fine (101x101) grid.

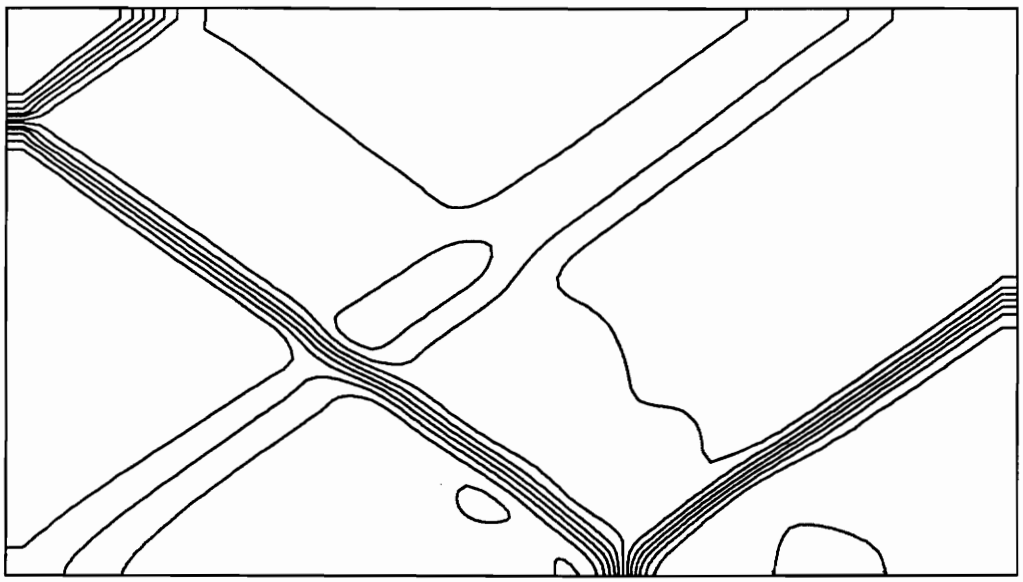

FIGURE 7.3: Shock-boundary layer unit problem TLNS fine grid pressure contour.

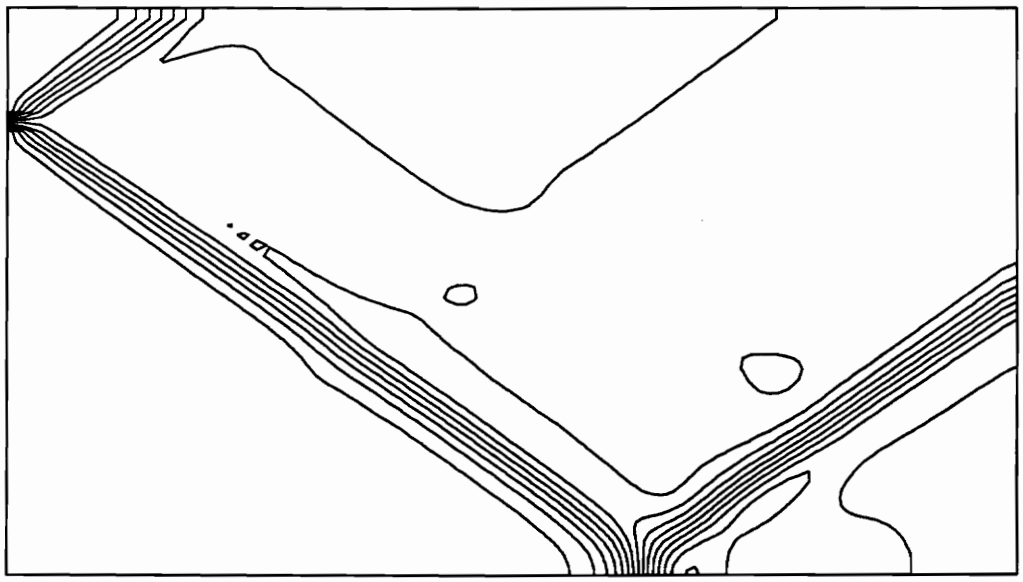

FIGURE 7.4: Shock-boundary layer unit problem PNS fine grid pressure contour.

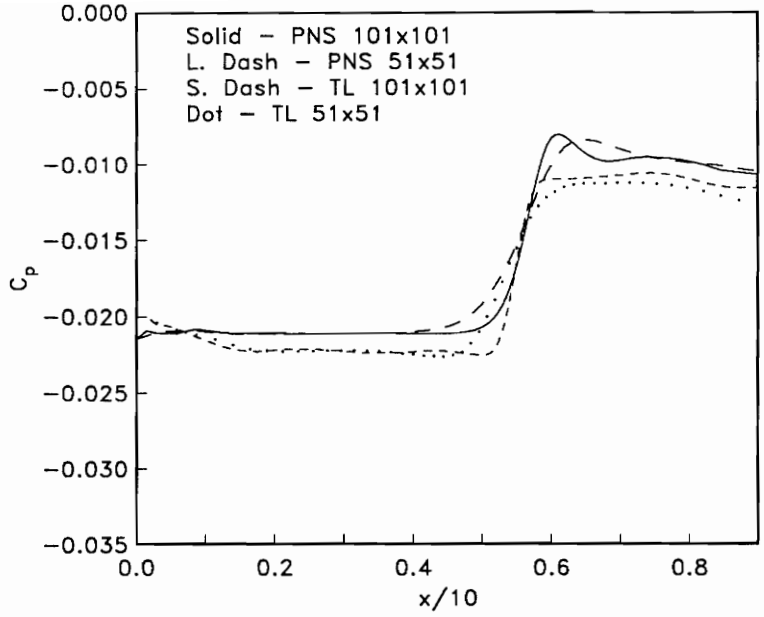

(a) Wall Pressure

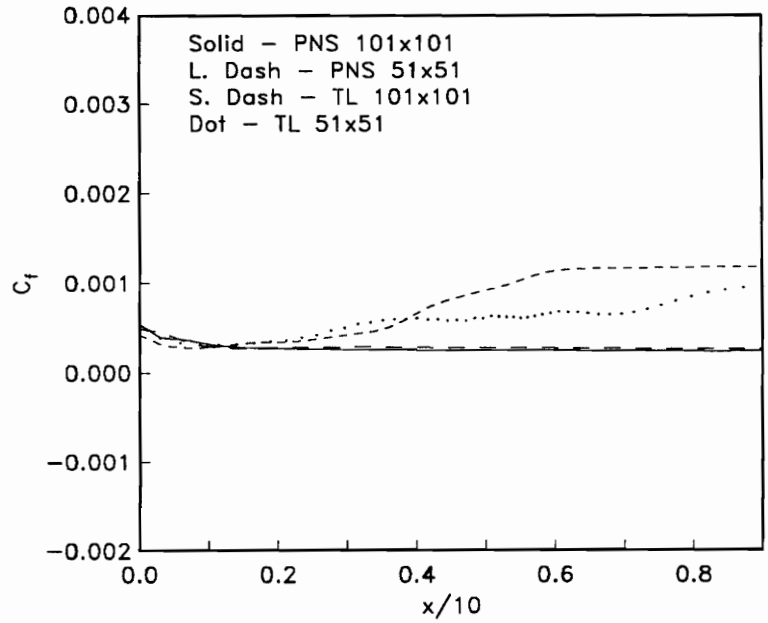

(b) Wall Skin Friction

FIGURE 7.5: Shock-boundary layer unit problem wall pressure and skin friction.

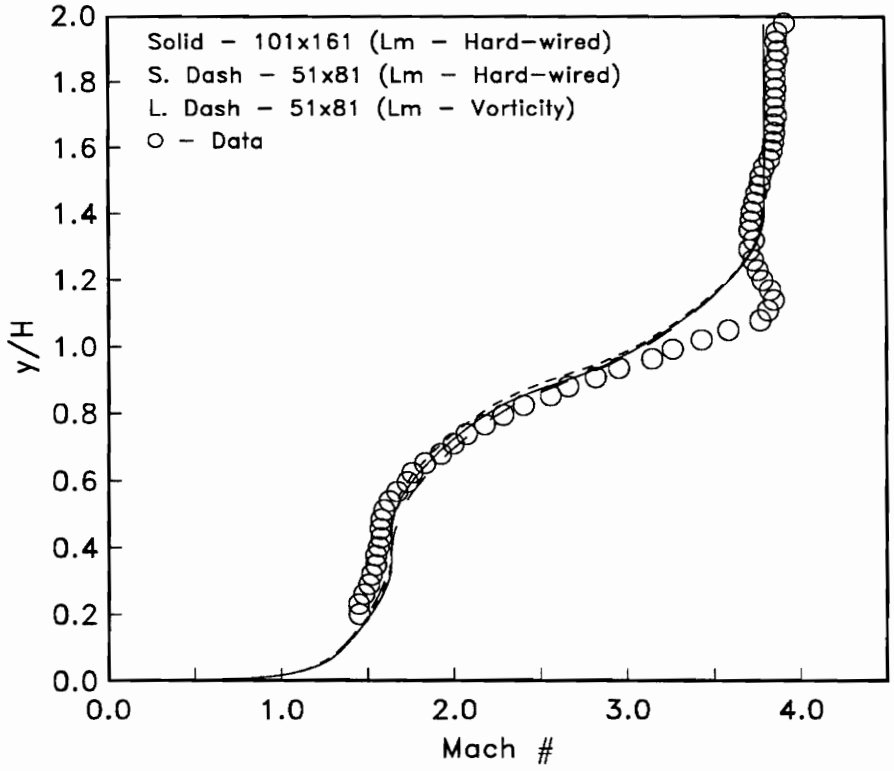

FIGURE 7.6: Present free shear numerical grid convergence and vorticity mixing length Mach number profile (x/H = 15).

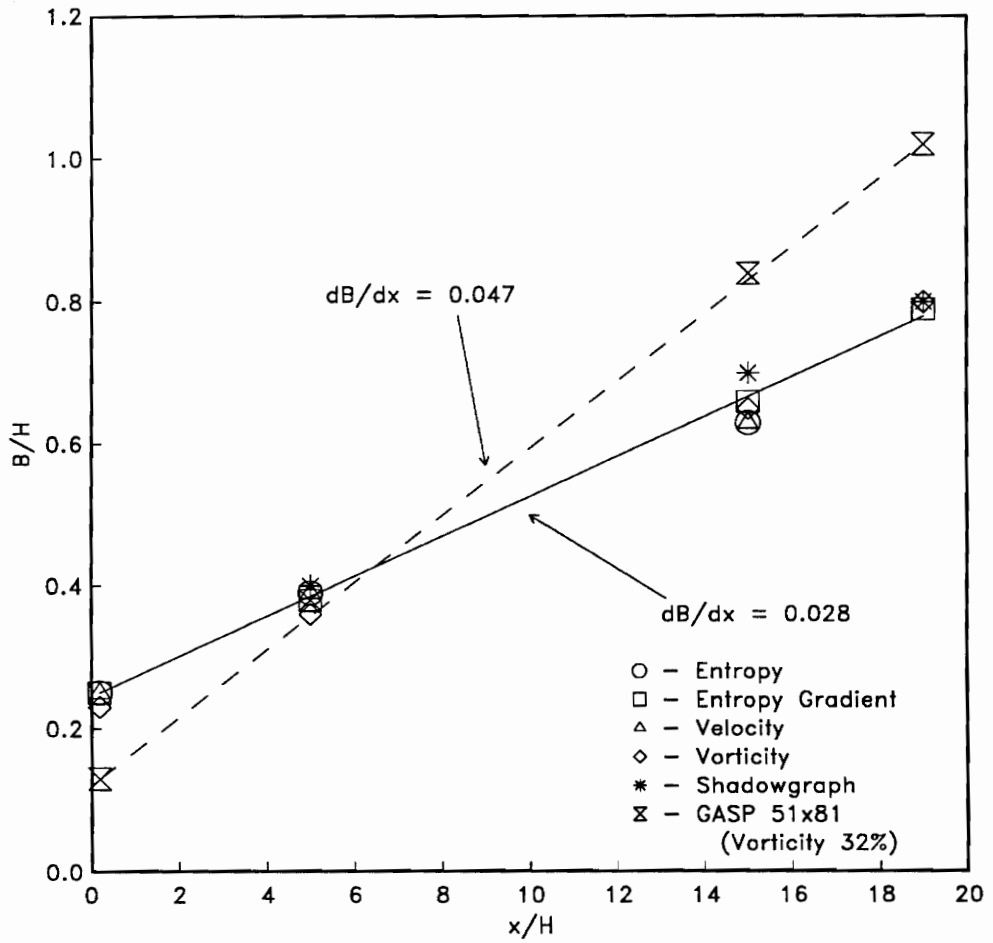

FIGURE 7.7: Comparison of the numerical and experimental shear layer spreading rate.

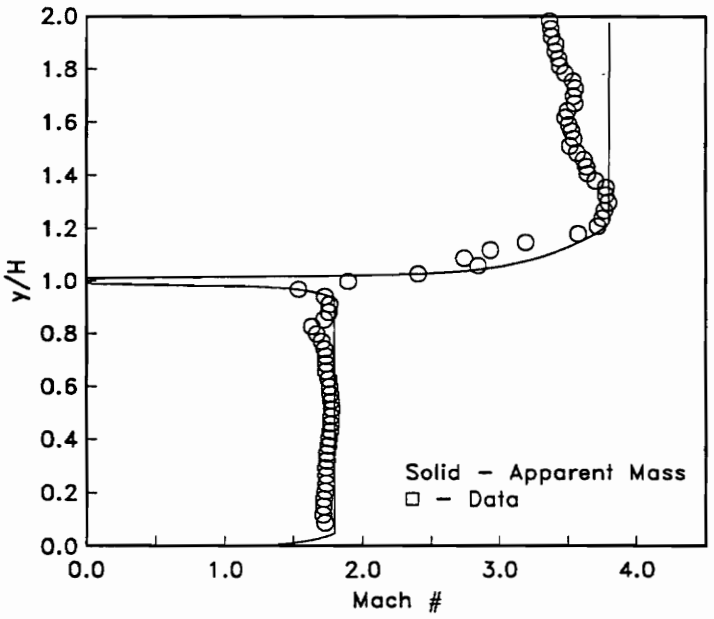

FIGURE 7.8: Numerical (CAMMLE fine grid with hard wired mixing length) and experimental Mach number results (x/H = 0.2).

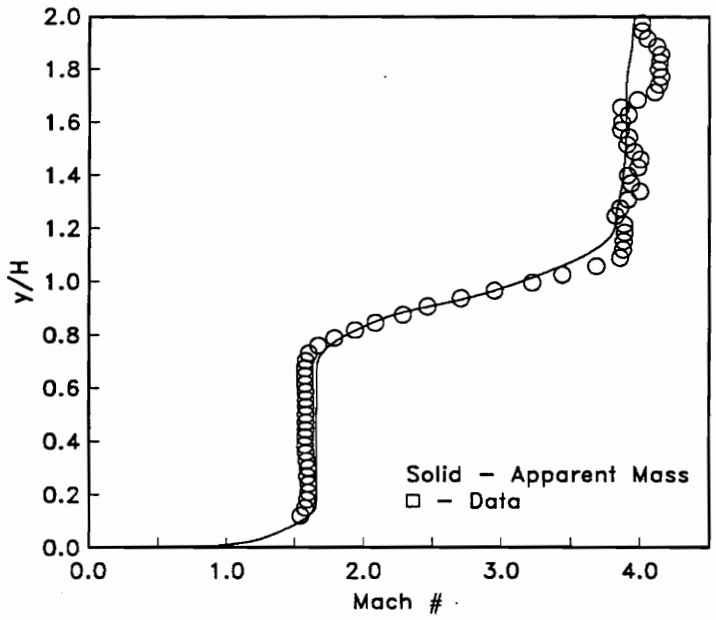

FIGURE 7.9: Numerical (CAMMLE fine grid with hard-wired mixing length) and experimental Mach number results (x/H = 5.0).

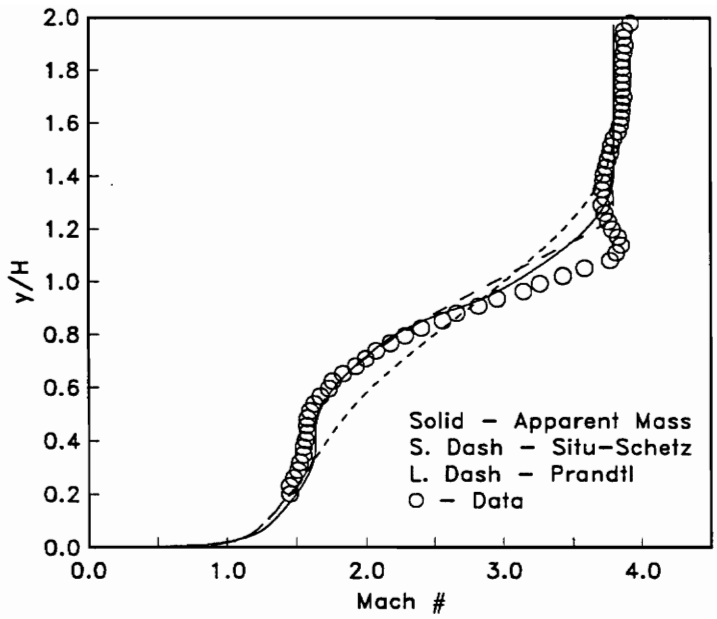

FIGURE 7.10: Numerical (CAMMLE, Situ-Schetz, and Prandtl fine grid with hard-wired mixing length) and experimental Mach number results (x/H = 15.).

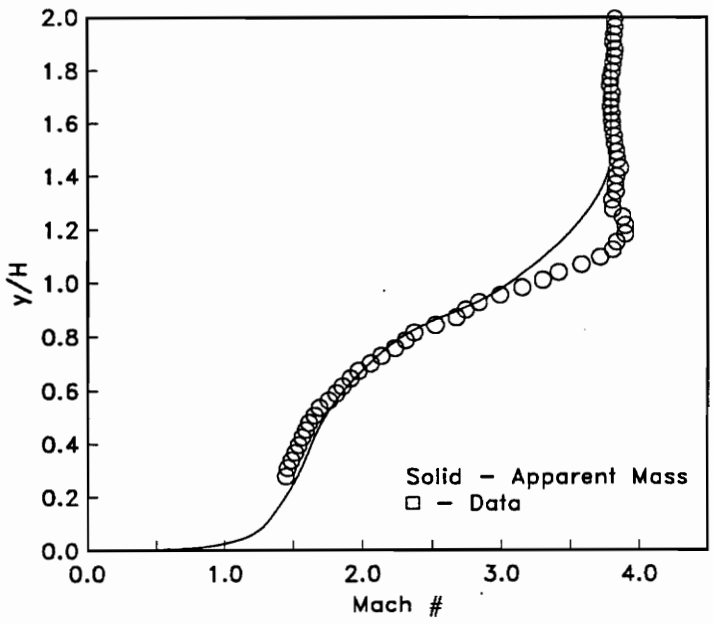

FIGURE 7.11: Numerical (CAMMLE fine grid with hard-wired mixing length) and experimental Mach number results (x/H = 19.).

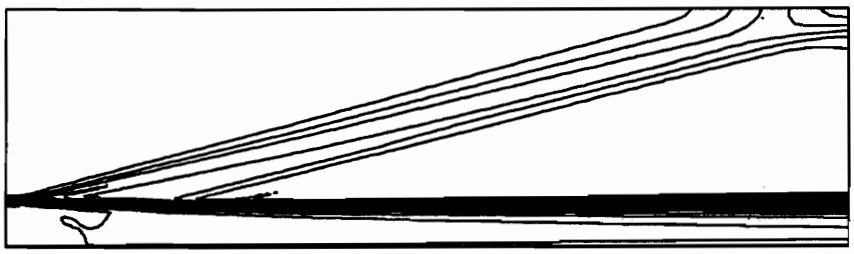

FIGURE 7.12: Numerical density contours (CAMMLE fine grid with hard-wired mixing length).

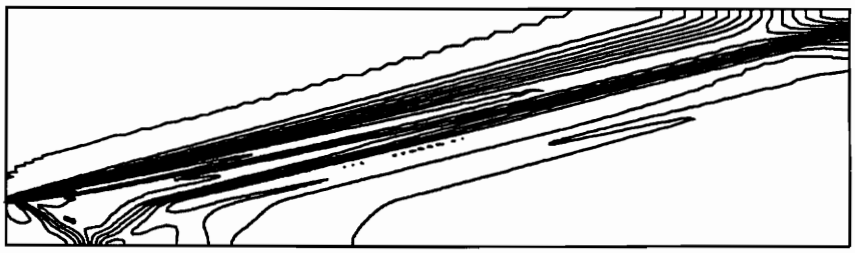

FIGURE 7.13: Numerical pressure contours (CAMMLE fine grid with hard-wired mixing length).

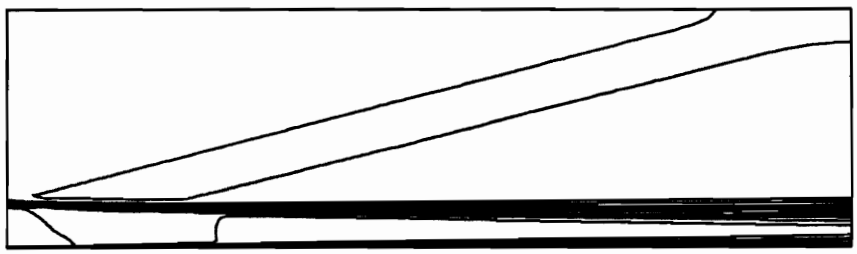

FIGURE 7.14: Numerical velocity contours (CAMMLE fine grid with hard-wired mixing length).

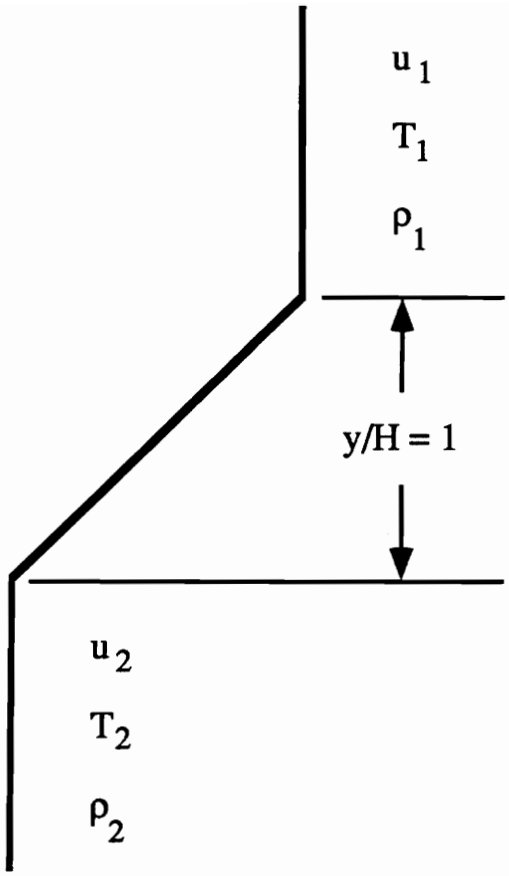

$$\overline{\phi} = (\phi_1 + \phi_2)/2$$

$$\frac{d\phi}{dy} = \frac{(\phi_1 - \phi_2)}{1}$$

FIGURE 7.15: Idealized injection profile.

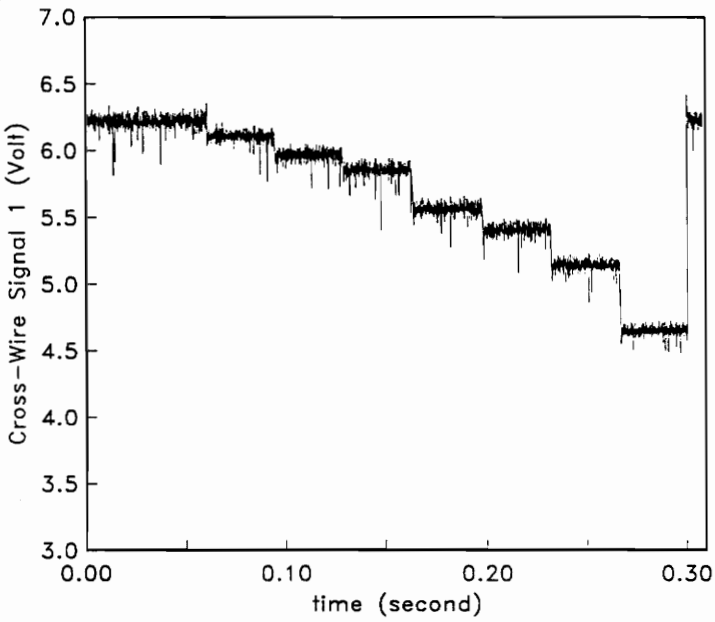

(a) y/H = 1.1

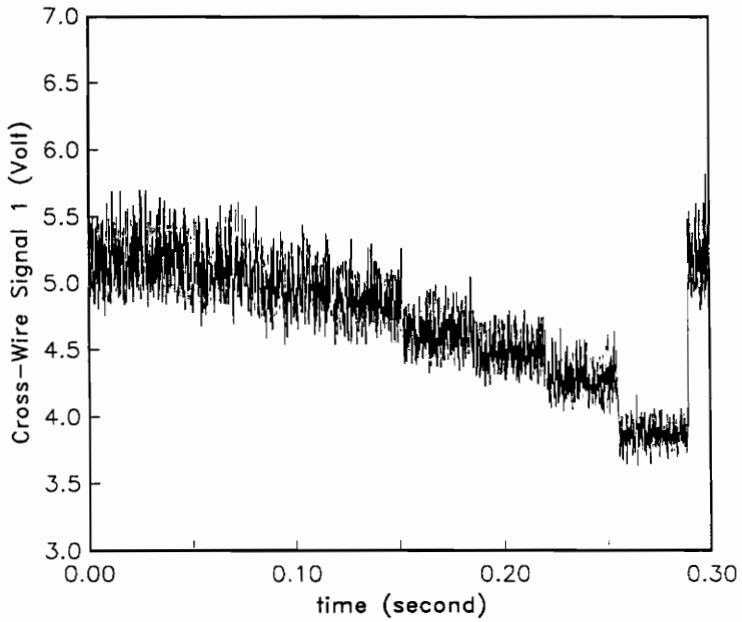

(b) y/H = 0.8

FIGURE A.1: Cross-wire 1 raw voltage time traces at y/H = 1.1 and 0.8 (x/H = 15.).

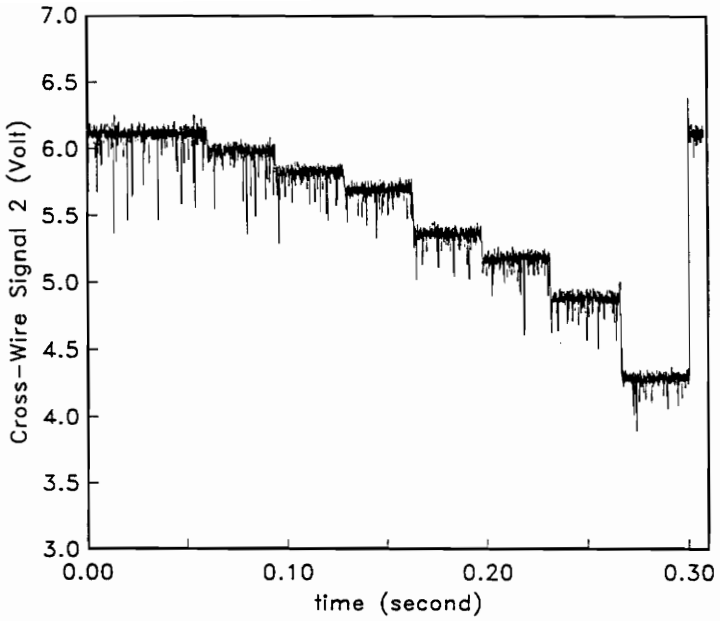

(a) y/H = 1.1

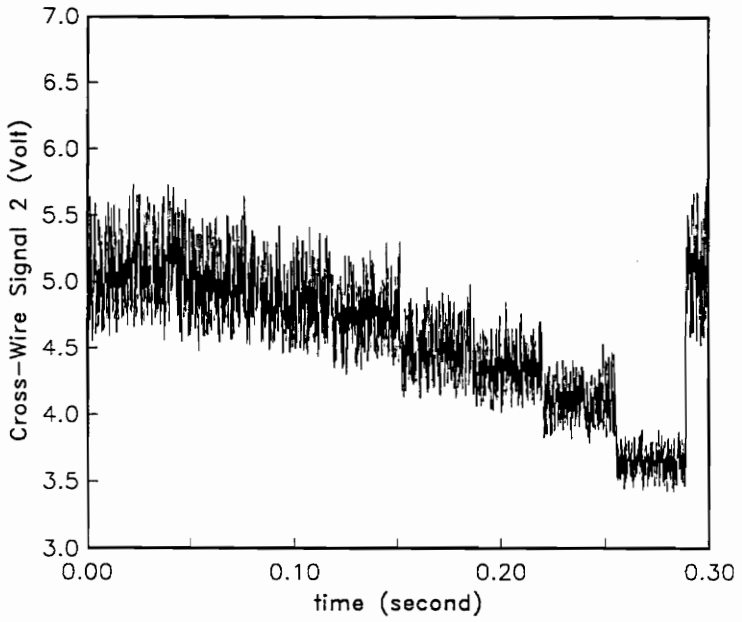

(b) y/H = 0.8

FIGURE A.2: Cross-wire 2 raw voltage time traces at y/H = 1.1 and 0.8 (x/H = 15.).

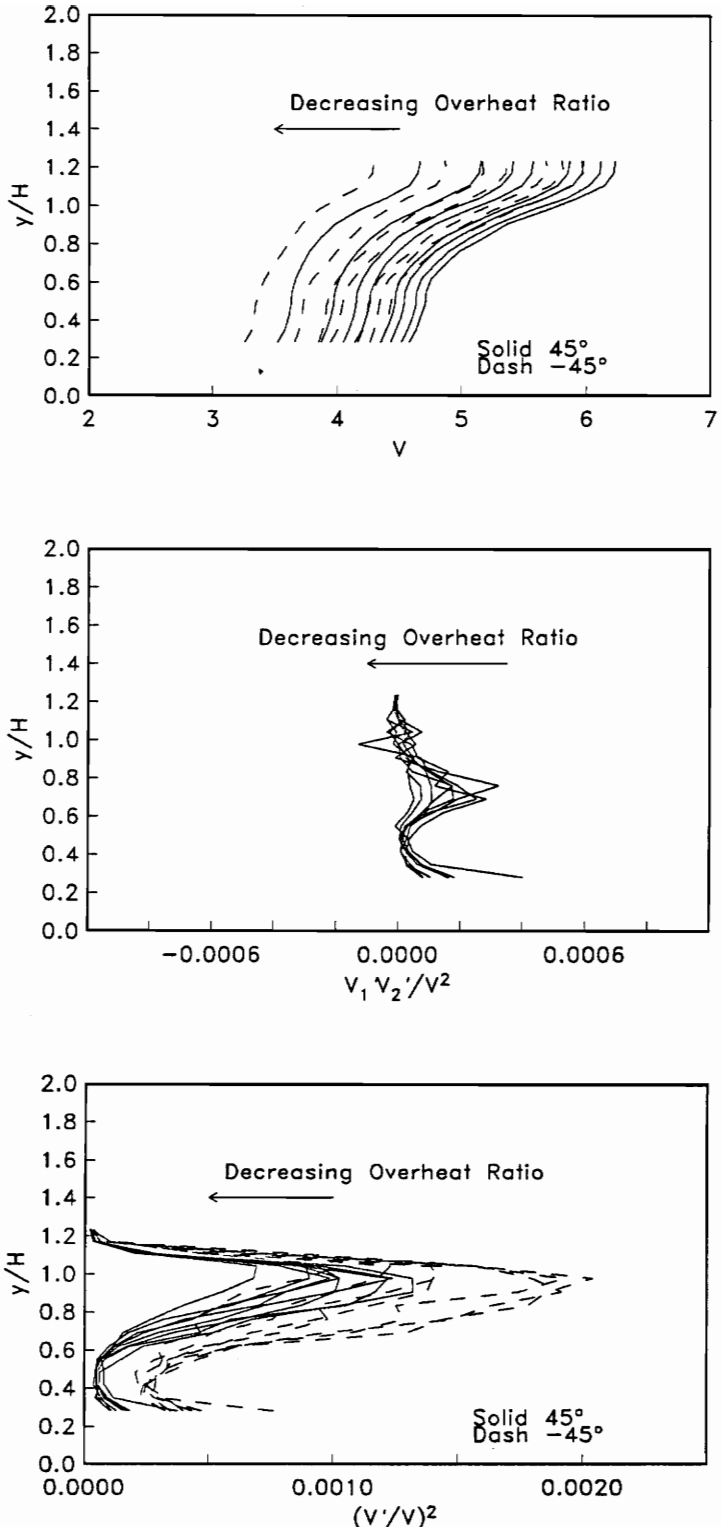

FIGURE A.3: Processed (mean, rms, and correlation) cross-wire voltage profiles (x/H = 15.).

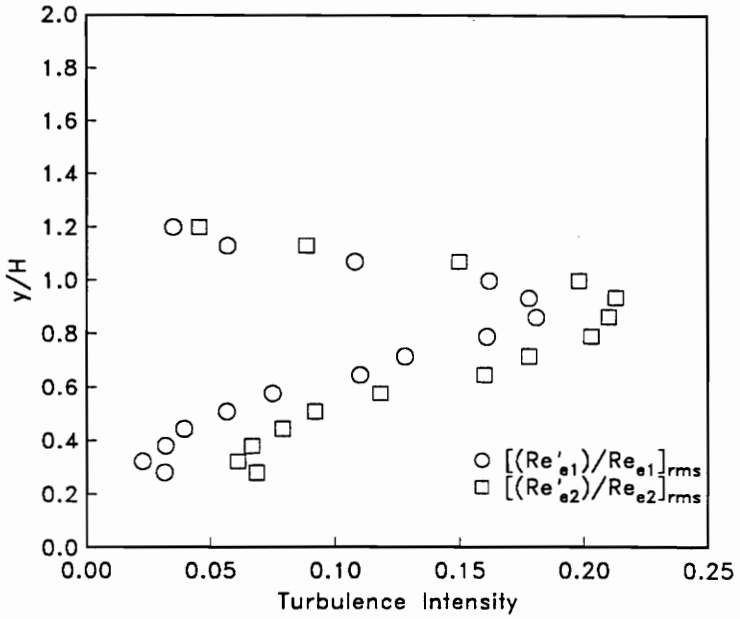

(a) Turbulence Intensity

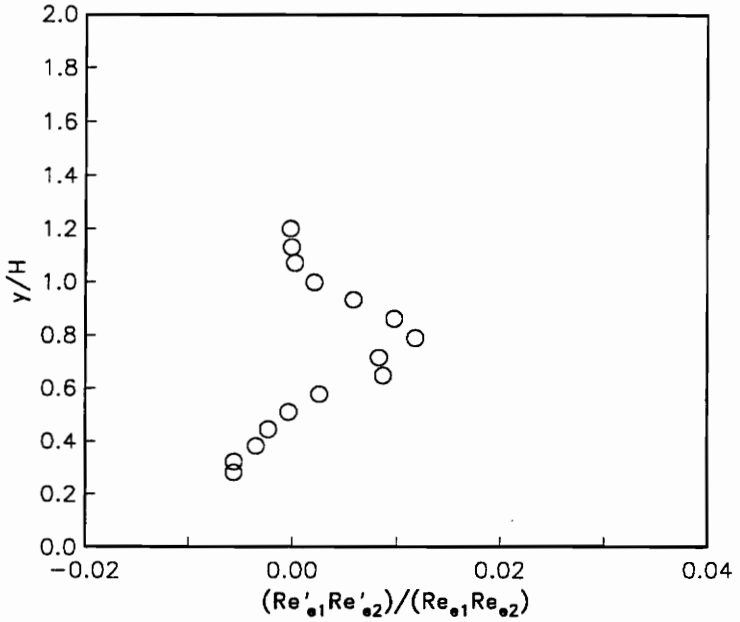

(b) Cross Term

FIGURE A.4: (a) Cross-wire Reynolds number turbulence intensity in cross-wire axes (x/H = 15.). (b) cross-wire Reynolds number correlation between wires 1 and 2.

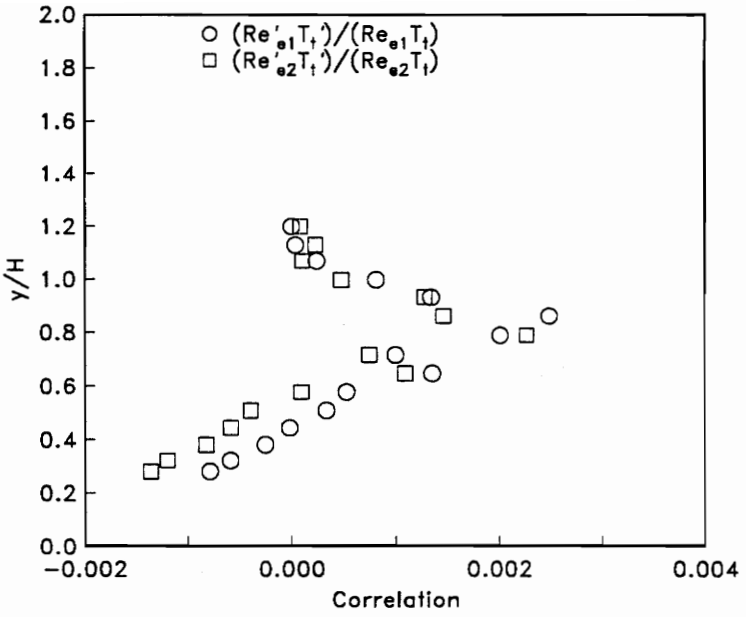

(c) Mass Flux Total Temperature Correlation

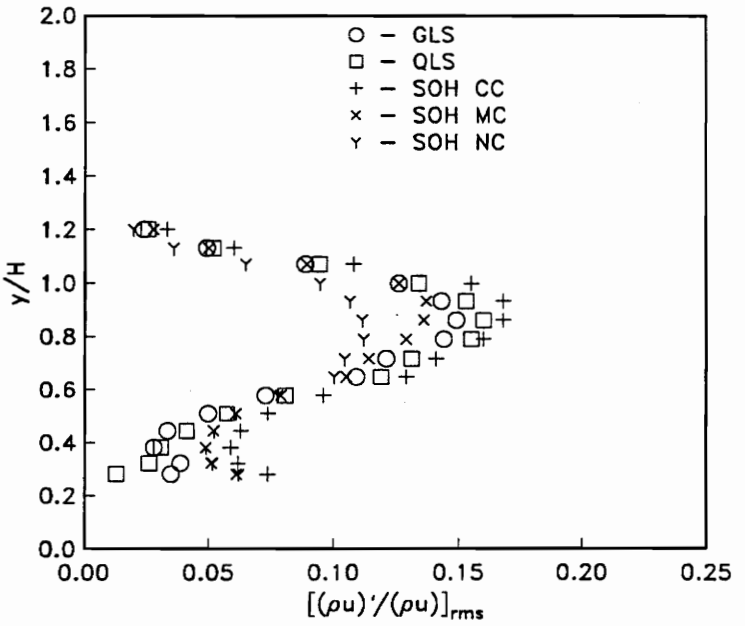

(d) Comparison of Techniques

FIGURE A.4: (c) Cross-wire Reynolds number-total temperature correlation. (d) axial mass flux turbulence intensity comparison of data reduction techniques.

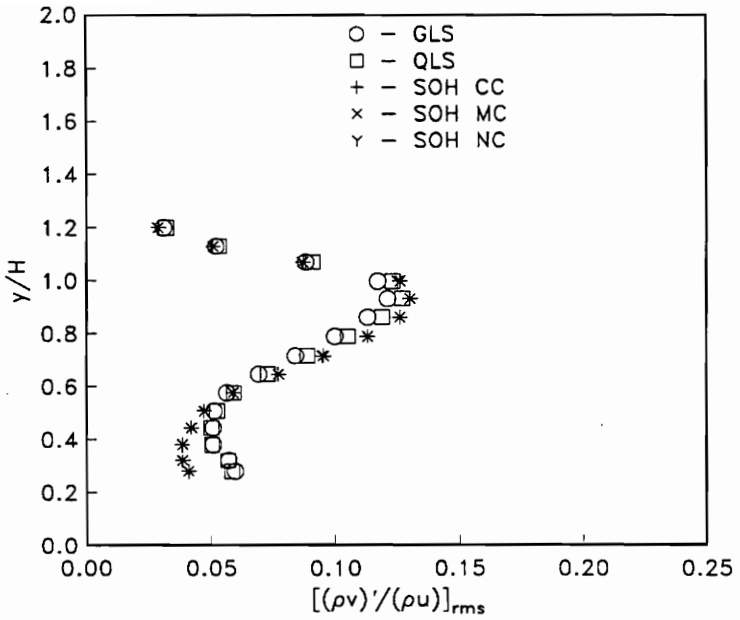

(e) Comparison of Techniques

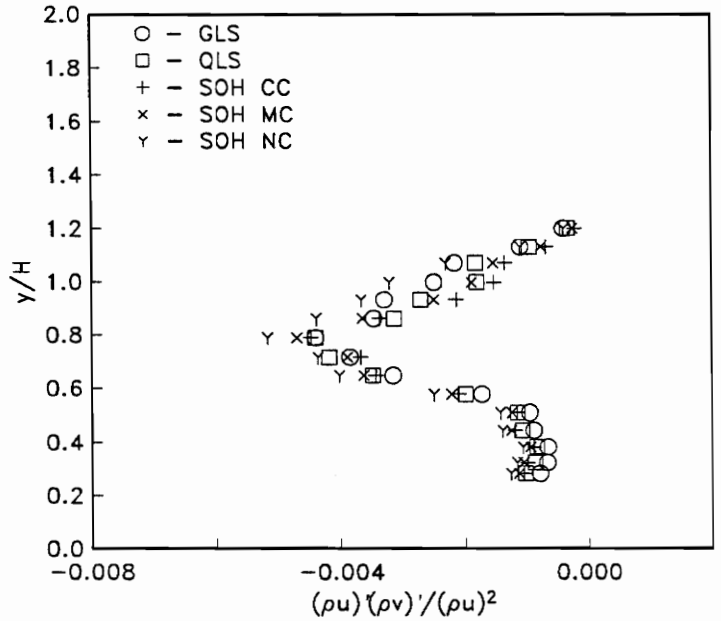

(f) Comparison of Techniques

FIGURE A.4: (e) transverse mass flux turbulence intensity comparison of data reduction techniques. (f) cross-wire shear comparison of data reduction techniques.

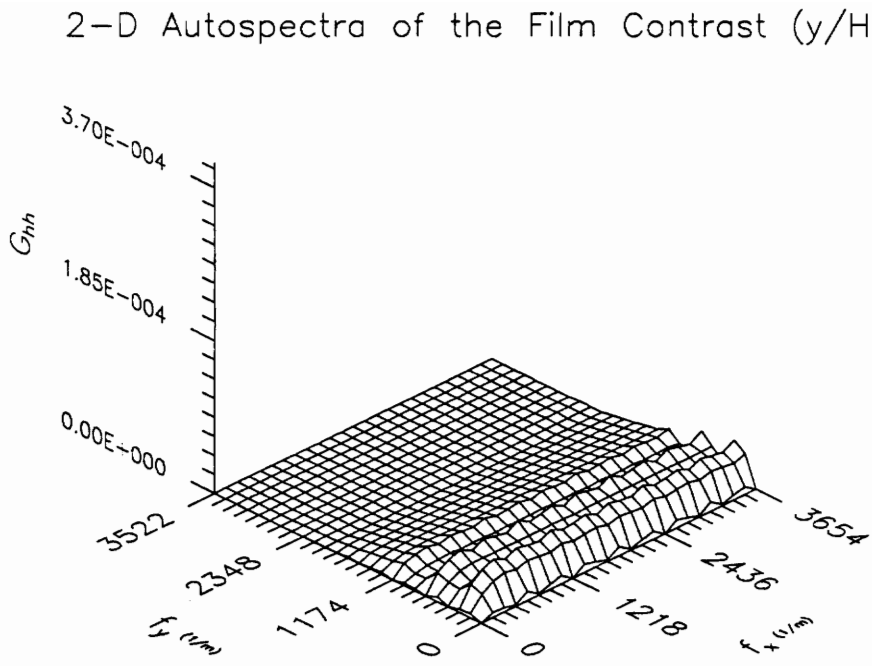

FIGURE A.5: (a) 2-D Shadowgraph film contrast autospectra at y/H = 1.4 (x/H = 15.).

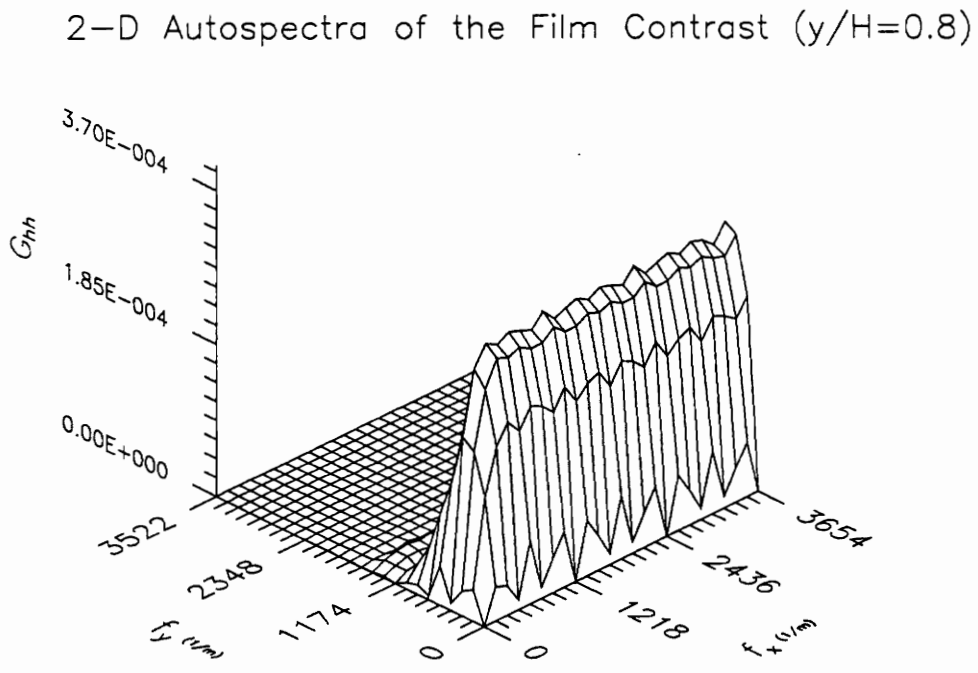

FIGURE A.5: (b) 2-D Shadowgraph film contrast autospectra at y/H = 0.8 (x/H = 15.).

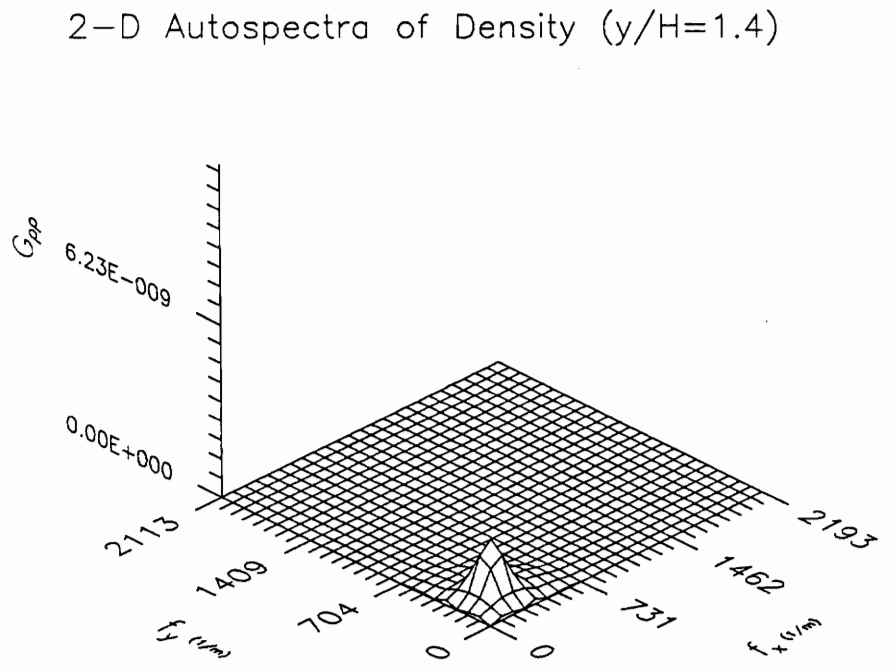

FIGURE A.6: (a) 2-D Shadowgraph density autospectra at y/H = 1.5 (x/H = 15.).

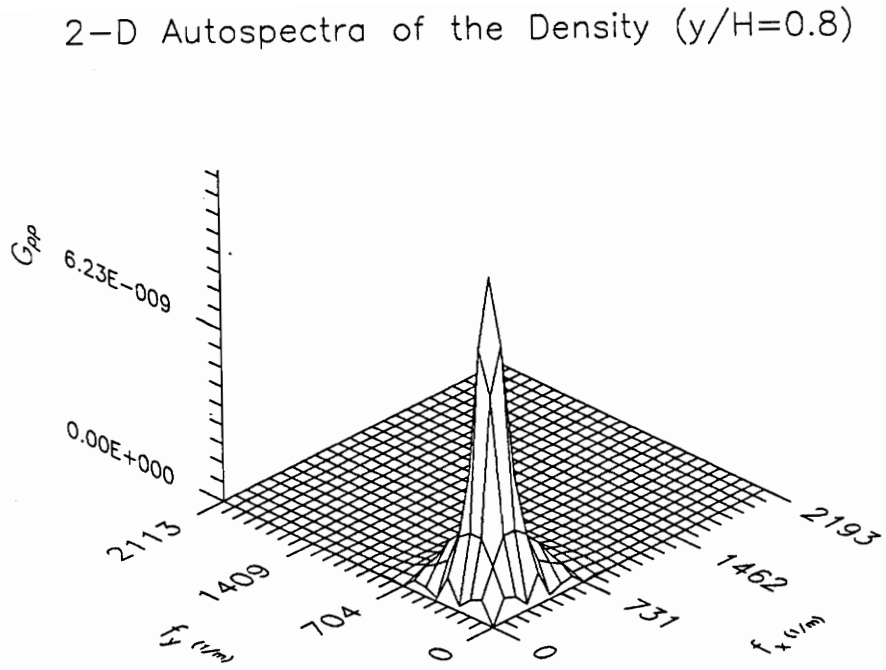

FIGURE A.6: (b) 2-D Shadowgraph density autospectra at y/H = 0.8 (x/H = 15.).

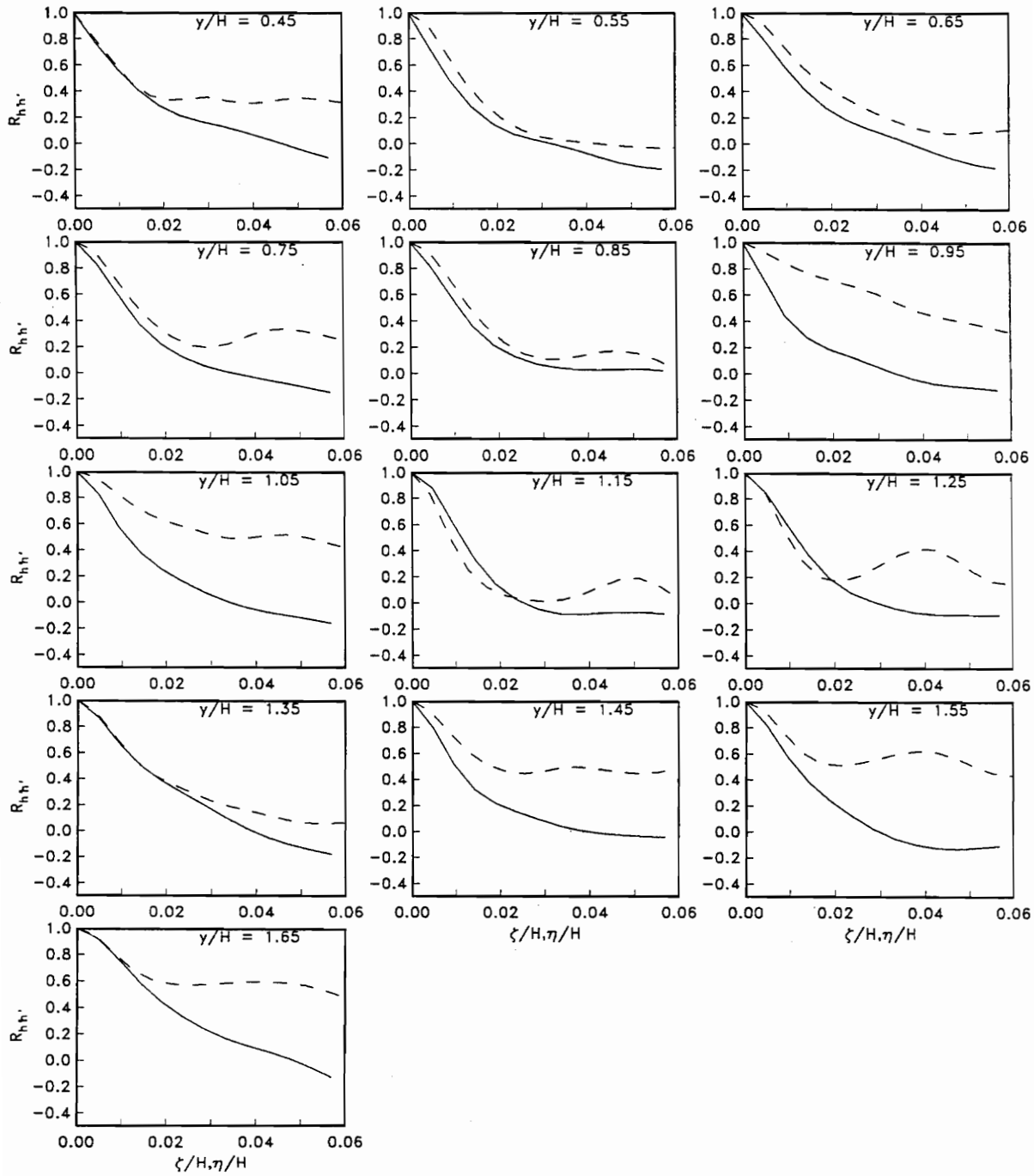

FIGURE A.7: (a) 2-D Shadowgraph film contrast auto correlations along correlation axes (x/H = 5.0).

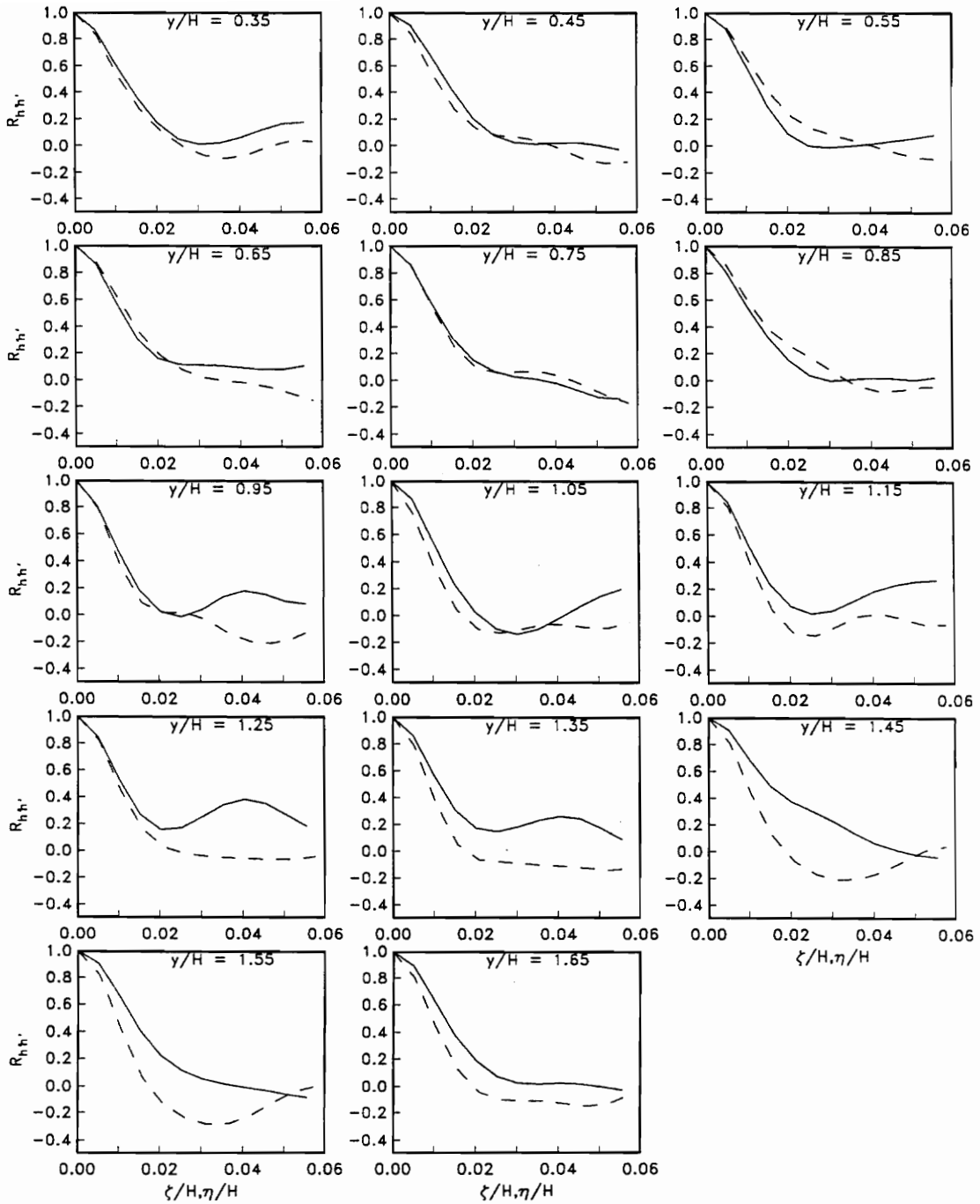

FIGURE A.7: (b) 2-D Shadowgraph film contrast auto correlations along correlation axes (x/H = 15.).

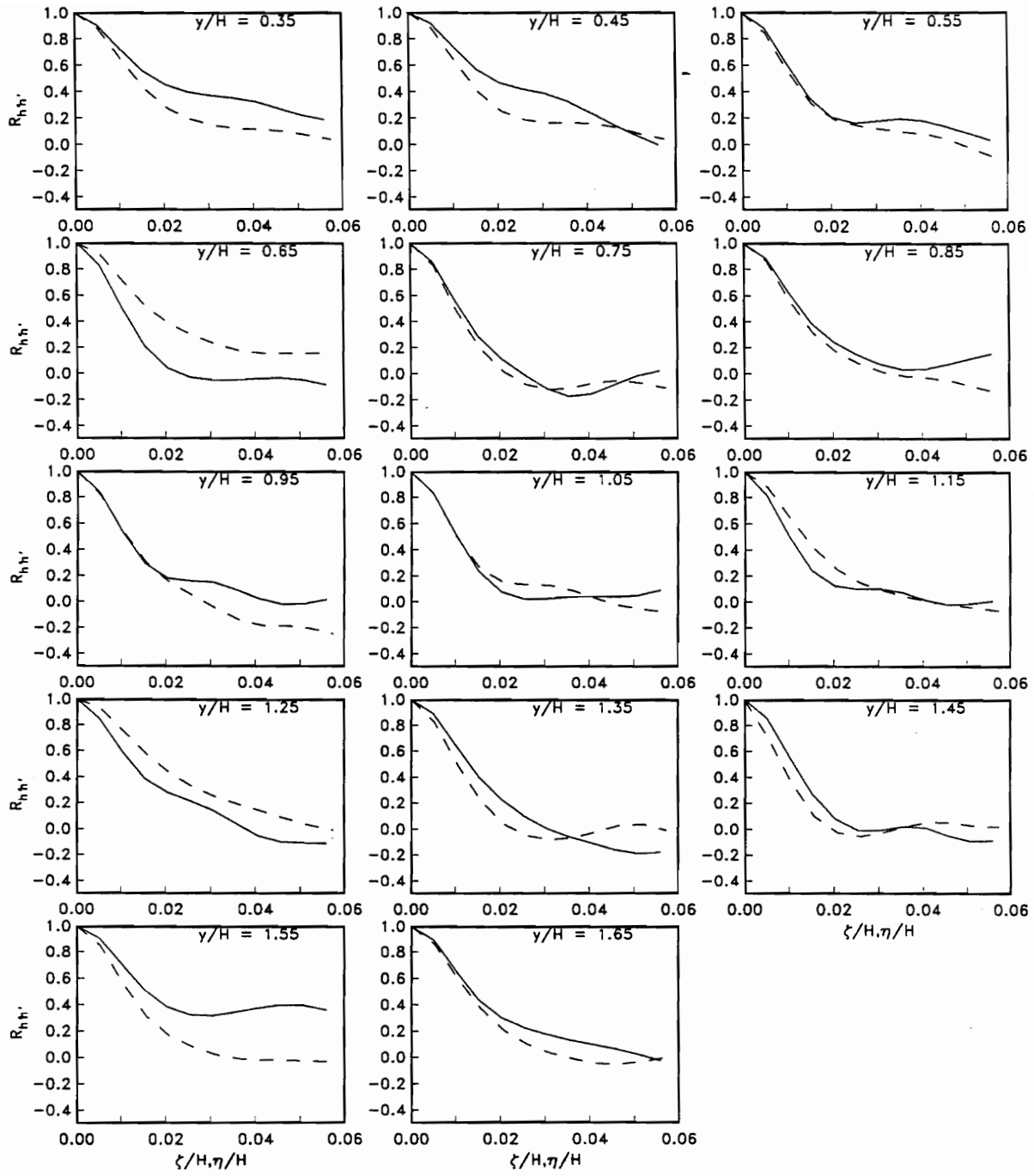

FIGURE A.7: (c) 2-D Shadowgraph film contrast auto correlations along correlation axes (x/H = 19.).

Rodney Dale Welch Bowersox was born July 28, 1965 to Richard D. W. and Shirley A. Bowersox. He graduated from Wilson Memorial High School in June of 1984. He entered Virginia Polytechnic Institute and State University in September 1983, and graduated, in May 1988, Magna Cum Laude with a Bachelor of Science in Aerospace Engineering. Upon completion of his undergraduate study, he entered graduate school in June of 1988. On July 16, 1988, Rodney married the former Selina Louise Berry. He then received his Master of Science degree, in Aerospace Engineering, in January of 1990. After receiving his Master of Science, he enrolled in the Aerospace Engineering Doctorate program, February 1990. He completed this endeavor on September 9, 1992.